The effects of zonal flow on rapidly rotating convection in planetary interiors

Robert John Teed

Submitted in accordance with the requirements for the degree of Doctor of Philosophy

The University of Leeds

Department of Applied Mathematics

July 2011

The candidate confirms that the work submitted is his own, except where work which has formed part of jointly-authored publications has been included. The contribution of the candidate and the other authors to this work has been explicitly indicated below . The candidate confirms that appropriate credit has been given within the thesis where reference has been made to the work of others.

Acknowledgements

I would like to thank all those people who have made it possible for me to complete this PhD. Specifically I would like to mention my parents and my late maternal grandmother; without their influence and support over many years of education I would not have made it to this stage. My wife has been fully supportive throughout my PhD: encouraging me during the difficult times and sharing in the joy of the good times.

Last, but not least, I would like to thank my supervisors Prof. Chris Jones and Prof. Rainer Hollerbach. They have always made the time to answer the numerous research related queries and problems that have arisen. I also thank them for the many informative discussions during the last four years.

The funding for this research was provided by the Science and Technology Funding Council and the University of Leeds.

This research has been carried out by a team which has included myself, Prof. Chris Jones and Prof. Rainer Hollerbach. My contribution to the work has been the adaptation of pre-existing numerical codes (provided by Prof. Chris Jones) to the problems discussed in the thesis as well as acquiring the numerical and analytical results presented throughout. Profs. Chris Jones and Rainer Hollerbach have provided guidance in accordance with standard supervisory roles. The article has been written by Robert Teed. Part of the work discussed in chapters 2 and 3 has been published in the journal ‘Geophysical and Astrophysical Fluid Dynamics’ as Teed *et al.* (2010).

Abstract

Convection in the fluid regions of planetary interiors plays an important role in determining the dynamics of many physical phenomena present there. The fluid motions driven by thermal and compositional convection in the Earth's core transport heat out from the planet's iron rich core and are thought to maintain the geomagnetic field via dynamo action. Convection is also believed to produce the zonal flows and multiple jets observed in the atmospheres of the gas giants, most famously in the Jovian atmosphere.

A particular interest in the interaction between convection and zonal flows, in the non-magnetic case, is maintained in this work. Equations relevant in plane layer geometry and the annulus geometry are derived. Linear and non-linear equations are solved numerically using a collocation and a semi-implicit method respectively. The onset of convection with a basic state zonal flow is studied in the linear cases. In the plane layer model the basic state zonal flow is maintained by a thermal wind. Conversely, the zonal flow is produced by the Reynolds stresses in the annulus model. Therefore two quite different models are considered in this work.

Thermal instabilities are studied with baroclinic and barotropic instabilities also arising in the plane layer and annular geometries respectively. Zonal flows are found to be both stabilising and destabilising depending on whether the instabilities associated with the shear can manifest themselves. The non-linear simulations provide strong zonal flows and multiple jets reminiscent of Jupiter's banded structure, as well as periodic bursts of convection. This bursting phenomenon is shown to be necessarily maintained by a zonal flow and a mean temperature gradient.

Contents

List of figures

List of tables

Chapter 1

Introduction

1.1 Motivation and background

Convection is a natural phenomenon affecting the dynamics of many fluids in geophysical and astrophysical systems. Numerous bodies have the need to transport heat out from their hot cores to the surface. When part of a system's structure contains a fluid, the heat can be transported by convection, via fluid motions, as well as conduction and radiation. Examples of bodies in our Solar system that are known to have convecting fluid regions include the Sun, the Earth and the gas giant planets (for example, Jupiter). Motion of an electrically conducting fluid was proposed by Larmor (1919) as a possible origin of the Sun and the Earth's magnetic fields, via dynamo action. Hence an understanding of convection is fundamental for developing theories to explain the existence of dynamos in geophysical and astrophysical bodies.

The laws governing dynamo theory arise from the equations of fluid dynamics and electromagnetism; namely the Navier-Stokes equations and Maxwell's equations respectively. Analytical solutions of these equations are available in only rather special circumstances, due to their complex nature. However, in recent years, numerical solutions have been possible with the aid of improved computer resources. Indeed, we shall look for numerical solutions as part of the work in this thesis. However, we shall not be including the effects of magnetic fields in order to first gain an understanding of the underlying convection. Further work could certainly be undertaken with the addition of magnetic fields to the models that we shall discuss. Due to the exclusion of electromagnetic effects we discuss the equations governing fluid motion, but not Maxwell's equations, in section 1.2.

Thermal convection originates from the tendency of warm fluid to expand, become less dense and rise above cooler, denser fluid. This process allows for the successful transport of heat from the centre of an astrophysical body assuming the core is warmer than the surface. However, there is also the possibility of compositional convection if the fluid is not compositionally homogeneous. This can occur even in isothermal conditions and is driven by light material released into the fluid where its surroundings are made up of more dense material. In this thesis we focus on thermal convection though much of the dynamics is similar for compositional convection. An interesting addition to the work in this thesis could be to include the effects of compositional convection to the models we discuss, which would create a 'double-diffusive' system.

We intend for the work in this thesis to be most relevant to dynamical processes in the Earth's interior and the Jovian atmosphere. However, there may be broader applications of the work in other areas of astrophysical fluid dynamics, planetary science and atmospheric science. In the following two subsections we discuss the structure of, as well as a background of convection in, the Earth and Jupiter. We also define and discuss *thermal winds* and *zonal flows* since they are of primary interest to the work undertaken in this thesis. Indeed, our study is largely concerned with how thermal winds and zonal flows interact with convection in various models. Although we shall not include the effects of magnetic fields in our models, we discuss some of their attributes in this section in order to gain an insight into why the study of convection is crucial to understanding dynamo action.

1.1.1 Convection in the Earth's core

We first discuss the structure of the Earth, which has been identified from seismic observations. Beneath the Earth's crust there is a high density core surrounded by a lower density mantle, with the core-mantle boundary (CMB) located approximately 3480km from the planet's centre. The core itself is subdivided into a solid inner part and a liquid outer part with the inner-core boundary (ICB) found approximately 1220km from the centre of the Earth. Hence the inner core radius is approximately 0.35 times smaller than the total core radius. Transverse seismic waves are unable to propagate in the outer core indicating that it must be a fluid. A diagram of the structure of the Earth is displayed in figure 1.1. Although convection in the mantle takes place (see, for example, Bercovici, 2007), the material is not sufficiently electrically conducting and the motion is too far slow to drive a dynamo. Consequently, the iron rich core is thought to be the source of the geodynamo. When modeling the fluid dynamics inside the Earth's core, spherical shells are the most relevant geometry although research is often performed in the simpler full sphere geometry. However, this neglects the inner core which may have significant influence on the magnetic field (Hollerbach & Jones, 1993).

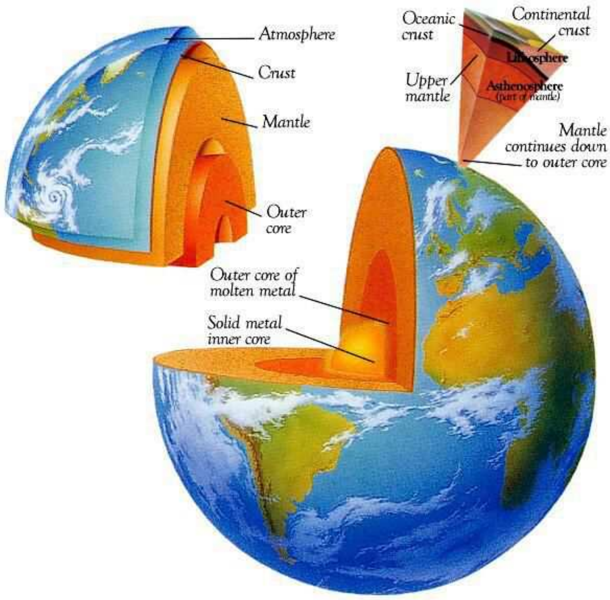

Figure 1.1: A diagram showing the structure of the Earth.

The iron in the outer core gives rise to the desired electrically conducting fluid for dynamo action described by Larmor (1919). This action maintains the geomagnetic field. When considered over a sufficiently long period of time, the Earth's magnetic field averages to a dipole aligned with the rotation axis. However, the field significantly changes on timescales varying from seconds to millennia; this is referred to as the secular variation. Examples include the reversal of the magnetic field, occurring over millennia (Jacobs, 1984) and the westward drift of magnetic features which is observable over much shorter timescales (Bullard *et al.*, 1950). Many of the geodynamo's characteristics are reproduced in numerical simulations (see, for example, Glatzmaier & Roberts, 1995; Sakuraba & Kono, 1998; Christensen *et al.*, 2001). The progress made on understanding the geodynamo has been reviewed by, for example, Hollerbach (1996); Fearn (2007).

The Earth is known to have possessed its magnetic field for at least 3.5 billion years (see, for example, Merrill *et al.*, 1996). However, the material in the core has electrical resistance, which leads to Ohmic dissipation. It has been shown (see, for example, Moffatt, 1978) that this dissipation would lead to the decay of the Earth's magnetic field on a 20,000 year timescale unless the fluid in the core is driven by some other source. The most likely driving force of fluid motion is thermal and compositional convection arising from the heat and light material leaving the inner core. However, other possible energy sources, such as precession and tidal forcing, have also been considered (Malkus, 1994). Compositional convection is certainly thought to supplement thermal convection in the Earth's core (Fearn, 1998), however we shall concentrate on the latter in this work. Geodynamo models driven by convection are discussed by Jones (2000). The outer core is thought to be in a turbulent state of motion since the viscosity there is very small. This causes significant numerical challenges when performing computer simulations and in fact the larger turbulent value of the viscosity has to be used since current computers cannot resolve the smallest length scales (see Braginsky & Roberts, 1995, for a discussion of core turbulence).

Heat is known to escape from the Earth at a rate of approximately 44TW. In order for the outer core to be convecting, the adverse temperature gradient must be steeper than the adiabatic temperature gradient. In other words, there must be enough heat flux to be transported so that convection as a transfer process of heat is favourable. We discuss a simple problem of the onset of thermal convection in section 1.4. Convection takes place when there is more heat flux to transport than is possible from conduction down the adiabat alone. The current thought is that, even with conservative estimates of the total heat flux, there must be convection occurring near the ICB. However, nearer to the CMB there may be regions stable to convection if the CMB heat flux is low enough for conduction alone to transport the necessary heat outwards. Jones (2007) discusses these ideas in more detail and Olson (2003) considers how the core and mantle interact. The additional possibility of compositional convection complicates matters further (Jones, 2007).

The fact that the Earth is rotating also has a role to play. We shall see in section 1.3 that strong rotation causes the fluid velocity to prefer to be independent of the axis parallel to rotation, z, say (Proudman, 1916; Taylor, 1922). This will cause the convection patterns to order themselves into columns in the z-direction (Roberts, 1968; Busse, 1970). For discussion of fluid motion in spherical shells such as the Earth's core it proves useful to define a hypothetical cylinder, which runs from pole to pole parallel to the z-axis and just touches the extrema of the inner core; the tangent cylinder (TC). We do this in order to divide the system into two distinct regions: inside the tangent cylinder (ITC) and outside the tangent cylinder (OTC). Columns of fluid will clearly be of significantly different lengths in the two regions. If a column of fluid moves from OTC to ITC then it necessarily must be split in two, which clearly requires strong z-dependent motion. This suggests that there is unlikely to be much transfer of fluid across the TC. Furthermore, due to the spherical geometry, the columns of fluid ITC will increase their length as they move out radially whereas OTC the opposite is true. The lack of z-dependent motion also has further consequences for convection. Heat can be more easily transported OTC since the predominant outward direction is perpendicular to z. However, ITC it is mostly motion in the z-direction that is required to transport heat out radially. Inevitably, this motion must vary more strongly with z and thus a stronger driving force is required for convection to onset ITC. This leads to differing efficiencies of heat transport inside and outside the TC.

The temperature profile of the Earth's core may vary in directions other than the radial. When this is the case a *thermal wind* is created, which is an azimuthal flow which varies with z. The jet stream in the Earth's atmosphere is a famous example of such a thermal wind, driven by the pole-equator temperature difference. Thermal winds are also believed to occur in the Earth's core (Olson & Aurnou, 1999; Sreenivasan & Jones, 2005, 2006) where warmer regions near the poles lead to anticyclonic vortices which can be detected in the secular variation as the geomagnetic field is advected by the flow. This process has been modeled in the laboratory by Aurnou *et al.* (2003). The warmer regions are believed to arise due to the differing efficiency of convection inside and outside the tangent cylinder (Tilgner & Busse, 1997).

Thermal winds inside the Earth's core could also arise because of a heterogeneous heat flux across the CMB. Seismic tomography uses seismic wave travel-time data to estimate flow velocities and can be used near the CMB. The seismic tomography suggests that heterogeneities in the CMB velocities exist, and a natural interpretation is that the variations in seismic velocity are due to thermal variations caused by a core-mantle heat flux that varies with latitude and longitude (Gubbins *et al.*, 2007). When this is the case and the system is stably stratified, and thus convectively stable, there must still be a non-zero flow since a thermal wind occurs (Zhang & Gubbins, 1996). This could lead to a baroclinic instability. Braginsky (1993) originally proposed the possibility that the inner core could be stably stratified just below the CMB. Whilst it is not currently known whether the core heat flux is low enough for such a subadiabatic region to exist, the estimates suggest that it is a possibility (Anufriev *et al.*, 2005). More recently Sreenivasan (2009); Sakuraba & Roberts (2009) have also suggested that thermal conditions at the boundaries of the core-mantle boundary may play an active role in generating large-scale convective flows and magnetic fields.

1.1.2 Convection in the Jovian atmosphere

We now discuss the structure of Jupiter since a significant part of our work will be relevant to convection in the Jovian atmosphere. Jupiter is believed to consist of a dense core made up of a mixture of elements including metallic hydrogen, which is approximately 55,000km in radius. Metallic hydrogen is a form of hydrogen produced when it is sufficiently compressed to allow a phase transition to take place (Wigner & Huntington, 1935). The electrons become unbound and thus can act like the conduction electrons of a metal. The core is surrounded by an outer layer atmosphere of molecular hydrogen and helium approximately 15,000km deep. Jupiter possesses a magnetic field, which again is expected to be driven by dynamo action, and it is thought to be generated in the metallic hydrogen core. However, the atmosphere of Jupiter is the region that we are concerned with since this is where large-scale zonal flows are observed. A zonal flow is an azimuthal flow often much larger in magnitude than the small-scale convective motions that are also occurring.

Zonal flows are known to occur frequently in nature with well known examples including the wind systems on the giant planets, including Jupiter. In the Jovian atmosphere there is a clear banded structure that is split into regions known as zones and belts. This structure is displayed in figure 1.2. The banded structure is accompanied by a complex array of prograde and retrograde zonal flows, which are referred to as jets (Porco *et al.*, 2003).

These jets are found at the boundaries between the zones and belts; the prevailing flows at the surface are shown in figure 1.3. The two sets of data in figure 1.3, obtained 20 years apart by the Voyager and Cassini spacecraft, show that the jet structure has barely changed in that time. Belts and zones alternate in colour and temperature with belts being dark and warm and zones light and cool. In figure 1.2 we also notice the appearance of large-scale vortices at the surface of the atmosphere such as the Great Red Spot. Most vortices are anticyclonic and are not thought to extend far into the interior of the atmosphere.

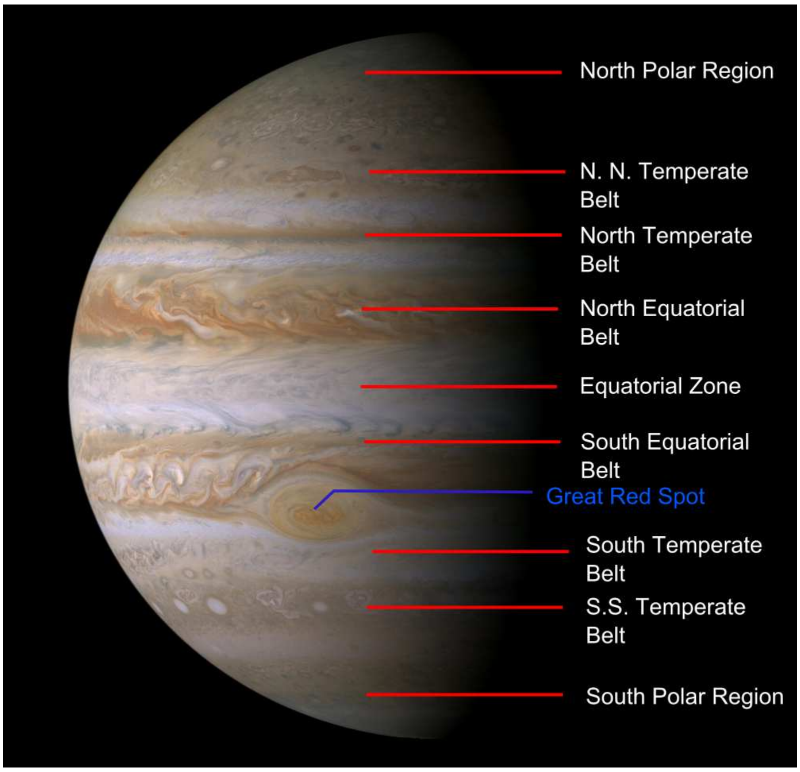

Figure 1.2: A diagram showing the various zones and belts visible at the surface of the Jovian atmosphere taken by the Cassini spacecraft in 2000 (credit to ESA and NASA for the original picture).

The origin of the jets, and in fact the banded structure itself, is an open question. The deep model, introduced by Busse (1976), proposes that the zonal flows are driven deep in the interior. Although this model is able to produce strong equatorial flows, it is often unable to reproduce the multiple jet structure seen in figure 1.3. However, this may be due to the inability to perform simulations at the realistic parameter regimes; that is, at sufficiently small Ekman number. Conversely, the shallow model assumes that the zonal flows are confined to a thin layer at the surface and driven by small-scale turbulence. This model also has problems. Whilst it can reproduce the multiple jet structure, the equatorial jet structure observed in figure 1.3 is absent in shallow models. Thus, it appears that

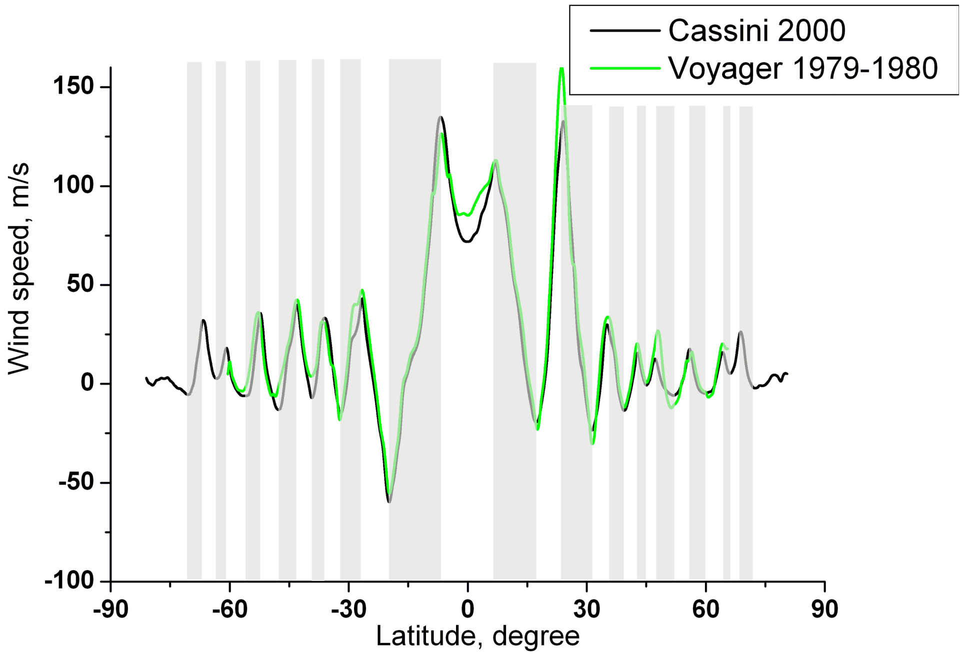

Figure 1.3: A diagram showing the direction and magnitude of the prevailing winds, known as jets, at the surface of the Jovian atmosphere. Adapted from original plot found in Vasavada & Showman (2005).

both deep and shallow processes are required in order to successfully model the Jovian atmosphere (Vasavada & Showman, 2005). A model that contains both shallow and deep processes and produces a much more realistic jet structure is presented by Heimpel *et al.* (2005).

1.2 The equations governing rotating fluids

The basic equations governing fluid dynamics are the Navier-Stokes equation, also referred to as the momentum equation or the equation of motion, and the continuity equation. The Navier-Stokes equation is a statement of the conservation of momentum for fluids and in its most general form, in an inertial frame, is written

$$\rho\frac{\partial U_i}{\partial t} + \rho U_j \frac{\partial U_i}{\partial x_j} = F_i + \frac{\partial P_{ij}}{\partial x_j}, \tag{1.1}$$

where U_i is the fluid velocity field, ρ is the density, P_{ij} is the stress, and the external forces, often due to gravity, are represented by F_j. The continuity equation is a statement of the conservation of mass and is

$$\frac{\partial \rho}{\partial t} + \frac{\partial}{\partial x_j}(\rho U_j) = 0. \tag{1.2}$$

These equations can be found in numerous textbooks, for example Batchelor (1967). The stress tensor is a measure of the internal forces acting within the fluid. Hence it consists of terms due to the pressure and viscosity. For our work it is sufficient to write

$$P_{ij} = -\mathcal{P}\delta_{ij} + \mu\left(\frac{\partial u_i}{\partial x_j} + \frac{\partial u_j}{\partial x_i}\right) - \frac{2}{3}\mu\frac{\partial u_k}{\partial x_k}\delta_{ij}, \tag{1.3}$$

where δ_{ij} is the Kronecker delta and μ is the viscosity. The viscous terms, proportional to μ, in this equation arise from the assumption of the stress being linearly proportional to the strain rate so that the fluid is Newtonian. The derivation of this form for the stress tensor can be found in, for example, Chandrasekhar (1961). The quantity $\mathcal{P}$ is the isotropic pressure in the absence of strain. Upon substituting the form for P_{ij} given by equation (1.3) into equation (1.1) the Navier-Stokes equation becomes

$$\rho\frac{\partial U_i}{\partial t} + \rho U_j\frac{\partial U_i}{\partial x_j} = F_i - \frac{\partial \mathcal{P}}{\partial x_i} + \frac{\partial}{\partial x_j}\left(\mu\left(\frac{\partial u_i}{\partial x_j} + \frac{\partial u_j}{\partial x_i}\right) - \frac{2}{3}\mu\frac{\partial u_k}{\partial x_k}\delta_{ij}\right). \tag{1.4}$$

In addition to these equations for the fluid velocity, one requires further equations to govern other physical quantities should any be present. In planetary bodies such as those which we shall be interested, the effects of temperature and magnetic fields are usually important. In this thesis we shall be working in the non-magnetic case. However, we shall be considering temperature fluctuations and thus we require an equation governing this quantity. Also, in the non-magnetic, non-isothermal case the only external body force we shall be interested in is that of the buoyancy so that we write

$$F_i = \rho g_i, \tag{1.5}$$

where g_i is the gravity vector. The relevant equation, the heat conduction equation, is derived (Chandrasekhar, 1961) from a consideration of the conservation of energy, which leads to

$$\rho\frac{\partial}{\partial t}(c_V T) + \rho U_j\frac{\partial}{\partial x_j}(c_V T) = \frac{\partial}{\partial x_j}\left(k\frac{\partial T}{\partial x_j}\right) - p\frac{\partial U_j}{\partial x_j} + \Phi, \tag{1.6}$$

where

$$\Phi = \frac{\mu}{2}\left(\frac{\partial U_i}{\partial x_j} + \frac{\partial U_j}{\partial x_i}\right)^2 - \frac{2}{3}\mu\left(\frac{\partial U_j}{\partial x_j}\right)^2. \tag{1.7}$$

Here we have introduced the parameters: c_V and k, which are the specific heat at constant volume and the thermal conductivity, respectively. Equations (1.2), (1.4) and (1.6) are our basic hydrodynamic equations and in addition to these we require an equation of state, which relates the temperature to the density. We use the approximation

$$\rho = \rho_0(1 - \alpha(T - \mathcal{T}_0)), \tag{1.8}$$

as the form for the density throughout our work, where α is the coefficient of thermal expansion and $\mathcal{T}_0$ is the temperature at which $\rho = \rho_0$.

1.2.1 The Boussinesq approximation and the addition of rotation

We now discuss an approximation that we use throughout our work in order to simplify the hydrodynamic equations we have discussed above. The Boussinesq approximation, named for Boussinesq (1903), arises due to the coefficient of thermal expansion being relatively small for a great deal of fluids, including those that we are interested in. For $\alpha \approx 10^{-4}$ the density varies by only small amounts provided the fluctuations in the temperature are not too large. Hence the variations in density are ignored in the Boussinesq approximation so that ρ is treated as a constant in our equations. However, there is one important exception: we do not treat the density as constant when it appears in the external forces term; that is F_i. This is because accelerations arising from the derivative of the density in this term can be comparable with other terms in the equation of motion. By assuming that the density is constant we are also able to assume that the coefficients μ, c_V, α and k are also constant since they will be of the same order as the density. The scalings of the various terms and other technicalities in the Boussinesq approximation are discussed by, for example, Chandrasekhar (1961) and Drazin & Reid (1981).

We are able to make significant modifications to equations (1.2), (1.4) and (1.6) when applying the Boussinesq approximation. We make the approximation $\rho \approx \rho_0$ in all terms other than the external force term where we retain the definition of the density given by equation (1.8). Firstly we note that the continuity equation, (1.2), reduces to

$$\frac{\partial U_j}{\partial x_j} = 0, \qquad \text{or} \qquad \nabla \cdot \mathbf{U} = 0. \tag{1.9}$$

Therefore the velocity field is solenoidal so that the fluid is incompressible in the Boussinesq approximation. Secondly, the Navier-Stokes equation, (1.4), with F_i

substituted from equation (1.5), becomes

$$\frac{\partial U_i}{\partial t} + U_j \frac{\partial U_i}{\partial x_j} = -\frac{1}{\rho_0}\frac{\partial \mathcal{P}}{\partial x_i} - \alpha(T - \mathcal{T}_0)g_i + \nu \frac{\partial^2 U_i}{\partial x_j^2}, \tag{1.10}$$

since the terms involving the divergence of the velocity now vanish due to equation (1.9). We have introduced the kinematic viscosity, also referred to as the momentum diffusivity, which is defined as: $\nu = \mu/\rho_0$. Thirdly, we consider the heat equation, (1.6), in the Boussinesq limit, which becomes

$$\frac{\partial T}{\partial t} + U_j \frac{\partial T}{\partial x_j} = \kappa \frac{\partial^2 T}{\partial x_j^2}, \tag{1.11}$$

where the thermal diffusivity is defined as: $\kappa = k/\rho_0 c_V$. The Φ term from equation (1.6) vanishes due to it being smaller than the convective terms (Drazin & Reid, 1981).

Since the physical systems that we shall be interested in are rotating bodies we also must include the effects of rotation in our equations. The rotational terms arise due to the fact that a rotating frame is accelerating and thus is not an inertial frame. Rotation only affects the Navier-Stokes equation, which becomes

$$\begin{aligned} \frac{\partial U_i}{\partial t} + U_j \frac{\partial U_i}{\partial x_j} + 2\epsilon_{ijk}\Omega_j U_k = \\ -\frac{1}{\rho_0}\frac{\partial \mathcal{P}}{\partial x_i} + \frac{1}{2}\frac{\partial}{\partial x_i}\left(|\epsilon_{jkl}\Omega_k x_l|^2\right) - \alpha(T - \mathcal{T}_0)g_i + \nu \frac{\partial^2 U_i}{\partial x_j^2}, \end{aligned} \tag{1.12}$$

where $2\rho\boldsymbol{\Omega}\times\mathbf{U}$ is the Coriolis force and $\frac{1}{2}\rho\nabla(|\boldsymbol{\Omega} \times \mathbf{x}|^2)$ is the centrifugal force. We assume that the Boussinesq approximation applies for both of these newly introduced terms so that the only term where the density is not constant remains the gravity term. Hence we have taken $\rho \approx \rho_0$ in the Coriolis and centrifugal force terms. In the case of the centrifugal force this amounts to assuming that $\Omega^2 d \ll g$ where d is a typical length scale of the system under consideration. The terms that are gradients of a scalar quantity can be gathered together to form a modified pressure and we can also incorporate the constant $\mathcal{T}_0$ into T. Equation (1.8) then becomes

$$\rho = \rho_0(1 - \alpha T), \tag{1.13}$$

and writing equation (1.12) in vector form we have

$$\frac{\partial \mathbf{U}}{\partial t} + (\mathbf{U}\cdot\nabla)\mathbf{U} + 2\boldsymbol{\Omega}\times\mathbf{U} = -\frac{1}{\rho_0}\nabla P - \alpha T\mathbf{g} + \nu\nabla^2\mathbf{U}, \tag{1.14}$$

where $P = \mathcal{P} - \rho_0 |\mathbf{\Omega} \times \mathbf{x}|^2/2$ is the modified pressure. The heat equation is unchanged by rotation and remains as

$$\frac{\partial T}{\partial t} + (\mathbf{U} \cdot \nabla) T = \kappa \nabla^2 T. \tag{1.15}$$

Throughout our work we will often use the vorticity equation, rather than the Navier-Stokes equation, since taking the curl of equation (1.14) eliminates the gradient term on the right-hand-side. This then results in the vorticity equation given by

$$\frac{\partial \mathbf{Z}}{\partial t} + (\mathbf{U} \cdot \nabla)\mathbf{Z} - ((2\mathbf{\Omega} + \mathbf{Z}) \cdot \nabla)\mathbf{U} = -\alpha \mathbf{g} \times \nabla T + \nu \nabla^2 \mathbf{Z}, \tag{1.16}$$

where $\mathbf{Z} \equiv \nabla \times \mathbf{U}$ is the vorticity. We have used equations (A.4) and (A.1) in order to take the curl of the advection term $(\mathbf{U} \cdot \nabla)\mathbf{U}$, noting that both $\mathbf{U}$ and $\mathbf{Z}$ are solenoidal. We have also used equation (A.1) and the solenoidal condition again to find the curl of the Coriolis term. Equations (1.9) and (1.14 - 1.16) are the governing equations that we shall call upon throughout our work.

1.2.2 Boundary conditions

In order to solve equations (1.9) and (1.14 - 1.16) we must also impose conditions on the fluid velocity and the heat at the fluid-solid boundaries. Clearly no fluid can pass through the solid boundary, which leads to the no penetration condition:

$$\mathbf{U} \cdot \hat{\mathbf{n}} = 0 \qquad \text{on all boundaries,} \tag{1.17}$$

where $\hat{\mathbf{n}}$ is a normal vector at the boundary. One of two further types of condition are commonly imposed on the fluid velocity. Firstly, the stress-free condition demands that no stresses act tangential to the boundary. From the definition of the stress tensor given in equation (1.3), this results in

$$\hat{\mathbf{n}} \cdot \nabla(\hat{\mathbf{n}} \times \mathbf{U}) = \mathbf{0} \qquad \text{on a free boundary.} \tag{1.18}$$

Secondly, the no-slip condition for a rigid surface demands that the horizontal components of the velocity vanish at the boundary so that

$$\hat{\mathbf{n}} \times \mathbf{U} = \mathbf{0} \qquad \text{on a rigid boundary.} \tag{1.19}$$

In the Earth's core, rigid boundaries are appropriate since the ICB and CMB are solid. However, as we shall discuss in section 1.3, the use of the no-slip condition introduces a thin boundary layer where the fluid velocity quickly changes from its interior value to zero on the boundaries. Due to the difficulty of numerically resolving such thin boundary layers, the more artificial stress-free boundaries are often used. In fact, we use both stress-free and no-slip boundary conditions in our work. There are also several possible thermal conditions that can be imposed on the boundaries. We choose to use boundaries that are held at a constant temperature throughout our work so that any perturbation to T must vanish on the boundaries. However, other conditions such as a constant heat flux passing through the boundary could also be used.

1.3 Properties of rotating fluids

Rotation has a profound affect on the dynamics of fluids due to the appearance of two new terms in the Navier-Stokes equation arising due to the non-inertial frame of reference. The introduction of the Coriolis term in particular has significant consequences. The importance of rotation in a given system is often measured using the Rossby number, which is the ratio of inertial forces to the Coriolis force. The Rossby number is defined as

$$Ro = \frac{U^*}{\Omega L}, \tag{1.20}$$

where U^* and L are typical velocity and length scales respectively. This non-dimensional number is small when rotational effects are important and is frequently used in atmospheric science and oceanography where large-scale structures such as ocean currents are significantly affected by rotation. Conversely, for many small-scale systems such as certain laboratory experiments the Rossby number is large and the Coriolis force can be ignored. However, some laboratory experiments do have large Rossby numbers due the rapid rotation of the system.

1.3.1 The Taylor-Proudman theorem

A significant consequence in rapidly rotating systems, where the Rossby number is small, can be identified when considering an inviscid, homogeneous fluid with slow, steady motions. In this case the equation of motion (1.14) reduces to

$$2\mathbf{\Omega} \times \mathbf{U} = -\frac{1}{\rho_0}\nabla P, \tag{1.21}$$

where products of the fluid velocity have been neglected due to the slow motion condition. The homogeneous condition also demands that the buoyancy term vanishes. The balance of the Coriolis force and the pressure gradient as in equation (1.21) is referred to as *geostrophic balance*. Although this balance does not hold identically in nature, since we have assumed that there is no viscosity, it is the predominant balance in certain systems.

In the Earth's core, for example, the Rossby number is small, $Ro \approx 3 \times 10^{-6}$. The Ekman number, $E = \nu/2\Omega d^2$, determines the relative strength of the viscous term compared with the Coriolis term and for the Earth's core: $E \approx 10^{-15}$. Therefore viscosity is negligible except on small length scales. Hence the Earth's core is an example of a rapidly rotating system where the effects of inertial forces and viscosity are small compared with the Coriolis force.

When geostrophic balance holds, an important results arises, best observed from the vorticity equation (1.16), which reduces to

$$(\mathbf{\Omega} \cdot \nabla)\mathbf{U} = 0. \tag{1.22}$$

Again products of $\mathbf{U}$ and $\mathbf{Z}$ are neglected due to the slow motion condition and the buoyancy term vanishes due to the homogeneous condition. Equation (1.22) is the mathematical statement of the Taylor-Proudman theorem, named for Taylor (1922) and Proudman (1916). Physically it states that the fluid velocity must be uniform in the direction of the axis of rotation of the body. This result implies that $\mathbf{U}$ is constant on columns and hence whole columns of fluid move as rigid bodies. As a consequence the fluid motion is also two-dimensional.

In convection problems where gravity and the rotation axis are parallel, a violation of the Taylor-Proudman theorem will take place in order to transport heat vertically. However, if the system is rotating sufficiently rapidly there will be a preference to limit the departure from geostrophy (Busse, 1970). This is achieved with large velocity components perpendicular to the rotation axis, compared with the component parallel to it, which creates a spiraling convection pattern (Chandrasekhar, 1961).

For systems where $\mathbf{g}$ and $\mathbf{\Omega}$ are perpendicular, the condition for geostrophy can hold exactly if the boundaries are flat. However, in systems with sloped or curved boundaries, such as a sphere, some z-dependent motion is inevitable. This is because although there is the possibility of purely geostrophic motion in the form of an azimuthal flow, this cannot transfer heat radially. Therefore some ageostrophic motion is required in order to do this. In a sphere, if a column of fluid moves out radially it must change its length via some sort of z-dependent motion. Therefore the columns preferred are tall and thin since they can transport the heat radially whilst minimising the departure from geostrophy. In the case of a spherical shell, which is relevant to the Earth's core, there are additional complications resulting from the existence of the tangent cylinder. As we discussed in section 1.1, there is unlikely to be significant motion across the TC since columns of fluid will have to be split in two, requiring strongly ageostrophic motion.

1.3.2 Ekman layers

As with many problems in fluid dynamics there is a boundary layer associated with no-slip boundaries in rotating systems. As we saw in section 1.2, the velocity field vanishes on rigid boundaries. Hence there must be a layer close to the boundaries where the velocity quickly changes from its interior value to zero. In rotating fluids the thickness of this layer is $O(E^{1/2})$ (Greenspan, 1968). In the boundary layer the primary balance is between the Coriolis, pressure and viscous forces so that

$$2\mathbf{\Omega} \times \mathbf{U} = -\frac{1}{\rho_0}\nabla\mathcal{P} + \nu\nabla^2\mathbf{U}. \tag{1.23}$$

The unusual property of Ekman layers compared with other boundary layers is their ability to attract or repel fluid from the boundary. This property, known as Ekman suction (or equivalently Ekman pumping), arises due to the velocity perpendicular to the boundary being non-zero just above the layer. This can significantly affect the spin up/down time of a rotating fluid.

For convenience let the rotation axis of a system be aligned with the z-coordinate. For a system where the boundary is perpendicular to the rotation axis and is located at $z = 0$, taking the curl of equation (1.23) and making use of equations (A.1) and (1.9) gives

$$-2\Omega\frac{\partial\mathbf{U}}{\partial z} = \nu\nabla^2\mathbf{Z}. \tag{1.24}$$

Then taking the curl of this again gives

$$-2\Omega\frac{\partial\mathbf{Z}}{\partial z} = -\nu\nabla^4\mathbf{U}, \tag{1.25}$$

where we have made use of equations (A.2) and (1.9). The assumption is now made that the z-derivatives are much larger than the horizontal derivatives since the flow must change from its interior value to zero at the boundary in a thin region. With this assumption the z-components of equations (1.24 - 1.25) are

$$-2\Omega\frac{\partial Z}{\partial z} = \nu\frac{\partial^2 U_z}{\partial z^2}, \qquad \text{and} \qquad 2\Omega\frac{\partial U_z}{\partial z} = \nu\frac{\partial^4 Z}{\partial z^4}, \tag{1.26}$$

where U_z and Z are the vertical components of the velocity and vorticity respectively. We combine these two coupled equations to give

$$\frac{\partial U_z}{\partial z} = -E^2 d^4\frac{\partial^5 U_z}{\partial z^5}, \tag{1.27}$$

where d is a typical length scale of the system. The solution of equation (1.27) yields expressions for the vertical velocity and vertical vorticity, which take the form

$$U_z = U_z^i + \exp\left(-\frac{z}{d\sqrt{E/2}}\right)\left(A\cos\left(\frac{z}{d\sqrt{E/2}}\right) + B\sin\left(\frac{z}{d\sqrt{E/2}}\right)\right), \tag{1.28}$$

$$Z = Z^i + \exp\left(-\frac{z}{d\sqrt{E/2}}\right)\left(\frac{A+B}{d\sqrt{E/2}}\cos\left(\frac{z}{d\sqrt{E/2}}\right) + \frac{B-A}{d\sqrt{E/2}}\sin\left(\frac{z}{d\sqrt{E/2}}\right)\right), \tag{1.29}$$

where A and B are constants. The interior values taken by the vertical velocity and vertical vorticity are represented by U_z^i and Z^i respectively. The boundary conditions at $z = 0$, which are $U_z = \partial U_z/\partial z = Z = 0$, then give $A = B = -U_z^i$ and

$$U_z^i = d\left(\frac{E}{2}\right)^{1/2} Z^i. \tag{1.30}$$

This form for U_z^i shows that the Ekman suction is proportional to the vertical vorticity outside the boundary layer. Hence anticyclonic vortices give rise to a suction of fluid into the boundary layer, whereas cyclonic vortices take fluid away from the boundary.

More generally, Greenspan (1968) shows that the Ekman suction takes the form

$$U_E = \mp d\left(\frac{E}{2}\right)^{1/2}\hat{\mathbf{n}}\cdot\nabla\times\left(\frac{1}{|\hat{\mathbf{n}}\cdot\hat{\mathbf{z}}|^{1/2}}(\hat{\mathbf{n}}\times\mathbf{U}+\mathbf{U})\right), \tag{1.31}$$

where $\hat{\mathbf{n}}$ is a vector normal to the boundary. Note that if $\hat{\mathbf{n}} = \hat{\mathbf{z}}$ we recover the result of equation (1.30) as expected. The suction is proportional to $E^{1/2}$ and is therefore small in rapidly rotating systems. Despite this, Ekman layers can have quite a significant effect on the dynamics of a system. Zhang & Jones (1993) investigated the effect of the Ekman suction on the onset of convection finding that it can be either stabilising or destabilising depending on the value of the Prandtl number, $Pr = \nu/\kappa$. The introduction of an Ekman layer has a profound effect on zonal flows and multiple jets, as we shall see in chapter 5.

1.4 Rayleigh-Bénard convection

In this section we discuss the most fundamental of problems involving thermal convection. This helps to introduce convection and its basic properties as well as the concepts of linear stability. The simplest model one can envisage is that of a horizontal plane layer of fluid that is heated from below. With the top boundary maintained at a lower temperature to the underside, an adverse temperature gradient is apparent. Hence, due to thermal expansion, the fluid near the bottom of the layer will be less dense than that above and the system is susceptible to thermal instabilities. However, viscous effects will inhibit the onset of convection and heat can also be transported vertically due to conduction. Therefore the temperature gradient must exceed some value for convection, which transports heat through fluid motion, to be efficient.

Thermal convection was recognised as a physical phenomenon by Rumford (1870) and Thomson (1882), though instabilities in the system described above were first demonstrated experimentally by Bénard (1900). Theoretical studies were also performed by Rayleigh (1916) who demonstrated that the non-dimensional Rayleigh number (we will introduce this later) must exceed a certain value for convection to onset. For these reasons the onset of thermal instabilities in a plane layer are commonly referred to as Rayleigh-Bénard convection.

The system described above is non-rotating and as such does not include all effects present in geophysical and astrophysical bodies. However, the problem does serve as a useful introduction to convection and linear stability theory. We derive Rayleigh's famous result for the critical Rayleigh number briefly here. We do not go into great depth in the derivation since we shall be considering more complicated stability problems in later chapters. When formulating the problem mathematically we are able to neglect the effects of rotation which occur only in the Coriolis force term of equation (1.14). We use Cartesian coordinates with the z-coordinate acting vertically and the boundaries of the layer are located in the xy-plane at $z = \pm d/2$. Gravity then acts in the negative z-direction so that $\mathbf{g} = -g\hat{\mathbf{z}}$ and a temperature gradient, β, is maintained across the layer. In linear stability we consider a state, known as the 'basic state', which is a *steady* solution to the governing equations and then perturb this state in order to ascertain whether perturbations are inclined to grow or not. When the onset of convection is of interest, the basic state will be at rest and the temperature will only depend on the vertical coordinate so that $\mathbf{U} = \mathbf{u_0} = \mathbf{0}$ and $T = T_0(z)$. Hydrostatic balance then takes place between the pressure and the buoyancy in equation (1.14) to give

$$\nabla p_0 = -g\alpha\rho_0 T_0, \tag{1.32}$$

where p_0 is the basic state pressure. The basic state temperature is governed by equation (1.15), which gives

$$\nabla^2 T_0 = 0. \tag{1.33}$$

The solution to equation (1.33) that maintains the correct temperature gradient is $T_0(z) = \beta(d/2 - z)$.

If small perturbations are now added to basic state so that $\mathbf{U} = \mathbf{u}$ and $T = T_0 + \theta$ we can consider the governing equations again. In fact, in order to simplify the mathematics the vorticity equation, (1.16), (again without the Coriolis term) and the curl of the vorticity equation are preferred in order to eliminate the pressure gradient term. The curl of the vorticity can be written using equation (A.2) so that $\nabla \times \mathbf{Z} = -\nabla^2 \mathbf{U}$ where the fact that the velocity is solenoidal has been used from equation (1.9). Products of the small perturbations are neglected so that we linearise the equations in the perturbations. Then the z-components of equation (1.16) and its curl are

$$\frac{\partial \zeta}{\partial t} = \nu \nabla^2 \zeta, \tag{1.34}$$

$$\frac{\partial \nabla^2 u_z}{\partial t} = g\alpha \nabla^2 \theta + \nu \nabla^4 u_z, \tag{1.35}$$

respectively. Here ζ and u_z are the z-components of the vorticity perturbation, $\boldsymbol{\zeta} = \nabla \times \mathbf{u}$, and velocity perturbation, $\mathbf{u}$, respectively. We also have the heat equation, which, with the perturbations inserted gives

$$\frac{\partial \theta}{\partial t} = \beta u_z + \kappa \nabla^2 \theta, \tag{1.36}$$

from equation (1.15). Equations (1.34 - 1.36) are the perturbation equations. We now non-dimensionalise the system using length scale, d, timescale, d^2/ν, and temperature scale, $\beta\nu d/\kappa$. Hence we let $\{x, y, z\} \rightarrow \{xd, yd, zd\}$, $t \rightarrow td^2/\nu$ and $\theta \rightarrow \theta\beta\nu d/\kappa$. The remaining quantities in the perturbation equations can be non-dimensionalised using these scales. Non-dimensionalisation is undertaken in order to write the physical parameters of the system more conveniently as several commonly reoccurring non-dimensional numbers. As their name suggests these numbers do not depend on the units used to measure the properties of the system.

The perturbations may grow or may simply decay away so that the system reverts to the basic state. This usually depends on whether some parameter of the system is greater than a certain value or not. In order to ascertain whether growing disturbances are possible the perturbations are decomposed so that a general disturbance is written in terms of normal modes with the following x, y and t dependence: $\exp(st + \mathrm{i}(k_x x + k_y y))$. The complex growth rate, $s = \sigma + \mathrm{i}\omega$ for $\sigma, \omega \in \mathbb{R}$ determines whether a disturbance is subject to growth with $\sigma > 0$ and $\sigma < 0$ indicating growth and decay respectively. The frequency of the disturbance is then given by ω. We have also introduced k_x and k_y, which are the wavenumbers in the x and y-directions respectively. When checking for instability we must check for *all* wavenumbers since if just one disturbance is found to be growing then the system is unstable. These topics are covered in more depth in, for example, Chandrasekhar (1961).

If we substitute the normal mode form for each perturbation into the perturbation equations and non-dimensionalise as discussed above, equations (1.34 - 1.36) become

$$\left(s + k^2 - \frac{\mathrm{d}^2}{\mathrm{d}z^2}\right)\zeta = 0, \tag{1.37}$$

$$\left(s + k^2 - \frac{\mathrm{d}^2}{\mathrm{d}z^2}\right)\left(k^2 - \frac{\mathrm{d}^2}{\mathrm{d}z^2}\right)u_z = Rak^2\theta, \tag{1.38}$$

$$\left(sPr + k^2 - \frac{\mathrm{d}^2}{\mathrm{d}z^2}\right)\theta = u_z, \tag{1.39}$$

where $k^2 = k_x^2 + k_y^2$ and we have introduced the Rayleigh number, Ra, and the Prandtl number, Pr, defined as

$$Ra = \frac{g\alpha\beta d^4}{\nu\kappa}, \qquad \text{and} \qquad Pr = \frac{\nu}{\kappa}, \tag{1.40}$$

respectively. The Prandtl number measures the relative strength of the two diffusivity rates ν and κ, and is approximately 0.1 in the Earth's core. The Rayleigh number is a fundamental dimensionless number in convection problems which shall be used throughout our work. Introduced by Rayleigh (1916) it indicates whether a system will be subject to convection. For a given system there exists a *critical* value of the Rayleigh number, Ra_c, where convective instabilities grow/decay if Ra is greater/less than this value. Therefore when $Ra = Ra_c$ the growth rate, σ, will vanish and we have marginal stability. Often the primary interest of linear stability problems considering convection is in determining the critical Rayleigh number, whence $\sigma = 0$ in the perturbation equations. This is the case here and throughout much of the work in this thesis. In fact, in the case of Rayleigh-Bénard convection we can also set $\omega = 0$ so that $s = 0$ since the problem does not admit oscillating solutions at onset (Chandrasekhar, 1961). However, as we shall see later, this is not the case in general.

For the problem currently in question, in order to determine the critical Rayleigh number we must first decide on which boundary conditions we wish to apply. If we recall section 1.2 we note that we must always apply $u_z = 0$ as the no penetration condition and also $\theta = 0$ as the constant temperature condition on the boundaries at $z = \pm 1/2$. Additionally, if stress-free boundaries are chosen then the problem can be solved analytically. Whilst making use of equation (1.9) we find from equation (1.18) that stress-free boundaries give the conditions: $\mathrm{d}^2 u_z/\mathrm{d}z^2 = 0 = \mathrm{d}\zeta/\mathrm{d}z$ on $z = \pm 1/2$. The perturbations in equations (1.37 - 1.39) (with $s = 0$) have the simple solution

$$u_z = A\cos(n\pi z), \tag{1.41}$$

$$\zeta = A\sin(n\pi z), \tag{1.42}$$

$$\theta = \frac{1}{k^2 + n^2\pi^2} A\cos(n\pi z), \tag{1.43}$$

where $n \in \mathbb{N}$ and A is a constant measuring the amplitude, provided

$$Ra = \frac{(n^2\pi^2 + k^2)^3}{k^2}. \tag{1.44}$$

This quantity must be minimised over n and k since the critical Rayleigh number is the smallest value that allows marginal stability for any disturbance; that is for any k. Clearly $n = 1$ minimises Ra over n and the minimising value of k is then

$$k_c = \frac{\pi}{\sqrt{2}} \approx 2.221, \tag{1.45}$$

whence

$$Ra_c = Ra(k_c) = \frac{27\pi^4}{4} \approx 657.511. \tag{1.46}$$

This is the famous result for the critical Rayleigh number of a layer of fluid heated from below found by Rayleigh (1916). However, stress-free boundaries have been implemented, which as discussed in section 1.2 are less physically realistic than no-slip boundaries. The case of no-slip boundaries, where the solution must be found numerically is discussed by Chandrasekhar (1961) where it is found that $Ra_c \approx 1707.762$ with $k_c \approx 3.117$. Experimental work is also reviewed by Chandrasekhar (1961) where the critical Rayleigh number is found to be approximately 1700, in agreement with the theoretical value for no-slip boundaries as expected.

One final point of interest in this section is the physical form of the convection patterns. At onset, where $Ra = Ra_c$, the disturbances are characterised by a particular wavenumber, which is of the order of the layer depth. However, since the wavevector $\mathbf{k} = (k_x, k_y)$ can be resolved in infinitely many directions the theory cannot uniquely predict the pattern of the convection. However, it is clear that the convection must take the form of periodically repeating cells where the normal component of the velocity vanishes on the cell walls. The magnitude of the vertical velocity is greatest at the centre of the cells and on the cell walls so that fluid rises and descends in these regions. If one of the wavenumbers is zero then the convection cells take the form of rolls, infinitely elongated in one horizontal direction. Several other possibilities based on symmetry arguments are also likely to arise naturally where the layer is composed of periodically repeating cells in the shape of regular polygons. We shall not discuss the form of the convection patterns here; see Chandrasekhar (1961) for a discussion. However, we note that periodic cell patterns of convection close to onset are also reproduced in experimental work; for example Bénard (1900) and Schmidt & Milverton (1935) among others.

Rayleigh-Bénard convection presents thermal instabilities in the most basic of cases. This system can be complicated further by including rotation, magnetic fields as well as other effects to the problem. This thesis will be concerned with rotating systems since they are relevant to geophysical and astrophysical bodies of interest. In particular, we introduce zonal flows, which are shear flows parallel to the axis of rotation. The study of the influence of magnetic fields, albeit of significant interest, is neglected in this thesis in order to gain an insight into the effects of zonal flows on rotating convection, without additional complication. However, further work could be undertaken where the effects of zonal flows *and* magnetic fields in a convectively unstable rotating system are taken into consideration.

1.5 Baroclinic instability

Baroclinic instabilities appear as an important feature in atmospheric science since they cause the large-scale westerly winds and the cyclones and anticyclones of the midlatitudes, which drive much of the Earth's weather. Much work on the modern understanding of baroclinic instabilities was instigated by Charney (1947) and many other papers dating from this time. In particular, the work by Eady (1949) is often cited as a fundamental example of the baroclinic instability.

We now briefly discuss the origin of baroclinic instabilities since they occur, along with thermal instabilities, later in our work. For a more in depth discussion of these instabilities see, for example, Drazin & Reid (1981). The baroclinic instability primarily occurs in rapidly rotating, stably stratified fluids; that is, where the temperature gradient is not adverse. The instability arises due to surfaces of constant pressure and constant density not coinciding. In a motionless state, surfaces of constant pressure will be perpendicular to the direction of gravity since hydrostatic balance demands that the derivatives of p_0 in the remaining directions vanish. In the setup described in the previous section, gravity acts in the z-direction and thus surfaces of constant pressure are in the xy-plane. When the density is of the form:

$$\rho = \rho_0(a - \delta z), \tag{1.47}$$

for some constants a and δ, the surfaces of constant density will also be in the xy-plane. When $\delta > 0$ this corresponds to a stably stratified fluid where neither thermal nor baroclinic instabilities are possible. In the case of $\delta < 0$ the system is unstably stratified, due to the adverse temperature gradient and thermal, but not baroclinic, instabilities are possible. The lighter fluid will tend to rise above the heavier fluid resulting in an instability.

If we now suppose that the density has form

$$\rho = \rho_0(a - \delta(z - \lambda y)), \tag{1.48}$$

where λ is a constant, then surfaces of constant density are inclined at an angle of

$\arctan(\lambda)$ to the horizontal. As before $\delta > 0$ represents a stably stratified system where thermal instabilities are not possible. However, the introduction of the lateral variation in temperature creates the possibility of a baroclinic instability. A schematic of the origin of the baroclinic instability is shown in figure 1.4. Surfaces of constant pressure are parallel to the y-axis whereas surfaces of constant density are inclined at an angle of $\arctan(\lambda)$ to the horizontal. Two parcels of fluid from different heights which are interchanged will have different densities to their new surroundings. There are then are two possibilities. Firstly, if the two fluid parcels interchanged are at the locations Q_1 and Q_2 in figure 1.4 then Q_2 is from a higher level than Q_1. Q_1 and Q_2 are also more and less dense than their new surroundings respectively since the vector pointing from Q_1Q_2 makes an angle greater than $\arctan(\lambda)$ with the horizontal. Therefore the parcels of fluid will tend to revert to their original positions so that the system is stable. Secondly, consider the situation when parcels of fluid from locations Q_1 and Q_3 are interchanged. Once again the parcel originally at Q_1 is from a lower level than the other parcel. However, due to the slanted nature of the lines of constant density, the vector Q_1Q_3 makes an angle with the horizontal which is less than $\arctan(\lambda)$. Therefore Q_1 is actually less dense than its new surroundings and the opposite is true of Q_3. The fluid parcel now at Q_3 rises whereas the parcel at Q_1 will fall. Thus, rather than moving back to their original heights the parcels of fluid will actually separate further resulting in instability. The above discussion gives an insight of how the baroclinic instability arises from the misalignment of constant density and constant pressure surfaces.

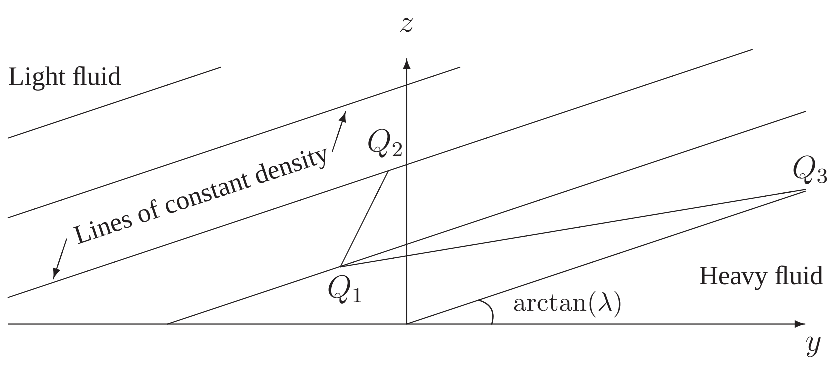

Figure 1.4: A diagram showing the origin of the baroclinic instability.

Chapter 2

Numerics for a linear plane layer model

Thermal convection in rotating systems is of great interest to geophysical and astrophysical fluid dynamics as we discussed in chapter 1. Our primary interest in this work is the effect zonal flows have on convection in various geometries. The onset of convection in rapidly rotating spheres and spherical shells is now well understood (Jones *et al.*, 2000; Dormy *et al.*, 2004). However, when introducing a new model it is often wise to begin by discussing the simplest relevant geometry. The simplest geometry which can be considered is that of a plane layer. Plane layer models allow for many of the aspects of convection in rotating systems to be observed and there is extensive literature available where plane layers have been used. For these reasons it is sensible for us also to begin with a study of how zonal flows interact with thermal convection in layers of fluid.

The classic problem of thermal instabilities in a rotating plane layer heated from below is reviewed in depth by Chandrasekhar (1961), along with other problems in stability theory. We have discussed, in chapter 1, several aspects which are relevant to plane layer convection. In section 1.4 we discussed the Rayleigh-Bénard problem, where thermal instabilities are considered in a layer that is not rotating. We have also seen, in section 1.3 how the Taylor-Proudman theorem places a restriction on the fluid motion of slow, steady, inviscid, rotating fluids. This restriction, which forbids motion parallel to the rotation axis, requires the fluid motion to be two-dimensional. However, convection is necessarily a three-dimensional phenomenon since heat cannot be transported from the bottom to the top of the layer without vertical motions. Thus, inviscid rotating fluids must be thermally stable *for all* temperature gradients, which is in contrast to the non-rotating case seen in section 1.4. Hence for thermal instabilities to arise, viscosity must be included in order to violate the Taylor-Proudman theorem.

The inclusion of rotation to the Rayleigh-Bénard problem also hinders the onset of convection by raising the critical Rayleigh number (Chandrasekhar, 1961). When we derive our perturbation equations later we will do so with a zonal flow occurring in the basic state. However, we will see that in the limit of no zonal flow the problem reverts to rotating plane layer convection and hence we shall see mathematically how the rotation increases the critical Rayleigh number from that of Rayleigh-Bénard convection. Another significant difference between the rotating and non-rotating cases is that for rotating convection oscillatory solutions are possible at onset, which is not true in the absence of rotation. This again is reviewed by Chandrasekhar (1961). In our model we shall only discuss situations where the rotation axis is aligned with the direction of gravity. The convective instability in the case where the rotation vector is oblique to gravity has also been discussed (Hathaway *et al.*, 1979, 1980).

As mentioned above, we wish to study the onset of convection in a rotating system in the presence of an imposed zonal flow; that is an axisymmetric, azimuthal flow. In our work in plane layer geometry we study the case where the zonal flow is a thermal wind, driven by latitudinal temperature gradients. Zonal flows and thermal winds were introduced in section 1.1. We only study the linear problem is this chapter, saving non-linear calculations for a second geometry in chapter 5. In section 2.1 we discuss the physical setup of the plane layer and describe how it can be modeled in Cartesian coordinates mathematically. We also discuss the basic state that is required to produce the zonal flow via a thermal wind and we reduce the governing equations by assuming the x and y dependence of the scalar fields in equations (1.9), (1.14) and (1.15). In section 2.2 we consider the boundary conditions imposed on the functions at the top and bottom of the layer. The numerical method used to solve the resulting 1D problem is discussed in section 2.4. Sections 2.5, 2.6 and 2.7 contain the numeric results of the linear theory for the plane layer. We split the results across three sections since various regimes appear. Finally, in section 2.8, we derive and discuss the implications of a thermodynamic equation, which helps to explain the interactions of the aforementioned regimes. Much of the work presented in this chapter also appears in sections 2 and 3 of Teed *et al.* (2010). As well as solving the problem numerically in this chapter, we also solve it analytically for certain asymptotic limits in chapter 3.

2.1 Mathematical setup

We begin by setting up the geometry of the problem mathematically. We consider a plane layer of depth d rotating about the vertical axis with angular velocity Ω. We choose a Cartesian coordinate system with the origin situated at the centre of the layer so that the boundaries are located at $z = \pm d/2$. The layer is unbounded in the x and y directions. In this geometry x and y are playing the role of the azimuthal and latitudinal coordinates respectively. The static temperature gradient in the absence of the zonal flow is such that $T = \beta d$ at $z = -d/2$ and $T = 0$ at $z = d/2$. Thus, the sign of β controls the direction of the temperature gradient. Gravity, g, acts downwards in the negative z-direction and thus is parallel to the temperature gradient. In classical convection problems $\beta > 0$ so that cold fluid sits above hot fluid and hence the conditions for convection are favourable since hot fluid is less dense than cold fluid. This type of setup is appropriate for polar regions of the Earth's core where gravity is near parallel to the rotation axis, the boundaries are approximately flat and the zonal flows are expected to depend on z.

We must first solve the governing equations for the steady basic state. From this basic state, perturbations can be added to analyse the stability of the system. In many models analysing convective instabilities the basic state has zero velocity field since there is interest in whether a small perturbation to a motionless state can grow. In this case all terms in the momentum equation involving the velocity vanish and we have hydrostatic balance; that is, balance between the pressure gradient and the buoyancy. When this is the case taking the curl of (1.14) results in a T that can only vary in the direction parallel to gravity, so that $\hat{\mathbf{z}} \times \nabla T = 0$ since all other terms vanish. The only source of energy then originates from the buoyancy. However if the basic state temperature varies in the x or y direction we must have a balance between the pressure gradient, buoyancy and Coriolis force in the momentum equation. By taking the curl of (1.14) in this case we obtain the thermal wind equation

$$2\Omega \frac{\partial \mathbf{U}}{\partial z} = g\alpha \hat{\mathbf{z}} \times \nabla T. \tag{2.1}$$

Here we have used the identity of equation (A.1) to give

$$\nabla \times (\hat{\mathbf{z}} \times \mathbf{U}) = \hat{\mathbf{z}}(\nabla \cdot \mathbf{U}) + (\mathbf{U} \cdot \nabla)\hat{\mathbf{z}} - \mathbf{U}(\nabla \cdot \hat{\mathbf{z}}) - (\hat{\mathbf{z}} \cdot \nabla)\mathbf{U} = -\frac{\partial \mathbf{U}}{\partial z}, \tag{2.2}$$

and noted that all but the final term vanish since $\hat{\mathbf{z}}$ is constant and $\mathbf{U}$ is solenoidal as seen by equation (1.9). Equation (2.1) generates an azimuthal zonal flow, the thermal wind, when T has y-dependence. Hence *horizontal* temperature gradients provide another possible energy source in addition to that arising from buoyancy. For this reason we consider both stably and unstably stratified cases since it may be possible for instability to arise in the stably stratified case (via a baroclinic instability) by exploiting the additional source of energy.

We desire a thermally induced z-dependent azimuthal zonal flow in our basic state so we set $\mathbf{U}$ to $\mathbf{u_0} = u_0(z)\hat{\mathbf{x}}$. We denote the basic state temperature and pressure by T_0 and p_0 respectively. We first consider the x-component of the thermal wind equation, (2.1), with these definitions to give

$$2\Omega \frac{\mathrm{d}u_0}{\mathrm{d}z} = -g\alpha \frac{\partial T_0}{\partial y}, \tag{2.3}$$

which results in

$$T_0 = -\frac{2\Omega y}{g\alpha}\frac{\mathrm{d}u_0}{\mathrm{d}z} + H_1(x,z), \tag{2.4}$$

for some function H_1. Now we consider the three components of equation (1.14), which give

$$\frac{\partial p_0}{\partial x} = \nu\rho_0 \frac{\mathrm{d}^2 u_0}{\mathrm{d}z^2}, \tag{2.5}$$

$$\frac{\partial p_0}{\partial y} = -2\Omega\rho_0 u_0, \tag{2.6}$$

$$\frac{\partial p_0}{\partial z} = g\alpha\rho_0 T_0. \tag{2.7}$$

Equation (2.5) can be integrated to give,

$$p_0 = \nu\rho_0 x \frac{\mathrm{d}^2 u_0}{\mathrm{d}z^2} + H_2(y,z), \tag{2.8}$$

for some function H_2. We insert this into equation (2.6) to determine the y-dependence of H_2 and hence also of p_0:

$$H_2(y,z) = -2\Omega\rho_0 u_0 y + H_3(z) \tag{2.9}$$

$$\Rightarrow \qquad p_0 = \nu\rho_0 x \frac{\mathrm{d}^2 u_0}{\mathrm{d}z^2} - 2\Omega\rho_0 u_0 y + H_3(z), \tag{2.10}$$

for some function H_3. Now we can insert this form of p_0 into equation (2.7) to find

$$\nu\rho_0 x\frac{\mathrm{d}^3u_0}{\mathrm{d}z^3} - 2\Omega\rho_0 y\frac{\mathrm{d}u_0}{\mathrm{d}z} + \frac{\mathrm{d}H_3}{\mathrm{d}z} = g\alpha\rho_0\left(-\frac{2\Omega y}{g\alpha}\frac{\mathrm{d}u_0}{\mathrm{d}z} + H_1(x,z)\right) \tag{2.11}$$

$$\Rightarrow \qquad H_1(x,z) = \frac{\nu x}{g\alpha}\frac{\mathrm{d}^3u_0}{\mathrm{d}z^3} + \frac{1}{g\alpha\rho_0}\frac{\mathrm{d}H_3}{\mathrm{d}z}. \tag{2.12}$$

This form of H_1 can be inserted into the expression for T_0 given by equation (2.4) where we see that we have determined all but the z-dependence of T_0:

$$T_0 = -\frac{2\Omega y}{g\alpha}\frac{\mathrm{d}u_0}{\mathrm{d}z} + \frac{\nu x}{g\alpha}\frac{\mathrm{d}^3u_0}{\mathrm{d}z^3} + \frac{1}{g\alpha\rho_0}\frac{\mathrm{d}H_3}{\mathrm{d}z}. \tag{2.13}$$

We choose the z-dependence of T_0 such that the static temperature gradient in the absence of zonal flow (that is $u_0 = 0$) is equivalent to Chandrasekhar (1961) for Rayleigh-Bénard convection; see section 1.4. Thus we set $\mathrm{d}H_3/\mathrm{d}z = g\alpha\rho_0(d/2 - z)\beta$. We also have to choose a form for $u_0(z)$, which must satisfy the temperature equation. By inserting the form of T_0 into equation (1.15) we clearly see that we require the third derivative of $u_0(z)$ to vanish. We choose $u_0 = U_0'z$ where U_0' is a parameter that measures the magnitude of the zonal flow. We choose this form for u_0, rather than the more general quadratic form, since it is the simplest case that can be considered where the zonal flow has z-dependence. Moreover by choosing a linear form for u_0 the pressure, given by equation (2.10), only depends on one horizontal coordinate. However, it should be noted that this form for the zonal flow does not satisfy stress-free nor no-slip boundary conditions though more crucially the no penetration condition does hold. By inserting these chosen forms for H_3 and u_0 into equations (2.10) and (2.13) we can determine the basic state velocity, temperature and pressure:

$$\mathbf{u_0} = U_0'z\hat{\mathbf{x}}, \tag{2.14}$$

$$T_0 = \beta\left(\frac{d}{2} - z\right) - \frac{2\Omega U_0'}{g\alpha}y, \tag{2.15}$$

$$p_0 = \frac{g\alpha\beta\rho_0 z}{2}(d - z) - 2\Omega\rho_0 U_0'yz + p_{\text{constant}}, \tag{2.16}$$

which is a solution to the system of equations (1.9), (1.14) and (1.15) and (2.1). Here p_{constant} is a constant of integration and represents the background pressure. Of particular note here is the fact that the temperature distribution depends on a coordinate other than the coordinate parallel to direction of gravity. Therefore the basic state is baroclinic since surfaces of constant pressure and constant density are not parallel, that is ∇p_0 is not parallel to $\nabla\rho = -\alpha\rho_0\nabla T_0$ where we have used equation (1.13). We can see this by evaluating these two expressions to give

$$\nabla p_0 = -\left(2\Omega\rho_0 U_0' z\right)\hat{\mathbf{y}} + \left(\frac{g\alpha\beta\rho_0}{2}(d-2z) - 2\Omega\rho_0 U_0' y\right)\hat{\mathbf{z}}, \tag{2.17}$$

$$-\alpha\rho_0\nabla T_0 = \left(\frac{2\Omega\rho_0 U_0'}{g}\right)\hat{\mathbf{y}} + \left(\alpha\beta\rho_0\right)\hat{\mathbf{z}}, \tag{2.18}$$

whereby it is clear that, in general, $\nabla p_0 \nparallel \nabla\rho$. We also note that if the zonal flow is removed by setting $U_0' = 0$, the temperature only depends on the coordinate parallel to gravity and the gradients of the pressure and density are also both in that direction. Hence the surfaces of constant pressure and constant density are once again parallel and the system is not baroclinic in the absence of the thermal wind.

In order to analyse linear stability we now add small perturbations to the basic state so that $\mathbf{U} = \mathbf{u_0} + \mathbf{u}$, $P = p_0 + p$ and $T = T_0 + \theta$. We insert the new forms of $\mathbf{U}$, P and T into equations (1.14) and (1.15) and since the perturbations are small we ignore terms that consist of a product of these perturbations (that is we linearise). So using the definition of the basic state from equations (2.14 - 2.16) we find that equations (1.14) and (1.15) give

$$\frac{\partial \mathbf{u}}{\partial t} + U_0' z\frac{\partial \mathbf{u}}{\partial x} + U_0' u_z\hat{\mathbf{x}} + 2\Omega\hat{\mathbf{z}}\times\mathbf{u} = -\frac{1}{\rho_0}\nabla p + g\alpha\theta\hat{\mathbf{z}} + \nu\nabla^2\mathbf{u}, \tag{2.19}$$

$$\frac{\partial \theta}{\partial t} + U_0' z\frac{\partial \theta}{\partial x} - \beta u_z - \frac{2\Omega U_0'}{g\alpha}u_y = \kappa\nabla^2\theta, \tag{2.20}$$

where terms involving only basic state fields cancel due to the construction of $\mathbf{u_0}$, p_0 and T_0.

We proceed by eliminating the pressure to leave four equations for four unknowns. We denote the vorticity, the curl of the velocity, by $\boldsymbol{\zeta}$ and consider the curl of equation (2.19). We make use of equation (A.5) so that the pressure term vanishes to give

$$\frac{\partial \boldsymbol{\zeta}}{\partial t} + U_0' z\frac{\partial \boldsymbol{\zeta}}{\partial x} + U_0'\hat{\mathbf{z}}\times\frac{\partial \mathbf{u}}{\partial x} + U_0'\nabla\times u_z\hat{\mathbf{x}} - 2\Omega\frac{\partial \mathbf{u}}{\partial z} = g\alpha\nabla\times\theta\hat{\mathbf{z}} + \nu\nabla^2\boldsymbol{\zeta}, \tag{2.21}$$

where we have also used the result of equation (2.2). We also require the double-curl of equation (2.19), or equivalently the curl of equation (2.21). We note from equation (A.2) that $\nabla\times\boldsymbol{\zeta} \equiv \nabla\times(\nabla\times\mathbf{u}) = -\nabla^2\mathbf{u}$ since $\mathbf{u}$ is solenoidal and then the curl of equation (2.21) is

$$\frac{\partial \nabla^2\mathbf{u}}{\partial t} + U_0' z\frac{\partial \nabla^2\mathbf{u}}{\partial x} - U_0'\hat{\mathbf{z}}\times\frac{\partial \boldsymbol{\zeta}}{\partial x} + U_0'\frac{\partial^2\mathbf{u}}{\partial z\partial x} - U_0'\left(\frac{\partial \nabla u_z}{\partial x} - \nabla^2 u_z\hat{\mathbf{x}}\right) + 2\Omega\frac{\partial \boldsymbol{\zeta}}{\partial z}$$
$$= -g\alpha\left(\frac{\partial \nabla\theta}{\partial z} - \nabla^2\theta\hat{\mathbf{z}}\right) + \nu\nabla^4\mathbf{u}. \tag{2.22}$$

We consider the z-components of equations (2.21 - 2.22) as this will help to reduce the system to three equations for three unknowns, namely θ and the z-components of the velocity and vorticity: u_z and ζ respectively. The remaining components of the velocity field (u_x and u_y) can then be found from the definition of the vorticity and equation (1.9) once u_z and ζ are known, as shown by equations (B.5 - B.6). The z-components of equations (2.21 - 2.22) are

$$\frac{\partial \zeta}{\partial t} + U_0' z \frac{\partial \zeta}{\partial x} - U_0' \frac{\partial u_z}{\partial y} - 2\Omega \frac{\partial u_z}{\partial z} = \nu \nabla^2 \zeta, \tag{2.23}$$

$$\frac{\partial \nabla^2 u_z}{\partial t} + U_0' z \frac{\partial \nabla^2 u_z}{\partial x} + 2\Omega \frac{\partial \zeta}{\partial z} = g\alpha \nabla_H^2 \theta + \nu \nabla^4 u_z, \tag{2.24}$$

respectively. Here $\nabla_H^2 = \partial^2/\partial x^2 + \partial^2/\partial y^2$ is the horizontal Laplacian. We can take the horizontal Laplacian of equation (2.20), which by utilising the identity given by equation (B.6) can be written

$$\nabla_H^2 \left(\frac{\partial \theta}{\partial t} + U_0' z \frac{\partial \theta}{\partial x} - \beta u_z - \kappa \nabla^2 \theta \right) = \frac{2\Omega U_0'}{g\alpha} \left(\frac{\partial \zeta}{\partial x} - \frac{\partial^2 u_z}{\partial y \partial z} \right). \tag{2.25}$$

We now have three equations (2.23 - 2.25) for three unknowns, namely: u_z, ζ and θ. Next we non-dimensionalise these equations using the depth of the layer, d, as the length scale, the viscous diffusion time, d^2/ν, as the time scale and temperature scale $\beta\nu d/\kappa$. Hence we substitute the formulae: $\{x, y, z\} \rightarrow \{\tilde{x}d, \tilde{y}d, \tilde{z}d\}$, $t \rightarrow \tilde{t}d^2/\nu$, $u_z \rightarrow \tilde{u}_z \nu/d$, $\zeta \rightarrow \tilde{\zeta}\nu/d^2$, $\theta \rightarrow \tilde{\theta}\beta\nu d/\kappa$, $\nabla^2 \rightarrow \tilde{\nabla}^2/d^2$ into equations (2.23 - 2.25), which become

$$\frac{\nu^2}{d^4}\frac{\partial \tilde{\zeta}}{\partial \tilde{t}} + \frac{\nu U_0'}{d^2} \tilde{z} \frac{\partial \tilde{\zeta}}{\partial \tilde{x}} - \frac{\nu U_0'}{d^2}\frac{\partial \tilde{u}_z}{\partial \tilde{y}} - \frac{2\Omega\nu}{d^2}\frac{\partial \tilde{u}_z}{\partial \tilde{z}} = \frac{\nu^2}{d^4}\tilde{\nabla}^2 \tilde{\zeta}, \tag{2.26}$$

$$\frac{\nu^2}{d^5}\frac{\partial \tilde{\nabla}^2 \tilde{u}_z}{\partial \tilde{t}} + \frac{\nu U_0'}{d^3} \tilde{z} \frac{\partial \tilde{\nabla}^2 \tilde{u}_z}{\partial \tilde{x}} + \frac{2\Omega\nu}{d^3}\frac{\partial \tilde{\zeta}}{\partial \tilde{z}} = \frac{g\alpha\beta\nu}{\kappa d}\tilde{\nabla}_H^2 \tilde{\theta} + \frac{\nu^2}{d^5}\tilde{\nabla}^4 \tilde{u}_z, \tag{2.27}$$

$$\left(\frac{\nu}{d^2}\frac{\partial}{\partial \tilde{t}} + U_0' \tilde{z}\frac{\partial}{\partial \tilde{x}} - \frac{\kappa}{d^2}\tilde{\nabla}^2 \right) \frac{\beta\nu}{\kappa d}\tilde{\nabla}_H^2 \tilde{\theta} = \frac{\beta\nu}{d^3}\tilde{\nabla}_H^2 \tilde{u}_z + \frac{2\Omega U_0' \nu}{g\alpha d^3} \left(\frac{\partial \tilde{\zeta}}{\partial \tilde{x}} - \frac{\partial^2 \tilde{u}_z}{\partial \tilde{y} \partial \tilde{z}} \right). \tag{2.28}$$

These equations can be considerably tidied up by introducing dimensionless parameters, whence they become

$$\left(\frac{\partial}{\partial \tilde{t}} + Re\tilde{z}\frac{\partial}{\partial \tilde{x}} - \tilde{\nabla}^2 \right) \tilde{\zeta} - Re\frac{\partial \tilde{u}_z}{\partial \tilde{y}} - E^{-1}\frac{\partial \tilde{u}_z}{\partial \tilde{z}} = 0, \tag{2.29}$$

$$\left(\frac{\partial}{\partial \tilde{t}} + Re\tilde{z}\frac{\partial}{\partial \tilde{x}} - \tilde{\nabla}^2 \right) \tilde{\nabla}^2 \tilde{u}_z + E^{-1}\frac{\partial \tilde{\zeta}}{\partial \tilde{z}} = Ra\tilde{\nabla}_H^2 \tilde{\theta}, \tag{2.30}$$

$$Pr\left(\frac{\partial}{\partial \tilde{t}} + Re\tilde{z}\frac{\partial}{\partial \tilde{x}} - Pr^{-1}\tilde{\nabla}^2 \right) \tilde{\nabla}_H^2 \tilde{\theta} = \tilde{\nabla}_H^2 \tilde{u}_z + \frac{PrRe}{ERa}\left(\frac{\partial \tilde{\zeta}}{\partial \tilde{x}} - \frac{\partial^2 \tilde{u}_z}{\partial \tilde{y} \partial \tilde{z}} \right), \tag{2.31}$$

where the Ekman number, E, Prandtl number, Pr, Rayleigh number, Ra, and Reynolds number, Re, are defined as

$$E = \frac{\nu}{2\Omega d^2}, \qquad Pr = \frac{\nu}{\kappa}, \qquad Ra = \frac{g\alpha\beta d^4}{\nu\kappa}, \qquad Re = \frac{U_0' d^2}{\nu}. \tag{2.32}$$

Equations (2.29 - 2.31) are the finite Ekman number equations for rapidly rotating plane layer convection with zonal flow. Our system is defined so that when $\beta > 0$ we have cold fluid sitting on top of hot fluid and thus the layer is buoyantly unstable. Therefore, as is usually the case when considering thermal convection, we require a positive Rayleigh number above some critical value, Ra_c, for convective motions to begin (Chandrasekhar, 1961). In the case where $\beta < 0$ the system is buoyantly stable, since hot fluid sits on top of cold fluid, and with a basic state temperature distribution only dependent on z, no instabilities are possible. However, when $\beta < 0$, and thus $Ra < 0$, the fluid is stably stratified in which case baroclinic instabilities may be possible since the basic state is baroclinic as mentioned earlier. Therefore it is not immediately clear if instabilities, and hence motions, are forbidden when $Ra < 0$ in our setup.

Next we explicitly choose the t, x and y-dependence of the solutions to be Fourier modes in order to reduce the system to a 1D problem in z. Hence we consider the following forms for our functions:

$$\tilde{u}_z(t,x,y,z) = \Re\Big[\hat{u}_z(z)\exp(st + \mathrm{i}(k_x x + k_y y))\Big], \tag{2.33}$$

$$\tilde{\zeta}(t,x,y,z) = \Re\Big[\hat{\zeta}(z)\exp(st + \mathrm{i}(k_x x + k_y y))\Big], \tag{2.34}$$

$$\tilde{\theta}(t,x,y,z) = \Re\Big[\hat{\theta}(z)\exp(st + \mathrm{i}(k_x x + k_y y))\Big], \tag{2.35}$$

where we have also dropped the remaining tildes. Equivalently we may write the expressions as

$$\tilde{u}_z(t,x,y,z) = \exp(st)\Big(\hat{u}_{\mathrm{r}}(z)\cos(k_x x + k_y y) - \hat{u}_{\mathrm{i}}(z)\sin(k_x x + k_y y)\Big), \tag{2.36}$$

$$\tilde{\zeta}(t,x,y,z) = \exp(st)\Big(\hat{\zeta}_{\mathrm{r}}(z)\cos(k_x x + k_y y) - \hat{\zeta}_{\mathrm{i}}(z)\sin(k_x x + k_y y)\Big), \tag{2.37}$$

$$\tilde{\theta}(t,x,y,z) = \exp(st)\Big(\hat{\theta}_{\mathrm{r}}(z)\cos(k_x x + k_y y) - \hat{\theta}_{\mathrm{i}}(z)\sin(k_x x + k_y y)\Big), \tag{2.38}$$

by evaluating the real part or as

$$\tilde{u}_z(t,x,y,z) = \frac{1}{2}\Big(\hat{u}_z(z)\exp(st + \mathrm{i}(k_x x + k_y y)) + \hat{u}_z^*(z)\exp(st - \mathrm{i}(k_x x + k_y y))\Big), \tag{2.39}$$

$$\tilde{\zeta}(t,x,y,z) = \frac{1}{2}\Big(\hat{\zeta}_z(z)\exp(st + \mathrm{i}(k_x x + k_y y)) + \hat{\zeta}_z^*(z)\exp(st - \mathrm{i}(k_x x + k_y y))\Big), \tag{2.40}$$

$$\tilde{\theta}(t,x,y,z) = \frac{1}{2}\Big(\hat{\theta}_z(z)\exp(st + \mathrm{i}(k_x x + k_y y)) + \hat{\theta}_z^*(z)\exp(st - \mathrm{i}(k_x x + k_y y))\Big). \tag{2.41}$$

Here the subscripts indicate the real and imaginary parts of the functions (so that, for example, $\hat{u}_z = \hat{u}_\mathrm{r} + \mathrm{i}\hat{u}_\mathrm{i}$) and '*' denotes the complex conjugate. The sets of equations (2.33 - 2.35), (2.36 - 2.38) and (2.39 - 2.41) are all equivalent definitions for the scalar fields. We primarily use equations (2.33 - 2.35) in our derivations where it is implicitly assumed that we are taking the real part. However, the other forms will also be useful later. In equations (2.33 - 2.35) we have also introduced s, which is the complex growth rate, and k_x and k_y, which are the wavenumbers of the disturbances in the x and y-directions respectively. We also assume that u_x and u_y take similar forms since they are related to ζ and u_z via equations (B.5 - B.6). The complex growth rate takes the form: $s = \sigma + \mathrm{i}\omega$. The sign of σ determines whether a disturbance grows or decays and if $\omega \neq 0$ the disturbance onsets as a traveling wave. If we substitute the form of the functions given by equations (2.33 - 2.35) into equations (2.29 - 2.31) the resulting equations are

$$\left(s + \mathrm{i}k_x Rez + k^2 - \frac{\mathrm{d}^2}{\mathrm{d}z^2}\right)\hat{\zeta} - \mathrm{i}k_y Re\hat{u}_z - E^{-1}\frac{\mathrm{d}\hat{u}_z}{\mathrm{d}z} = 0, \tag{2.42}$$

$$\left(s + \mathrm{i}k_x Rez + k^2 - \frac{\mathrm{d}^2}{\mathrm{d}z^2}\right)\left(\frac{\mathrm{d}^2}{\mathrm{d}z^2} - k^2\right)\hat{u}_z + E^{-1}\frac{\mathrm{d}\hat{\zeta}}{\mathrm{d}z} = -k^2 Ra\hat{\theta}, \tag{2.43}$$

$$\left(sPr + \mathrm{i}k_x PrRez + k^2 - \frac{\mathrm{d}^2}{\mathrm{d}z^2}\right)\hat{\theta} = \hat{u}_z - \frac{\mathrm{i}PrRe}{ERak^2}\left(k_x\hat{\zeta} - k_y\frac{\mathrm{d}\hat{u}_z}{\mathrm{d}z}\right), \tag{2.44}$$

where $k^2 = k_x^2 + k_y^2$.

2.2 Boundary conditions

In order to solve the eighth-order system of equations, (2.42 - 2.44), we require a total of eight boundary conditions at the two boundaries $z = \pm 1/2$. We discussed the various boundary conditions that we shall impose in section 1.2.2. In addition to demanding that there be no penetration and a constant surface temperature at the boundaries, we consider two cases separately, namely stress-free and no-slip boundary conditions on both the upper and lower boundaries. The first four boundary conditions on $z = \pm 1/2$ are

$$\hat{u}_z = 0 \quad \text{(no penetration)}\ , \tag{2.45}$$
$$\hat{\theta} = 0 \quad \text{(constant surface temperature)}\ . \tag{2.46}$$

From the continuity equation, (1.9), we have

$$\nabla \cdot \mathbf{U} \equiv \nabla \cdot \mathbf{u} = \frac{\partial u_x}{\partial x} + \frac{\partial u_y}{\partial y} + \frac{\partial u_z}{\partial z} = 0 \tag{2.47}$$
$$\Rightarrow \quad \frac{\partial u_z}{\partial z} = -\left(\frac{\partial u_x}{\partial x} + \frac{\partial u_y}{\partial y}\right) \tag{2.48}$$
$$\Rightarrow \quad \frac{\mathrm{d}\hat{u}_z}{\mathrm{d}z} = -\mathrm{i}(k_x \hat{u}_x + k_y \hat{u}_y), \tag{2.49}$$

and from the definition of ζ:

$$\zeta = \frac{\partial u_y}{\partial x} - \frac{\partial u_x}{\partial y} \tag{2.50}$$
$$\Rightarrow \quad \hat{\zeta} = \mathrm{i}(k_x \hat{u}_y - k_y \hat{u}_x). \tag{2.51}$$

The stress-free case, by definition from equation (1.18), demands that on the boundaries

$$\frac{\partial u_x}{\partial z} + \frac{\partial u_z}{\partial x} = 0 = \frac{\partial u_y}{\partial z} + \frac{\partial u_z}{\partial y}. \tag{2.52}$$

However, the no penetration condition given by equation (2.45) informs us that u_z is constant on the boundary so that the stress-free condition reduces to

$$\frac{\partial u_x}{\partial z} = 0 = \frac{\partial u_y}{\partial z} \quad \Rightarrow \quad \frac{\mathrm{d}\hat{u}_x}{\mathrm{d}z} = 0 = \frac{\mathrm{d}\hat{u}_y}{\mathrm{d}z}. \tag{2.53}$$

If we take the z-derivative of equations (2.49) and (2.51) we find that

$$\frac{\mathrm{d}^2\hat{u}_z}{\mathrm{d}z^2} = -\mathrm{i}\left(k_x \frac{\mathrm{d}\hat{u}_x}{\mathrm{d}z} + k_y \frac{\mathrm{d}\hat{u}_y}{\mathrm{d}z}\right) = 0, \tag{2.54}$$
$$\text{and} \quad \frac{\mathrm{d}\hat{\zeta}}{\mathrm{d}z} = \mathrm{i}\left(k_x \frac{\mathrm{d}\hat{u}_y}{\mathrm{d}z} - k_y \frac{\mathrm{d}\hat{u}_x}{\mathrm{d}z}\right) = 0, \tag{2.55}$$

using equation (2.53). Also for the no-slip case we have, by definition from equation (1.19), that on the boundaries

$$u_x = 0 = u_y \quad \Rightarrow \quad \hat{u}_x = 0 = \hat{u}_y, \tag{2.56}$$

whereby equations (2.49) and (2.51) indicate that

$$\frac{\mathrm{d}\hat{u}_z}{\mathrm{d}z} = 0, \tag{2.57}$$

$$\text{and} \quad \hat{\zeta} = 0. \tag{2.58}$$

Thus, from equations (2.45), (2.46), (2.54), (2.55), (2.57) and (2.58) our eight boundary conditions on $z = \pm 1/2$ are

$$\hat{u}_z = 0 = \hat{\theta}, \tag{2.59}$$

along with *either*

$$\frac{\mathrm{d}^2\hat{u}_z}{\mathrm{d}z^2} = 0 = \frac{\mathrm{d}\hat{\zeta}}{\mathrm{d}z}, \tag{2.60}$$

for the stress-free case, *or*

$$\frac{\mathrm{d}\hat{u}_z}{\mathrm{d}z} = 0 = \hat{\zeta}, \tag{2.61}$$

for the no-slip case.

2.3 The solution in the absence of zonal flow

We are now in a position where we can solve the perturbation equations (2.42 - 2.44) numerically for various parameter regimes. We do this in the next section. However, we first consider the limit of $Re = 0$, where the problem reverts to rotating plane layer convection; essentially the rotating equivalent of Rayleigh-Bénard convection from section 1.4. This problem is studied thoroughly by Chandrasekhar (1961) and we only present the results here in order to observe the effect of rotation on convection.

Unlike in the non-rotating case, oscillatory solutions, so that $\omega \neq 0$, are now possible for certain wavenumbers. However, in order to compare with section 1.4 we first continue to consider the marginal *steady* solutions where $\omega = 0$ so that $s = 0$. We also set $Re = 0$ so that the zonal flow vanishes. Equations (2.42 - 2.44) then reduce to

$$\left(k^2 - \frac{\mathrm{d}^2}{\mathrm{d}z^2}\right)\hat{\zeta} - E^{-1}\frac{\mathrm{d}\hat{u}_z}{\mathrm{d}z} = 0, \tag{2.62}$$

$$\left(k^2 - \frac{\mathrm{d}^2}{\mathrm{d}z^2}\right)^2\hat{u}_z - E^{-1}\frac{\mathrm{d}\hat{\zeta}}{\mathrm{d}z} = k^2 Ra\hat{\theta}, \tag{2.63}$$

$$\left(k^2 - \frac{\mathrm{d}^2}{\mathrm{d}z^2}\right)\hat{\theta} = \hat{u}_z, \tag{2.64}$$

and an analytic solution is possible when using stress-free boundaries as was the case for Rayleigh-Bénard convection. We consider the stress-free case here since it demonstrates the effects of rotation most clearly. The solution is

$$\hat{u}_z = A\cos(n\pi z), \tag{2.65}$$

$$\hat{\zeta} = -\frac{n\pi}{E(k^2+n^2+\pi^2)}A\sin(n\pi z), \tag{2.66}$$

$$\hat{\theta} = \frac{1}{k^2+n^2\pi^2}A\cos(n\pi z), \tag{2.67}$$

where $n \in \mathbb{N}$ and the constant, A, is the amplitude. This solution satisfies the boundary conditions given by equations (2.59 - 2.60) and also equations (2.62 - 2.64) provided

$$Ra = \frac{(n^2\pi^2+k^2)^3}{k^2} + \frac{n^2\pi^2}{E^2k^2}. \tag{2.68}$$

This expression for the Rayleigh number reduces to that of equation (1.44) for Rayleigh-Bénard convection in the limit of no rotation; that is $E \to \infty$. Since the additional term appearing in the expression for Ra in equation (2.68) is always greater than zero, it is clear that rotation raises the Rayleigh number that must be exceeded for disturbances with wavenumber k to occur. If expression (2.68) is minimised over all k (and n) to find the critical Rayleigh number we find that k must satisfy

$$(2k^2+\pi^2)(k^2+\pi^2)^2 = \frac{\pi^2}{E^2}. \tag{2.69}$$

For a given Ekman number, the critical wavenumber, k_c, can be found from this equation and then the critical Rayleigh number can be found by substituting k_c into equation (2.68). In the limit of rapid rotation where $E \to 0$, scalings for k_c and Ra_c can be found:

$$k_c = \frac{\pi^{2/3}}{2^{1/6}}E^{-1/3} \qquad \text{and} \qquad Ra_c = \frac{3\pi^{4/3}}{2^{2/3}}E^{-4/3}. \tag{2.70}$$

The case where the convection onsets as oscillations, known as *overstability*, is also discussed by Chandrasekhar (1961). This is done by inserting $s = \mathrm{i}\omega$, rather than $s = 0$, into equations (2.42 - 2.44) and considering the real and imaginary parts of the equation containing the Rayleigh number. An expression for ω is found and in order for it to be real two conditions must be satisfied. The conditions are that $Pr < 1$ and

$$E^{-2} > \frac{(1+Pr)(\pi^2+k^2)}{\pi^2(1-Pr)}, \tag{2.71}$$

in order for a disturbance with wavenumber, k, to occur as an overstable solution. There is an expression for the Rayleigh number associated with the overstable solutions, which as before can be minimised over all k for which overstability is possible. We then acquire the critical Rayleigh number for the onset of *overstable* solutions, Ra_c^o, for given values of the Prandtl and Ekman numbers. The value of Ra_c^o may or may not be less than that of the critical Rayleigh number, Ra_c, for the steady solutions with the equivalent Pr and E. If $Ra_c^o > Ra_c$ then steady solutions appear at onset. However, if $Ra_c^o < Ra_c$ then the instability will manifest itself as oscillatory modes at onset. Chandrasekhar (1961) shows that a necessary condition for the latter to be the case is $Pr < 0.67659$.

The above discussion has indicated that overstable solutions of the perturbation equations are possible and that, depending on the values of the Prandtl and Ekman numbers, the solution at onset can either be steady or oscillatory. However, the critical Rayleigh number in the rotating case is always greater than that of the non-rotating case, regardless of the nature of the onset solutions. We should also note that if the overstable form for the complex growth rate ($s = \mathrm{i}\omega$) is used in the equations for Rayleigh-Bénard convection in section 1.4, no real solutions for ω are possible. This indicates that oscillating solutions at onset are not permissible in the non-rotating case as we mentioned earlier.

2.4 Numerical method

In this section we wish to solve the differential eigenvalue problem given by equations (2.42 - 2.44) subject to the boundary conditions (2.59) and (2.60) or (2.61). To make it clear that this is an eigenvalue problem we rewrite equations (2.42 - 2.44) as

$$s\hat{\zeta} = \left(\frac{\mathrm{d}^2}{\mathrm{d}z^2} - \mathrm{i}k_x Rez - k^2\right)\hat{\zeta} + \left(\mathrm{i}k_y Re + E^{-1}\frac{\mathrm{d}}{\mathrm{d}z}\right)\hat{u}_z, \tag{2.72}$$

$$s\left(\frac{\mathrm{d}^2}{\mathrm{d}z^2} - k^2\right)\hat{u}_z = \left(\frac{\mathrm{d}^2}{\mathrm{d}z^2} - \mathrm{i}k_x Rez - k^2\right)\left(\frac{\mathrm{d}^2}{\mathrm{d}z^2} - k^2\right)\hat{u}_z - E^{-1}\frac{\mathrm{d}\hat{\zeta}}{\mathrm{d}z} - k^2 Ra\hat{\theta}, \tag{2.73}$$

$$sPr\hat{\theta} = \left(\frac{\mathrm{d}^2}{\mathrm{d}z^2} - \mathrm{i}k_x PrRez - k^2\right)\hat{\theta} + \left(1 + \frac{\mathrm{i}PrRek_y}{ERak^2}\frac{\mathrm{d}}{\mathrm{d}z}\right)\hat{u}_z - \frac{\mathrm{i}PrRek_x}{ERak^2}\hat{\zeta}. \tag{2.74}$$

In this system of equations the eigenvalue is the complex growth rate of the mode, s, and the corresponding set of eigenfunctions is the set $\Psi = \{\hat{u}_z, \hat{\zeta}, \hat{\theta}\}$.

We use the method of collocation to solve the eigenvalue problem. Collocation involves choosing a finite-dimensional space of candidate solutions and a number of 'collocation' points. The solution is then chosen to be the one that satisfies the equations at these points. For a thorough discussion of collocation, see Boyd (2001) or Canuto *et al.* (2006). Specifically, we use Chebyshev collocation and hence we begin by expanding the elements of Ψ in terms of Chebyshev polynomials:

$$\hat{u}_z(z) = \sum_{n=1}^{N+4} u_n T_{n-1}(X), \tag{2.75}$$

$$\hat{\zeta}(z) = \sum_{n=1}^{N+2} \zeta_n T_{n-1}(X), \tag{2.76}$$

$$\hat{\theta}(z) = \sum_{n=1}^{N+2} \theta_n T_{n-1}(X), \tag{2.77}$$

where z and X are related by $X = 2z$. That is, the interval $z \in [-1/2, 1/2]$ is mapped to $X \in [-1, 1]$, which is the usual interval used for Chebyshev polynomials. The coefficients u_n, ζ_n and θ_n are constants which are, in general, complex. Here N is the truncation parameter. The resolution of the numerical solution improves as N increases, that is as more polynomials are used. For any $\xi \in \Psi$, the sum over the Chebyshev polynomials runs from 1 to $N + N'$ where N' is the number of boundary conditions on ξ.

We now substitute the Chebyshev expansions into equations (2.72 - 2.74) and evaluate at a set of points, z_p, where $p = 1, ..., N$. By doing this we have converted the differential eigenvalue problem into a matrix eigenvalue problem of the form $sA_{jk}w_k = B_{jk}w_k$, where $\mathbf{w} = [u_1, ..., u_{N+4}, \zeta_1, ..., \zeta_{N+2}, \theta_1, ..., \theta_{N+2}]^{\mathrm{T}}$. We note that the matrices $\mathbf{A}$ and $\mathbf{B}$ contain the terms from the left-hand-side and right-hand-side of equations (2.72 - 2.74) respectively. The rows and columns of $\mathbf{A}$ and $\mathbf{B}$ correspond to the collocation points, X_p, and Chebyshev polynomials, T_{n-1} respectively. Hence, for $1 \leq j \leq N$, the jth row contains the coefficients of the w_ns of the first equation evaluated at the jth collocation point, X_j. For $N + 1 \leq j \leq N + 4$ the rows contain the information of the boundary conditions on $\hat{u}_z$. The remaining rows follow a similar pattern involving the coefficients for the second and third equations and the boundary conditions on $\hat{\zeta}$ and $\hat{\theta}$. Similarly, for each row the first $N+4$ columns contain the coefficients of the u_ns, the next $N+2$ columns contain the coefficients of the ζ_ns and the final $N + 2$ columns contain the coefficients of the θ_ns. The collocation points, X_p, rather than being equally spaced, are chosen to be the

N zeroes of the Chebyshev polynomial $T_N(X)$.

With this method in place the code is written in Fortran and we use a NAG routine, namely F02GBF, to calculate the eigenvalues and eigenvectors of this matrix eigenvalue problem given values for our input parameters. The system has the following six input parameters: k_x, k_y, Pr, E, Re and Ra, which can be varied to obtain the outputs: s and $\mathbf{w}$, the eigenvector. We can reconstruct the elements of Ψ from $\mathbf{w}$ using equations (2.75 - 2.77) to obtain the eigenfunctions, which are complex. We normalise the eigenfunctions using the value of the real part of the vertical vorticity eigenfunction at $z = 0$ so that $\hat{\zeta}(z) \rightarrow \hat{\zeta}(z)/\hat{\zeta}_{\mathrm{r}}(0)$, $\hat{u_z}(z) \rightarrow \hat{u}_z(z)/\hat{\zeta}_{\mathrm{r}}(0)$ and $\hat{\theta}(z) \rightarrow \hat{\theta}(z)/\hat{\zeta}_{\mathrm{r}}(0)$. If the real part of the vertical velocity eigenfunction at $z = 0$ happens to be zero we interchange the real and imaginary parts of all the eigenfunctions by multiplying through by $-\mathrm{i}$ and then normalise. The three-dimensional scalar fields ζ, u_z and θ are then constructed from the normalised eigenfunctions using equations (2.36 - 2.38).

If we let $\Gamma = \{k_x, k_y, Pr, E, Re\}$ we can test the stability of a given set Γ by gradually increasing Ra and solving the matrix eigenvalue problem until a marginal mode, where $\Re[s] \equiv \sigma = 0$, appears. We then record this value of the Rayleigh number, which is the value at the onset of convection, Ra^*, say. We mostly run the code at a resolution of $N = 100$, although we use some larger resolutions, $100 < N < 150$, to fully resolve the solutions for small values of the Ekman number and large values of the other parameters.

Figure 2.1 shows how the onset of convection changes as the azimuthal wavenumber and the zonal wind are varied for a particular choice of the Ekman number, Prandtl number and the latitudinal wavenumber, for both choices of boundary conditions. It should be noted that the data in figure 2.1 is represented on a log-log plot due to the varying magnitudes involved, and a log scale is necessary for the values of Ra^* also. Since we have positive and negative Rayleigh numbers, we plot only contours with $|Ra^*| > 1$, but this excludes only a tiny region in figures 2.1(a) and 2.1(b). Also of note is the fact that the quantity which has been plotted, Ra^*, is not the same as the critical Rayleigh number, Ra_c, since the latter is minimised over the wavenumbers, k_x and k_y. We plot Ra^* here rather than the critical Rayleigh number due to reasons discussed in section 2.6. Plots for Ra_c are displayed later. The solid green line, on both plots, divides regions of steady and oscillating modes. The oscillating modes are found to the right of this line in both cases.

The initial striking feature of both sets of results is the appearance of marginal modes with negative Rayleigh number. We see that these modes only appear under certain parameter regimes, namely for sufficiently large Re and sufficiently small k_x. Hence we are able to divide the parameter space into two regimes driven by different types of instability: the convective regime and the baroclinic regime, which are discussed individually in the next two sections. In the convective/baroclinic regime it is the buoyancy/shear, which is driving the instability. The form of the fields in xz-space for various parameter sets are shown in figures 2.2 and 2.3. The parameter values for all plots are displayed in table 2.1. Where possible, that is for the plots of figure 2.2 where $E = 10^{-4}$, the plots are marked in parameter space in figure 2.1. Further plots with $E \neq 10^{-4}$ are displayed in figure 2.3.

Point	E	Re	Ra	k_x
$\times_1$	10^{-4}	5	$Ra_c \equiv 1.8889 \times 10^6$	$k_{x_c} \equiv 27.9610$
$\times_2$	10^{-4}	$Re^* \equiv 10.9599$	-10^6	0.1
$\times_3$	10^{-4}	4000	$Ra^* \equiv -1.357111 \times 10^{11}$	0.1
$\times_4$	10^{-4}	5	$Ra_c \equiv 1.5193 \times 10^6$	$k_{x_c} \equiv 24.5630$
$\times_5$	10^{-4}	$Re_c \equiv 43.4458$	-10^6	3.8551
$\times_6$	10^{-4}	4000	$Ra^* \equiv 3.1259 \times 10^7$	30
$\times_7$	10^{-3}	5	$Ra_c \equiv 9.0528 \times 10^4$	$k_{x_c} \equiv 12.7334$
$\times_8$	10^{-3}	$Re^* \equiv 10.9720$	-10^6	0.1
$\times_9$	10^{-3}	4000	$Ra^* \equiv -1.3445 \times 10^9$	0.1
$\times_{10}$	10^{-5}	5	$Ra_c \equiv 4.0432 \times 10^7$	$k_{x_c} \equiv 60.4938$
$\times_{11}$	10^{-5}	$Re^* \equiv 10.95955831$	-10^6	0.1
$\times_{12}$	10^{-5}	4000	$Ra_c \equiv -1.3573 \times 10^{13}$	0.1

Table 2.1: Parameter values used for the plots of figures 2.2 and 2.3.

2.5 Convective regime

For low values of the zonal wind we expect to find the usual convective columnar roll solutions that we mentioned in section 2.3 and as described by Chandrasekhar (1961). These modes are steady, so that $\omega = 0$, and we refer to them as the ‘convective modes’.

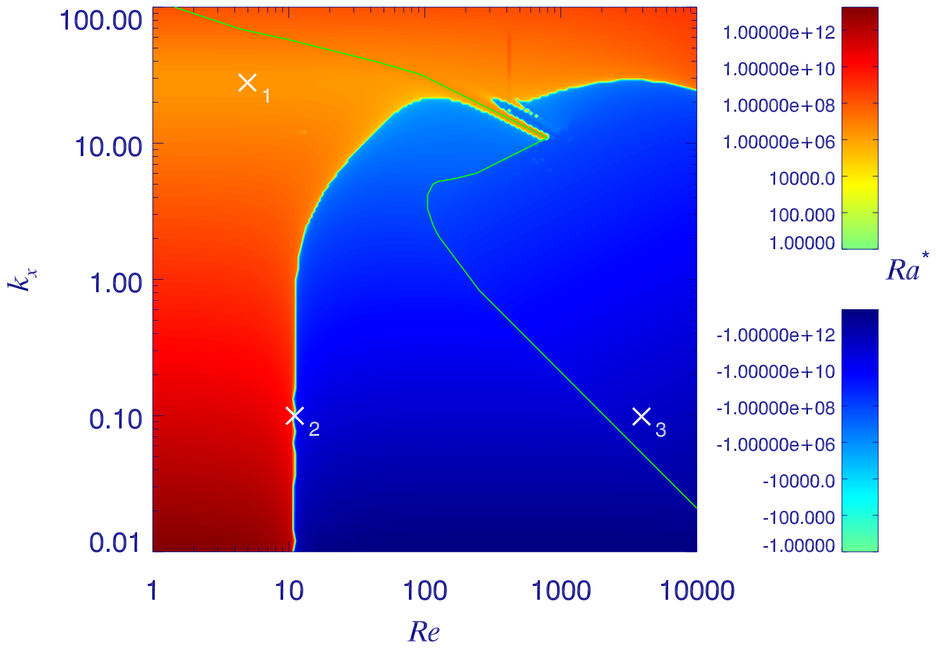

(a) Stress-free boundaries.

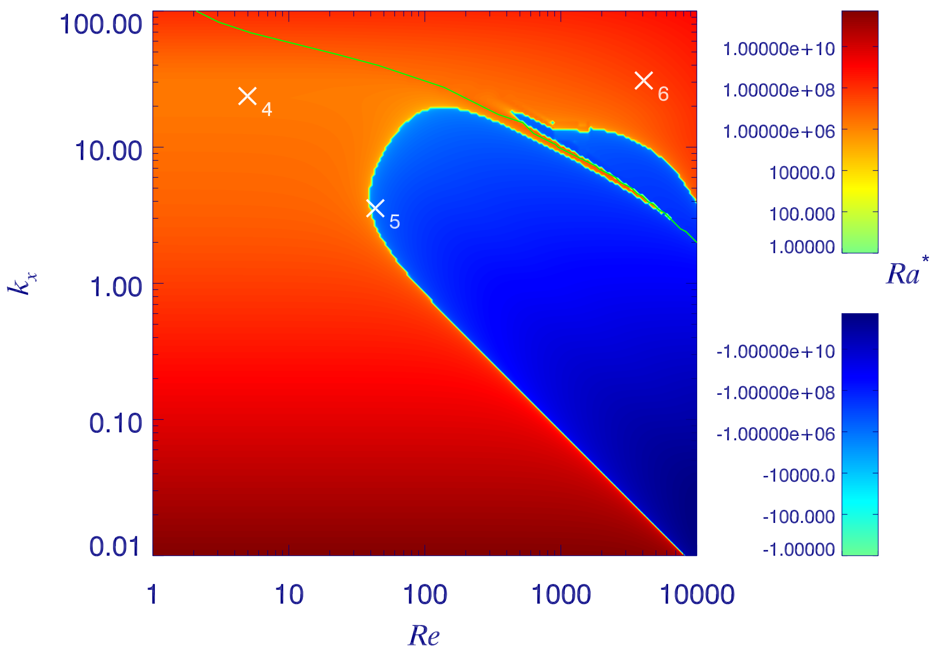

(b) No-slip boundaries.

Figure 2.1: Contour plots of the numerical results for the Rayleigh number at onset for Re against k_x with $E = 10^{-4}$, $Pr = 1$, $k_y = k_{y_c} = 0$. The colour scales denote the value of the Rayleigh number at onset, Ra^*. The green curves divide the regions of steady modes and oscillatory modes; onset being oscillatory to the right of these curves. $\times_1$ to $\times_6$ represent points in parameter space for which the fields have been plotted.

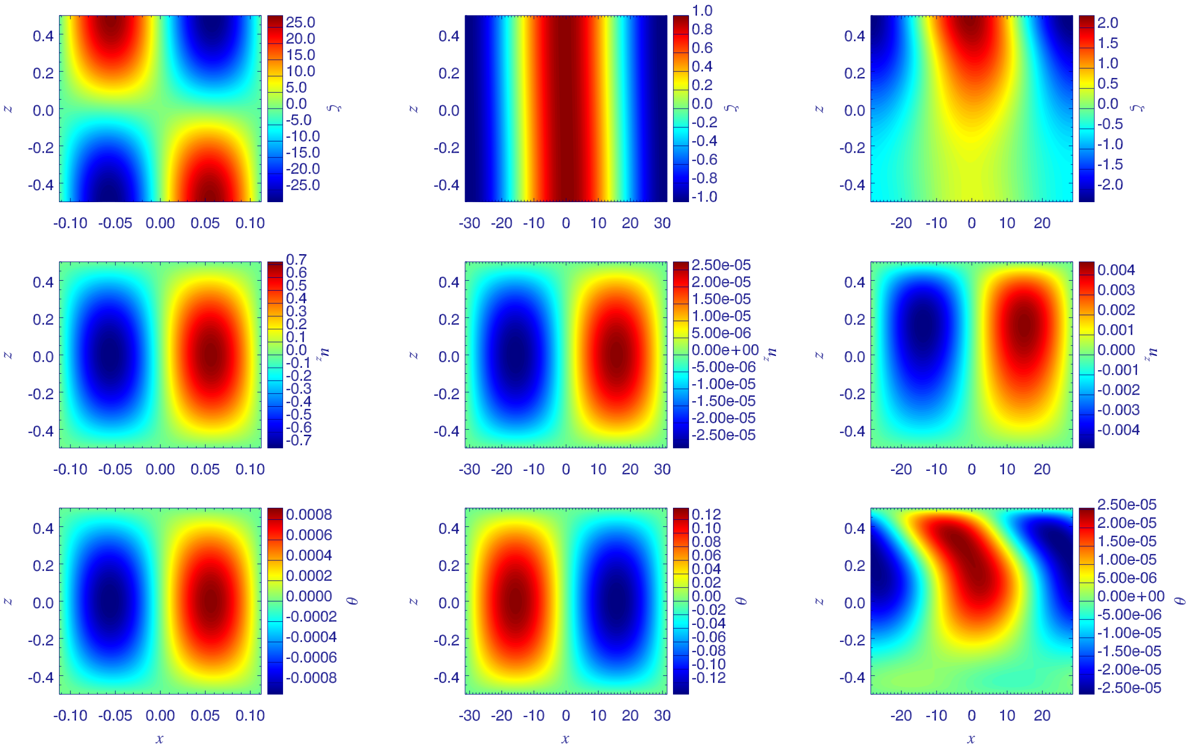

(a) $\times_1$ (b) $\times_2$ (c) $\times_3$

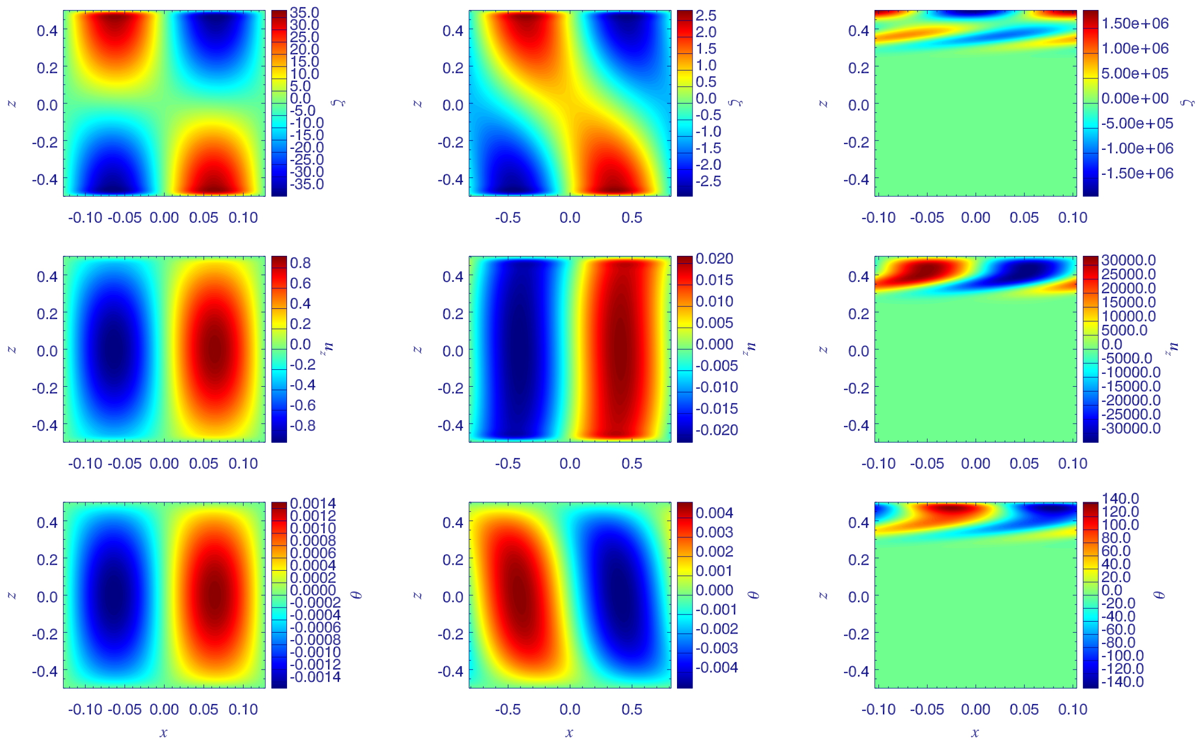

(d) $\times_4$ (e) $\times_5$ (f) $\times_6$

Figure 2.2: Plots of the fields corresponding to points marked on figure 2.1 where $E = 10^{-4}$, $Pr = 1$ and $k_y = k_{y_c} \equiv 0$. See table 2.1 for the parameter values of each plot.

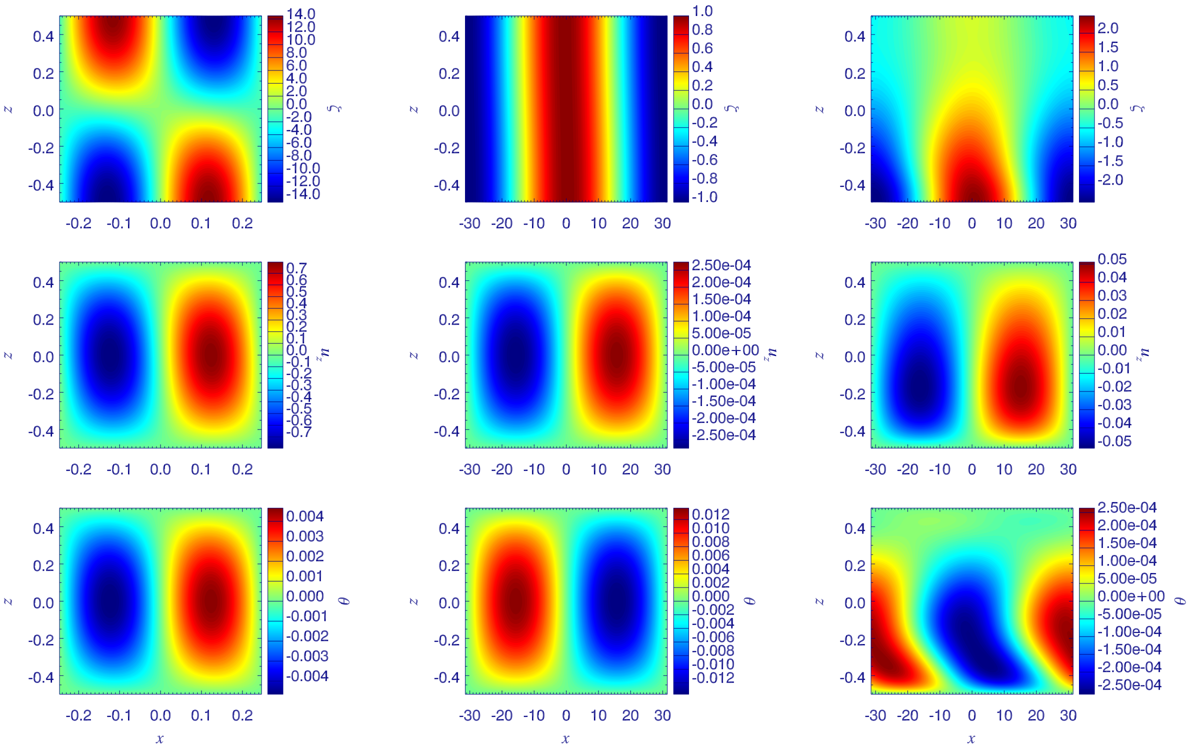

(a) $\times_7$ (b) $\times_8$ (c) $\times_9$

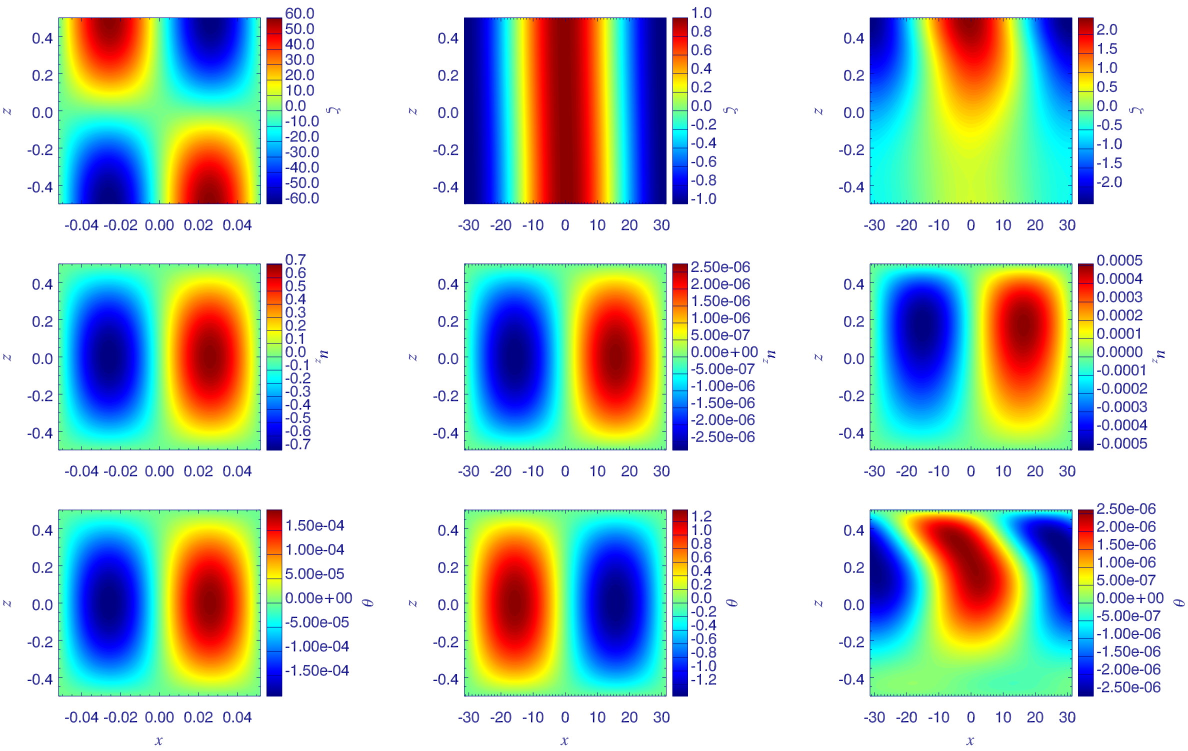

(d) $\times_{10}$ (e) $\times_{11}$ (f) $\times_{12}$

Figure 2.3: Plots of the fields for cases where $E \neq 10^{-4}$ with stress-free boundaries. See table 2.1 for the parameter values of each plot, $\times_i$.

Convective modes with the z-vorticity antisymmetric about the equator are expected as the most unstable modes in plane layer convection; the converse is true in the case of the full sphere as originally noted by Busse (1970). Indeed for the point marked $\times_1$ we find the mode to be of this form, as shown by figure 2.2(a). The structure has tall thin cells with hot fluid rising and cold fluid sinking as expected. This is the case for both types of boundary conditions as is evident from the similarity of figure 2.2(d), point $\times_4$, for the no-slip case. The form of the solution does not alter with different Ekman numbers as evidenced by figures 2.3(a) and 2.3(d), which are for $E = 10^{-3}$ and $E = 10^{-5}$, respectively. We also note that for $Re = 0$ if we minimise the Rayleigh number at onset over k, to find the critical Rayleigh number, the preferred values are $Ra_c \sim 1.8970 \times 10^6$ with $k_c \sim 28.0243$ for the stress-free case and $Ra_c \sim 1.5251 \times 10^6$ with $k_c \sim 24.6366$ for the no-slip case, for the values of E and Pr used in figure 2.1. This is in agreement with the previous literature; compare with table VII and VIII of Chandrasekhar (1961).

The critical values of the wavenumbers do however depend on Re. In the case of $Re = 0$ the system has complete symmetry in the x and y directions, so all wavenumbers k_x and k_y satisfying $k_x^2 + k_y^2 = k_c^2$ onset at Ra_c. However, as the zonal wind strength is increased from zero we find that there is immediately a preference for two-dimensional modes with $k_{y_c} = 0$. This is the case for all modes with $Re \neq 0$. Hence the convection cells are, in fact, rolls elongated in the y-direction. Unfortunately, equations (2.42 - 2.44) are too complex to be able to perform Squire's transformation (Squire, 1933), though this can be done for non-rotating shear flows (Drazin & Reid, 1981). We also find that the value of the critical Rayleigh number decreases, for both types of boundary conditions, as shown by figure 2.4. Hence the zonal wind has a destabilising effect on the system and aids the onset of convection as well as setting a preference for convective rolls aligned with the y-axis. This is in contrast with the non-rotating case where, in the presence of the same shear, the preference is for rolls with $k_x = 0$, $k_y \neq 0$ (Deardorff, 1965). Thus, the addition of rotation alters the convection pattern, from rolls aligned with the flow to rolls perpendicular to the flow. The critical azimuthal wavenumber, k_{x_c}, also decreases as Re is increased for both types of boundary conditions as shown by figure 2.4. The two plots of the fields in the convective regime, $\times_1$ and $\times_4$, whose positions in parameter space are also indicated in figure 2.4, are for critical values of k_x and Ra^* with $Re = 5$.

As Re is increased we move into the baroclinic regime and hence the values of Re chosen for the plot in figure 2.4 are relatively low in order to remain in the convective regime. For modes in the convective regime the main energy balance is between the buoyancy and the viscous stresses. However as Re is increased, the baroclinic basic state means that buoyancy can do work at lower critical Rayleigh number, and indeed even at negative Rayleigh number. This is discussed in section 2.8.

2.6 Baroclinic regime

As the zonal wind strength is increased further we find a second type of mode, which allows for instability regardless of how negative the Rayleigh number is. In other words this mode can be unstable no matter how stably stratified the system is. For this reason we refer to them as ‘baroclinic modes’, which are distinct from the convective modes that are usually found as the most unstable modes. They are related to the unstable modes of the Eady problem (Pedlosky, 1987), which we later discuss in section 3.4. This suggests that we should consider a critical Reynolds number, rather than a critical Rayleigh number, for the baroclinic modes since it is the shear that is driving this instability. Hence we introduce a critical Reynolds number, Re_c, and corresponding critical wavenumbers, k_{x_c} and k_{y_c} for the baroclinic regime. For a given Ekman number, Prandtl number and Rayleigh number Re_c is the value of the Reynolds number for which a marginal baroclinic mode can appear (analogous to the critical Rayleigh number in the convective regime). As with all modes with a non-zero Reynolds number we find that $k_{y_c} = 0$. The modes remain steady in the baroclinic regime for low values of Re. However, oscillating modes appear at onset for larger values of Re, which are found in the regimes of parameter space to the right of the green line in figure 2.1.

From figure 2.5 we see how Re^* varies with k_x for several negative values of the Rayleigh number for both types of boundary conditions. For stress-free boundaries we see from figure 2.5(a) that in all cases $k_{x_c} = 0$ and $Re_c \sim 10.95$. Therefore reducing k_x allows for instability with an ever more negative Rayleigh number as shown by table 2.2. It is for this reason that Ra^* rather than Ra_c is plotted in figure 2.1. An asymptotic theory highlighting these results and which obtains a value of Re_c for any given Ra and Pr in the small E limit, is discussed in chapter 3. The form of a typical baroclinic mode at onset is shown in

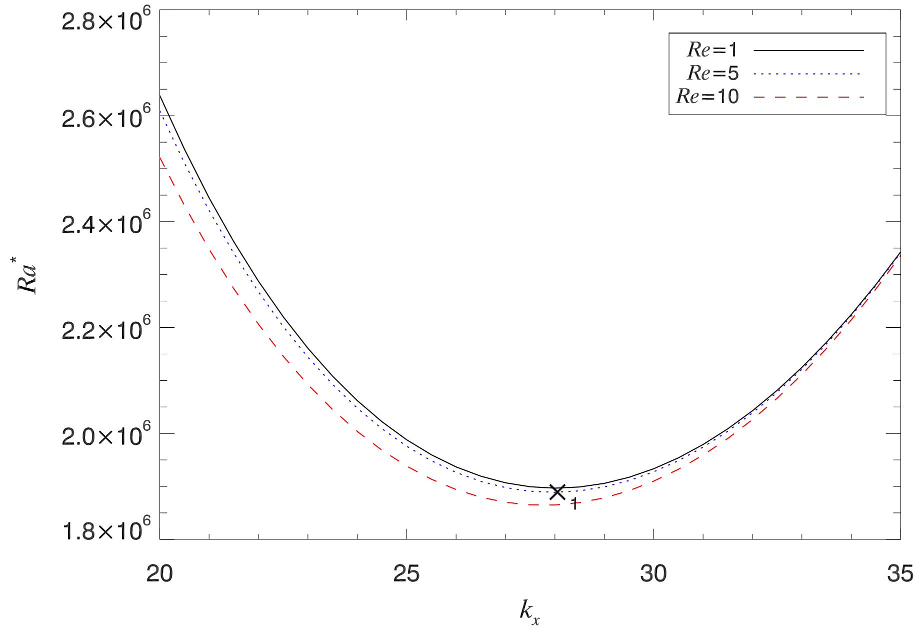

(a) Stress-free boundaries.

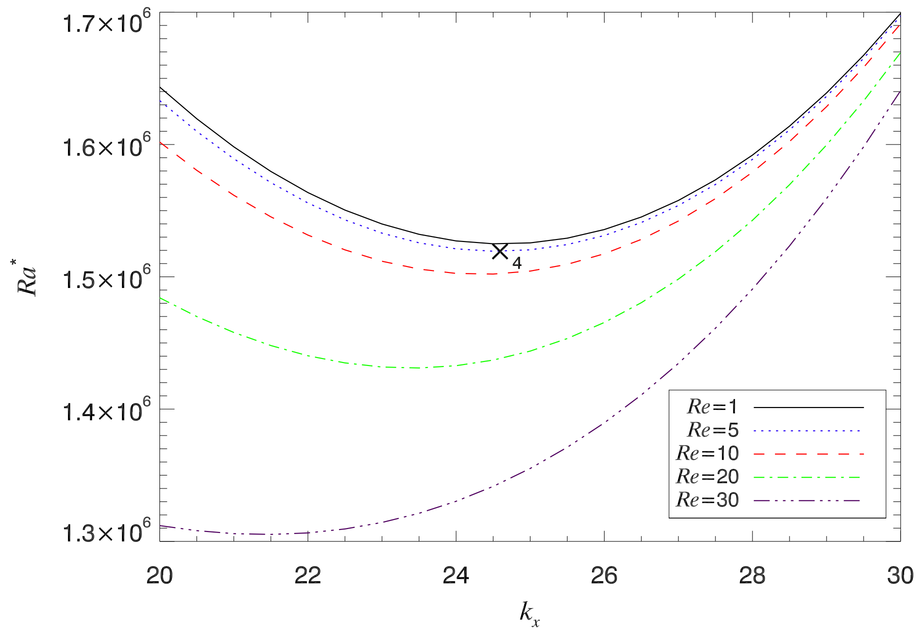

(b) No-slip boundaries.

Figure 2.4: Plots of the numerical results for the onset parameters in the convective regime against k_x with $E = 10^{-4}$, $Pr = 1$, $k_y = k_{y_c} = 0$. The onset parameter is the Rayleigh number in the convective regime.

figure 2.2(b), point $\times_2$. We see that the vorticity is independent of z and that θ has flipped signs for this type of mode so that the hot fluid is sinking and the cold fluid is rising. This is directly related to the change in sign of the Rayleigh number and is due to the fact that the baroclinic basic state allows buoyancy to fully balance the viscous stresses even at negative Rayleigh number (see section 2.8). However, the magnitude of the vertical velocity is small, indicating that the shear is dominating the flow in these modes. Again, the form of the eigenfunctions does not vary with the Ekman number as we can see from figures 2.3(b) and 2.3(e). However, the magnitudes of the fields do seem to scale with the Ekman number. This suggests that an asymptotic analysis may be possible for small E, which is developed in chapter 3. The general form of the eigenfunctions remains similar to that shown in figure 2.2(b) as k_x is reduced towards the true critical value; namely $k_{x_c} = 0$.

	Ra^*		
k_x	$E = 10^{-3}$	$E = 10^{-4}$	$E = 10^{-5}$
0.01	-9.6562×10^{10}	-9.6578×10^{12}	-9.6577×10^{14}
0.05	-3.8618×10^{9}	-3.5057×10^{11}	-3.8624×10^{13}
0.1	-9.6496×10^{8}	-9.6511×10^{10}	-9.6511×10^{12}
0.5	-3.7972×10^{7}	-3.7980×10^{9}	-3.7980×10^{11}
1	-9.0591×10^{6}	-9.0636×10^{8}	-9.0637×10^{10}

Table 2.2: Numerically computed values of Ra^* for various E and k_x in the case $Re = 100$, $Pr = 1$ and $k_y = k_{y_c} = 0$ for stress-free boundaries.

For no-slip boundaries we see from figure 2.5(b) that there is a non-zero critical azimuthal wavenumber, which varies with Ra. As the Rayleigh number is made more negative the critical azimuthal wavelength lengthens and the critical Reynolds number increases. Figure 2.2(e), point $\times_5$, shows the form of the eigenfunctions at critical for $Ra = -10^6$. As with the stress-free case, the sign of θ has changed from the convective regime and the magnitude of u_z is small. However the vorticity now takes a more complicated slanted structure, which is asymmetric in z, in contrast to the stress-free case where ζ was independent of z.

The baroclinic modes are only found for certain parameter regimes as highlighted by

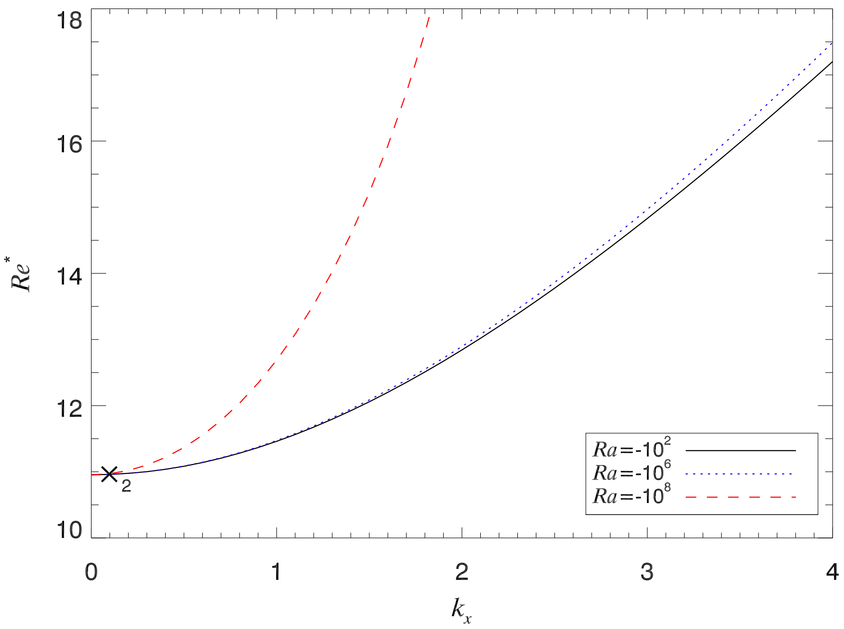

(a) Stress-free boundaries.

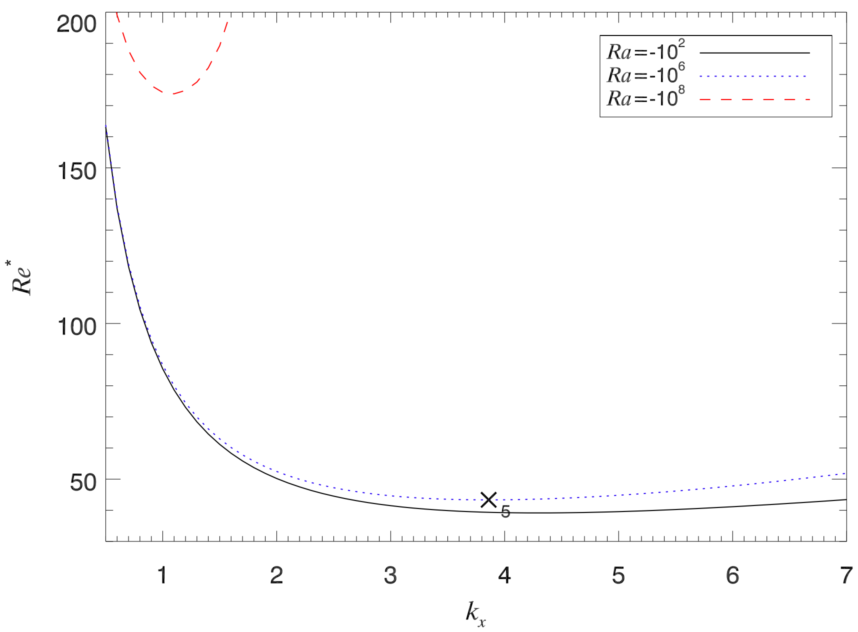

(b) No-slip boundaries.

Figure 2.5: Plots of the numerical results for the onset parameters in the baroclinic regime against k_x with $E = 10^{-4}$, $Pr = 1$, $k_y = k_{y_c} = 0$. The onset parameter is the Reynolds number in the baroclinic regime.

figure 2.1. For stress-free boundaries we must have $k_x \lesssim 30$ and $Re \gtrsim 10$ for these modes to appear and as such this is a constraint on their existence. For no-slip boundaries the parameter regime for the existence of the baroclinic modes is altered slightly but we still require a sufficiently large Re and sufficiently small k_x. Outside of these regimes we recover the convective modes at onset, which have positive Rayleigh number. This is demonstrated by considering the $Re = 1$ line in figure 2.1(a), which has solely positive Ra^*. In the stress-free case, for a sufficiently large Re, the Rayleigh number is negative and depends on k_x and E such that reducing either of these parameters towards zero makes the Rayleigh number more negative. In fact from table 2.2 it is clear that the magnitude of Ra^* is inversely proportional to both k_x^2 and E^2. This remains true for different values of Re. In this way we see that it is possible to have instability regardless of how negative the Rayleigh number is by choosing a small enough k_x and sufficiently large Re.

Baroclinic instabilities driven by a zonal flow of the same form as that considered here were investigated by Rashid *et al.* (2008). However, their model assumed that the fluid was always stably stratified so that convective instabilities were not permitted. This was because their interest lay in the strongly stably stratified solar tachocline. Our work has investigated the transition between convective and baroclinic instabilities by allowing for both stable and unstable stratification. Rashid *et al.* (2008) found two types of mode appearing and they concentrated on how the strength of the modes changes under various parameter regimes. This resulted in a focus on the low Ekman number and low Prandtl number limits. By considering finite Pr we have found baroclinic instabilities with $k_x = 0 = k_y$ in contrast to Rashid *et al.* (2008) who found that $k_x = 0, k_y \neq 0$.

2.7 Further observations from the numerics

Between the regions of positive and negative Rayleigh number there is a sharp *transition region* where the Rayleigh number passes through zero in a relatively small region of Re-space. The Rayleigh number varies smoothly from positive to negative values across the transition region. The values of the Reynolds number at onset in the case of stress-free boundaries, for a given k_x, Re^*, for the transition region at which $Ra^* = 0$ are given in table 2.3. As E is reduced Re^* at transition converges to a value independent of the

	Re^*							
	$E = 10^{-4}$				$E = 10^{-5}$			
k_x	$Pr = 0.1$	$Pr = 1$	$Pr = 10$	$Pr = 20$	$Pr = 0.1$	$Pr = 1$	$Pr = 10$	$Pr = 20$
0.1	34.8718	10.9610	3.4646	1.5386	34.6946	10.9550	3.4644	1.5388
0.5	35.0289	11.0731	3.4705	1.5055	34.9326	11.0255	3.4681	1.5107
1.0	36.3620	11.6266	3.5264	1.4283	36.3097	11.6129	3.5200	1.4270
5.0	64.7904	19.8318	5.0890	1.5917	64.7775	19.8296	5.0881	1.5914
10.0	115.4635	35.1904	10.5572	4.8452	114.6989	35.1208	10.5128	4.8066

Table 2.3: Numeric results showing the position of the transition region, the point where $Ra^* = 0$, in Re-space for various values of k_x, E and Pr in the case $k_y = k_{y_c} = 0$ with stress-free boundaries.

Ekman number. From table 2.3 we also notice that reducing k_x lowers the Reynolds number at onset suggesting once again that the minimising k_x is zero (that is $k_{x_c} = 0$) and Re_c is converging to a value dependent on the Prandtl number.

The modes described so far have all been steady. Steady modes are usually preferred for the onset of convection in a rotating plane layer at $Pr = 1$, unsteady modes being possible at lower Pr, as we discussed in section 2.3. However, by increasing Re further we also found unsteady modes appearing at onset even at $Pr = 1$. These modes are found in the region of parameter space shown in figures 2.1(a) and 2.1(b) to the right of the dividing curve, the solid line in both figures. We see that these unsteady modes can onset with either positive or negative Rayleigh number. Figure 2.2(c), point $\times_3$, shows the eigenfunctions for such an oscillatory mode in the case of stress-free boundaries. These modes onset as pairs of traveling wall modes with frequencies which are equal but opposite in sign. Oscillatory modes are found at larger k_x and Re for the no-slip case, an example being shown in figure 2.2(f), point $\times_6$. The fields of these oscillatory modes maintain the same form for different Ekman numbers as shown by figures 2.3(c) and 2.3(f). If the domain is infinite in the x and y directions, all wavenumbers k_x and k_y are allowed, and the critical mode is always steady, either at fixed Ra as Re is gradually increased or at fixed Re as Ra is gradually increased. However, if the domain is finite, and for example periodic boundary conditions in x and y are imposed, thus restricting the possible choice of wavenumbers to a discrete set, then it would be possible for oscillatory modes to be preferred.

In the work displayed so far we have varied the parameters of most interest: k_x, Re and Ra whilst looking at specific values for Pr and E. We have also found that $k_{y_c} = 0$ for the modes of interest (that is modes with $Re \neq 0$). Although instability is possible with $k_y \neq 0$ in both the convective and baroclinic regimes, we find that increasing k_y from zero only serves to stabilise the system by increasing the Rayleigh number or Reynolds number for which onset occurs. Here we consider the effects of varying the Ekman and Prandtl numbers.

We first look at two further values for the Ekman number: 10^{-3} and 10^{-5}. We find that changing E alters the magnitude of the Rayleigh number at onset but does not affect the position of the baroclinic parameter regime in $k_x - Re$ space. The results in table 2.2 highlight the fact that for the baroclinic mode Ra^* is inversely proportional to E^2. Therefore if we increase the Rayleigh number from $-\infty$ changing the Ekman number controls how soon the instability occurs. However we still require the same sufficiently large Re and small values of k_x.

We consider further values of the Prandtl number: $Pr = 0.1$, $Pr = 10$ and $Pr = 20$. In a way the effect of changing the Prandtl number is opposite to that of altering the Ekman number. This is because although the Rayleigh number remains largely unaffected for various Pr, the position of the baroclinic regime in $k_x - Re$ space changes. This can be seen in table 2.3 where the transition region occurs at a higher/lower value of Re^* for a lower/higher value of Pr. We see that for $Pr = 10$ the baroclinic modes are able to appear at a lower value of the zonal wind ($Re \sim 3.5$), compared to the $Pr = 1$ case. The converse is true when $Pr = 0.1$ where the baroclinic modes cannot appear until $Re \sim 35$. The behaviour of the critical parameters at moderate values of the Prandtl number $(Pr = 0.1 - 10)$ remains largely the same with $k_{x_c} = 0$ continuing to be preferred in the stress-free baroclinic regime. However we note that there is a non-zero minimising k_x for larger values of Pr so long as the magnitude of Ra is not too large. An example of this can be seen in table 2.3 when $Pr = 20$, for both values of the Ekman number. Two further cases, with Ra non-zero, are displayed in figure 2.6 where we find $k_{x_c} \sim 1.5$ and $k_{x_c} \sim 2.7$ for $Pr = 20$ and $Pr = 50$, respectively. Note, in contrast, that the line for the case of $Pr = 10$ takes its minimum value when the azimuthal wavenumber is zero so that $k_{x_c} = 0$. The critical values of the Reynolds number for these two cases are also smaller than for the other Prandtl numbers considered, as expected. The asymptotic theory in

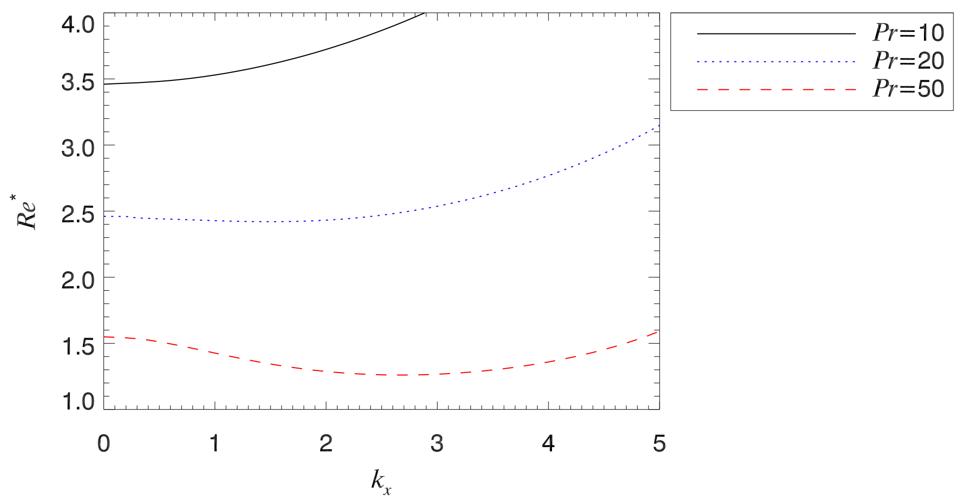

Figure 2.6: Plot showing how the Reynolds number at onset varies with k_x for several values of Pr and $E = 10^{-4}$, $Ra = -1$ and $k_y = k_{y_c} = 0$ with stress-free boundaries.

chapter 3 is able to explain this dependence of k_{x_c} on Pr.

2.8 Thermodynamic equation

In this section we derive a thermodynamic equation from the equations in section 2.1 in order to analyse how terms representing different physical effects interact for various values of the input parameters. In particular we see how varying the parameter controlling the size of the basic state zonal flow, Re, affects the balance between terms. In the absence of the zonal flow we should recover the condition that $Ra > 0$ for motions to occur.

We continue to enforce $k_y = 0$, which is the case most favourable when $Re \neq 0$, and also $s = 0$ for marginal, non-oscillating modes. It should also be noted that we are able to use the results of appendix C here since the fields take the form (see equations (2.39 - 2.41)) given at the start of appendix C. We begin by considering the dot product of $\mathbf{u}$ with equation (2.19). We then form the energy equation by integrating over a periodic box on the intervals $x \in [-\pi/k_x, \pi/k_x]$, $y \in [-\pi/k_y, \pi/k_y]$ and $z \in [-d/2, d/2]$, which since $k_y = 0$ amounts to integrating over x and z only. This gives,

$$\begin{aligned}\int \mathbf{u}\cdot\frac{\partial \mathbf{u}}{\partial t}\mathrm{d}V + \int U_0' z\mathbf{u}\cdot\frac{\partial \mathbf{u}}{\partial x}\mathrm{d}V + \int U_0' u_z u_x \mathrm{d}V + \int \mathbf{u}\cdot 2\boldsymbol{\Omega}\times\mathbf{u}\mathrm{d}V \\ = -\int (\mathbf{u}\cdot\nabla)p\mathrm{d}V + g\alpha\int \theta u_z\mathrm{d}V + \nu\int \mathbf{u}\cdot\nabla^2\mathbf{u}\mathrm{d}V,\end{aligned} \tag{2.78}$$

where

$$\int \mathrm{d}V = \int_{-d/2}^{d/2} \int_{-\pi/k_x}^{\pi/k_x} \mathrm{d}x\mathrm{d}z. \tag{2.79}$$

The first term vanishes for marginal, non-oscillating modes and the fourth term vanishes due to $\mathbf{u}$ being perpendicular to $\boldsymbol{\Omega} \times \mathbf{u}$. Now we consider the remaining terms separately and first note that the second term, using equation (A.3), can be written

$$\begin{aligned}
\int U_0' z \mathbf{u} \cdot \frac{\partial \mathbf{u}}{\partial x} \mathrm{d}V &= \int \frac{1}{2} \left(U_0' z \frac{\partial |\mathbf{u}|^2}{\partial x} \right) \mathrm{d}V && (2.80)\\
&= \frac{1}{2} \int U_0' \frac{\partial}{\partial x} \left(z \left(u_x^2 + u_y^2 + u_z^2 \right) \right) \mathrm{d}V && (2.81)\\
&= \frac{1}{4} \int U_0' \frac{\partial}{\partial x} \left(z \left(\hat{u}_x \hat{u}_x^* + \hat{u}_y \hat{u}_y^* + \hat{u}_z \hat{u}_z^* \right) \right) \mathrm{d}V && (2.82)\\
&= 0, && (2.83)
\end{aligned}$$

where we have also used (C.10). The term involving the pressure becomes

$$\begin{aligned}
\int (\mathbf{u} \cdot \nabla) p \mathrm{d}V &= \int \nabla \cdot (p\mathbf{u}) \mathrm{d}V - \int p \nabla \cdot \mathbf{u} \mathrm{d}V && (2.84)\\
&= \int \frac{\partial}{\partial x_k} (p u_k) \mathrm{d}V && (2.85)\\
&= \int p u_k \mathrm{d}S_k, && (2.86)
\end{aligned}$$

since $\nabla \cdot \mathbf{u} = 0$ and where $\mathrm{d}S_k$ is the surface element of our periodic box. Here we have also used the Divergence theorem to convert the volume integral into a surface integral. Hence

$$\int p u_k \mathrm{d}S_k = \int_{-d/2}^{d/2} p u_x \mathrm{d}z \bigg|_{x=\pm\pi/k_x} + \int_{-\pi/k_x}^{\pi/k_x} p u_z \mathrm{d}x \bigg|_{z=\pm d/2}. \tag{2.87}$$

The first of these terms vanishes since p and u_x are both periodic in x; that is $u_x(x = -\pi/2, z) = u_x(x = \pi/2, z)$ and similarly for p. Therefore the z-integral will take the same value on the two surfaces $x = \pm\pi/k_x$ and hence cancel. In other words, the flux is the same through both x-surfaces. The second term also vanishes because $u_z = 0$ on $z = \pm d/2$. Hence this surface integral term is identically zero and from equation (2.86) we have

$$\int (\mathbf{u} \cdot \nabla) p \mathrm{d}V = 0. \tag{2.88}$$

We now consider the final term of equation (2.78), which can be simplified as

$$\begin{aligned}\nu \int \mathbf{u}\cdot\nabla^2\mathbf{u}\mathrm{d}V &= \nu \int u_j \frac{\partial}{\partial x_k}\frac{\partial}{\partial x_k}u_j\mathrm{d}V & (2.89)\\ &= \nu \int \frac{\partial}{\partial x_k}\left(u_j\frac{\partial}{\partial x_k}u_j\right)\mathrm{d}V - \nu\int \frac{\partial u_j}{\partial x_k}\frac{\partial u_j}{\partial x_k}\mathrm{d}V & (2.90)\\ &= \nu \int u_j\frac{\partial}{\partial x_k}u_j\mathrm{d}S_k - \nu\int \frac{\partial u_j}{\partial x_k}\frac{\partial u_j}{\partial x_k}\mathrm{d}V, & (2.91)\end{aligned}$$

where, again, $\mathrm{d}S_k$ is the surface element of our periodic box and we have used the Divergence theorem. Now we can expand the surface integral term so that

$$\begin{aligned}\nu\int u_j\frac{\partial}{\partial x_k}u_j\mathrm{d}S_k = \nu &\int_{-d/2}^{d/2}\left(u_y\frac{\partial u_y}{\partial x}+u_z\frac{\partial u_z}{\partial x}\right)\mathrm{d}z\Bigg|_{x=\pm\pi/k_x}\\ &+\nu\int_{-\pi/k_x}^{\pi/k_x}\left(u_y\frac{\partial u_y}{\partial z}+u_z\frac{\partial u_z}{\partial z}\right)\mathrm{d}x\Bigg|_{z=\pm d/2}.\end{aligned} \quad (2.92)$$

Both of these terms vanish via a similar argument to the surface integral involving the pressure vanishing where we note that either $u_y = 0$ (if we have no-slip boundaries) *or* $\partial u_y/\partial z = 0$ (if we have stress-free boundaries) on $z = \pm d/2$. Hence the surface integral term is identically zero and from equation (2.91) we have

$$\nu\int \mathbf{u}\cdot\nabla^2\mathbf{u}\mathrm{d}V = -\nu\int\frac{\partial u_j}{\partial x_k}\frac{\partial u_j}{\partial x_k}\mathrm{d}V, \quad (2.93)$$

and we are then left with only three terms of equation (2.78):

$$g\alpha\int\theta u_z\mathrm{d}V = \nu\int\frac{\partial u_j}{\partial x_k}\frac{\partial u_j}{\partial x_k}\mathrm{d}V + U_0'\int u_z u_x\mathrm{d}V. \quad (2.94)$$

Now we also multiply equation (2.20) by θ and integrate over the periodic box to acquire

$$\int\theta\frac{\partial\theta}{\partial t}\mathrm{d}V + \int U_0' z\theta\frac{\partial\theta}{\partial x}\mathrm{d}V - \beta\int\theta u_z\mathrm{d}V - \frac{2\Omega U_0'}{g\alpha}\int\theta u_y\mathrm{d}V = \kappa\int\theta\nabla^2\theta\mathrm{d}V. \quad (2.95)$$

As with the energy equation the first term vanishes since we are considering marginal, non-oscillating modes and the second term also vanishes by a similar argument to the second term in the energy equation above. Again by a similar argument to the final term of the energy equation above, the final term of equation (2.95) also can be written

$$\kappa\int\theta\nabla^2\theta\mathrm{d}V = -\kappa\int\left(\frac{\partial\theta}{\partial x_k}\frac{\partial\theta}{\partial x_k}\right)\mathrm{d}V = -\kappa\int(\nabla\theta)^2\mathrm{d}V. \quad (2.96)$$

Then equation (2.95) reduces to

$$-\beta\int\theta u_z\mathrm{d}V - \frac{2\Omega U_0'}{g\alpha}\int\theta u_y\mathrm{d}V = -\kappa\int(\nabla\theta)^2\mathrm{d}V, \quad (2.97)$$

and we now eliminate the rate of working of the buoyancy force (the θu_z-integral) using equation (2.94) to give

$$g\alpha\kappa\int(\nabla\theta)^2\mathrm{d}V - 2\Omega U_0'\int\theta u_y\mathrm{d}V = \beta\nu\int\frac{\partial u_j}{\partial x_k}\frac{\partial u_j}{\partial x_k}\mathrm{d}V + \beta U_0'\int u_z u_x\mathrm{d}V. \quad (2.98)$$

We non-dimensionalise as before using the same scales as in section 2.1, which gives

$$g\alpha\kappa\int\frac{\beta^2\nu^2}{\kappa^2}(\nabla\theta)^2\mathrm{d}V - 2\Omega U_0'\int\frac{\beta\nu^2}{\kappa}\theta u_y\mathrm{d}V = \beta\nu\int\frac{\nu^2}{d^4}\frac{\partial u_j}{\partial x_k}\frac{\partial u_j}{\partial x_k}\mathrm{d}V + \beta U_0'\int\frac{\nu^2}{d^2}u_z u_x\mathrm{d}V, \quad (2.99)$$

and using the dimensionless numbers from equation (2.32) this can be written

$$Ra\int(\nabla\theta)^2\mathrm{d}V - PrE^{-1}Re\int\theta u_y\mathrm{d}V - \int\frac{\partial u_j}{\partial x_k}\frac{\partial u_j}{\partial x_k}\mathrm{d}V - Re\int u_z u_x\mathrm{d}V = 0,$$
$$\text{or}\quad I_1 + I_2 + I_3 + I_4 = 0. \quad (2.100)$$

We refer to this integral equation as the thermodynamic equation and the solutions to the earlier numerics must satisfy it. The thermodynamic equation is comprised of four integrals representing a different physical process. The first term, I_1, is effectively the work done by the buoyancy. The second integral, I_2, is related to the heat flux carried in the y direction, and is only non-zero when the zonal flow is non-zero due to the presence of Re in the term. The third term, I_3, is the rate of viscous dissipation. Finally, I_4 is a component of the Reynolds stresses. We note here that if $Re = 0$ then the Rayleigh number is the ratio of two positive definite integrals:

$$Ra = \frac{\int\left(\frac{\partial u_j}{\partial x_k}\right)^2\mathrm{d}V}{\int(\nabla\theta)^2\mathrm{d}V}, \quad (2.101)$$

and hence we recover the condition that $Ra \geq 0$ as expected and as derived by Chandrasekhar (1961).

We can write equation (2.100) in terms of the real and imaginary parts of $\hat{u}_z$, $\hat{\zeta}$ and $\hat{\theta}$ and their derivatives, all of which have been calculated in the numerics earlier. We do this term by term making use of appendix C and once the x-dependence of the integrand of each term has been accounted for the x-integral can be evaluated, noting that

$$\int_{-\pi/k_x}^{\pi/k_x}\mathrm{d}x = \frac{2\pi}{k_x}. \quad (2.102)$$

We also use equations (B.5) and (B.6) to note that

$$u_x = \frac{1}{k_x^2}\frac{\partial^2 u_z}{\partial x\partial z}, \quad (2.103)$$
$$u_y = -\frac{1}{k_x^2}\frac{\partial\zeta}{\partial x}, \quad (2.104)$$

since $k_y = 0$, which will be useful shortly. We begin with the first term of equation (2.100), which is

$$I_1 = Ra\int(\nabla\theta)^2\mathrm{d}V = Ra\int\left(\left(\frac{\partial\theta}{\partial x}\right)^2+\left(\frac{\partial\theta}{\partial z}\right)^2\right)\mathrm{d}V \tag{2.105}$$

$$= \frac{Ra}{2}\int\left(k_x^2\left(\hat{\theta}_\mathrm{r}^2+\hat{\theta}_\mathrm{i}^2\right)+\left(\frac{\mathrm{d}\hat{\theta}_\mathrm{r}}{\mathrm{d}z}\right)^2+\left(\frac{\mathrm{d}\hat{\theta}_\mathrm{i}}{\mathrm{d}z}\right)^2\right)\mathrm{d}V \tag{2.106}$$

$$= \frac{\pi Ra}{k_x}\int_{-1/2}^{1/2}\left(k_x^2\left(\hat{\theta}_r^2+\hat{\theta}_i^2\right)+\left(\frac{\mathrm{d}\hat{\theta}_\mathrm{r}}{\mathrm{d}z}\right)^2+\left(\frac{\mathrm{d}\hat{\theta}_\mathrm{i}}{\mathrm{d}z}\right)^2\right)\mathrm{d}z, \tag{2.107}$$

where we have used equations (C.11) and (C.9). Next we replace u_y in the second term of equation (2.100) with ζ using equation (2.104) to give

$$-PrE^{-1}Re\int\theta u_y\mathrm{d}V = \frac{PrE^{-1}Re}{k_x^2}\int\theta\frac{\partial\zeta}{\partial x}\mathrm{d}V. \tag{2.108}$$

Hence

$$I_2 = -PrE^{-1}Re\int\theta u_y\mathrm{d}V = \frac{PrE^{-1}Re}{2k_x}\int\left(\hat{\theta}_\mathrm{i}\hat{\zeta}_\mathrm{r}-\hat{\theta}_\mathrm{r}\hat{\zeta}_\mathrm{i}\right)\mathrm{d}V \tag{2.109}$$

$$= \frac{\pi PrE^{-1}Re}{k_x^2}\int_{-1/2}^{1/2}\left(\hat{\theta}_\mathrm{i}\hat{\zeta}_\mathrm{r}-\hat{\theta}_\mathrm{r}\hat{\zeta}_\mathrm{i}\right)\mathrm{d}z, \tag{2.110}$$

using equation (C.14). Thirdly we consider the third term of equation (2.100), where we note that

$$-\int\frac{\partial u_j}{\partial x_k}\frac{\partial u_j}{\partial x_k}\mathrm{d}V = -\int\left((\nabla u_x)^2+(\nabla u_y)^2+(\nabla u_z)^2\right)\mathrm{d}V. \tag{2.111}$$

We consider the three terms of this equation in turn beginning with the first term where we substitute for u_x, using equation (2.103), to give

$$\int(\nabla u_x)^2\mathrm{d}V = \int\left(\left(\frac{\partial u_x}{\partial x}\right)^2+\left(\frac{\partial u_x}{\partial z}\right)^2\right)\mathrm{d}V \tag{2.112}$$

$$= \frac{1}{k_x^4}\int\left(\left(\frac{\partial^3 u_z}{\partial x^2\partial z}\right)^2+\left(\frac{\partial^3 u_z}{\partial x\partial z^2}\right)^2\right)\mathrm{d}V \tag{2.113}$$

$$= \frac{1}{k_x^4}\int\left(\left(-k_x^2\frac{\partial u_z}{\partial z}\right)^2+\left(\frac{\partial^3 u_z}{\partial x\partial z^2}\right)^2\right)\mathrm{d}V \tag{2.114}$$

$$= \frac{1}{2}\int\left(\left(\frac{\mathrm{d}\hat{u}_\mathrm{r}}{\mathrm{d}z}\right)^2+\left(\frac{\mathrm{d}\hat{u}_\mathrm{i}}{\mathrm{d}z}\right)^2+\frac{1}{k_x^2}\left(\left(\frac{\mathrm{d}^2\hat{u}_\mathrm{r}}{\mathrm{d}z^2}\right)^2+\left(\frac{\mathrm{d}^2\hat{u}_\mathrm{i}}{\mathrm{d}z^2}\right)^2\right)\right)\mathrm{d}V \tag{2.115}$$

$$= \frac{\pi}{k_x}\int_{-1/2}^{1/2}\left(\left(\frac{\mathrm{d}\hat{u}_\mathrm{r}}{\mathrm{d}z}\right)^2+\left(\frac{\mathrm{d}\hat{u}_\mathrm{i}}{\mathrm{d}z}\right)^2+\frac{1}{k_x^2}\left(\left(\frac{\mathrm{d}^2\hat{u}_\mathrm{r}}{\mathrm{d}z^2}\right)^2+\left(\frac{\mathrm{d}^2\hat{u}_\mathrm{i}}{\mathrm{d}z^2}\right)^2\right)\right)\mathrm{d}z, \tag{2.116}$$

where we have used equations (C.6), (C.9) and (C.11). For the second term of equation (2.111) we can substitute for u_y in terms of ζ, from equation (2.104), and we acquire

$$\begin{aligned}
\int (\nabla u_y)^2 \mathrm{d}V &= \int \left(\left(\frac{\partial u_y}{\partial x} \right)^2 + \left(\frac{\partial u_y}{\partial z} \right)^2 \right) \mathrm{d}V && (2.117)\\
&= \frac{1}{k_x^2} \int \left(\left(\frac{\partial \zeta}{\partial x} \right)^2 + \left(\frac{\partial \zeta}{\partial z} \right)^2 \right) \mathrm{d}V && (2.118)\\
&= \frac{1}{2} \int \left(\hat{\zeta}_\mathrm{r}^2 + \hat{\zeta}_\mathrm{i}^2 + \frac{1}{k_x^2} \left(\left(\frac{\mathrm{d}\hat{\zeta}_\mathrm{r}}{\mathrm{d}z} \right)^2 + \left(\frac{\mathrm{d}\hat{\zeta}_\mathrm{i}}{\mathrm{d}z} \right)^2 \right) \right) \mathrm{d}V && (2.119)\\
&= \frac{\pi}{k_x} \int_{-1/2}^{1/2} \left(\hat{\zeta}_\mathrm{r}^2 + \hat{\zeta}_\mathrm{i}^2 + \frac{1}{k_x^2} \left(\left(\frac{\mathrm{d}\hat{\zeta}_\mathrm{r}}{\mathrm{d}z} \right)^2 + \left(\frac{\mathrm{d}\hat{\zeta}_\mathrm{i}}{\mathrm{d}z} \right)^2 \right) \right) \mathrm{d}z, && (2.120)
\end{aligned}$$

where we have again used equations (C.11) and (C.9). By a similar method to equations (2.105 - 2.107) we also have that

$$\int (\nabla u_z)^2 \mathrm{d}V = \frac{\pi}{k_x} \int_{-1/2}^{1/2} \left(k_x^2 \left(\hat{u}_\mathrm{r}^2 + \hat{u}_\mathrm{i}^2 \right) + \left(\frac{\mathrm{d}\hat{u}_\mathrm{r}}{\mathrm{d}z} \right)^2 + \left(\frac{\mathrm{d}\hat{u}_\mathrm{i}}{\mathrm{d}z} \right)^2 \right) \mathrm{d}z. \quad (2.121)$$

Thus,

$$\begin{aligned}
I_3 = -\int \frac{\partial u_j}{\partial x_k} \frac{\partial u_j}{\partial x_k} \mathrm{d}V = -\frac{\pi}{k_x} \int_{-1/2}^{1/2} \Bigg[& \hat{\zeta}_\mathrm{r}^2 + \hat{\zeta}_\mathrm{i}^2 + \frac{1}{k_x^2} \left(\left(\frac{\mathrm{d}\hat{\zeta}_\mathrm{r}}{\mathrm{d}z} \right)^2 + \left(\frac{\mathrm{d}\hat{\zeta}_\mathrm{i}}{\mathrm{d}z} \right)^2 \right) \\
& + k_x^2 \left(\hat{u}_\mathrm{r}^2 + \hat{u}_\mathrm{i}^2 \right) + 2 \left(\left(\frac{\mathrm{d}\hat{u}_\mathrm{r}}{\mathrm{d}z} \right)^2 + \left(\frac{\mathrm{d}\hat{u}_\mathrm{i}}{\mathrm{d}z} \right)^2 \right) \quad (2.122) \\
& + \frac{1}{k_x^2} \left(\left(\frac{\mathrm{d}^2\hat{u}_\mathrm{r}}{\mathrm{d}z^2} \right)^2 + \left(\frac{\mathrm{d}^2\hat{u}_\mathrm{i}}{\mathrm{d}z^2} \right)^2 \right) \Bigg] \mathrm{d}z.
\end{aligned}$$

Finally we consider the I_4 term of equation (2.100), again substituting for u_x

$$\begin{aligned}
I_4 = -Re \int u_z u_x \mathrm{d}V &= -\frac{Re}{k_2^2} \int u_z \frac{\partial^2 u_z}{\partial x \partial z} \mathrm{d}V && (2.123)\\
&= -\frac{Re}{2k_x} \int \left(\hat{u}_\mathrm{i} \frac{\mathrm{d}\hat{u}_\mathrm{r}}{\mathrm{d}z} - \hat{u}_\mathrm{r} \frac{\mathrm{d}\hat{u}_\mathrm{i}}{\mathrm{d}z} \right) \mathrm{d}V && (2.124)\\
&= -\frac{\pi Re}{k_x^2} \left([\hat{u}_\mathrm{i} \hat{u}_\mathrm{r}]_{-1/2}^{1/2} - 2 \int_{-1/2}^{1/2} \hat{u}_\mathrm{r} \frac{\mathrm{d}\hat{u}_\mathrm{i}}{\mathrm{d}z} \right) \mathrm{d}z && (2.125)\\
&= \frac{2\pi Re}{k_x^2} \int \hat{u}_\mathrm{r} \frac{\mathrm{d}\hat{u}_\mathrm{i}}{\mathrm{d}z} \mathrm{d}z, && (2.126)
\end{aligned}$$

where we have made use of equation (C.14).

Equations (2.107), (2.110), (2.122) and (2.126) give the terms of equation (2.100) in terms of the eigenfunctions (and their derivatives) calculated in the numerics. Thus we can calculate the four integrals using the trapezium rule, given values for the parameters: Ra, Re, E, Pr, k_x, which appear in the expressions for I_1 to I_4. For ease of comparison with figure 2.1 we consider $E = 10^{-4}$ and $Pr = 1$, and we have implicitly taken $Ra = Ra^*$ by setting $s = 0$ earlier. Figure 2.7 shows how the four terms in equation (2.100) vary as a function of Re for two choices of k_x. In this scenario each plot represents the values taken by I_1 to I_4 on a line of constant k_x in figure 2.1, namely the lines $k_x = 0.1$ and $k_x = 5$. Plots for other k_x where baroclinic modes exist are similar with the position of the transition region changing accordingly.

We first note that, in both plots of figure 2.7, the I_4 integral is very small indeed. This was also the case for all other k_x values tested. This term is small because we are considering a rapidly rotating system where the motions prefer to be two-dimensional as we discussed in section 1.3. In fact, in the rapidly rotating limit the velocity field can be written as a streamfunction with a small ageostrophic component in the z-direction so that $\mathbf{u} = -\nabla \times \psi\hat{\mathbf{z}} + u_z\hat{\mathbf{z}}$. If this is the case then $u_x = -\partial\psi/\partial y = -\mathrm{i}k_y\psi = 0$ since $k_y = 0$. Thus, in the limit of rapid rotation I_4 vanishes. For systems with finite Ekman number, such as ours, the I_4 term appears but does not significantly contribute to the balancing of the thermodynamic equation.

As mentioned earlier we must have $Ra > 0$ in the case $Re = 0$. This is the well understood case where the Rayleigh number must be positive for the system to be convectively unstable. At low Re this remains the predominant balance and the Rayleigh number remains positive. However with $Re \neq 0$ the baroclinic term can partially balance the viscous stresses and thus as Re is increased the Rayleigh number is reduced to allow equation (2.100) to balance. This can be seen in both plots of figure 2.7 where the I_2 contribution slowly increases in magnitude as Re increases.

As Re is increased further and we enter the transition region (located at $Re \sim 10.95$ for $k_x = 0.1$ and $Re \sim 19.86$ for $k_x = 5$) we see that both I_1 and the baroclinic flux, I_2, change sign. In the transition region the main balance is between these two terms as the magnitude of the rate of working of the viscous stresses is small. However the sum of I_1 and I_2 must still balance the solely negative I_3 term. The transition region represents the point in Re-space where I_2 becomes large enough in magnitude to solely overcome I_3 without the need for a contribution from I_1. Hence I_1 can change sign (that is Ra

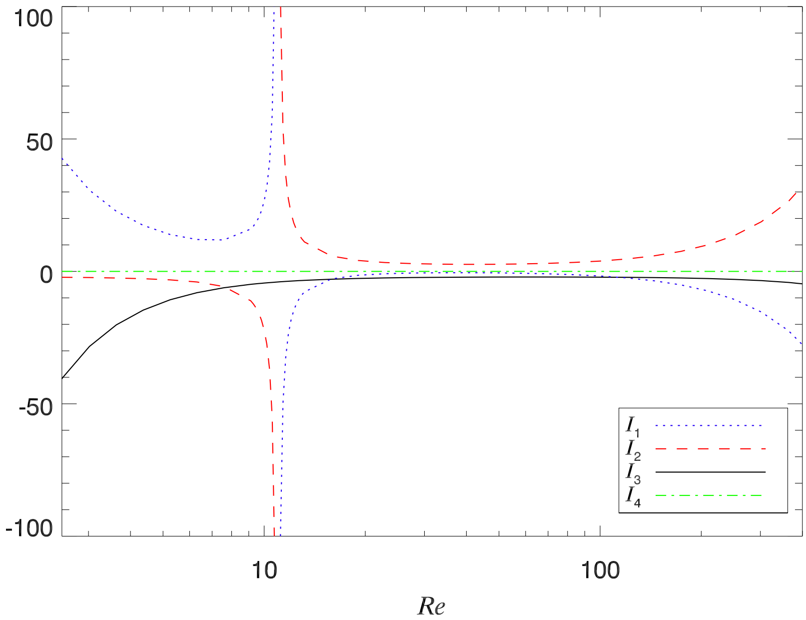

(a) $k_x = 0.1$

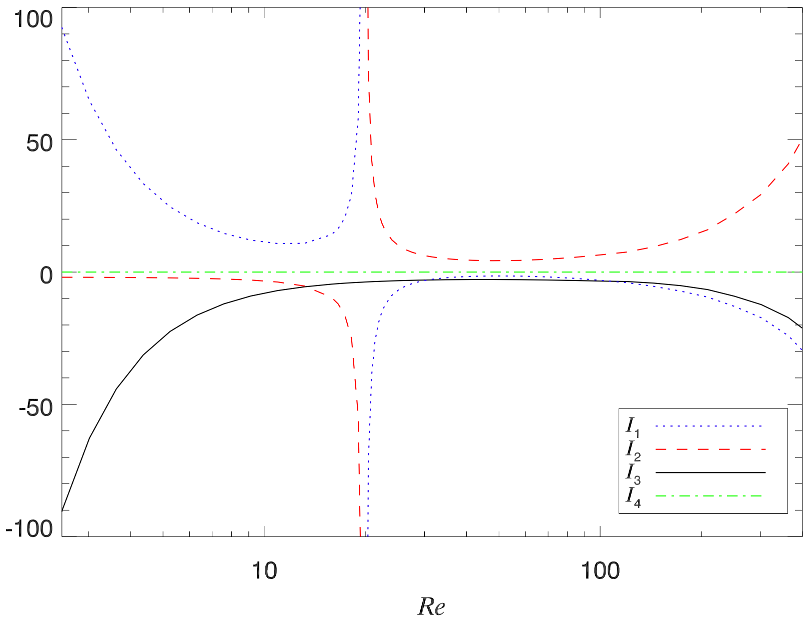

(b) $k_x = 5$

Figure 2.7: Plots showing how the integrals in the thermodynamic equation (2.100) vary as a function of Re with $E = 10^{-4}$ and $Pr = 1$. We use stress-free boundaries with $k_y = k_{y_c} = 0$. The eigenvalues that appear in the expressions for integrals (equations (2.107), (2.110), (2.122) and (2.126)) are found from the numerics and the integrals are evaluated using the trapezium rule.

change sign). This explains why a sufficiently large value of the zonal wind is required to allow for modes with negative Rayleigh number to appear. It also indicates that the term, I_1 or I_2, in equation (2.100) which is positive, and thus is able to balance I_3, contains the parameter that is driving the instability. In other words it is the Rayleigh/Reynolds number and thus the work done by buoyancy/baroclinic heat flux, which is balancing the viscous dissipation in the convective/baroclinic regime.

Equation (2.100) can also explain the results of changing the Prandtl number given by table 2.3. The second integral, I_2, is proportional to Pr. Therefore increasing or decreasing the Prandtl number means that a lower or higher value of Re respectively is required before I_2 is able to balance I_3. Hence the transition region appears at smaller values of Re as Pr is increased, as we saw in table 2.3. This argument is slightly crude since it assumes that the values of the integrals in equation (2.100) do not change with Pr. This is not the case, which is why increasing the Prandtl number by an order of magnitude does not result in the zonal wind decreasing by the same amount. For example the position of the transition region for $Pr = 10$ in table 2.3 has only moved from $Re \sim 10$ (in the $Pr = 1$ case) to $Re \sim 3.5$ rather than $Re \sim 1$. Despite this, the form of I_2 in the thermodynamic equation serves to explain the general dependency of the transition region on the Prandtl number.

Chapter 3

Asymptotics for a linear plane layer model

Here we develop asymptotic theories, which approximate the plane layer numeric results with stress-free boundaries very well. By developing these theories we are able to reduce the order of the equations, which then either results in a simpler ODE to solve numerically or a system that can be partially solved analytically. Thus, we are able to cover a larger parameter space than was possible in the numerics of chapter 2. Much of the work presented in this chapter has been published in section 4 of Teed *et al.* (2010).

In the numerical work previously discussed in chapter 2 we considered small, but finite, values of the Ekman number since these correspond to rapidly rotating systems, which are of particular physical interest. Hence we take as our first limit the quasi-geostrophic limit, which is that of asymptotically small E. In this limit the velocity will be almost independent of z due to the Taylor-Proudman theorem. We use the numerics of chapter 2 to ascertain the required asymptotic scalings. From table 2.2 and the field plots of figures 2.2 and 2.3 we see that the vertical vorticity appears to be independent of the Ekman number. Conversely, the vertical velocity scales like the Ekman number whereas $Ra\theta$ scales like the inverse of the Ekman number. This last scaling can be seen from the θ plots of figures 2.2(b), 2.3(b) and 2.3(e) where the Rayleigh number is held constant so θ scales like the inverse of the Ekman number. However, table 2.2 shows that the Rayleigh number scales like the inverse of the Ekman number squared when the Reynolds number is held constant. Therefore, this requires that θ scales like the Ekman number, which is the scaling we make here. Hence, guided by the numerics, we rescale the dependent variables as $\hat{\zeta} = \tilde{\zeta}$, $\hat{u}_z = E\tilde{u}_z$, $\hat{\theta} = E\tilde{\theta}$, and $Ra = \widetilde{Ra}/E^2$ and we substitute these scalings into equations (2.42 - 2.44), whence

$$\left(s + \mathrm{i}k_x Rez + k^2 - \frac{\mathrm{d}^2}{\mathrm{d}z^2}\right)\tilde{\zeta} - \mathrm{i}k_y ReE\tilde{u}_z - \frac{\mathrm{d}\tilde{u}_z}{\mathrm{d}z} = 0, \tag{3.1}$$

$$\left(s + \mathrm{i}k_x Rez + k^2 - \frac{\mathrm{d}^2}{\mathrm{d}z^2}\right)\left(\frac{\mathrm{d}^2}{\mathrm{d}z^2} - k^2\right)E\tilde{u}_z + E^{-1}\frac{\mathrm{d}\tilde{\zeta}}{\mathrm{d}z} = -k^2\widetilde{Ra}E^{-1}\tilde{\theta}, \tag{3.2}$$

$$\left(sPr + \mathrm{i}k_x PrRez + k^2 - \frac{\mathrm{d}^2}{\mathrm{d}z^2}\right)E\tilde{\theta} = E\tilde{u}_z - \frac{\mathrm{i}PrReE}{\widetilde{Ra}k^2}\left(k_x\tilde{\zeta} - k_y E\frac{\mathrm{d}\tilde{u}_z}{\mathrm{d}z}\right). \tag{3.3}$$

We then take the leading order terms of these equations in the limit $E \to 0$, which gives

$$\left(s + \mathrm{i}k_x Rez + k^2 - \frac{\mathrm{d}^2}{\mathrm{d}z^2}\right)\tilde{\zeta} = \frac{\mathrm{d}\tilde{u}_z}{\mathrm{d}z}, \tag{3.4}$$

$$\frac{\mathrm{d}\tilde{\zeta}}{\mathrm{d}z} = -k^2\widetilde{Ra}\tilde{\theta}, \tag{3.5}$$

$$\left(sPr + \mathrm{i}k_x PrRez + k^2 - \frac{\mathrm{d}^2}{\mathrm{d}z^2}\right)\tilde{\theta} = \tilde{u}_z - \frac{\mathrm{i}k_x PrRe}{k^2\widetilde{Ra}}\tilde{\zeta}. \tag{3.6}$$

Due to the much simplified form of the curl of the vorticity equation, namely equation (3.5), where a fourth order derivative has been lost in the small E limit we have reduced the system from an eighth order to a fourth order system. We are able to eliminate $\tilde{\theta}$ by taking the double-derivative of equation (3.5) and substituting for $\mathrm{d}^2\tilde{\theta}/\mathrm{d}z^2$ in equation (3.6) to give

$$\frac{\mathrm{d}^3\tilde{\zeta}}{\mathrm{d}z^3} = \left(sPr + \mathrm{i}k_x PrRez + k^2\right)\frac{\mathrm{d}\tilde{\zeta}}{\mathrm{d}z} - \mathrm{i}k_x PrRe\tilde{\zeta} + \widetilde{Ra}k^2\tilde{u}_z. \tag{3.7}$$

In fact, we could also easily write this system of equations as a single fourth order ODE in $\tilde{\zeta}$ by eliminating $\tilde{u}_z$. However we retain the use of equations (3.4 - 3.7) only in this chapter, as well as the integral form of equation (3.4), which is derived later.

We must also consider the boundary conditions on the variables. We use stress-free boundary conditions in this chapter and since the higher order derivatives of $\tilde{u}_z$ have vanished we only retain the following boundary conditions at $z = \pm 1/2$ from equations (2.59 - 2.60):

$$\tilde{u}_z = 0, \tag{3.8}$$

$$\frac{\mathrm{d}\tilde{\zeta}}{\mathrm{d}z} = 0, \tag{3.9}$$

$$\tilde{\theta} = 0. \tag{3.10}$$

Since this is now a fourth order system of equations we only actually require four boundary conditions and in fact (3.9) and (3.10) are equivalent due to equation (3.5). In sections 3.1 and 3.2 we shall eliminate $\tilde{\theta}$ from the system of equations we solve and thus we require the use of the boundary conditions on only $\tilde{u}_z$ and $\tilde{\zeta}$. However, in section 3.3 we solve the equations that retain $\tilde{\theta}$, namely equations (3.4 - 3.6), rather than making use of equation (3.7). Hence we shall require the boundary condition on $\tilde{\theta}$ from equation (3.10).

We are able to solve the equations derived here as a boundary value problem, which we consider in section 3.1. In sections 3.2 and 3.3 we take a further asymptotic limit, namely that of small k_x since the baroclinic modes onset with zero azimuthal wavenumber. By doing this we are able to find an expression for Re in terms of Pr and Ra (section 3.2) and we are also able to predict the value of Ra and the form of the fields, given Pr and Re (section 3.3). Since we use equations (3.4 - 3.7) in each section of this chapter, the asymptotic theories will only be accurate for small Ekman numbers. Equations (3.4 - 3.7) are related to the quasi-geostrophic equations used by atmospheric scientists (though in this work diffusion is still included), which we discuss in section 3.4. Also of note is that Rashid *et al.* (2008) performed an asymptotic analysis under a small Ekman number limit for a similar set of equations to (2.42 - 2.44). However, they also took the small Prandtl number limit whereas we retain finite Pr here.

3.1 Asymptotics for small Ekman number

In this section we solve the coupled system of ODEs given by equations (3.4) and (3.7) without further asymptotic assumptions. We do this to show that the solutions in this small Ekman number limit match our numeric solutions from chapter 2. In particular we compare the position of the transition region. We expect the solutions to share the same properties since throughout the numerics we used small, but finite, Ekman numbers. We set $s = 0$ because we are approximating the numerics where we searched for steady, marginal modes. Since the critical latitudinal wavenumber vanishes for all modes of interest, we also set $k_y = k_{y_c} = 0$ so that $k = k_x$. We rewrite equations (3.4) and (3.7) as four equations by taking the real and imaginary parts separately to give

$$-k_x Rez\tilde{\zeta}_{\mathrm{i}} + k^2\tilde{\zeta}_{\mathrm{r}} - \frac{\mathrm{d}^2\tilde{\zeta}_{\mathrm{r}}}{\mathrm{d}z^2} = \frac{\mathrm{d}\tilde{u}_{\mathrm{r}}}{\mathrm{d}z}, \tag{3.11}$$

$$k_x Rez\tilde{\zeta}_{\mathrm{r}} + k^2\tilde{\zeta}_{\mathrm{i}} - \frac{\mathrm{d}^2\tilde{\zeta}_{\mathrm{i}}}{\mathrm{d}z} = \frac{\mathrm{d}\tilde{u}_{\mathrm{i}}}{\mathrm{d}z}, \tag{3.12}$$

$$\frac{\mathrm{d}^3\tilde{\zeta}_{\mathrm{r}}}{\mathrm{d}z^3} = -k_x PrRez\frac{\mathrm{d}\tilde{\zeta}_{\mathrm{i}}}{\mathrm{d}z} + k^2\frac{\mathrm{d}\tilde{\zeta}_{\mathrm{r}}}{\mathrm{d}z} + k_x PrRe\tilde{\zeta}_{\mathrm{i}} + \widetilde{Ra}k^2\tilde{u}_{\mathrm{r}}, \tag{3.13}$$

$$\frac{\mathrm{d}^3\tilde{\zeta}_{\mathrm{i}}}{\mathrm{d}z^3} = k_x PrRez\frac{\mathrm{d}\tilde{\zeta}_{\mathrm{r}}}{\mathrm{d}z} + k^2\frac{\mathrm{d}\tilde{\zeta}_{\mathrm{i}}}{\mathrm{d}z} - k_x PrRe\tilde{\zeta}_{\mathrm{r}} + \widetilde{Ra}k^2\tilde{u}_{\mathrm{i}}. \tag{3.14}$$

We must also consider the boundary conditions on the four functions: $\tilde{\zeta}_{\mathrm{r}}$, $\tilde{\zeta}_{\mathrm{i}}$, $\tilde{u}_{\mathrm{r}}$ and $\tilde{u}_{\mathrm{i}}$. From the no penetration condition and the stress-free boundary conditions we obtain

$$\tilde{u}_{\mathrm{r}}(1/2) = \tilde{u}_{\mathrm{i}}(1/2) = 0 \quad \text{and} \quad \tilde{\zeta}_{\mathrm{r}}'(1/2) = \tilde{\zeta}_{\mathrm{i}}'(1/2) = \tilde{u}_{\mathrm{r}}(1/2) = \tilde{u}_{\mathrm{i}}(1/2) = 0, \tag{3.15}$$

respectively. Here the primes indicate the z-derivatives of the eigenfunctions. We introduce a normalisation condition such that $\tilde{\zeta}_{\mathrm{r}}(0) = 1$. Also, due to the known symmetry of the numeric solutions from chapter 2, we are able to impose symmetry conditions on the functions at $z = 0$. We know that for the baroclinic modes the vertical vorticity and the vertical velocity are symmetric and antisymmetric in x about $z = 0$, respectively. The vertical vorticity and vertical velocity can be written in terms of sines and cosines as follows

$$\zeta = \tilde{\zeta}_{\mathrm{r}}\cos(k_x x) - \tilde{\zeta}_{\mathrm{i}}\sin(k_x x), \tag{3.16}$$

$$u_z = \tilde{u}_{\mathrm{r}}\cos(k_x x) - \tilde{u}_{\mathrm{i}}\sin(k_x x), \tag{3.17}$$

from the definitions of equations (2.36 - 2.37) with $s = 0 = k_y$. Hence for the vertical vorticity to be symmetric in x about $z = 0$ we must have that $\tilde{\zeta}_{\mathrm{i}}(0) = 0$. Likewise we must have $\tilde{u}_{\mathrm{r}}(0) = 0$ since u_z is antisymmetric about $z = 0$. Also, the derivatives of ζ must obey alternating symmetry conditions since they will also alternate between being symmetric and antisymmetric in x. Hence we also must have that $\tilde{\zeta}_{\mathrm{r}}'(0) = 0 = \tilde{\zeta}_{\mathrm{i}}''(0)$.

Thus we now have the following nine real boundary conditions, including a normalisation condition,

$$\tilde{\zeta}_{\mathrm{r}}(0) = 1, \tag{3.18}$$

$$\tilde{\zeta}_{\mathrm{i}}(0) = \tilde{\zeta}_{\mathrm{r}}'(0) = \tilde{\zeta}_{\mathrm{i}}''(0) = \tilde{u}_{\mathrm{r}}(0) = 0, \tag{3.19}$$

$$\tilde{\zeta}_{\mathrm{r}}'(1/2) = \tilde{\zeta}_{\mathrm{i}}'(1/2) = \tilde{u}_{\mathrm{r}}(1/2) = \tilde{u}_{\mathrm{i}}(1/2) = 0. \tag{3.20}$$

The system defined by (3.11 - 3.14) is an eighth order homogeneous system in the real variables, with eight homogeneous boundary conditions and a normalisation condition, so it has an eigenvalue, Re. Hence given specific values of k, Pr and $\widetilde{Ra}$ we can find a value for Re. We solve this system using a simple boundary value problem (BVP) solver in Maple and results for the transition region case (that is, $\widetilde{Ra} = 0$) are displayed in table 3.1. Recall that the transition region is found at the boundary between the orange and blue sections of figure 2.1(a). Hence we can compare the values of Re in table 3.1 with the location of the transition region from figure 2.1(a) and also table 2.3. We see that the small Ekman number asymptotic theory predicts the location of the transition region very well. In particular, we see that the position of the transition region is converging, as we reduce E, to a value similar to that predicted by the asymptotics in all cases. Also of note is that for $Pr = 20$ and $Pr = 50$ there are non-zero minimising values of the azimuthal wavenumber, which we also saw for large Pr in the numerics (figure 2.6).

	Re				
k_x	$Pr = 0.1$	$Pr = 1$	$Pr = 10$	$Pr = 20$	$Pr = 50$
0.01	34.64108	10.95447	3.46410	2.44948	1.54917
0.10	34.65831	10.95961	3.46475	2.44918	1.54754
0.50	35.07369	11.08347	3.48056	2.44245	1.51100
1.00	36.34019	11.46042	3.52963	2.42794	1.42646
1.50	38.35637	12.05843	3.61070	2.42013	1.34371
2.00	41.00963	12.84220	3.72316	2.43154	1.28719
2.50	44.18317	13.77610	3.86686	2.46939	1.26193
3.00	47.77158	14.82920	4.04217	2.53699	1.26634
5.00	64.77836	19.83002	5.08823	3.14797	1.59143
10.0	114.69132	35.11997	10.51240	7.57080	4.80621

Table 3.1: Values for the Reynolds number for various k_x and Pr in the case $\widetilde{Ra} = 0$ found by solving the BVP described by equations (3.11 - 3.20)

3.2 Small wavenumber asymptotics 1: Fixed Rayleigh number

In this section we develop a theory relevant in the small k_x limit since the numerics indicate from section 2.6 that the preference for baroclinic instabilities is $k_x = 0$. Hence we are able to obtain an expression for the critical Reynolds number in terms of the Prandtl and Rayleigh numbers. In other words, given a Pr and a Ra we are approximating the value of Re needed for growing baroclinic modes to appear. In this theory we expand the Reynolds number in terms of a small parameter and assume that the Rayleigh number is an input parameter. We set $s = 0$ and $k_y = 0$ for the same reasons discussed at the start of section 3.1 and then $k = k_x$, which we use as an expansion parameter. It will be useful to obtain the integral form of equation (3.4) and thus we take the z-integral across the layer and apply the boundary conditions given by equations (3.8) and (3.9) to give

$$\int_{-1/2}^{1/2} \left(\mathrm{i}kRez + k^2\right)\tilde{\zeta}\,\mathrm{d}z - \left[\frac{\mathrm{d}\tilde{\zeta}}{\mathrm{d}z}\right]_{-1/2}^{1/2} = [\tilde{u}_z]_{-1/2}^{1/2} \tag{3.21}$$

$$\Rightarrow \quad \int_{-1/2}^{1/2} \left(\mathrm{i}kRez + k^2\right)\tilde{\zeta}\,\mathrm{d}z = 0, \tag{3.22}$$

since the final two terms vanish at the boundaries. The numerics suggest that the critical azimuthal wavenumber is zero for baroclinic modes (see figure 2.5(a)) and thus we consider the expansion of $\tilde{\zeta}$, $\tilde{u}_z$ and Re in powers of the small parameter k as follows:

$$\tilde{\zeta} = \sum_{n=0}^{\infty} k^n \zeta_n = \zeta_0 + k\zeta_1 + k^2\zeta_2 + \cdots, \tag{3.23}$$

$$\tilde{u}_z = \sum_{n=0}^{\infty} k^{n+1} u_n = k\left(u_0 + ku_1 + k^2 u_2 + \cdots\right), \tag{3.24}$$

$$Re = \sum_{n=0}^{\infty} k^n Re_n = Re_0 + kRe_1 + k^2 Re_2 + \cdots. \tag{3.25}$$

We must substitute these expansions into the relevant equations and consider the resulting equations at increasing order; that is increasing powers in k. By applying the boundary conditions and a normalisation condition we are able to obtain expressions for the expansion variables (ζ_n, u_n and Re_n). Each expansion variable must satisfy the boundary conditions of equations (3.8 - 3.9) individually so that

$$u_n = 0, \tag{3.26}$$
$$\frac{\mathrm{d}\zeta_n}{\mathrm{d}z} = 0, \tag{3.27}$$

at $z = \pm 1/2\, \forall n$. We must also choose a normalisation condition, which is a value that one of the functions takes at a specific value of z. The remaining functions are then measured in relation to this value. For simplicity we choose

$$\tilde{\zeta}(0) = 1, \tag{3.28}$$

since $\tilde{\zeta}$ is non-zero at $z = 0$.

We now proceed by substituting the expansions (3.23 - 3.25) into equations (3.4), (3.7) and (3.22), which give

$$\left(\mathrm{i}kz(Re_0 + kRe_1 + k^2 Re_2) + k^2 - \frac{\mathrm{d}^2}{\mathrm{d}z^2}\right)\left(\zeta_0 + k\zeta_1 + k^2\zeta_2\right) = k\frac{\mathrm{d}}{\mathrm{d}z}\left(u_0 + ku_1 + k^2 u_2\right), \tag{3.29}$$

$$\begin{aligned}\frac{\mathrm{d}^3}{\mathrm{d}z^3}\left(\zeta_0 + k\zeta_1 + k^2\zeta_2\right) = &\left(\mathrm{i}kPrz\left(Re_0 + kRe_1 + k^2 Re_2\right) + k^2\right)\frac{\mathrm{d}}{\mathrm{d}z}\left(\zeta_0 + k\zeta_1 + k^2\zeta_2\right) \\ &- \mathrm{i}kPr\left(Re_0 + kRe_1 + k^2 Re_2\right)\left(\zeta_0 + k\zeta_1 + k^2\zeta_2\right) + \widetilde{Ra}k^3\left(u_0 + ku_1 + k^2 u_2\right),\end{aligned} \tag{3.30}$$

$$\int_{-1/2}^{1/2}\left(\mathrm{i}kz\left(Re_0 + kRe_1 + k^2 Re_2\right) + k^2\right)\left(\zeta_0 + k\zeta_1 + k^2\zeta_2\right)\mathrm{d}z = 0. \tag{3.31}$$

We have included only terms up to $n = 2$ here, although in reality each sum is infinite. We can now consider these equations at increasing order in k; that is $O(k^n)$ for increasing $n \in \mathbb{N}_0$. First we consider $O(k^0) = O(1)$ and note that equation (3.29) demands that

$$\frac{\mathrm{d}^2\zeta_0}{\mathrm{d}z^2} = 0, \tag{3.32}$$

and hence in general $\zeta_0 = c_1 z + c_0$. The normalisation condition, equation (3.28), then requires that $c_0 = 1$ and $c_1 = 0$ and hence

$$\zeta_0 = 1. \tag{3.33}$$

As a consequence of this choice of ζ_0, all other expansion variables in the expansion for $\tilde{\zeta}$ must vanish at $z = 0$; that is

$$\zeta_n(0) = 0 \quad \forall n > 0. \tag{3.34}$$

We also note that this choice of ζ_0 satisfies equation (3.27) as required. Equation (3.30) taken at $O(1)$ demands that the third derivative of ζ_0 vanishes, which is satisfied as a consequence of equation (3.32). We now consider equations (3.30) and (3.29) at order $O(k)$, which give

$$\frac{\mathrm{d}^3\zeta_1}{\mathrm{d}z^3} = -\mathrm{i}PrRe_0, \tag{3.35}$$

$$\mathrm{i}Re_0 z - \frac{\mathrm{d}^2\zeta_1}{\mathrm{d}z^2} = \frac{\mathrm{d}u_0}{\mathrm{d}z}, \tag{3.36}$$

respectively, using equation (3.33). We integrate the first of these equations and apply equations (3.27) and (3.34) to give an expression for ζ_1:

$$\zeta_1 = -\mathrm{i}PrRe_0\left(\frac{z^3}{6} - \frac{z}{8}\right), \tag{3.37}$$

which can be used in equation (3.36) to find u_0:

$$u_0 = \mathrm{i}Re_0(1+Pr)\left(\frac{z^2}{2} - \frac{1}{8}\right), \tag{3.38}$$

where equation (3.26) has been used.

Next we consider equations (3.31) and (3.30) at $O(k^2)$, where, recalling that $\zeta_0 = 1$, we find

$$\int_{-1/2}^{1/2}(\mathrm{i}Re_0 z\zeta_1 + \mathrm{i}Re_1 z + 1)\mathrm{d}z = 0, \tag{3.39}$$

$$\frac{\mathrm{d}^3\zeta_2}{\mathrm{d}z^3} = \mathrm{i}PrRe_0 z\frac{\mathrm{d}\zeta_1}{\mathrm{d}z} - \mathrm{i}PrRe_0\zeta_1 - \mathrm{i}PrRe_1. \tag{3.40}$$

We can use the definition of ζ_1 from equation (3.37) to evaluate the integral in equation (3.39) to acquire

$$\int_{-1/2}^{1/2}\left(PrRe_0^2\left(\frac{z^4}{6} - \frac{z^2}{8}\right) + \mathrm{i}Re_1 z + 1\right)\mathrm{d}z = 0 \tag{3.41}$$

$$\Rightarrow \quad PrRe_0^2\left[\frac{z^5}{30} - \frac{z^3}{24}\right]_{-1/2}^{1/2} + 1 = 0 \tag{3.42}$$

$$\Rightarrow \quad Re_0 = \sqrt{\frac{120}{Pr}}, \tag{3.43}$$

where we have used the fact that the integral of odd functions vanish over symmetric limits. Equation (3.43) gives the leading order approximation to the critical Reynolds number. We can also find ζ_2 from equation (3.40) by inserting the definition of ζ_1 and using the boundary and normalisation conditions to get

$$\zeta_2 \quad = \quad Pr^2Re_0^2\left(\frac{z^6}{360} - \frac{z^2}{1920}\right) - \mathrm{i}PrRe_1\left(\frac{z^3}{6} - \frac{z}{8}\right). \tag{3.44}$$

Once again considering equations (3.31) and (3.30), now at $O(k^3)$, we obtain

$$\int_{-1/2}^{1/2} (\mathrm{i}Re_0 z\zeta_2 + \mathrm{i}Re_1 z\zeta_1 + \mathrm{i}Re_2 z + \zeta_1)\mathrm{d}z = 0, \tag{3.45}$$

$$\frac{\mathrm{d}^3\zeta_3}{\mathrm{d}z^3} = \mathrm{i}PrRe_0 z\frac{\mathrm{d}\zeta_2}{\mathrm{d}z} + \mathrm{i}PrRe_1 z\frac{\mathrm{d}\zeta_1}{\mathrm{d}z} + \frac{\mathrm{d}\zeta_1}{\mathrm{d}z} - \mathrm{i}PrRe_0\zeta_2 - \mathrm{i}PrRe_1\zeta_1 - \mathrm{i}PrRe_2 + \widetilde{Ra}u_0, \tag{3.46}$$

respectively. We insert the definitions of ζ_1 and ζ_2 into equation (3.45), evaluate the integral and find

$$\int_{-1/2}^{1/2} \left(\mathrm{i}Pr^2Re_0^3\left(\frac{z^7}{360} - \frac{z^3}{1920}\right) + 2PrRe_0Re_1\left(\frac{z^4}{6} - \frac{z^2}{8}\right) + \mathrm{i}Re_2 z - \mathrm{i}PrRe_0\left(\frac{z^3}{6} - \frac{z}{8}\right)\right)\mathrm{d}z = 0 \tag{3.47}$$

$$\Rightarrow \quad 2PrRe_0Re_1\left[\frac{z^5}{30} - \frac{z^3}{24}\right]_{-1/2}^{1/2} = 0 \tag{3.48}$$

$$\Rightarrow \quad -\frac{PrRe_0Re_1}{120} = 0, \tag{3.49}$$

where again the integrals of the odd functions vanish. Thus $Re_1 = 0$ since Pr and Re_0 are both non-zero. By inserting the definitions of ζ_1, ζ_2 and u_0 into equation (3.46) and applying the boundary and normalisation conditions, we find

$$\zeta_3 = \mathrm{i}Pr^3Re_0^3\left(\frac{z^9}{36288} - \frac{z^5}{115200} + \frac{z}{573440}\right) - \mathrm{i}Re_0\left(Pr - \widetilde{Ra}(1+Pr)\right)\left(\frac{z^5}{120} - \frac{z^3}{48} + \frac{5z}{384}\right) - \mathrm{i}PrRe_2\left(\frac{z^3}{6} - \frac{z}{8}\right). \tag{3.50}$$

We are now able to find an expression for Re_2 using equation (3.31) at $O(k^4)$, which is

$$\int_{-1/2}^{1/2} (\mathrm{i}Re_0 z\zeta_3 + \mathrm{i}Re_2 z\zeta_1 + \mathrm{i}Re_3 z + \zeta_2)\,\mathrm{d}z = 0. \tag{3.51}$$

We insert the expressions for ζ_1, ζ_2 and ζ_3 into equation (3.51) and evaluate the integral to find

$$\int_{-1/2}^{1/2} \left(-Pr^3Re_0^4\left(\frac{z^{10}}{36288} - \frac{z^6}{115200} + \frac{z^2}{573400}\right) + Re_0^2(Pr - \widetilde{Ra}(1+Pr))\left(\frac{z^6}{120} - \frac{z^3}{48} + \frac{5z^2}{384}\right) + 2PrRe_0Re_2\left(\frac{z^4}{6} - \frac{z^2}{8}\right) + Pr^2Re_0^2\left(\frac{z^6}{360} - \frac{z^2}{1920}\right)\right)\mathrm{d}z = 0 \tag{3.52}$$

$$\Rightarrow \quad -\frac{41 Pr^3 Re_0^4}{319334400} + \frac{17 Re_0^2 (Pr - \widetilde{Ra}(1+Pr))}{20160} - \frac{Pr Re_0 Re_2}{60} - \frac{Pr^2 Re_0^2}{26810} = 0 \tag{3.53}$$

$$\Rightarrow \quad Re_2 = \sqrt{\frac{30}{Pr}} \left[\frac{17}{168} \left(1 - \frac{\widetilde{Ra}(1+Pr)}{Pr} \right) - \frac{5Pr}{792} \right]. \tag{3.54}$$

where we have substituted for Re_0 from equation (3.43). We have now acquired the leading order term, Re_0, and the first non-zero correction term, Re_2 in the expansion for Re. Hence from equation (3.25) we find

$$Re \approx Re_0 + k^2 Re_2 = \sqrt{\frac{120}{Pr}} + k^2 \sqrt{\frac{30}{Pr}} \left[\frac{17}{168} \left(1 - \frac{\widetilde{Ra}(1+Pr)}{Pr} \right) - \frac{5Pr}{792} \right], \tag{3.55}$$

which yields an approximation to the Reynolds number given Pr, $\widetilde{Ra}$ and a small k. The form of this expression for Re is able to explain the dependence of the critical wavenumber on Pr as seen in section 2.7. For a given Prandtl number the Re_0 term in the expression for Re given by (3.55) gives an approximation to the critical Reynolds number. For example, with $Pr = 1$ we have $Re_0 = 10.9545$, which is in excellent agreement with the numerics discussed in section 2.6. The second term of equation (3.55) then gives an adjustment to the leading order value for Re. The sign of this term determines whether $k_c = 0$ or not. If, for a given Pr and $\widetilde{Ra}$, the value of Re_2 is positive then the adjustment to Re_0 can only serve to increase the Reynolds number and hence the preferred value of k to minimise Re is $k = 0$ as expected given the numeric results from section 2.6. However, if the value of Re_2 is negative (again for given Pr and $\widetilde{Ra}$) a non-zero k must be preferred as the inclusion of this term now lowers the Reynolds number from the Re_0 value.

Table 3.2 displays quantities for Re_0 and Re_2, given by equation (3.55), for various values of Pr and $\widetilde{Ra}$. Since Re_0 is independent of $\widetilde{Ra}$, this only varies with Pr and the values predicted for the Reynolds number match the numerics of table 2.3 very well. We notice that for most combinations of Pr and $\widetilde{Ra}$ the value of Re_2 is positive, confirming that $k_c = 0$ and $Re_c = Re_0$. Hence when $Re_2 > 0$ this asymptotic theory is able to predict accurate values for the critical wavenumber and critical Reynolds number. However for certain choices of the parameters we obtain negative values for Re_2 indicating that there is a non-zero minimising value of k. This was seen in the numerics where we recall from figure 2.6 that there was a non-zero k_c for $Pr = 50$ and $Ra = -1$. The equivalent values of the Prandtl and Rayleigh numbers in the asymptotic theory ($Pr = 50$ and

$\widetilde{Ra} = -1$) give a negative value of Re_2 agreeing with the numerics that there is a non-zero minimising k. From the results of table 3.2 it is also evident that for increasingly negative values of the Rayleigh number, the Prandtl number is required to be increasingly large for a non-zero minimising wavenumber. Thus for a given $\widetilde{Ra}$ there is a critical value of the Prandtl number, Pr_c, for which $k_c \neq 0$ if $Pr > Pr_c$.

		Re_2			
Pr	Re_0	$\widetilde{Ra} = 0$	$\widetilde{Ra} = -1$	$\widetilde{Ra} = -10$	$\widetilde{Ra} = -1000$
0.1	34.64102	1.74174	21.02111	194.53549	19281.11679
1	10.95445	0.51966	1.62815	11.60453	1109.00579
10	3.46410	0.065920	0.25871	1.99386	192.85967
50	1.54919	−0.16612	−0.086175	0.63337	79.78332
100	1.09545	−0.29036	−0.23438	0.26943	55.68819

Table 3.2: Values for Re_0 and Re_2 for various Prandtl and Rayleigh numbers as given by the expression in equation (3.55).

This asymptotic theory is unable to predict the critical wavenumber and critical Reynolds number when $Re_2 < 0$ (for given $\widetilde{Ra}$ and Pr) without including higher order terms, which would give an $O(k^4)$ term in equation (3.55). However, it does indicate the values of the Prandtl and Rayleigh numbers for which we would expect to find a non-zero critical wavenumber.

3.3 Small wavenumber asymptotics 2: Fixed Reynolds number

In this section we develop a second asymptotic theory with small k_x and stress-free boundaries. This theory enables us to predict the Rayleigh numbers and eigenfunctions found in the numerics of section 2 very well, given Pr and Re. This section differs from section 3.2, which, although also considered small k_x, predicted the critical Reynolds number for the onset of baroclinic instability, given Pr and Ra. Here, given a Pr and a Re, the theory approximates the value of Ra required for growing baroclinic modes to appear. In this theory we expand the Rayleigh number in terms of a small parameter and assume that the Reynolds number is an input parameter, also in contrast to section 3.2.

We introduce a small parameter ϵ, measuring the magnitude of the horizontal wavenumbers since the numerics suggest that both k_x and k_y are zero for baroclinic instabilities at onset (see figure 2.5(a)). As discussed in section 2.6 and indicated by the results of table 2.2, the numerics inform us that the Rayleigh number is proportional to k_x^2. Hence we set $\widetilde{Ra} = \widehat{Ra}/k_x^2$ and we also use the same expansions for the eigenfunctions as those in section 3.2, albeit now in terms of ϵ, since we are considering the same small k_x limit. Hence we consider the following expansions:

$$\begin{aligned}
k_x &= \epsilon\hat{k}_x, \qquad k_y = \epsilon\hat{k}_y, && (3.56)\\
\tilde{\zeta} &= \sum_{n=0}^{\infty}\epsilon^n\zeta_n = \zeta_0 + \epsilon\zeta_1 + \epsilon^2\zeta_2 + \cdots, && (3.57)\\
\tilde{u}_z &= \sum_{n=0}^{\infty}\epsilon^{n+1}u_n = \epsilon\Big(u_0 + \epsilon u_1 + \epsilon^2 u_2 + \cdots\Big), && (3.58)\\
\tilde{\theta} &= \sum_{n=0}^{\infty}\epsilon^{n+1}\theta_n = \epsilon\Big(\theta_0 + \epsilon\theta_1 + \epsilon^2\theta_2 + \cdots\Big), && (3.59)\\
k_x^2\widetilde{Ra} = \widehat{Ra} &= \sum_{n=0}^{\infty}\epsilon^n Ra_n = Ra_0 + \epsilon Ra_1 + \epsilon^2 Ra_2 + \cdots, && (3.60)
\end{aligned}$$

where we assume that $Ra_0 < 0$ since we are considering marginal baroclinic instabilities in this asymptotic expansion, which have a negative Rayleigh number. Note that the expansion variables ζ_n and u_n in the above expansions are not the same as those of section 3.2. However, we have the same boundary and normalisation conditions as in section 3.2, which are given by equations (3.26 - 3.28). We set $s = 0$ for the same reason discussed at the start of section 3.1 and we insert the expansions given by equations (3.56 - 3.60) into equations (3.4 - 3.6) to give

$$\left(\mathrm{i}\epsilon\hat{k}_x Rez + \epsilon^2\hat{k}^2 - \frac{\mathrm{d}^2}{\mathrm{d}z^2}\right)\Big(\zeta_0 + \epsilon\zeta_1 + \epsilon^2\zeta_2\Big) = \epsilon\frac{\mathrm{d}}{\mathrm{d}z}\Big(u_0 + \epsilon u_1 + \epsilon^2 u_2\Big), \tag{3.61}$$

$$\frac{\mathrm{d}}{\mathrm{d}z}\Big(\zeta_0 + \epsilon\zeta_1 + \epsilon^2\zeta_2\Big) = -\epsilon\hat{k}^2(Ra_0 + \epsilon Ra_1 + \epsilon Ra_2)\Big(\theta_0 + \epsilon\theta_1 + \epsilon^2\theta_2\Big), \tag{3.62}$$

$$\begin{aligned}
\left(\mathrm{i}\epsilon\hat{k}_x PrRez + \epsilon^2\hat{k}_x - \frac{\mathrm{d}^2}{\mathrm{d}z^2}\right)\epsilon\Big(\theta_0 + \epsilon\theta_1 + \epsilon^2\theta_2\Big) &= \epsilon\Big(u_0 + \epsilon u_1 + \epsilon^2 u_2\Big)\\
&\quad - \frac{\mathrm{i}\epsilon\hat{k}_x PrRe}{\hat{k}^2(Ra_0 + \epsilon Ra_1 + \epsilon^2 Ra_2)}\Big(\zeta_0 + \epsilon\zeta_1 + \epsilon^2\zeta_2\Big).
\end{aligned} \tag{3.63}$$

Now we consider the resulting equations at increasing order in ϵ; that is $O(\epsilon^n)$ for $n \in \mathbb{N}_0$.

If we first take equation (3.61) at $O(1)$ we have

$$\frac{\mathrm{d}^2\zeta_0}{\mathrm{d}z^2} = 0, \tag{3.64}$$

which yields

$$\zeta_0 = 1, \tag{3.65}$$

for the same reasons discussed in section 3.2. Once again this choice of ζ_0 satisfies the stress-free boundary conditions and normalisation condition on $\tilde{\zeta}$ given by (3.27) and (3.28), and so no thin boundary layer to match these conditions is required. Also, as seen in section 3.2, a consequence of this choice of ζ_0 is

$$\zeta_n(0) = 0 \quad \forall n > 0. \tag{3.66}$$

Next we consider equations (3.61 - 3.63) at $O(\epsilon)$ and we find that

$$\mathrm{i}\hat{k}_x Re z - \frac{\mathrm{d}^2\zeta_1}{\mathrm{d}z^2} = \frac{\mathrm{d}u_0}{\mathrm{d}z}, \tag{3.67}$$

$$\frac{\mathrm{d}\zeta_1}{\mathrm{d}z} = -Ra_0\theta_0, \tag{3.68}$$

$$-\frac{\mathrm{d}^2\theta_0}{\mathrm{d}z^2} = u_0 - \frac{\mathrm{i}\hat{k}_x RePr}{Ra_0}, \tag{3.69}$$

where we have used equation (3.65). We integrate (3.67) to give

$$\frac{\mathrm{i}\hat{k}_x Re z^2}{2} - \frac{\mathrm{d}\zeta_1}{\mathrm{d}z} = u_0 + c_2, \tag{3.70}$$

and if we evaluate this equation at either boundary we find that

$$c_2 = \frac{\mathrm{i}\hat{k}_x Re}{8}, \tag{3.71}$$

using equations (3.26) and (3.27). We can substitute for u_0 and ζ_1 in equation (3.69), using equations (3.70) and (3.68) respectively, to find

$$-\frac{\mathrm{d}^2\theta_0}{\mathrm{d}z^2} = \frac{\mathrm{i}\hat{k}_x Re z^2}{2} - \frac{\mathrm{d}\zeta_1}{\mathrm{d}z} - \frac{\mathrm{i}\hat{k}_x Re}{8} - \frac{\mathrm{i}\hat{k}_x RePr}{Ra_0} \tag{3.72}$$

$$\Rightarrow \quad \frac{\mathrm{d}^2\theta_0}{\mathrm{d}z^2} + Ra_0\theta_0 = -\frac{\mathrm{i}\hat{k}_x Re z^2}{2} + \frac{\mathrm{i}\hat{k}_x Re}{8} + \frac{\mathrm{i}\hat{k}_x RePr}{Ra_0}. \tag{3.73}$$

This is a second order inhomogeneous ordinary differential equation (ODE) in θ_0 of which the solution to the homogeneous part is

$$\theta_0^{\mathrm{H}} = A\sinh\left(\sqrt{-Ra_0}z\right) + B\cosh\left(\sqrt{-Ra_0}z\right) \tag{3.74}$$

since we are assuming that $Ra_0 < 0$. We then assume that the particular solution takes the form: $\theta_0^{\mathrm{P}} = c_3 z^2 + c_4$, substitute into equation (3.73) to find c_3 and c_4 and then the general solution for θ_0 is

$$\theta_0 = \theta_0^{\mathrm{H}} + \theta_0^{\mathrm{P}} = A \sinh\left(\sqrt{-Ra_0} z\right) + B \cosh\left(\sqrt{-Ra_0} z\right) - \frac{\mathrm{i}\hat{k}_x Re z^2}{2Ra_0} + \frac{\mathrm{i}\hat{k}_x Re}{Ra_0}\left(\frac{1+Pr}{Ra_0} + \frac{1}{8}\right). \tag{3.75}$$

Due to the symmetry of the boundary conditions we must have that $A = 0$ so that in fact

$$\theta_0 = B \cosh\left(\sqrt{-Ra_0} z\right) - \frac{\mathrm{i}\hat{k}_x Re z^2}{2Ra_0} + \frac{\mathrm{i}\hat{k}_x Re}{Ra_0}\left(\frac{1+Pr}{Ra_0} + \frac{1}{8}\right), \tag{3.76}$$

$$u_0 = B Ra_0 \cosh\left(\sqrt{-Ra_0} z\right) + \frac{\mathrm{i}\hat{k}_x Re}{Ra_0}(1+Pr), \tag{3.77}$$

$$\zeta_1 = B\sqrt{-Ra_0} \sinh\left(\sqrt{-Ra_0} z\right) + \frac{\mathrm{i}\hat{k}_x Re z^3}{6} - \mathrm{i}\hat{k}_x Re z\left(\frac{1+Pr}{Ra_0} + \frac{1}{8}\right), \tag{3.78}$$

where the expressions for u_0 and ζ_1 have been found via equations (3.69) and (3.68) respectively. We have integrated to obtain ζ_1 but any constant of integration in (3.78) must vanish due to the normalisation condition given by (3.65). We can also determine B by considering the no penetration condition on this expression for u_0. Hence, at either boundary, we have

$$0 = B Ra_0 \cosh\left(\sqrt{-Ra_0}/2\right) + \frac{\mathrm{i}\hat{k}_x Re}{Ra_0}(1+Pr) \tag{3.79}$$

$$\Rightarrow \quad B = \frac{-\mathrm{i}\hat{k}_x Re(1+Pr)}{Ra_0^2 \cosh\left(\sqrt{-Ra_0}/2\right)}. \tag{3.80}$$

With this expression for B we have acquired the complete expressions for ζ_1, u_0 and θ_0, given by equations (3.76 - 3.78).

Thus we now look at the next order in ϵ. From equation (3.61) at $O(\epsilon^2)$ we find

$$\mathrm{i}\hat{k}_x Re z \zeta_1 + \hat{k}^2 - \frac{\mathrm{d}^2\zeta_2}{\mathrm{d}z^2} = \frac{\mathrm{d}u_1}{\mathrm{d}z} \tag{3.81}$$

$$\Rightarrow \quad \mathrm{i}\hat{k}_x Re B\sqrt{-Ra_0} z \sinh\left(\sqrt{-Ra_0} z\right) - \frac{\hat{k}_x^2 Re^2 z^4}{6} + \hat{k}_x^2 Re^2 z^2\left(\frac{1+Pr}{Ra_0} + \frac{1}{8}\right) + \hat{k}^2 - \frac{\mathrm{d}^2\zeta_2}{\mathrm{d}z^2} = \frac{\mathrm{d}u_1}{\mathrm{d}z} \tag{3.82}$$

where we have substituted the form of ζ_1 from equation (3.78). We now integrate this equation to give

$$\mathrm{i}\hat{k}_x ReBz\cosh\left(\sqrt{-Ra_0}z\right) - \frac{\mathrm{i}\hat{k}_x ReB\sinh\left(\sqrt{-Ra_0}z\right)}{\sqrt{-Ra_0}} - \frac{\hat{k}_x^2 Re^2 z^5}{30} + \frac{\hat{k}_x^2 Re^2 z^3}{3}\left(\frac{1+Pr}{Ra_0} + \frac{1}{8}\right) + \hat{k}^2 z - \frac{\mathrm{d}\zeta_2}{\mathrm{d}z} = u_1, \quad (3.83)$$

where again there is no constant of integration due to the symmetry of the boundary conditions. If we now evaluate this equation at either boundary, the final two terms vanish and we obtain

$$\frac{\hat{k}_x^2 Re^2(1+Pr)}{2Ra_0^2} - \frac{\hat{k}_x^2 Re^2(1+Pr)\tanh\left(\sqrt{-Ra_0}/2\right)}{\sqrt{-Ra_0}Ra_0^2} - \frac{\hat{k}_x^2 Re^2}{960} + \frac{\hat{k}_x^2 Re^2}{24}\left(\frac{1+Pr}{Ra_0} + \frac{1}{8}\right) + \frac{\hat{k}^2}{2} = 0 \quad (3.84)$$

$$\Rightarrow \quad \frac{1+Pr}{Ra_0^2} - \frac{2(1+Pr)\tanh(\sqrt{-Ra_0}/2)}{\sqrt{-Ra_0}Ra_0^2} + \frac{1+Pr}{12Ra_0} + \frac{1}{120} + \frac{1}{Re^2}\left(1 + \frac{k_y^2}{k_x^2}\right) = 0, \quad (3.85)$$

where we have substituted for B from equation (3.80). Since the wavenumbers only appear as the ratio of $\hat{k}_x$ and $\hat{k}_y$ we have been able to drop the circumflexes on them using their definitions from equation (3.56). With this result we have derived a condition, which Ra_0 must satisfy, given values for Pr, Re and k_y/k_x. Equation (3.85) is solved numerically for Ra_0 with results displayed in table 3.3.

If we first consider the case $Pr = 1$, $k_y/k_x = 0$ and $Re = 100$ we can directly compare the numeric results given by table 2.2 with the equivalent asymptotic results of table 3.3. We find that the asymptotics predict the numerics very well. For example, at asymptotically small azimuthal wavenumber table 2.2 shows that the Rayleigh number at onset will tend towards the value $-9.6577E^{-2}k_x^{-2}$. We see from table 3.3 that the value of Ra_0 predicted for the $(Re, k_y/k_x) = (100, 0)$ case is -9.6578. When recalling that Ra has been scaled as $Ra = E^{-2}k_x^{-2}Ra_0$ in the asymptotics we see that this gives excellent agreement. In fact, for modes with $k_y/k_x = 0$ the asymptotics predict that Ra_0 is converging to approximately -9.9 with increasing zonal flow, which is also in excellent agreement with the numerics. Also of note is that equation (3.85) has no negative Ra_0 solutions for $Re < 10.9496$. As a result of this the asymptotic results, in table 3.3, predict only modes with $Ra_0 > 0$ for $Re = 10$. This again agrees with the numerics as baroclinic instabilities were found to decay, in the $Pr = 1$ case, for values of the Reynolds number less than approximately 10.95. Hence the asymptotics are predicting a very similar critical value of the Reynolds number that was found in the numerics.

More generally, table 3.3 shows that as Re is increased the value of Ra_0 required for instability becomes smaller and then more negative once it changes sign. Additionally, larger Pr allows onset with smaller values of Re. The asymptotics of table 3.3 also predict that increasing k_y only serves to stabilise the system by increasing the Rayleigh number at onset in all cases. This matches the numerics as described in section 2.7 where for a non-zero Reynolds number the preference for instability was $k_y = 0$.

		Ra_0		
Re	k_y/k_x	$Pr = 0.1$	$Pr = 1$	$Pr = 10$
10	0	4.9382	0.8983	−39.6579
	0.1	4.9649	0.9470	−39.3883
	1	6.6795	4.0672	−22.1361
30	0	0.2906	−7.5633	−86.4877
	0.1	0.3019	−7.5633	−86.4877
	1	1.3001	−5.7250	−76.3117
100	0	−0.8594	−9.6578	−98.0825
	0.1	−0.8581	−9.6555	−98.0696
	1	−0.7335	−9.4285	−96.8131
1000	0	−0.9870	−9.8903	−99.3692
	0.1	−0.9870	−9.8903	−99.3691
	1	−0.9857	−9.8879	−99.3561

Table 3.3: Values for Ra_0 found by solving equation (3.85) for various values of Re, k_y/k_x and Pr.

In figure 3.1 we have plotted the fields predicted by the lowest order asymptotics as given by equations (3.65), (3.76) and (3.77) scaled using $u_z = Eu_0$, $\theta = E\theta_0$ in order to compare with the equivalent parameter values at point $\times_2$ from figure 2.1(a). By comparing this plot with that of 2.2(b) we can clearly see that the small wavenumber asymptotic theory is also predicting the correct form and magnitude of the fields. The asymptotics continue to predict the correct form of ζ, u_z and θ for both larger and smaller values of the Reynolds number. In the latter case the onset parameter becomes the Rayleigh number, Ra^*.

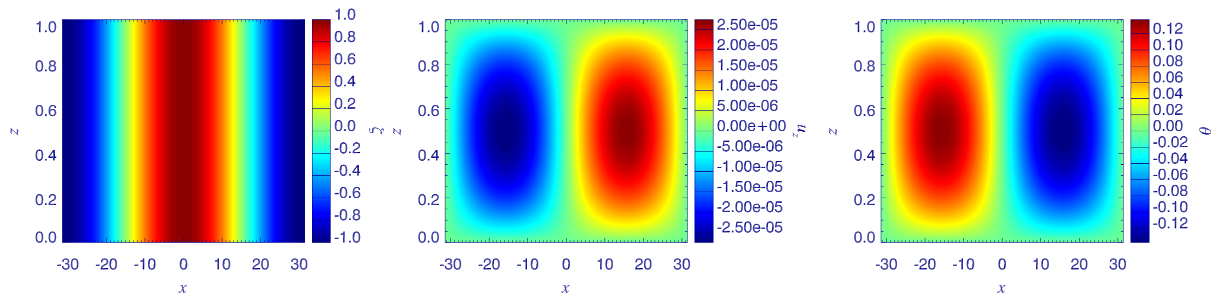

Figure 3.1: Eigenfunction plots as predicted by the small wavenumber asymptotic theory of section 3.3. This is the equivalent of point $\times_2$ from figure 2.1(a) where $E = 10^{-4}$, $Pr = 1$, $Ra = -10^6$, $Re = Re^* \equiv 10.9599$, $k_x = 0.1$ and $k_y = k_{y_c} = 0$.

3.4 Relation to the Eady problem

We have seen how baroclinic instabilities have arisen in our model throughout this chapter and the last. In this section we consider how the equations we have derived in the small Ekman number limit relate to the governing equations of the Eady problem (Eady, 1949), which is a classic problem involving the baroclinic instability. We discussed the origin of the baroclinic instability in section 1.5 where we recall that it can occur when surfaces of constant pressure and constant density do not coincide. This is equivalent to the density taking the form given in equation (1.48). In our current setup (see equations (1.13) and (2.15)) we have that density is related to the temperature such that

$$\rho = \rho_0(1 - \alpha T_0) \tag{3.86}$$

$$\Rightarrow \quad \rho = \rho_0 \left(1 - \alpha \left(\frac{\beta d}{2} - \beta z - \frac{2\Omega U_0' y}{g\alpha}\right)\right), \tag{3.87}$$

which is of the form of equation (1.48) with

$$a = 1 - \frac{\alpha\beta d}{2}, \qquad \delta = -\alpha\beta, \qquad \lambda = -\frac{2\Omega U_0'}{g\alpha\beta}. \tag{3.88}$$

We see from this form of ρ that when $\beta > 0$ the fluid is not stably stratified since density increases with z and we would expect thermal instabilities to dominate. However, when $\beta < 0$ the fluid is stably stratified and although thermal instabilities will not occur, baroclinic instabilities will be possible.

The small Ekman number equations (3.4 - 3.6) are related to the quasi-geostrophic (QG) equations used in atmospheric science (see, for example, Pedlosky, 1987). The geostrophic component of the velocity is given by $2\Omega(u_x^{\mathrm{G}}, u_y^{\mathrm{G}}) = (-\partial p/\partial y, \partial p/\partial x)$, as seen by equation (45.25) of Drazin & Reid (1981). Hence, from equation (2.51),

$$\zeta = \frac{\partial u_y^{\mathrm{G}}}{\partial x} - \frac{\partial u_x^{\mathrm{G}}}{\partial y} \tag{3.89}$$

$$= \frac{1}{2\Omega}\left(\frac{\partial^2 p}{\partial x^2} + \frac{\partial^2 p}{\partial y^2}\right) \tag{3.90}$$

$$= -\frac{k^2 p}{2\Omega}, \tag{3.91}$$

and the pressure perturbation is simply proportional to the vertical vorticity. Thus equation (3.5) is simply the hydrostatic equation used in the QG approximation, where vertical accelerations are neglected. In section 1.3 we mentioned that the parameter often used to determine whether a system is rapidly rotating is the Rossby number, defined by equation (1.20). The terms containing k_y in equations (3.1) and (3.3) are also dropped in the Eady problem when the small Rossby number limit is taken, see section 45 of Drazin & Reid (1981). The equivalent limit here, which is $ReE << 1$, has been taken by considering finite Re and $E \to 0$ resulting in equations (3.4 - 3.6). If we take the z-derivative of (3.6) and eliminate $\tilde{u}_z$ and $\tilde{\theta}$ using (3.4) and (3.5), we obtain

$$\left(sPr + \mathrm{i}k_x PrRez + k^2 - \frac{\mathrm{d}^2}{\mathrm{d}z^2}\right)\frac{\mathrm{d}\tilde{\theta}}{\mathrm{d}z} + \mathrm{i}k_x PrRe\tilde{\theta} = \frac{\mathrm{d}\tilde{u}_z}{\mathrm{d}z} - \frac{\mathrm{i}k_x PrRe}{k^2\widetilde{Ra}}\frac{\mathrm{d}\tilde{\zeta}}{\mathrm{d}z} \tag{3.92}$$

$$\Rightarrow \quad \left(sPr + \mathrm{i}k_x PrRez + k^2 - \frac{\mathrm{d}^2}{\mathrm{d}z^2}\right)\left(\frac{-1}{k^2\widetilde{Ra}}\frac{\mathrm{d}^2\tilde{\zeta}}{\mathrm{d}z^2}\right) - \frac{\mathrm{i}k_x PrRe}{k^2\widetilde{Ra}}\frac{\mathrm{d}\tilde{\zeta}}{\mathrm{d}z} \tag{3.93}$$

$$= \left(s + \mathrm{i}k_x Rez + k^2 - \frac{\mathrm{d}^2}{\mathrm{d}z^2}\right)\tilde{\zeta} - \frac{\mathrm{i}k_x PrRe}{k^2\widetilde{Ra}}\frac{\mathrm{d}\tilde{\zeta}}{\mathrm{d}z}$$

$$\Rightarrow \quad \left(sPr + \mathrm{i}k_x PrRez + k^2 - \frac{\mathrm{d}^2}{\mathrm{d}z^2}\right)\frac{\mathrm{d}^2\tilde{\zeta}}{\mathrm{d}z^2} + \left(s + \mathrm{i}k_x Rez + k^2 - \frac{\mathrm{d}^2}{\mathrm{d}z^2}\right)\widetilde{Ra}\tilde{\zeta} = 0. \tag{3.94}$$

In the QG approximation, diffusion is usually ignored, which is the case in the Eady problem. Hence the $k^2 - \mathrm{d}^2/\mathrm{d}z^2$ terms, which arise from the dissipative terms (originally involving ν and κ) are dropped in (3.94). This then leads to the classical Eady equation

$$(s + \mathrm{i}k_x Rez)\left(\frac{\mathrm{d}^2\tilde{\zeta}}{\mathrm{d}z^2} + \frac{\widetilde{Ra}}{Pr}\tilde{\zeta}\right) = 0, \tag{3.95}$$

which is equivalent to equation (45.28) of Drazin & Reid (1981). The only boundary condition to survive the neglect of diffusion is $\tilde{u}_z = 0$, which, from equation (3.6), leads to

$$
\begin{aligned}
&(sPr + \mathrm{i}k_x PrRez)\,\tilde{\theta} = -\frac{\mathrm{i}k_x PrRe}{k^2\widetilde{Ra}}\tilde{\zeta} &\quad (3.96)\\
\Rightarrow\quad &(s + \mathrm{i}k_x Rez)\,\frac{\mathrm{d}\tilde{\zeta}}{\mathrm{d}z} = \mathrm{i}k_x Re\tilde{\zeta}, \quad \text{on} \quad z = \pm\frac{1}{2}, &\quad (3.97)
\end{aligned}
$$

where we have, again, dropped the diffusion terms and substituted for $\tilde{\theta}$ from equation (3.5). Equation (3.97) is equivalent to the boundary condition given by equation (45.30) of Drazin & Reid (1981). Instability in the Eady problem occurs as an oscillatory mode, $\Im[s] \equiv \omega \neq 0$. The relevant part of our parameter space to the Eady problem is where Re is large, since then the viscosity is small. There we do indeed find oscillatory baroclinic modes to the right of the green lines in figure 2.1. One such mode is displayed in figure 2.2(c), point $\times_3$. Therefore our theory agrees with the results of the Eady problem when the relevant rapidly rotating, inviscid limit is taken.

Chapter 4

A linear theory for the annulus model

In chapters 2 and 3 we have investigated convection in the simplest of models, that of the plane layer. Plane layer models are relevant to certain regions of astrophysical and geophysical bodies, namely polar regions. However they can only give an insight into the nature of convection and, in particular, do not take into account the fact that the boundaries in the spherical geometry of planetary bodies are not flat. Ideally, investigations would always be performed in spherical geometry. The linear theory of convection in spheres and spherical shells has now been comprehensively investigated. Roberts (1968) and Busse (1970) derived some of the basic principles and the small Ekman number limit was discussed by Jones *et al.* (2000) and Dormy *et al.* (2004). However, performing three-dimensional simulations in spherical geometry can be computationally expensive. It is for this reason that quasi-geostrophic models have been developed to reduce the number of dimensions in the problem. The quasi-geostrophic approximation takes advantage of the strong Coriolis force in rapidly rotating systems in order to ignore the z-structure of the vertical vorticity of the system (Gillet & Jones, 2006). One such model that has been widely used, due to its ability to replicate results seen in fully three-dimensional simulations, is the Busse annulus (Busse, 1970). This model has the rotation axis and the direction of gravity orthogonal to one another. Thus it is relevant to the region of the Earth's core outside the tangent cylinder and also to the atmospheres of the gas giants. Much pioneering work in developing the annulus model as a model for geophysical and astrophysical bodies was completed by Busse and collaborators in a series of papers (Busse, 1970; Busse & Or, 1986; Busse, 1986; Or & Busse, 1987; Schnaubelt & Busse, 1992). Magnetic instabilities within an annulus model have also been investigated by Hutcheson & Fearn (1995) though we continue to consider the non-magnetic case here.

Our work on the Busse annulus, throughout the next two chapters, maintains an interest in the interaction between convection and zonal flows. We postpone a more in depth discussion of previous work on this subject, especially non-linear results, to chapter 5, although we shall briefly discuss the linear theory in section 4.2. For this chapter it suffices to know that the Busse annulus replicates several of the key aspects of convection in spherical geometry. For example, convection in the annulus occurs in the form of tall thin columns which onset as thermal Rossby waves (Busse & Or, 1986). This is in agreement with the linear theory of convection at onset in spherical geometry (Jones *et al.*, 2000; Dormy *et al.*, 2004). Additionally, of particular relevance to the subject of this thesis is the non-linear model's ability to develop large zonal flows which may have a multiple jet structure (see, for example, Jones *et al.*, 2003).

In this chapter we discuss the effects of adding an azimuthal zonal flow to the basic state of the Busse annulus by considering the linear theory. Linear theories cannot produce zonal flows since they are generated by the non-linear interaction of the small-scale perturbations as evidenced by their lack of appearance in Jones *et al.* (2000) and Dormy *et al.* (2004). However, by adding the zonal flow to the basic state we can investigate whether such flows of various magnitude and form aid or hinder the onset of convection. In addition to this motivation, we are also aware from our discussion in section 1.1 that zonal flows occur in astrophysical bodies such as the Earth and the gas giants. It is also worth noting that in this chapter we will essentially be considering the analogous study to chapters 2 and 3 but for the annulus model rather than a plane layer model. Thus, it is also sensible to consider this linear theory in order to compare with that of the plane layer geometry.

We begin in section 4.1 with a mathematical description of the problem, which includes a general derivation of our equations. Therefore we retain non-linear terms in the derivation for later use in chapter 5. We then describe how we solve the linear stability problem in section 4.2 and discuss the limits that have been considered in previous work. In sections 4.3 and 4.4 we discuss novel results for the linear theory of the annulus model with an imposed azimuthal zonal flow for two different flow patterns.

4.1 Mathematical setup

We begin with a description of the mathematical setup of the problem. We consider a fluid filled cylindrical annulus with inclined bounding surfaces for the top and bottom lids. These top and bottom end surfaces are sloped in opposite directions so that the outer cylinder is shorter than the inner cylinder. The mean radius of the annulus is r_0, the gap between the two cylinders, referred to as the width is D and the height of the annulus at the outer cylindrical wall is L. The annulus rotates about the axial direction with angular velocity Ω and a temperature difference of ΔT is maintained between the two walls such that the outer and inner walls are at temperatures $T = 0$ and $T = \Delta T$ respectively. We also take the gravity force to be acting radially inward and the annular end walls make an angle χ to the horizontal.

The setup described here is, as desired, representative of a planetary atmosphere or the region of the Earth's outer core outside the tangent cylinder. This is because the annulus model exhibits key properties of these spherical physical regions including gravity acting perpendicular to the rotation axis (true near equatorial regions) and sloped 'horizontal' boundaries representing the curvature of the outer boundaries of the spherical bodies. This is contrast to the plane layer model discussed in chapters 2 and 3 which is relevant to the polar regions of geophysical and astrophysical bodies.

In fact, the annulus model acts as the simplest model of convection in spherical geometry that includes the effects of rotation. This is because the model allows near geostrophic flow, which is the case in a sphere. We saw in chapter 1 how the Taylor-Proudman theorem is effectively a consequence of the condition for geostrophic motion where the Coriolis force is balanced exactly by the pressure gradient. In section 1.3 we discussed how, as a result of the Taylor-Proudman theorem, tall thin columns are the preference in spherical geometry. These tall thin columns are also found at the onset of convection in the annulus model. The annulus model does however have some disadvantages due to its simplistic nature. For example, although the end wall boundaries are sloped in order to mimic spherical geometry, in reality they would, of course, be curved. By omitting the curvature of these boundaries we neglect any preference that there may be for waves to propagate in one azimuthal direction over the other. Thus, with sloped boundaries we cannot distinguish between eastward and westward propagating waves (Busse & Or, 1986).

Another difference between the model discussed here and the plane layer model of chapters 2 and 3 is the origin of the zonal flow itself. In the plane layer model the basic state zonal flow was driven as a thermal wind by a radially dependent temperature gradient. However, in the annulus model the zonal flow can be maintained by geostrophic balance since azimuthal flows can be geostrophic. Hence we envisage a zonal flow driven by non-linear interactions (specifically the Reynolds stresses), which is then maintained by the geostrophic basic state.

The natural choice of coordinate system for the annulus model would be cylindrical polar coordinates: (r, ϕ, z). However, by making the small-gap approximation of $D/r_0 \ll 1$ the curvature terms of cylindrical polars can be neglected and we are able instead to choose a Cartesian coordinate system. Therefore we choose coordinates such that x is the azimuthal coordinate and increases eastwardly (acting like ϕ) and $0 \leq y \leq D$ is the radial coordinate (acting like $-r$). The axial coordinate, z, remains unchanged from cylindrical polars and ranges from $-L/2$ to $L/2$. Hence, gravity acts in the positive y-direction and the direction of rotation is in the z-direction so that $\mathbf{g} = g\hat{\mathbf{y}}$ and $\mathbf{\Omega} = \Omega\hat{\mathbf{z}}$. The setup described above is shown in figure 4.1. The fluid is bounded within the annulus and hence we must demand a no penetration condition on all boundaries. The no penetration condition at the sloped end walls of the annulus is dependent on the inclination, χ, so that

$$\cos(\chi)u_z \mp \sin(\chi)u_y = 0 \quad \text{on} \quad z \pm L/2, \tag{4.1}$$

from equation (1.17). Boundary conditions on the inner and outer cylindrical walls will be discussed in the next section.

The linear theory of the annulus model was originally discussed and solved by Busse (1970). In this work we go further by imposing an azimuthal zonal flow in the basic state. The zonal flow takes the form of a radial shear and is thus solely dependent on the y-coordinate so that

$$\mathbf{u_0} = U_0(y)\hat{\mathbf{x}}. \tag{4.2}$$

This form of the zonal flow is, of course, similar to that of the plane layer model since it acts azimuthally and the shearing is again radial, though this now requires a y rather than

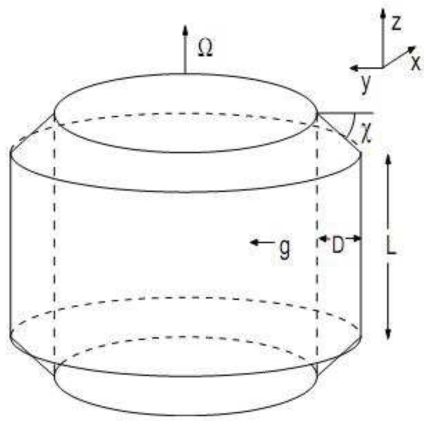

Figure 4.1: Diagram depicting the physical setup of the Busse annulus; taken from Abdulrahman *et al.* (2000).

z-dependence. The basic state vorticity in the z-direction is then

$$\zeta_0 = \hat{\mathbf{z}} \cdot \nabla \times \mathbf{u_0} = -\frac{\mathrm{d}U_0}{\mathrm{d}y}. \tag{4.3}$$

The basic state temperature is given by

$$T_0 = \frac{\Delta T y}{D}, \tag{4.4}$$

so that $T_0 = 0$ and $T_0 = \Delta T$ at the outer and inner cylindrical walls respectively, as discussed above.

We now derive a set of equations from equations (1.9), (1.15) and (1.16) following a similar procedure to that of the aforementioned early annulus papers (see, for example, Busse & Or, 1986). We use the vorticity equation (1.16) rather than the momentum equation (1.14) since the former does not contain the pressure. In particular, we shall use the z-component of equation (1.16), which is

$$\frac{\partial Z}{\partial t} + \mathbf{U} \cdot \nabla Z - 2\Omega \hat{\mathbf{z}} \cdot \frac{\partial \mathbf{U}}{\partial z} = -g\alpha \frac{\partial T}{\partial x} + \nu \nabla^2 Z, \tag{4.5}$$

where Z is the z-component of the vorticity. Here we have substituted the definitions of $\mathbf{\Omega}$ and $\mathbf{g}$ discussed above and ignored the $(\mathbf{Z} \cdot \nabla)\mathbf{U}$ term in equation (1.16). This is justified since we are interested in the small Rossby number limit of rapid rotation where the planetary vorticity $2\mathbf{\Omega}$ dominates over the fluid vorticity $\mathbf{Z}$. Additionally, the vorticity acts only in the z-direction (as we shall see later) so that $(\mathbf{Z} \cdot \nabla)\mathbf{U}$ produces only a z-derivative acting on $\mathbf{U}$. The quantity $\partial\mathbf{U}/\partial z$ will be small because the length scale in the horizontal direction is much shorter than that of the vertical direction due to the rapid rotation. Conversely, the term $(\mathbf{U} \cdot \nabla)\mathbf{Z}$ is retained since it consists of horizontal derivatives of the vorticity which are not small in general.

We perturb around the basic state to acquire a set of equations similar to those of Busse but now with several terms involving U_0. Although this chapter deals with the linear theory of the model, in this derivation we retain the non-linear terms for later use in chapter 5. However, we note that when considering the non-linear theory in the following chapter we must set $U_0 = 0$ in these equations. Similarly, the non-linear terms appearing in the derived equations will be dropped in this chapter from section 4.2 onwards.

We begin the derivation by perturbing so that $\mathbf{U} = \mathbf{u_0} + \mathbf{u}$, $T = T_0 + \theta$ and $Z = \zeta_0 + \zeta$. We assume that $\chi \ll 1$ and hence the boundaries are nearly flat, the flow is nearly geostrophic and z-component of the velocity is small compared with the horizontal components. This allows us to make the ansatz

$$\mathbf{u} = -\nabla \times \psi(x, y)\hat{\mathbf{z}} + u_z\hat{\mathbf{z}} \tag{4.6}$$

$$= -\frac{\partial\psi}{\partial y}\hat{\mathbf{x}} + \frac{\partial\psi}{\partial x}\hat{\mathbf{y}} + u_z\hat{\mathbf{z}}, \tag{4.7}$$

where the vertical velocity, u_z, is a small ageostrophic part of the flow of order χ. Also, in the limit of small χ, the end wall boundary conditions, given by equation (4.1), become

$$u_z = \pm\chi u_y \quad \text{on} \quad z = \pm L/2. \tag{4.8}$$

We substitute the perturbed forms of $\mathbf{U}$, T and Z into equation (4.5) to give

$$\frac{\partial\zeta}{\partial t} + U_0\frac{\partial\zeta}{\partial x} + u_y\frac{\partial\zeta_0}{\partial y} + u_x\frac{\partial\zeta}{\partial x} + u_y\frac{\partial\zeta}{\partial y} - 2\Omega\frac{\partial u_z}{\partial z} = -g\alpha\frac{\partial\theta}{\partial x} + \nu\nabla^2\zeta \tag{4.9}$$

$$\Rightarrow \quad \frac{\partial\zeta}{\partial t} + U_0\frac{\partial\zeta}{\partial x} + \frac{\partial\psi}{\partial x}\frac{\partial\zeta_0}{\partial y} + \frac{\partial\psi}{\partial x}\frac{\partial\zeta}{\partial y} - \frac{\partial\psi}{\partial y}\frac{\partial\zeta}{\partial x} - 2\Omega\frac{\partial u_z}{\partial z} = -g\alpha\frac{\partial\theta}{\partial x} + \nu\nabla^2\zeta \tag{4.10}$$

$$\Rightarrow \quad \frac{\partial\zeta}{\partial t} + U_0\frac{\partial\zeta}{\partial x} - \frac{\mathrm{d}^2U_0}{\mathrm{d}y^2}\frac{\partial\psi}{\partial x} + \frac{\partial(\psi, \zeta)}{\partial(x, y)} - 2\Omega\frac{\partial u_z}{\partial z} = -g\alpha\frac{\partial\theta}{\partial x} + \nu\nabla^2\zeta, \tag{4.11}$$

where we have substituted for u_x and u_y in terms of ψ using equation (4.7) and substituted for ζ_0 using equation (4.3). Here we have also introduced the Jacobian defined as

$$\frac{\partial(h_1, h_2)}{\partial(x, y)} = \frac{\partial h_1}{\partial x}\frac{\partial h_2}{\partial y} - \frac{\partial h_2}{\partial x}\frac{\partial h_1}{\partial y}, \tag{4.12}$$

for some functions h_1 and h_2.

In order to eliminate u_z we note that the only z-dependence of equation (4.11) appears in the u_z term and thus we integrate over z (between $z = -L/2$ and $z = L/2$) to give

$$L\frac{\partial \zeta}{\partial t} + LU_0\frac{\partial \zeta}{\partial x} - L\frac{\mathrm{d}^2 U_0}{\mathrm{d}y^2}\frac{\partial \psi}{\partial x} + L\frac{\partial(\psi,\zeta)}{\partial(x,y)} - 2\Omega[u_z]_{-L/2}^{L/2} = -Lg\alpha\frac{\partial T}{\partial x} + L\nu\nabla^2\zeta \tag{4.13}$$

$$\Rightarrow \quad \frac{\partial \zeta}{\partial t} + U_0\frac{\partial \zeta}{\partial x} - \frac{\mathrm{d}^2 U_0}{\mathrm{d}y^2}\frac{\partial \psi}{\partial x} + \frac{\partial(\psi,\zeta)}{\partial(x,y)} - \frac{4\chi\Omega}{L}\frac{\partial \psi}{\partial x} = -g\alpha\frac{\partial T}{\partial x} + \nu\nabla^2\zeta, \tag{4.14}$$

where we have used the fact that $u_z = \pm\chi u_y = \pm\chi\partial\psi/\partial x$ on $z = \pm L/2$ from equation (4.8). By using this form for u_z we have implicitly assumed that the boundaries are also stress-free. In order to use rigid boundaries we must incorporate the effects of an Ekman layer, which we shall consider in chapter 5.

We must also consider the heat equation and so we substitute the perturbed forms of $\mathbf{U}$ and T into equation (1.15) to give

$$\frac{\partial \theta}{\partial t} + U_0\frac{\partial \theta}{\partial x} + u_y\frac{\partial T_0}{\partial y} + u_x\frac{\partial \theta}{\partial x} + u_y\frac{\partial \theta}{\partial y} = \kappa\nabla^2\theta \tag{4.15}$$

$$\Rightarrow \quad \frac{\partial \theta}{\partial t} + U_0\frac{\partial \theta}{\partial x} + \frac{\Delta T}{D}\frac{\partial \psi}{\partial x} + \frac{\partial(\psi,\theta)}{\partial(x,y)} = \kappa\nabla^2\theta. \tag{4.16}$$

If we take the curl of equation (4.7) we also find that the vorticity can be written in terms of ψ since

$$\boldsymbol{\zeta} \equiv \nabla\times\mathbf{u} = -\nabla\times\nabla\times\psi\hat{\mathbf{z}} \tag{4.17}$$

$$= -\nabla(\nabla\cdot\psi\hat{\mathbf{z}}) + \nabla^2\psi\hat{\mathbf{z}} \tag{4.18}$$

$$= \nabla^2\psi\hat{\mathbf{z}}, \tag{4.19}$$

where we have used equation (A.2) and neglected u_z, which is small compared to ψ. Hence the vertical vorticity is

$$\zeta = \nabla^2\psi. \tag{4.20}$$

We non-dimensionalise using length scale D, the viscous timescale D^2/ν and the temperature scale $\nu\Delta T/\kappa$. We also suppose that our zonal flow has a typical velocity of U^*. Hence we substitute the formulae: $\{x,y\} \to D\{\tilde{x},\tilde{y}\}$, $t \to \tilde{t}D^2/\nu$, $\psi \to \tilde{\psi}\nu$, $\zeta \to \tilde{\zeta}\nu/D^2$, $\theta \to \tilde{\theta}\nu\Delta T/\kappa$ and $U_0 \to \tilde{U}_0U^*$ into equations (4.14) and (4.16) to give

$$\frac{\nu^2}{D^4}\frac{\partial\tilde{\zeta}}{\partial\tilde{t}} + \frac{\nu U^* U_0}{D^3}\frac{\partial\tilde{\zeta}}{\partial\tilde{x}} - \frac{\nu U^* U_0''}{D^3}\frac{\partial\tilde{\psi}}{\partial\tilde{x}} + \frac{\nu^2}{D^4}\frac{\partial(\tilde{\psi},\tilde{\zeta})}{\partial(\tilde{x},\tilde{y})} - \frac{4\chi\Omega\nu}{DL}\frac{\partial\tilde{\psi}}{\partial\tilde{x}} = -\frac{g\alpha\nu\Delta T}{D\kappa}\frac{\partial\tilde{\theta}}{\partial\tilde{x}} + \frac{\nu^2}{D^4}\nabla^2\tilde{\zeta}, \tag{4.21}$$

$$\frac{\nu^2\Delta T}{\kappa D^2}\frac{\partial\tilde{\theta}}{\partial\tilde{t}} + \frac{\nu\Delta T U^* U_0}{\kappa D}\frac{\partial\tilde{\theta}}{\partial\tilde{x}} + \frac{\nu\Delta T}{D^2}\frac{\partial\tilde{\psi}}{\partial\tilde{x}} + \frac{\nu^2\Delta T}{\kappa D^2}\frac{\partial(\tilde{\psi},\tilde{\theta})}{\partial(\tilde{x},\tilde{y})} = \frac{\nu\Delta T}{D^2}\nabla^2\tilde{\theta}. \tag{4.22}$$

We can tidy up these equations by introducing dimensionless parameters and dropping the tildes to give

$$\frac{\partial \zeta}{\partial t} + ReU_0 \frac{\partial \zeta}{\partial x} + \frac{\partial(\psi, \zeta)}{\partial(x, y)} - (\beta + ReU_0'')\frac{\partial \psi}{\partial x} = -Ra\frac{\partial \theta}{\partial x} + \nabla^2 \zeta, \tag{4.23}$$

$$Pr\left(\frac{\partial \theta}{\partial t} + ReU_0 \frac{\partial \theta}{\partial x} + \frac{\partial(\psi, \theta)}{\partial(x, y)}\right) = -\frac{\partial \psi}{\partial x} + \nabla^2 \theta, \tag{4.24}$$

where the beta parameter, β, Prandtl number, Pr, Rayleigh number, Ra, and Reynolds number, Re, are defined as

$$\beta = \frac{4\chi\Omega D^3}{\nu L}, \qquad Pr = \frac{\nu}{\kappa}, \qquad Ra = \frac{g\alpha\Delta T D^3}{\nu\kappa}, \qquad Re = \frac{DU^*}{\nu}. \tag{4.25}$$

In the annulus model the beta parameter effectively acts as an inverse Ekman number (compare with equation (2.32)) and therefore in the limit of rapid rotation we expect β to be large. The other three parameters are equivalent to those in the plane layer model of chapters 2 and 3 with slight changes to account for the annulus geometry (again compare with equation (2.32)).

From equation (4.20) we can also eliminate ζ in equation (4.23) to leave a just two equations for two unknowns, ψ and θ:

$$\frac{\partial \nabla^2\psi}{\partial t} + ReU_0 \frac{\partial \nabla^2\psi}{\partial x} + \frac{\partial(\psi, \nabla^2\psi)}{\partial(x, y)} - (\beta + ReU_0'')\frac{\partial \psi}{\partial x} = -Ra\frac{\partial \theta}{\partial x} + \nabla^4 \psi, \tag{4.26}$$

$$Pr\left(\frac{\partial \theta}{\partial t} + ReU_0 \frac{\partial \theta}{\partial x} + \frac{\partial(\psi, \theta)}{\partial(x, y)}\right) = -\frac{\partial \psi}{\partial x} + \nabla^2 \theta. \tag{4.27}$$

Equations (4.26 - 4.27) are a coupled set of partial differential equations that describe the time evolution of the fluid flow and temperature perturbations in the annulus model where the basic state has an azimuthal zonal flow given by $U_0(y)$. We note that if $U_0 = 0$ the equations are equivalent to those derived in previous literature. In particular, compare with equations (2.8a) and (2.8b) from Busse & Or (1986). If we additionally demand that $\beta = 0$ we note that equations (4.26 - 4.27) reduce down to the basic equations for Rayleigh-Bénard convection. This is because the rotation enters only though the β term.

4.2 Numerical method and the solution in two limits

We wish to perform a linear stability analysis of the mathematical setup we have derived in section 4.1. To do this we drop the non-linear terms in equations (4.26 - 4.27) and we choose the t and x-dependence of the solutions to be traveling waves resulting in a 1D problem in y. Hence we choose the following form for our functions:

$$\psi = \hat{\psi}(y)\exp(st + \mathrm{i}kx), \tag{4.28}$$

$$\theta = \hat{\theta}(y)\exp(st + \mathrm{i}kx), \tag{4.29}$$

where s is the complex growth rate. If we substitute these forms for the functions into equations (4.26 - 4.27) and drop the non-linear Jacobian terms we acquire

$$s\left(\frac{\mathrm{d}^2}{\mathrm{d}y^2} - k^2\right)\hat{\psi} + \mathrm{i}kReU_0\left(\frac{\mathrm{d}^2}{\mathrm{d}y^2} - k^2\right)\hat{\psi} - \mathrm{i}k(\beta + ReU_0'')\hat{\psi} = - \mathrm{i}kRa\hat{\theta} + \left(\frac{\mathrm{d}^2}{\mathrm{d}y^2} - k^2\right)^2\hat{\psi}, \tag{4.30}$$

$$sPr\hat{\theta} + \mathrm{i}kPrReU_0\hat{\theta} = -\mathrm{i}k\hat{\psi} + \left(\frac{\mathrm{d}^2}{\mathrm{d}y^2} - k^2\right)\hat{\theta}. \tag{4.31}$$

We now consider the boundary conditions. Since we have used the boundary conditions on the sloped end walls in order to integrate z out of the problem, the only boundaries left to consider at those at the inner and outer walls of the cylinders. Equations (4.30 - 4.31) form a sixth order system of equations and thus we require six boundary conditions at $y = 0$ and $y = 1$. As well as there being no penetration we also require these boundaries to be stress-free and have constant surface temperature. Hence, by a similar argument to that of section 2.2, at $y = 0$ and $y = 1$ we demand that

$$u_y = 0 \quad \text{(no penetration)}, \tag{4.32}$$

$$\frac{\partial u_x}{\partial y} = 0 \quad \text{(stress-free)}, \tag{4.33}$$

$$\theta = 0 \quad \text{(constant surface temperature)}, \tag{4.34}$$

which using equation (4.7) and the form of the functions from equations (4.28 - 4.29) gives

$$\frac{\partial \psi}{\partial x} = 0 \quad \Rightarrow \quad \hat{\psi} = 0, \tag{4.35}$$

$$\frac{\partial^2 \psi}{\partial y^2} = 0 \quad \Rightarrow \quad \frac{\mathrm{d}^2\hat{\psi}}{\mathrm{d}y^2} = 0, \tag{4.36}$$

$$\hat{\theta} = 0. \tag{4.37}$$

Therefore the six boundary conditions we impose on $y = 0$ and $y = 1$ are

$$\hat{\psi} = \frac{\mathrm{d}^2\hat{\psi}}{\mathrm{d}y^2} = \hat{\theta} = 0. \tag{4.38}$$

We now wish to solve the differential eigenvalue problem given by equations (4.30 - 4.31) subject to the boundary conditions given by equation (4.38). However, we first note the solutions to these equations in two important limits. The results discussed here are well known and thus are not derived in detail.

The first limit is that of inviscid flow with no driving from buoyancy where the only driving force then arises from the horizontal shear in the basic state. The viscosity is small in the giant planets, as well as the Earth's core, so this is a sensible limit to consider. In this case the problem reduces to an example of a barotropic instability discussed by, for example, Vallis (2006). For an inviscid, homogeneous fluid we drop the heat equation (4.31) and equation (4.30) becomes

$$(s + \mathrm{i}kReU_0)\left(\frac{\mathrm{d}^2}{\mathrm{d}y^2} - k^2\right)\hat{\psi} - \mathrm{i}k(\beta + ReU_0'')\hat{\psi} = 0. \tag{4.39}$$

This is Rayleigh's equation (Rayleigh, 1880) in the presence of rotation; equivalent to equation (6.20) of Vallis (2006). The regular basic state vorticity, $\zeta_0 = -ReU_0'$, of Rayleigh's equation has been replaced by the (basic state) *potential vorticity* (PV): $q_0 = -(\beta y + ReU_0')$. In fact, if we define the PV, q, as

$$q = \zeta - ReU_0' - \beta y, \tag{4.40}$$

then equation (4.23), in the absence of viscosity and buoyancy, can be written as

$$\frac{Dq}{Dt} = 0, \tag{4.41}$$

where D/Dt is the material derivative. Thus, PV is conserved moving with the fluid when friction and buoyancy are ignored. Some models attempt to explain the existence of zonal flows and multiple jets in terms of PV when the flow is weakly forced (Marcus & Lee, 1998). In our full model the viscosity is small; the buoyancy force however is not and so we shall be considering a different regime.

Despite the relatively simple form of equation (4.39) it is difficult to solve analytically for an arbitrary $U_0(y)$. However, by multiplying Rayleigh's equation through by the complex conjugate of $\hat{\psi}$ and integrating over the domain we obtain:

$$\int_0^1 \hat{\psi}^* \left(\frac{\mathrm{d}^2}{\mathrm{d}y^2} - k^2\right)\hat{\psi}\mathrm{d}y = \int_0^1 \frac{\mathrm{i}k(\beta + ReU_0'')}{\sigma + \mathrm{i}\omega + \mathrm{i}kReU_0}|\hat{\psi}|^2\mathrm{d}y. \tag{4.42}$$

The left-hand-side can be integrated by parts and applying the boundary conditions results in an expression that is real. Hence the imaginary part of the right-hand-side must vanish so that

$$\int_0^1 \frac{\mathrm{i}k\sigma(\beta + ReU_0'')}{\sigma^2 + (\omega + kReU_0)^2}|\hat{\psi}|^2 \mathrm{d}y = 0. \tag{4.43}$$

In order for instability to occur the growth rate, σ, cannot vanish and therefore the quantity $\beta + ReU_0''$ must change sign somewhere in the domain so that the integral can cancel. Equivalently, the PV must have a stationary value. This condition, known as Rayleigh's inflection-point criterion, in our notation can be written as

$$\beta + ReU_0'' = 0 \qquad \text{somewhere in the domain.} \tag{4.44}$$

Fjørtoft (1950) added to this criterion by proving that the stationary value of the PV must be a maximum. In our work we consider $\beta > 0$ and $Re > 0$. Thus in order for equation (4.44) to be satisfied we must have that $U_0'' < 0$ somewhere in the domain. The Reynolds number must also be large enough to overcome the rotational term. We therefore expect the possibility of instabilities arising at large enough Re, even with negative Rayleigh number.

Another limit to discuss is the problem with no zonal flow in the basic state, which is equivalent to the original annulus problem developed by Busse (1970). In the case with $U_0 = 0$, as already noted, equations (4.30 - 4.31) reduce to those of the Busse annulus and the simple solution:

$$\hat{\psi} = \sin(\pi y), \qquad \hat{\theta} = \frac{-\mathrm{i}k}{\pi^2 + k^2 + \mathrm{i}\omega Pr}\hat{\psi}, \tag{4.45}$$

arises provided

$$\omega = \frac{-\beta k}{(1+Pr)(\pi^2+k^2)} \quad \text{and} \quad Ra = \frac{(\pi^2+k^2)^3}{k^2} + \frac{Pr^2\beta^2}{(1+Pr)^2(\pi^2+k^2)}. \tag{4.46}$$

Here we have taken $s = \mathrm{i}\omega$ so that we are looking at marginal stability and ω is the frequency of the disturbances at onset. These results provide significant information. The form of ψ and θ shows that the preference is for convection cells that stretch across the full radial extent of the annular layer. The expression for Ra here is the value of the Rayleigh number for which modes with wavenumber k will onset. As usual, the expression can be minimised over k in order to find a necessary condition (that is, $Ra > Ra_c$) for instability to occur. We notice that the expression for Ra in equation (4.46) resembles that of equation (2.68) for rotating plane layer convection. As in that case, we can immediately note that the expression for the Rayleigh number is smallest when rotation is removed; that is when $\beta = 0$. Thus rotation postpones the onset of convection for all modes and therefore has a stabilising effect. In the rotating plane layer case we saw that both steady and oscillating modes were possible at onset depending on the parameter regimes. However, the convection *always* onsets as oscillatory modes in the annulus and hence solutions with $s = 0$ are not possible, provided $\beta \neq 0$. The expression for ω is a dispersion relation and when $\beta = 0$, we find that the convection which onsets is steady since $\omega = 0$. However, with $\beta = 0$ the problem has reverted to that of Rayleigh-Bénard convection since the expression for the Rayleigh number in equation (4.46) reduces to that found by Rayleigh (1916) (see equation (1.44)). When $\beta \neq 0$ the convection onsets in the form of unsteady thermal Rossby waves (Busse & Or, 1986) due to columns of fluid being different lengths at different radii.

The expression for Ra can also be minimised over k in the case with $\beta \neq 0$ though Ra_c can no longer be found analytically. However, in the limit of rapid rotation ($\beta \to \infty$), which is of interest in many astrophysical bodies, we are able to find that

$$k_c = \frac{Pr^{1/3}\beta^{1/3}}{2^{1/6}(1+Pr)^{1/3}}, \quad \omega_c = \frac{-2^{1/6}\beta^{2/3}}{Pr^{1/3}(1+Pr)^{1/3}}, \quad Ra_c = \frac{3Pr^{4/3}\beta^{4/3}}{2^{2/3}(1+Pr)^{2/3}}. \tag{4.47}$$

As $\beta \propto E^{-1}$ we effectively have that $k_c \propto E^{-1/3}$, $\omega_c \propto E^{-2/3}$ and $Ra_c \propto E^{-4/3}$. These scalings agree with those found in section 2.3 as well as those found in numerical results found in spherical models (Jones *et al.*, 2000). Also of note are the forms of the phase and group velocities, which are found from the dispersion relation. They take the form

$$\frac{\omega}{k} = \frac{-\beta}{(1+Pr)(\pi^2+k^2)} \quad \text{and} \quad \frac{\partial\omega}{\partial k} = \frac{\beta(k^2-\pi^2)}{(1+Pr)(\pi^2+k^2)^2}, \tag{4.48}$$

and we see that the phase speed depends on the sign of β. This is of specific significance when considering the tangent cylinder: OTC $\beta > 0$, as the angle of the slope of the boundaries have the same magnitude. However, ITC $\beta < 0$ since the angle of the slope at the inner boundary is greater than that of the outer boundary. Therefore the waves travel eastward OTC and westward ITC, which as mentioned earlier is another reason why flow across the TC is likely to be minimal.

So far we have discussed two limits of the full equations that we have derived: the inviscid, homogeneous case and the case without zonal flow. As we have seen for both of these situations there is a criterion for the onset of instability. In order to solve the full viscous, rotating problem with buoyancy and zonal flow we must solve the differential eigenvalue problem numerically. This will enable us to investigate the interaction between the convective and barotropic instabilities. We rearrange equations (4.30 - 4.31) as

$$s\left(\frac{\mathrm{d}^2\hat{\psi}}{\mathrm{d}y^2}-k^2\hat{\psi}\right)=-(\mathrm{i}kReU_0+k^2)\left(\frac{\mathrm{d}^2}{\mathrm{d}y^2}-k^2\right)\hat{\psi}+\mathrm{i}k(\beta+ReU_0'')\hat{\psi}-\mathrm{i}kRa\hat{\theta}, \tag{4.49}$$

$$sPr\hat{\theta}=-(\mathrm{i}kPrReU_0+k^2)\hat{\theta}-\mathrm{i}k\hat{\psi}+\frac{\mathrm{d}^2\hat{\theta}}{\mathrm{d}y^2}, \tag{4.50}$$

which shows that this is indeed a differential eigenvalue problem with eigenvalue s. We solve this eigenvalue problem using the same numerical method of Chebyshev collocation discussed in chapter 2 with a truncation value N=100. For that reason we do not discuss the method again here and the reader is directed to the discussion of the method in section 2.4. The set of eigenfunctions in this case is $\Psi=\{\hat{\psi},\hat{\theta}\}$ and the eigenvector is now $\mathbf{w}=[\psi_1,...,\psi_{N+4},\theta_1,...,\theta_{N+2}]^{\mathrm{T}}$. The system we have setup in this chapter has the following input parameters: k, Pr, β, Re and Ra as well as the function $U_0(y)$, which can be varied to obtain the outputs: s and $\mathbf{w}$. The elements of the set Ψ can be then reconstructed from $\mathbf{w}$ and these eigenfunctions are normalised using the method discussed in section 2.4. However, in this linear theory we use the value of the real part of ψ, rather than ζ, to normalise. The 2D fields, ψ and θ, are then constructed using equations (4.28 - 4.29) and we use equation (4.20) to calculate the vertical vorticity, ζ.

We let Γ be the set $\Gamma=\{k,Pr,\beta,Re\}$ and assume we have chosen the form of the zonal flow, that is we have explicitly chosen the function $U_0(y)$. Then when performing a linear stability analysis considering the onset of convection we wish to slowly increase the Rayleigh number for a given Γ until a marginal mode (with $\Re[s]\equiv\sigma=0$) appears. This value of the Rayleigh number is then the value for the onset of convection for the given set Γ and hence it is for a *specific* value of k. In other words, it is the value of the Rayleigh number needed for the disturbance with wavelength $2\pi/k$ to onset. Since the onset value of Ra is a function of k, in order to find the *critical* Rayleigh number we must minimise the Rayleigh number over all possible disturbances; that is over all k. The value of k that yields the critical value of the Rayleigh number for onset is the critical wavenumber, k_c, and we denote the frequency of this mode by ω_c.

β	k_c	Ra_c	ω_c
10^3	6.216051	8107.860409	-64.071201
10^4	14.851700	1.639668×10^5	-322.242706
10^5	32.645162	3.491914×10^6	-1517.564194

Table 4.1: Critical results for the Rayleigh number, wavenumber and frequency for various β in the case $U_0 = 0$ and $Pr = 1$.

The method described in the previous paragraph will be used in the following two sections and also in parts of chapter 5 where we consider various forms for $U_0(y)$ acquired from non-linear simulations of the problem. In order to check the Chebyshev collocation code described above reproduces familiar results we first briefly consider the case of $U_0 = 0$ here, which is equivalent to the $Re = 0$ case. We refer to this as the *base case* since it has been comprehensively investigated in previous work on the annulus model. We perform the linear stability analysis for this case and the results for a few values of β with $Pr = 1$ are shown in table 4.1. The results in this table agree with those from previous work; for example, Busse & Or (1986). Since the critical Rayleigh number is a function of the Prandtl number, the beta parameter and the Reynolds number we can write $Ra_c = Ra_c(Pr, \beta, Re)$. We then define Ra_c^* to be the critical Rayleigh number in the absence of any zonal flow, that is $Ra_c^* = Ra_c(Pr, \beta, 0)$ for given values of the Prandtl number and the beta parameter. In figure 4.3(a) we have also plotted the form of ζ, ψ and θ for the case where $U_0 = 0$, $\beta = 10^3$ and $Pr = 1$. These plots also match the results from previous work; for example, Busse & Or (1986).

4.3 Results for a linear flow pattern

In this section we choose a form for the zonal flow, which is the annular analogy of the zonal flow chosen in the plane layer model discussed in chapters 2 and 3. We then solve the linear equations (4.49 - 4.50) with this zonal flow to find marginal modes. In section 2.1 we chose a radially dependent linear flow that was greatest in magnitude at the boundaries of the layer and vanished at the centre of the layer. In the plane layer model the radial direction refers to the vertical coordinate z since the layer is thought to be in the polar regions of a planetary interior. The equivalent radial direction in the annulus model is the y-coordinate. Thus we choose

$$U_0 = y - \frac{1}{2}, \tag{4.51}$$

as the form of the zonal flow. We now insert this into equations (4.49 - 4.50) and solve the eigenvalue problem for various parameter regimes using the method described in section 4.2. We work with typical values of the beta parameter, $10^3 \leq \beta \leq 10^5$, which are equivalent to the values of the Ekman number considered in chapters 2 and 3. We vary the Reynolds number so that $0 \leq Re \leq 10000$ and we work with $Pr = 1$.

In figure 4.2 we plot how the critical values of the Rayleigh number, wavenumber and frequency respectively, vary with the Reynolds number for the case of $Pr = 1$. The Reynolds number is represented on a logarithmic axis on all three plots as is the critical Rayleigh number in figure 4.2(a). This is done due to the magnitudes of the parameters involved. We immediately see from figure 4.2(a) that the critical Rayleigh number is larger than Ra_c^* for all non-zero values of Re, for all values of β considered. In fact, the critical Rayleigh number increases monotonically from Ra_c^* as the strength of the zonal flow increases. Therefore the form of the zonal flow discussed in this section, given by equation (4.51), has a stabilising effect on the thermal instability and hence is not favourable for the onset of convection. Figures 4.2(b) and 4.2(c) inform us that increasing the strength of the zonal flow lengthens the azimuthal wavelength and increases the magnitude of the frequency of the modes.

In figure 4.3 we plot the form of the fields for a base case, namely $\beta = 10^3$ where the parameter values can be found in table 4.1. We also plot the fields for the points marked on the plots of figure 4.2. Table 4.2 contains the parameter values used for the plots, as well as those for the next section. Figure 4.3(a) shows the form of the fields in the case of no zonal flow for $\beta = 10^3$ and $Pr = 1$. In this case the mode is symmetric in y and aligned such that heat is transported outward by the rolls since positive ψ corresponds to a roll rotating clockwise. As we increase the zonal flow we see that the rolls are forced to adopt a slanted structure, in line with the zonal flow and hence are no longer symmetric in y. This can be seen in figure 4.3(b). When we increase the zonal flow strength further, in figure 4.3(c), we see increased alignment of the rolls with the zonal flow and the modes no longer fill the entire annular channel. There is a preference for the rolls to localise in the region of the channel where the zonal flow acts in the positive azimuthal direction. Hence

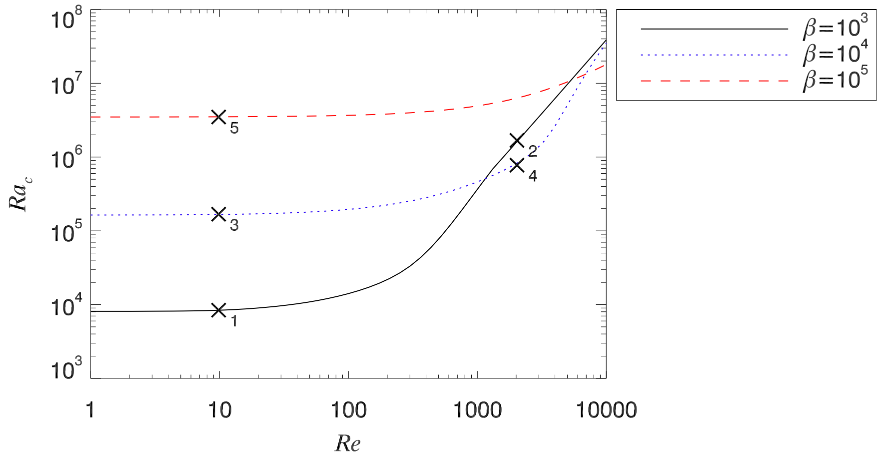

(a) Critical Rayleigh number.

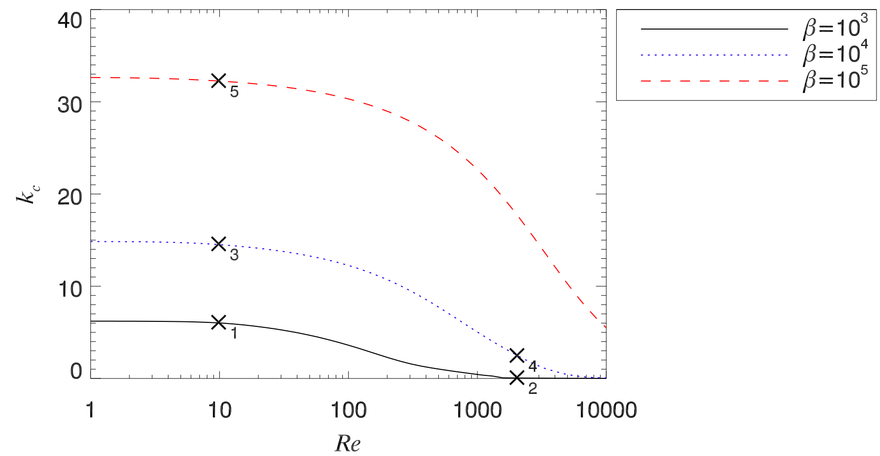

(b) Critical wavenumber.

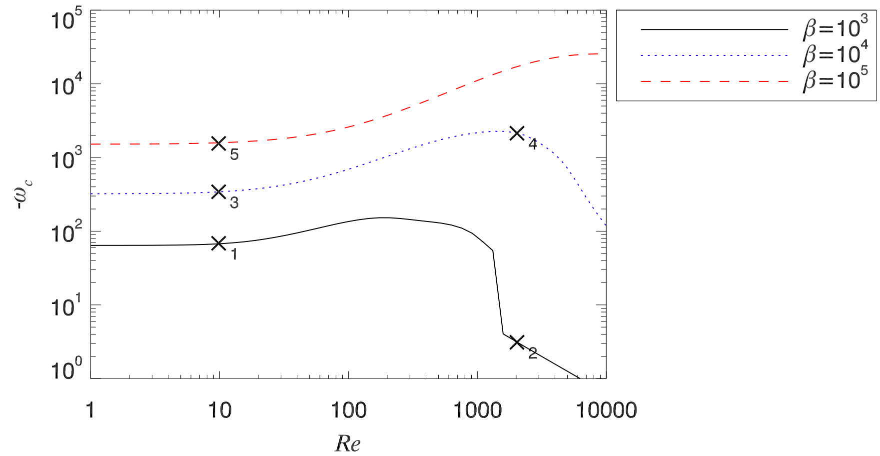

(c) Critical frequency.

Figure 4.2: Plot of how the critical values of the variables vary with zonal flow strength for the linear flow pattern for several values of β and with $Pr = 1$.

the preference is for the disturbances to appear where the zonal flow is prograde. Figures 4.3(d), 4.3(e) and 4.3(f) show field plots for $\beta \neq 10^3$. We see that the same general pattern emerges though for larger β a smaller value of Re is required before the rolls become localised. This can be seen by comparing figures 4.3(b) and 4.3(c) with 4.3(d) and 4.3(e), which are for the same two values of Re but for $\beta = 10^3$ and $\beta = 10^4$ respectively. In the case of $\beta = 10^5$, the roll has already become fully localised at $Re = 10$ as shown by figure 4.3(f).

In shear flow instabilities the modes often peak where the phase velocity is equal to the flow velocity; that is at a specific value of y called the 'critical level'. The localisation of the convective instability in this flow pattern occurs for the same reason. We can see this be considering the left-hand-side of equation (4.31) where there is a factor of

$$\mathrm{i}\omega Pr + \mathrm{i}k Pr Re U_0, \tag{4.52}$$

multiplying $\hat{\theta}$. For large values of Re this will cause $\hat{\theta}$ to be small unless the expression in equation (4.52) vanishes resulting in

$$\frac{\omega}{k} = -ReU_0(y_c), \tag{4.53}$$

where y_c is the value of y at the critical level. From table 4.2 we can take the values of the Reynolds number, wavenumber and frequency for point $\times_4$, for example, and insert them into equation (4.53). The phase speed from the left-hand-side of the equation is then approximately -844. From the definition of the flow profile in equation (4.51) we then find that $y_c \approx 0.92$ for this value of the phase speed. The instability, as seen in figure 4.3(e), is certainly located close to $y = y_c$, near to the inner annular boundary, as expected. This argument does not hold for all modes but it does serve as a possible explanation of how a localisation of the instability can occur. It could also be the case that the modes are simply localising near to the boundaries in order to minimise the effect of the shear.

We conclude that although a similar form of the zonal flow destabilised the system in the plane layer case (see chapters 2 and 3), we find that in the annulus problem a linear form for the zonal flow is stabilising. In the plane layer case the zonal flow was generated by lateral variations in the temperature profile, which gave rise to the possibility an extra energy source via a baroclinic instability. In the annulus model a barotropic instability

Point	β	Re	M	k_c	Ra_c	ω_c
$\times_1$	10^3	10	–	6.017626	8398.757029	-67.549019
$\times_2$	10^3	2000	–	0.049002	1.579294×10^6	-3.175682
$\times_3$	10^4	10	–	14.509451	1.665828×10^5	-342.314153
$\times_4$	10^4	2000	–	2.560117	8.110634×10^5	-2160.567526
$\times_5$	10^5	10	–	32.247225	3.515021×10^6	-1585.925208
$\times_6$	10^5	1	3	32.565198	3.494965×10^6	-1527.246378
$\times_7$	10^5	1	4	32.604833	3.493438×10^6	-1522.031853
$\times_8$	10^5	1	5	32.622686	3.492734×10^6	-1520.071030
$\times_9$	10^5	10	3	31.947182	3.510795×10^6	-1739.925827
$\times_{10}$	10^5	10	4	31.761350	3.512503×10^6	-1703.003862
$\times_{11}$	10^5	10	5	31.727903	3.511715×10^6	-1667.319081
$\times_{12}$	10^5	500	3	21.434026	2.217932×10^6	-11273.527962
$\times_{13}$	10^5	500	4	14.709166	9.924381×10^5	-7623.141583
$\times_{14}$	10^5	500	5	8.127157	-4.027874×10^6	-2686.160279
$\times_{15}$	10^3	10	3	6.008849	7321.798057	-71.541211
$\times_{16}$	10^3	10	4	6.201079	8040.135239	-69.093637
$\times_{17}$	10^3	10	5	6.209197	8277.020421	-67.707283
$\times_{18}$	10^4	90	3	9.437706	6.242689×10^4	-890.211187
$\times_{19}$	10^4	90	4	9.997292	2.095357×10^4	-789.561651
$\times_{20}$	10^4	90	5	11.070873	-1.620262×10^4	-713.785013
$\times_{21}$	10^4	800	3	8.074829	-6.982823×10^6	-926.266122
$\times_{22}$	10^4	800	4	10.708329	-1.704844×10^7	-698.393958
$\times_{23}$	10^4	800	5	13.314943	-2.962544×10^7	-561.411438

Table 4.2: Parameter values for the plots of figures 4.3, 4.5, 4.6 and 4.7.

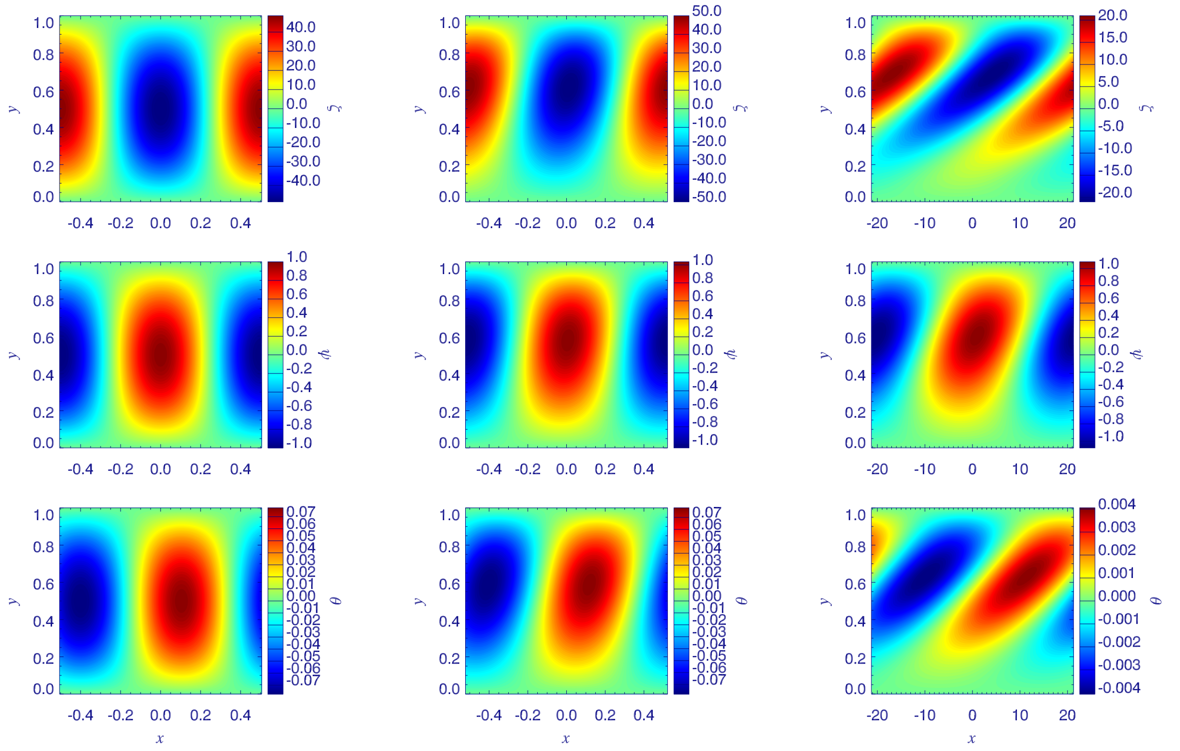

(a) $Re = 0, \beta = 10^3$ (b) $\times_1$ (c) $\times_2$

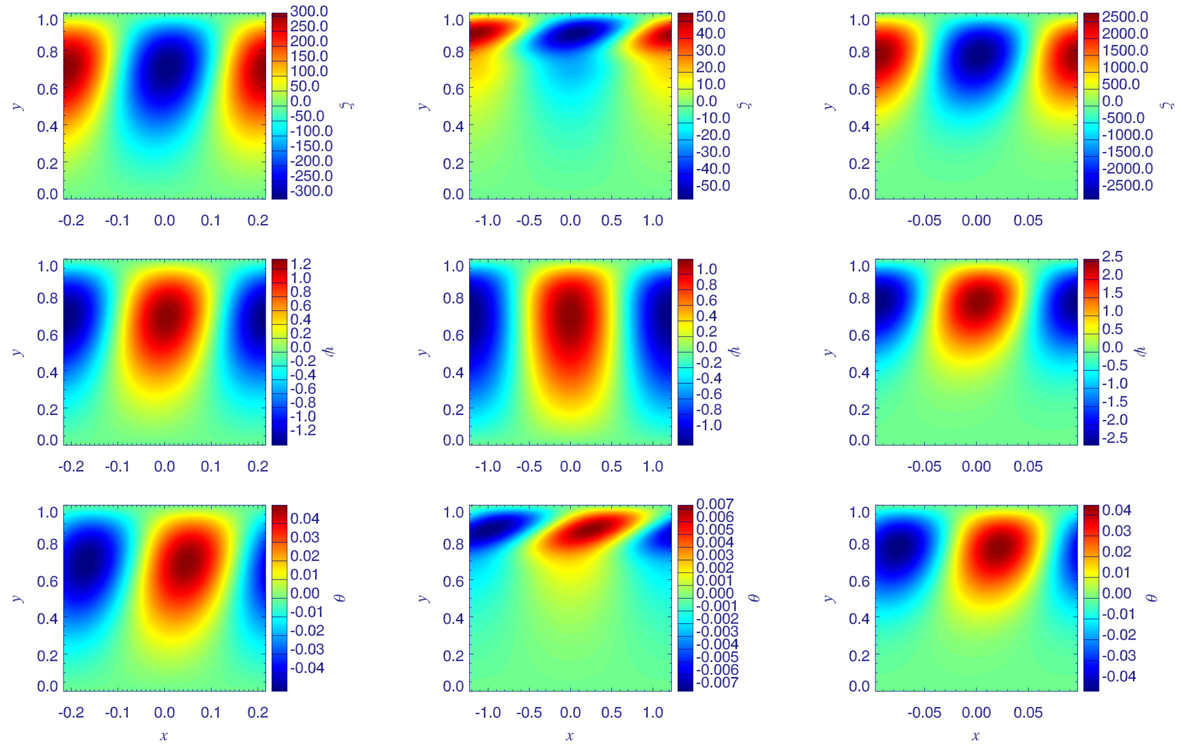

(d) $\times_3$ (e) $\times_4$ (f) $\times_5$

Figure 4.3: Contour plots, with $Pr = 1$, of the fields for a base case and for the fields corresponding to the points in parameter space marked on the plots of figure 4.2.

is possible due to the horizontal shear in the basic state as we discussed in section 4.2. However, for the linear flow pattern discussed in this section Rayleigh's criterion given by equation (4.44) is not satisfied since $U_0'' = 0$ and β is a (non-zero) constant. Therefore the system is not susceptible to barotropic instabilities and buoyancy with a positive Rayleigh number is necessary for instability. This serves to explain why essentially analogous forms of the zonal flow affect the two models' stability in such different ways.

4.4 Results for a sinusoidal flow pattern

In this section we choose a sinusoidal form for the zonal flow and solve the linear equations (4.49 - 4.50) looking for marginal modes. A sinusoidal flow is studied in the hope that it can act as a simple model for the form of the jets seen most famously on Jupiter, but also other gas giant planets.

In order to crudely model this pattern of jets we envisage a zonal flow which periodically alternates between positive and negative maxima and minima of equal magnitude. This produces a pattern of periodically repeating regions of positive and negative zonal flow, which we refer to as prograde and retrograde jets respectively. The only boundary condition concerned with the azimuthal flow is the stress-free condition, which demands that $U_0' = 0$ on $y = 0$ and $y = 1$. Hence we choose

$$U_0 = \cos(M\pi y), \tag{4.54}$$

as the form of the zonal flow. By choosing this form for U_0 we have introduced a new parameter, $M \in \mathbb{N}$, to the problem, which controls the number of jets. Therefore the critical Rayleigh number in this section will depend on M as well as the aforementioned parameters so that $Ra_c \equiv Ra_c(Pr, \beta, Re, M)$ where we continue to use Ra_c^* to denote the case in the absence of the zonal flow so that $Ra_c^* = Ra_c(Pr, \beta, 0, M)$. We insert the form of the zonal flow, given by equation (4.54), into equations (4.49 - 4.50) and solve the eigenvalue problem for various parameter regimes using the method described in section 4.2. We work with moderate values for the beta parameter $10^3 \leq \beta \leq 10^5$, Reynolds numbers $0 \leq Re \leq 10000$ and $Pr = 1$. We also vary the number of jets: $3 \leq M \leq 5$. We choose this range for M since we wish to look at parameter space that is of interest to the jets of Jupiter, which is known to possess multiple jets. The critical values of the

Rayleigh number, wavenumber and the frequency are plotted in figures 4.4(a), 4.4(b) and 4.4(c) respectively, for various values of β and M in the case of $Pr = 1$. The Reynolds number is represented on a logarithmic axis on all three plots as is the critical Rayleigh number in figure 4.4(a). This is done due the magnitudes of the parameters involved.

From figure 4.4(a) there are several observations to note. Firstly we see that, for a given $\{\beta, M\}$, as Re is increased from zero the value of Ra_c decreases from the value of the critical Rayleigh number in the absence of the zonal flow. In other words, $Ra_c < Ra_c^*$ for non-zero values of the Reynolds number. Therefore the sinusoidal form of the zonal flow has a destabilising effect on the system and hence it aids the onset of convection. It is also apparent that this destabilisation persists for all values of β and M tested. This result is in contrast with that for a linear flow pattern, discussed in section 4.3, where increasing the strength of the zonal flow always had a stabilising effect.

Secondly, we note that as the Reynolds number is increased further there is a sharp transition region where we pass smoothly through a bifurcation in all cases of $\{\beta, M\}$ where Ra_c becomes negative. Thus, unlike the form of the zonal flow discussed in section 4.3, the sinusoidal zonal flow admits instability with negative Rayleigh numbers. We see that for all combinations of β and M plotted the critical Rayleigh number becomes negative for a large enough value of the Reynolds number. The regimes with negative critical Rayleigh numbers are stably stratified and hence the instability is driven by the shearing of the zonal flow.

Thirdly, we note that, in general, in order to aid convection there is a preference for smaller and larger values of β and M, respectively. This preference is also true of the transfer to the shear-dominated modes. This can be seen in figure 4.4(a) where the coloured lines (larger β) and solid lines (smaller M) appear, almost exclusively, at larger values of the critical Rayleigh numbers compared with their black, dotted counterparts. The preference for smaller β is expected since we know from the base case that rotation delays the onset of convection so that $Ra_c^*(Pr, \beta_1, 0, M) < Ra_c^*(Pr, \beta_2, 0, M)$ for $\beta_1 < \beta_2$. The more interesting point is that there is a preference for larger values of M. This tells us that a greater number of jets actually aids the onset of convection despite the fact that one might expect the shearing of the jets to hinder the appearance of convection rolls.

In figures 4.5, 4.6 and 4.7 we plot the forms of the fields for the points marked on the plots

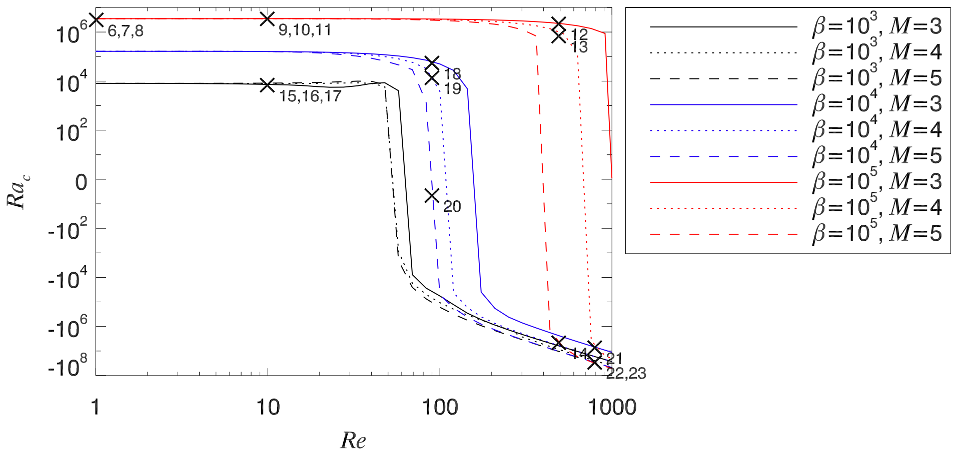

(a) Critical Rayleigh number.

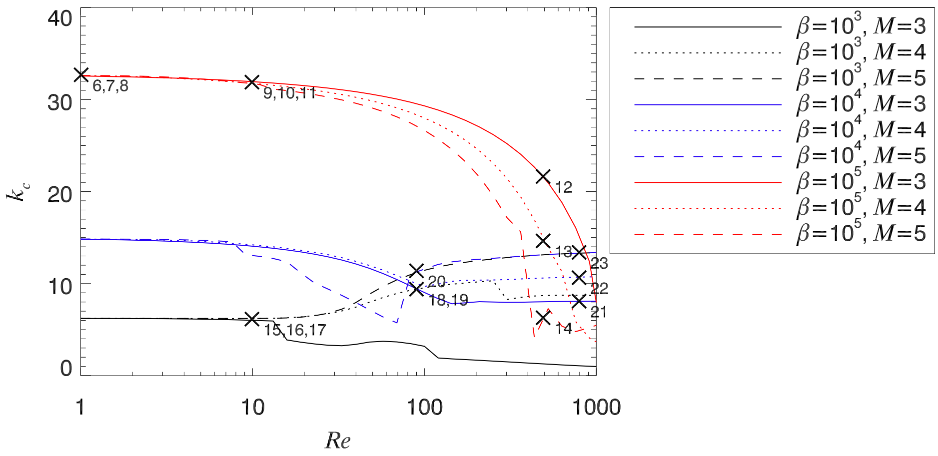

(b) Critical wavenumber.

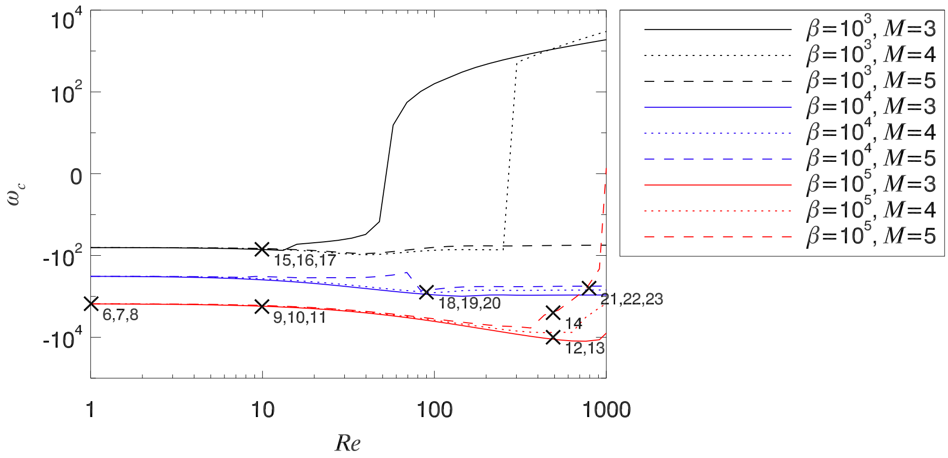

(c) Critical frequency.

Figure 4.4: Plot of how the critical values of the variables vary with zonal flow strength for the sinusoidal flow pattern for several values of β and with $Pr = 1$.

of figure 4.4. In each of the subfigures we plot ζ, ψ and θ. Each row of three subfigures correspond to a particular value of the Reynolds number and each column corresponds to a particular number of jets. The first three rows of plots are for $\beta = 10^5$ followed by a row with $\beta = 10^3$ and two with $\beta = 10^4$. Table 4.2 contains the parameter values used for the plots.

We see that for small values of the Reynolds number (figures 4.5(a), 4.5(b) and 4.5(c)) the addition of the zonal flow has little effect on the form of the fields so that these figures are comparable with the base case of no zonal flow shown in 4.3(a). However, we note that the form of the fields is no longer symmetric and there appears to be the start of a localisation of the convection. As the Reynolds number is increased we are able to see clearly from the next row of figures (4.5(d), 4.5(e) and 4.5(f)) that the fields have indeed become localised. The convection now onsets in regions with prograde jets, which are found where U_0 takes its maximum value. Therefore we see from the form of the zonal flow given by equation (4.54) that the location of the prograde jets is given by $\cos(M\pi y) = 1$. Hence for $M = 3$ and $M = 4$ a prograde jet is located at $y = 2/3$ and $y = 1/2$, respectively. For $M = 5$ there are two prograde jets located at $y = 2/5$ and $y = 4/5$. We see from figures 4.5(d), 4.5(e) and 4.5(f) that the instability has localised to onset at these locations. As the Reynolds number is increased further we see the same localisation of the modes at these positions in figures 4.6(a), 4.6(b) and 4.6(c).

We now consider figures 4.6(d), 4.6(e) and 4.6(f) where the beta parameter has been decreased to $\beta = 10^3$. We see that the same localisation of the modes at the location of prograde jets occurs, although less strongly enforced now that the rotation is weaker. This can been seen by comparing figures 4.6(d), 4.6(e) and 4.6(f) with 4.5(d), 4.5(e) and 4.5(f), which are for the same value of the Reynolds number but have a difference in the beta parameter of two orders of magnitude. The localisation is clearly stronger in the larger β case. Figures 4.7(a), 4.7(b) and 4.7(c), where now $\beta = 10^4$, are similar to the $\beta = 10^3$ case. However, once the Reynolds number becomes large enough for negative critical Rayleigh numbers to be permitted the modes become dominated by the shear as show in figures 4.7(d), 4.7(e) and 4.7(f). The instability is now largely correlated with the form of the zonal flow and thus the modes appear as sinusoidal disturbances themselves.

In order to understand why the instabilities localise on the prograde jets in the convective

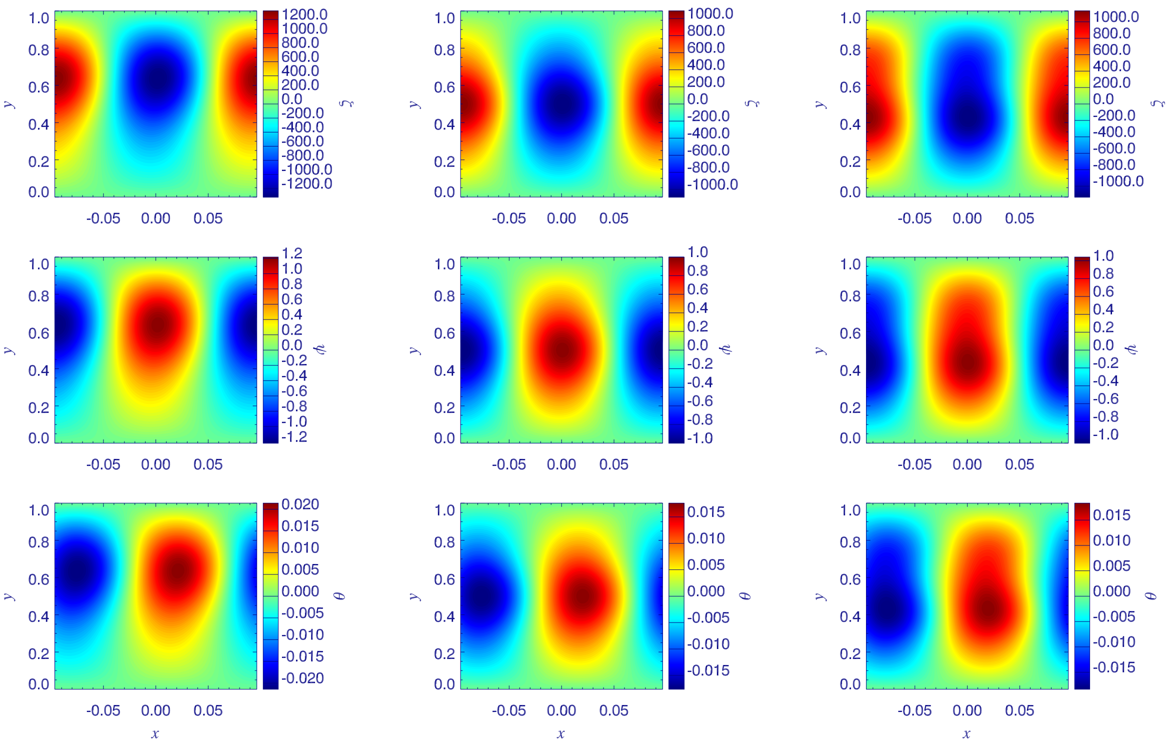

(a) $\times_6$ (b) $\times_7$ (c) $\times_8$

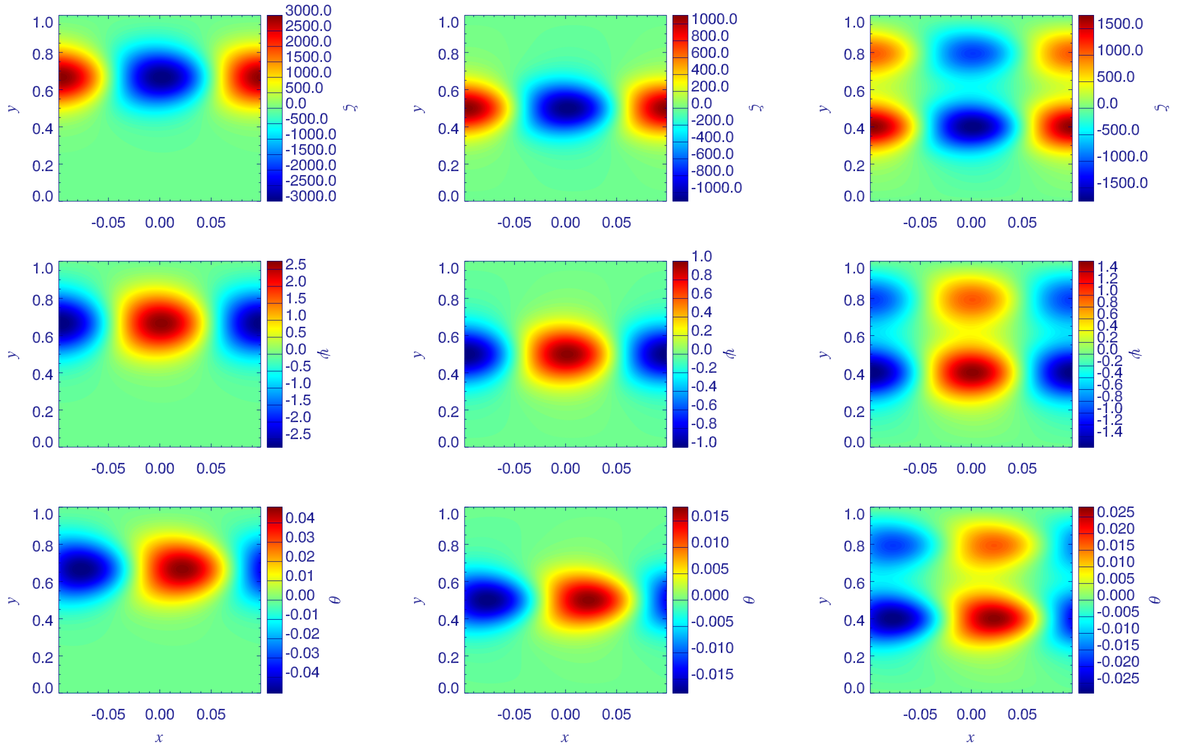

(d) $\times_9$ (e) $\times_{10}$ (f) $\times_{11}$

Figure 4.5: Contour plots, with $Pr = 1$, of the fields corresponding to the points in parameter space marked on the plots of figure 4.4.

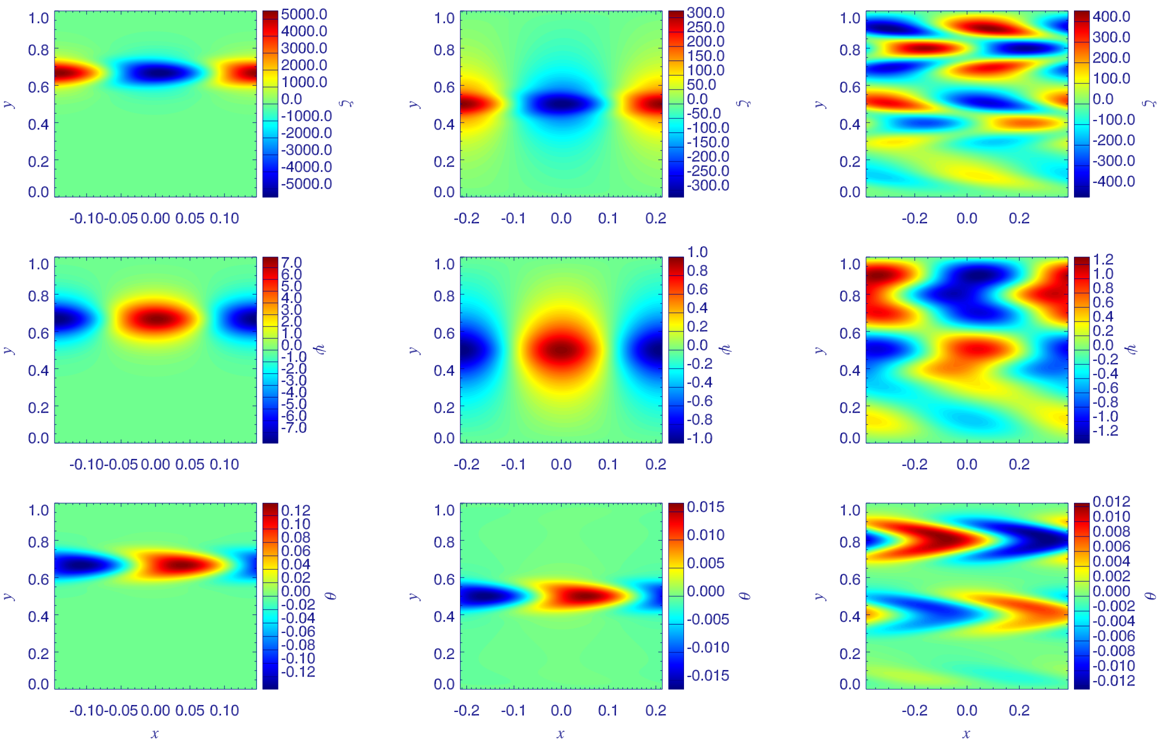

(a) $\times_{12}$ (b) $\times_{13}$ (c) $\times_{14}$

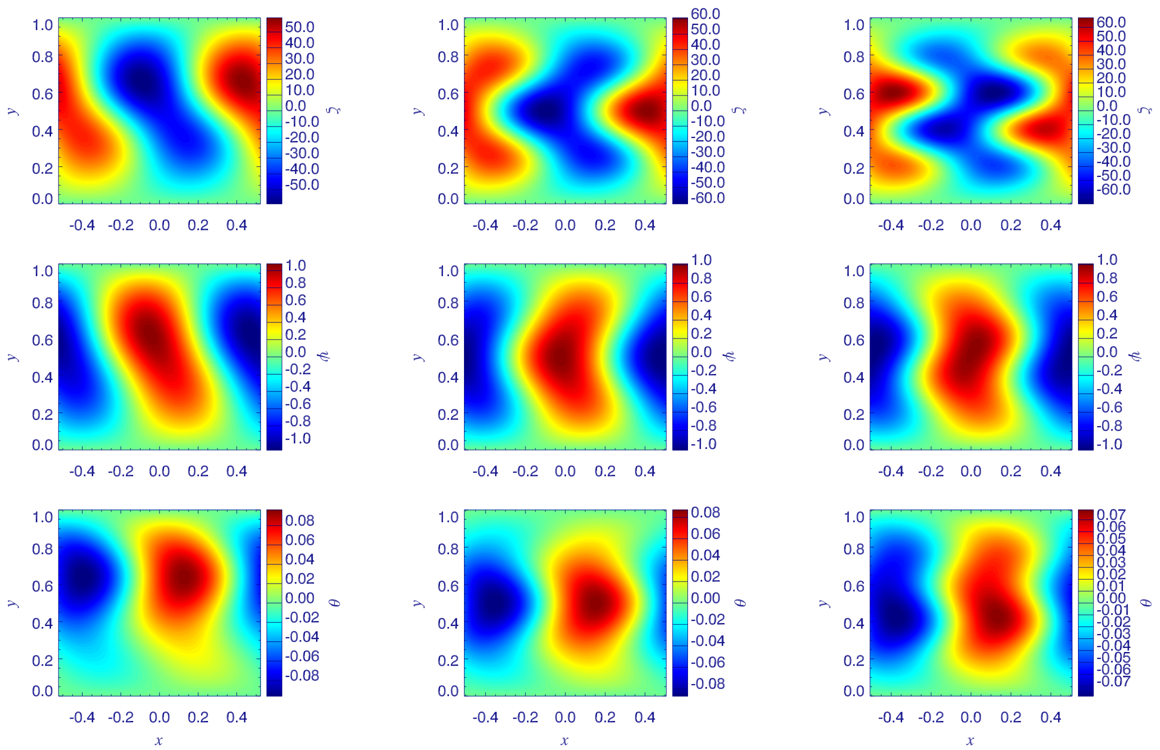

(d) $\times_{15}$ (e) $\times_{16}$ (f) $\times_{17}$

Figure 4.6: Contour plots, with $Pr = 1$, of the fields corresponding to the points in parameter space marked on the plots of figure 4.4.

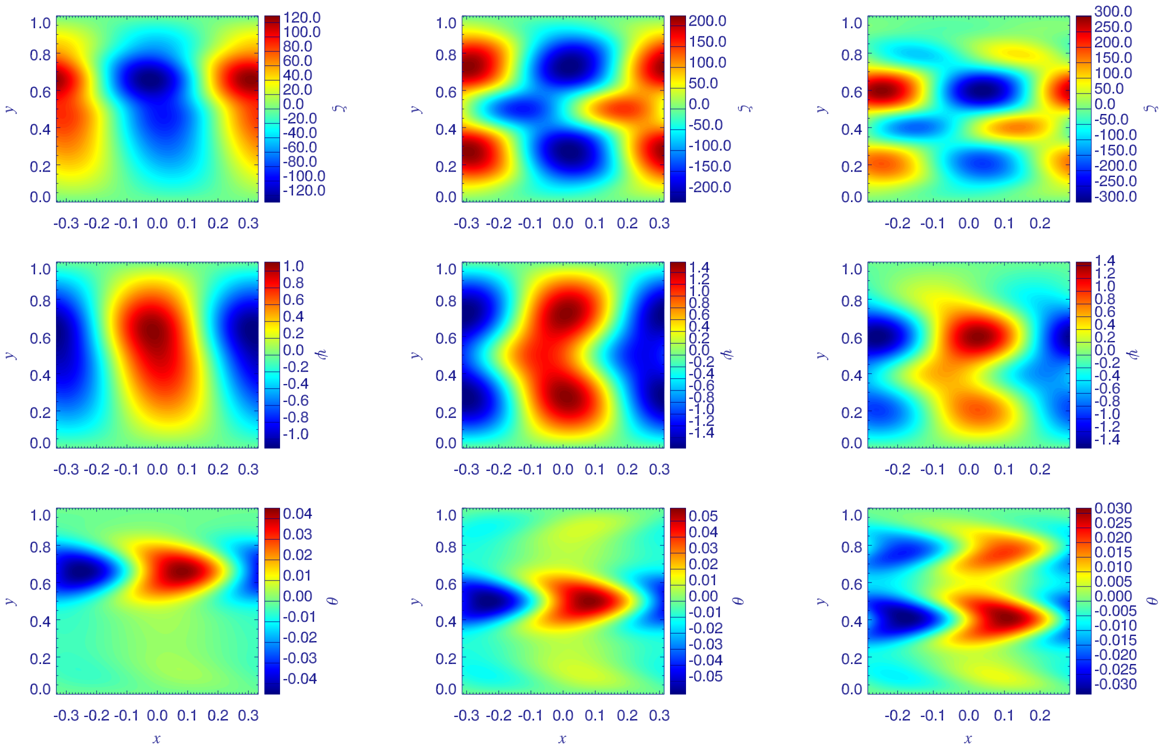

(a) $\times_{18}$ (b) $\times_{19}$ (c) $\times_{20}$

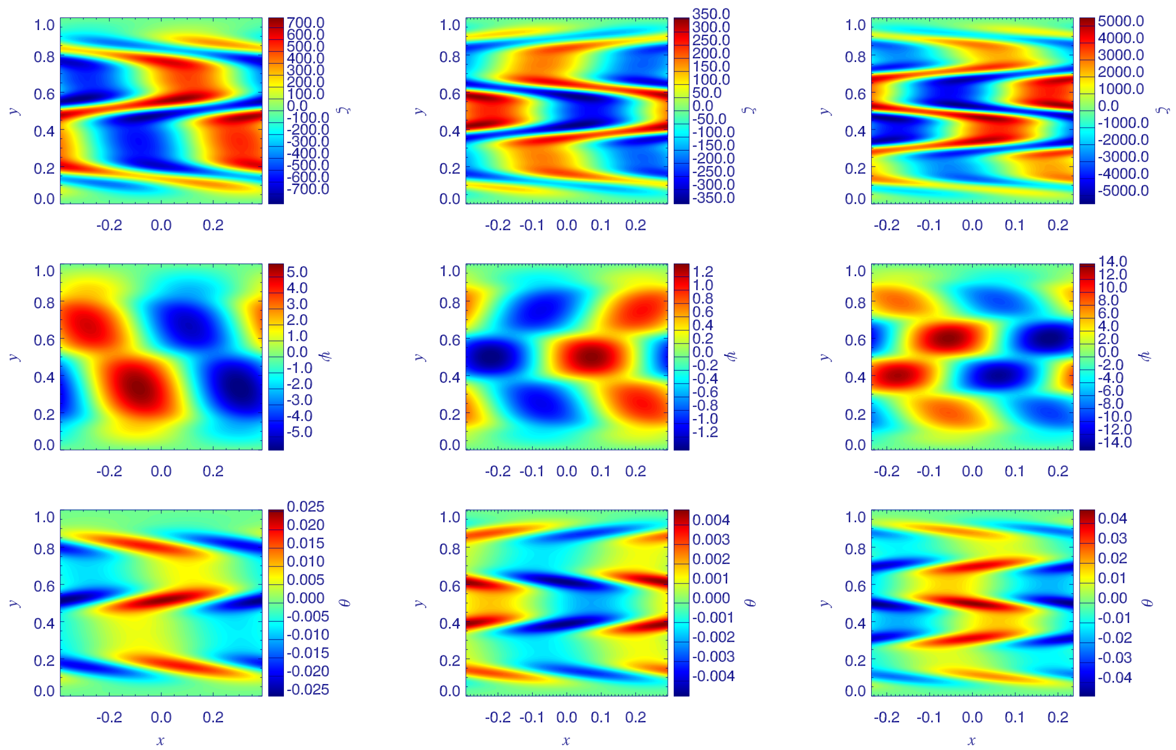

(d) $\times_{21}$ (e) $\times_{22}$ (f) $\times_{23}$

Figure 4.7: Contour plots, with $Pr = 1$, of the fields corresponding to the points in parameter space marked on the plots of figure 4.4.

regime it is useful to return to the potential vorticity defined in equation (4.40). Potential vorticity gradients are thought to play an important role in determining the jet structure seen in many astrophysical bodies. The asymmetry of the eastward and westward jets seen in figure 1.3 may be controlled by the tendency of the fluid to organise itself so that the PV takes the form of a step function, known as the 'PV staircase' (Marcus & Lee, 1998). The staircase forms since the mixing of PV is blocked at the staircase steps and then bands with homogenised PV are separated by regions with infinite PV gradient. Eastward and westward jets form where the gradient of the PV attains its maxima and minima respectively. Read *et al.* (2006, 2009) presented evidence that the PV gradient may change sign in the atmospheres of Jupiter and Saturn suggesting that barotropic instabilities could affect the zonal flows there.

The basic state potential vorticity given by the basic state terms in equation (4.40) is $q_0 = -(ReU_0' + \beta y)$. This shows that we can attribute the origin of the basic state PV to the rotation and the zonal flow. Hence the PV is a combination of the planetary (due to the solid body rotation of the system) and fluid (due to the zonal flow of the basic state) vorticity. There are then three cases we can consider:

- $q_0 = 0 \; \forall y \Rightarrow \beta = 0 = Re$ so that there is no rotation and no zonal flow and hence no planetary nor fluid vorticity in the basic state. This results is the classic problem of Rayleigh-Bénard convection (see section 1.4).

- $q_0 = -\beta y \Rightarrow Re = 0$ so that there is no zonal flow and hence there is planetary but no fluid vorticity in the basic state. This corresponds to the problem originally studied by Busse (1970).

- $q_0 = -(ReU_0' + \beta y)$ so that there is both rotation and zonal flow and hence there is both planetary and fluid vorticity in the basic state. This yields the problem we are considering in this chapter.

In general, the gradient of the basic state potential vorticity is then

$$\frac{\mathrm{d}q_0}{\mathrm{d}y} = -(ReU_0'' + \beta), \tag{4.55}$$

which appears in equation (4.26) as the 'effective rotation' of the system. We know from the original analysis performed by Busse that the addition of rotation delays the onset of convection so that a larger rotation rate results in a higher critical Rayleigh number; recall equation (4.46). Also in the case studied by Busse (1970), the PV gradient is constant (and equal in magnitude to β) and hence there is no position in the annulus that is preferred for instability. With the addition of a basic state zonal flow and thus a basic state *fluid* vorticity it is possible to counteract the stabilising effect of rotation depending on the form of U_0 chosen. By using the definition of U_0 from equation (4.54) we find that

$$\frac{\mathrm{d}q_0}{\mathrm{d}y} = ReM^2\pi^2\cos(M\pi y) - \beta. \tag{4.56}$$

Due to the form of U_0 the PV gradient is no longer a constant and is now a function of y unlike in the case studied by Busse (1970). Hence the magnitude of the PV gradient may vary considerably at different radii of the annular channel. The convective instability attempts to localise at the radii where the magnitude of the PV gradient is smallest since regions with a lower 'effective rotation' are preferable for instability. This naturally results in a lowering of the critical Rayleigh number of the whole system. We see from equation (4.56) that the basic state PV gradient has its minima when $\cos(M\pi y) = 1$, which implies that $y = 2m/M$ for $m \in \mathbb{N}_0$ in general. However, in reality the fact that the fluid is bounded between $y = 0$ and $y = 1$ means that only a finite number of these solutions are permissible. The condition that the PV gradient has its minima when $\cos(M\pi y)$ has its maxima ensures that the instability onsets at the location of the prograde jets for $Re > 0$. This explains how the addition of a sinusoidal zonal flow allows for the reduction of the critical Rayleigh number and the localisation of the instability as seen in the numeric results. We have been considering only cases where $Re > 0$. However, the above analysis is also true for $Re < 0$ albeit with adjustments in the location of the instability. If $Re < 0$ then the magnitude of the basic state PV of equation (4.56) attains its minima when $\cos(M\pi y) = -1$ so that the instability instead onsets at the location of the retrograde jets.

The above discussion is relevant to the convective modes for which the Rayleigh number is positive. In this case the shear is able to reduce the magnitude of the PV gradient at certain locations of the annular layer. However, once Re becomes large enough we have seen how the instability becomes dominated by the shear. This occurs because the sinusoidal form of the zonal flow satisfies Rayleigh's criterion (from section 4.2) and hence barotropic instabilities are possible. In fact, for large enough β, the transition between convective and shear-dominated modes occurs when the shear is large enough to allow the PV gradient to vanish somewhere in the domain. This is equivalent to Rayleigh's criterion being satisfied. From equation (4.56) we see that (for $Re > 0$) $\mathrm{d}q_0/\mathrm{d}y$ vanishes for the smallest value of Re when $\cos(M\pi y) = 1$ and $\beta = ReM^2\pi^2$. Therefore we can predict that

$$Re_* \approx \beta/M^2\pi^2, \tag{4.57}$$

where Re_* is the value that the Reynolds number must exceed for shear-dominated modes to be most unstable. Equation (4.57) gives an expression for Re_* that is inversely proportional to M^2 and thus explains why systems with a greater number of jets transfer to shear-dominated instabilities at lower values of the Reynolds number. This was observed in the results of figure 4.4(a). The expression given by equation (4.57) is only an approximation since we are implicitly assuming that the rotation and shear are strong enough to dominant over other terms in the governing equations. In the homogeneous, inviscid case the condition holds exactly and reduces to Rayleigh's criterion for barotropic instability. In our work viscous effects are small but the buoyancy is large meaning that equation (4.57) is only an approximation for the onset of shear instabilities. For $\beta = 10^3$ equation (4.57) predicts that $Re_* \approx (11.258, 6.333, 4.053)$ for $M = (3, 4, 5)$. From figure 4.4(a) we see that the transition to instabilities dominated by the shear do not arise until Re is approximately an order of magnitude larger than Re_*. However, for cases with stronger rotation, for example $\beta = 10^5$, equation (4.57) gives $Re_* \approx (1125.8, 633.3, 405.3)$ for $M = (3, 4, 5)$. When these values are compared with the relevant plots in figure 4.4(a) it is clear that the predicted values agree very well.

We also note that the linear form of the zonal flow discussed in section 4.3 does not alter the gradient of the basic state PV from Busse (1970). This is because $U_0'' = 0$ for a linear zonal flow. Hence the effective rotation remains constant throughout the annular layer in that case. Therefore, as expected and as observed in the numerics of section 4.3, we do not see any reduction of the critical Rayleigh number in the case of a linear zonal flow. Finally we also note that there are, of course, infinitely many choices for the form of the zonal flow, $U_0(y)$. The results presented in this chapter only discuss two possibilities for U_0 and it is possible to envisage a more complicated zonal flow, which better matches the pattern of the jets seen in astrophysical bodies such as Jupiter. In fact, in chapter 5 we acquire zonal flows from the integration of the non-linear equations; these zonal flows therefore take more realistic forms than the flows considered in this chapter. Hence in the next chapter we are able to consider the linear problem with the form of $U_0(y)$ given by the zonal flows generated in the non-linear theory.

Chapter 5

A non-linear theory for the annulus model

We have investigated the linear theory of convection in the annulus with an imposed zonal flow in chapter 4. With the insight given by the linear theory where we found that azimuthal zonal flows with certain y-structures could aid the onset of convection, in this chapter we solve the full non-linear equations without an imposed zonal flow. A drawback of the linear model of chapter 4 was that there were infinitely many forms that the zonal flow, $U_0(y)$, could take. In this chapter we expect to find strong zonal flows appearing as we integrate forward in time, which arise due to the non-linear Reynolds stresses. Hence we are able to use the zonal flows arising in the non-linear theory as an informed choice for the form of the basic state zonal flows of the linear theory, which we also consider in this chapter. However, we first discuss previous work undertaken on zonal flows in the field of planetary science.

Recall that our interest in zonal flows originates from a desire to better explain various phenomena observed in geophysical and astrophysical bodies. The large zonal flows found in the atmospheres of the gas giants as well as planetary cores are thought to be driven by the interaction of convection and rotation. Jupiter, for example, as we discussed in chapter 1 has a banded structure of jets, made up of alternating prograde and retrograde zonal flows (Limaye, 1986; Porco *et al.*, 2003). This pattern extends over the whole planet and the zonal flows are considerably stronger than the radial convection. Although the convection in both the Jovian atmosphere and the Earth's outer core will be affected by their respective magnetic fields, an understanding of the non-magnetic problem can provide insight to the physical structures observed. The depth to which the zonal flows extend in Jupiter's atmosphere is not known, though there is evidence to suggest that flows are considerably weaker in the core compared with the surface (Starchenko & Jones, 2002). Busse (1976) suggested a model for convection in the Jovian atmosphere where zonal flows are not confined to the surface. The difficulties in modeling the interiors of the major planets has been discussed by Yano (1998).

As we mentioned at the start of chapter 4, the annulus model provides a simplified model for convection in a spherical shell, which is relevant to planetary science. Non-linear simulations in the more physically realistic spherical shell geometry have been performed in previous work (Gilman, 1977, 1978a,b; Zhang, 1992; Tilgner & Busse, 1997; Grote & Busse, 2001; Christensen, 2001, 2002; Busse, 2002; Heimpel *et al.*, 2005). Non-linear simulations specifically using the Busse annulus have also been presented (Brummell & Hart, 1993; Jones *et al.*, 2003; Rotvig & Jones, 2006). Recall from chapter 4 that the quasi-geostrophic approximation (QGA) can be used in order to reduce three dimensional systems to two dimensional systems. The essence of the QGA is to assume that the vertical vorticity is constant in the coordinate parallel to the rotation axis, z. This assumption can be justified by the rapid rotation of the system (Gillet & Jones, 2006) and it consequently leads to the horizontal velocity components also being independent of z. Hence there is a suppressed z-structure throughout the system despite the fact that the original assumption cannot be derived in any asymptotic limit. The annulus model is one such quasi-geostrophic model taking advantage of a strong Coriolis force to reduce the dimension of the system. Other quasi-geostrophic models have been investigated (Gillet & Jones, 2006; Rotvig, 2007) but we continue to focus on the annulus model here.

Laboratory experiments such as those undertaken by Busse & Carrigan (1976); Manneville & Olson (1996); Aubert *et al.* (2001) have also been performed. A difficulty when performing experiments can be replicating the effect of gravity, which should, of course, act radially inwards. This issue is resolved by using the centrifugal acceleration to mimic gravity. Since the centrifugal acceleration acts radially outwards the inner spherical (or cylindrical) surface must be cooled rather than heated. Zonal flows are found, thus showing that they can occur naturally in such experiments.

Zonal flows are a common feature of the aforementioned previous work when performing simulations. The nature and dynamics of the zonal flows found have varied in the previous work due to different geometries, conditions and parameter regimes being used. Early pioneering simulations of rotating convection in spherical shells were undertaken by Gilman (1977, 1978a,b). These non-linear three-dimensional simulations were performed for slowly rotating systems, relevant to the Sun, where the Coriolis force is not as significant as in rapidly rotating systems such as the Earth's core and planetary atmospheres. However, Gilman (1977) did find influence of the Coriolis force when the driving was weak enough. Rapidly rotating three-dimensional simulations in spherical shells were performed by Zhang (1992), who considered the generation of zonal flows by the Reynolds stresses. With the vast improvement in computation power over the last two decades further simulations were undertaken (Tilgner & Busse, 1997; Aurnou & Olson, 2001; Christensen, 2001, 2002; Busse, 2002; Heimpel *et al.*, 2005). These simulations produced strong zonal flows with Rossby numbers of the correct order of magnitude, which are driven by the Reynolds stresses. Interestingly both steady and oscillatory zonal flows were found resulting in the discovery of a 'bursting phenomenon' (Grote & Busse, 2001).

The bursting phenomenon, investigated within the annulus model by Rotvig & Jones (2006), refers to the observation that convection can occur as short-lived bursts rather than the system evolving into a quasi-steady equilibrium. These bursts of convection are currently thought to be a result of a competition between the zonal flow, which disrupts convection, and the fact that in the absence of zonal flow the system favours convection as a method of heat transport. When the zonal flow is small in magnitude, the convection is able to build up and efficiently transport heat radially outwards. However, the velocity fluctuations associated with the convection drive large-scale zonal flows, which then hinder convection and can in fact cause it to cease. With the convection depleted the zonal flow has lost its source of energy and therefore it too reduces in magnitude, whereby the process can repeat.

A failure of some of the three-dimensional simulations discussed above is their inability to produce a multiple jet structure of the zonal flow. The reason for this, as discussed by Jones *et al.* (2003), is that in order to produce multiple jets very low values of the Ekman number, or equivalently, very large values of β, are required. Due to numerical difficulties the fully three-dimensional models have often been unable to achieve the rotation rate required, though this is not always the case (Heimpel *et al.*, 2005). The asymptotic model discussed by Abdulrahman *et al.* (2000), performed in the limit of rapid rotation ($\beta \to \infty$), is able to produce multiple jets though it is only valid close to critical. Multiple jet solutions are relevant to the strongly banded structure seen on the gas giant planets and hence to the linear model with a sinusoidal zonal flow that we discussed in section 4.4. The jet width is believed to be controlled by the Rhines scaling theory (Rhines, 1975) where the 'Rhines length' is proportional to $\beta^{-1/2}$. Heimpel *et al.* (2005) discuss a model in a thin spherical shell, which is capable of reproducing both multiple jets at high-latitudes and strong equatorial flows. The idea is that there is a separation of the types of structure possible caused by the bounding bottom surface inside the tangent cylinder. Outside the TC, equatorial structures can be driven by deep model convection due to the domain extending across the whole of the sphere there. However, inside the TC the thinness of the spherical shell creates a shallow layer model with bottom-bounded flow structures such as multiple jets arising.

One of the attractions of the annulus model, as a simplified model for convection in the Jovian atmosphere, lies in its ability to produce both multiple jets and the bursts of convection. For stress-free top and bottom boundaries, it has been shown in the three-dimensional simulations, that stronger zonal flows are produced compared with when no-slip conditions are imposed (Gilman, 1978b; Christensen, 2001). This is also observed in the annulus model (Brummell & Hart, 1993). However, as evidenced by Jones *et al.* (2003), with stress-free boundaries imposed the search for multiple jet solutions is not promising, with only very small windows of parameter regimes producing them. Therefore it seems that stronger zonal flows are associated with stress-free boundaries where multiple jets are less likely to be found. The lack of multiple jet solutions can be overcome by the addition of no-slip boundaries in the form of an Ekman layer bottom friction term in the equations. We discussed the origin of Ekman layers in section 1.3 and we shall derive the relevant term in the next section. When this term is introduced, even with a small magnitude, multiple jets become a feature of many parameter regimes. This was later investigated thoroughly by Rotvig & Jones (2006) for the case where the Prandtl number is unity.

The work of Rotvig & Jones (2006) also showed that it was necessary to omit the aforementioned Ekman layer in order for bursts of convection to be observed. Hence bursting solutions and multiple jet solutions seem to be almost mutually exclusive, occurring simultaneously in only very small windows of parameter space. As we shall see in this work, the existence of the bursting phenomenon also appears to be dependent on the evolution of a mean temperature gradient, which, like the zonal flows, arises due to the non-linear interaction of the small-scale perturbations. This novel result appears to have been overlooked in previous work and adds an extra constraint for the observation of bursting.

This chapter is structured as follows. In section 5.1 we discuss the mathematical setup of the non-linear problem and, in particular, the introduction of the bottom friction term. Then in section 5.2 we explain the numerical method used to solve the non-linear equations and how we define the zonal flow at a given time. We present the results of the simulations in section 5.3 where we expect to find agreement with previous work undertaken by Jones *et al.* (2003); Rotvig & Jones (2006). Finally in section 5.4 we feed the zonal flows and mean temperature gradients obtained in the non-linear simulations back into the linear theory discussed in chapter 4. By doing this we are able to obtain growth rates of disturbances for more realistic zonal flows than those used in the previous chapter. This final section then leads us on to chapter 6 where a simple model is developed showing that a mean temperature gradient is indeed a requirement for bursting convection.

5.1 Mathematical setup

We use the same basic annulus model setup discussed in section 4.1 so that the physical geometry of the model remains unchanged from that in figure 4.1. However we make certain changes in order for this work to be comparable to previous work on the subject of multiple jets. We wish for the simulations we will run to generate zonal flows via the Reynolds stresses and hence without the need for a zonal flow in the basic state of the system. Therefore we set all basic state velocities to zero in the perturbed equations, (4.26 - 4.27), for the non-linear simulations in this chapter. In order for multiple jet zonal flows to evolve we require the effects of an Ekman layer, also known as the bottom friction, to be included in the theory (Jones *et al.*, 2003; Rotvig & Jones, 2006). As we discussed in chapter 1, Ekman layers are thin boundary layers that arise in rotating fluids when rigid boundaries are implemented. The Ekman layer effects can be added to the equation of motion using the definition of the Ekman suction given by equation (1.31). This idea has often been employed in previous work on rotating fluids and the practice is to follow the theory as discussed by Greenspan (1968). In our case we implemented the boundary conditions on the sloped end surfaces by integrating over z (see equations (4.13 - 4.14)). Therefore rather than writing $u_z = \pm\chi u_y$, as we did in chapter 4, we now set

$$u_z = \pm\chi u_y + U_E \tag{5.1}$$

$$= \pm\chi\frac{\partial\psi}{\partial x} \mp D\left(\frac{E}{2}\right)^{1/2}\zeta, \tag{5.2}$$

at $z = \pm L/2$ where we have substituted for U_E from equation (1.31) and used D as our typical length scale. We have ignored terms proportional to χ in the Ekman suction since they are small due to the small sloping boundaries condition: $\chi \ll 1$. By noting that $E = 2D\chi\beta^{-1}/L$ we can now write the Coriolis term of equation (4.13) as

$$-2\Omega[u_z]^{L/2}_{-L/2} = -2\Omega\left(2\chi\frac{\partial\psi}{\partial x} - 2D\left(\frac{D\chi}{L}\right)^{1/2}\beta^{-1/2}\zeta\right). \tag{5.3}$$

Under the same non-dimensionalisation as performed in chapter 4 the expression on the right-hand-side becomes

$$-\frac{4\chi\Omega\nu}{D}\frac{\partial\psi}{\partial x} + \frac{4\chi\Omega\nu}{D}\beta^{-1/2}\left(\frac{D}{L\chi}\right)^{1/2}\zeta, \tag{5.4}$$

and multiplying through by $D^4/\nu^2 L$ to tidy up as we did in chapter 4 we find that

$$-\beta\frac{\partial\psi}{\partial x} + C|\beta|^{1/2}\zeta, \tag{5.5}$$

replaces the $-\beta\partial\psi/\partial x$ term in equation (4.23). Here we have used the definition of β from equation (4.25) and we have introduced the parameter C, defined as:

$$C = \left(\frac{D}{L\chi}\right)^{1/2}. \tag{5.6}$$

Equation (5.5) shows that in our model the requirement of a rigid boundary gives rise to an extra term, due to Ekman suction, via the integration of the Coriolis term of the original equations from chapter 4. We shall typically work with $C \leq 0.5$ when we consider rigid boundaries. However, for stress-free boundaries we explicitly set $C = 0$ throughout since the Ekman suction only arises when the boundaries are no-slip.

We bear in mind what we have discussed above and hence set $U_0 = 0$ and introduce the bottom friction term in equations (4.26 - 4.27) to give

$$\frac{\partial \nabla^2 \psi}{\partial t} + \frac{\partial(\psi, \nabla^2 \psi)}{\partial(x, y)} - \beta \frac{\partial \psi}{\partial x} = -Ra \frac{\partial \theta}{\partial x} - C|\beta|^{1/2} \nabla^2 \psi + \nabla^4 \psi, \tag{5.7}$$

$$Pr \left(\frac{\partial \theta}{\partial t} + \frac{\partial(\psi, \theta)}{\partial(x, y)} \right) = -\frac{\partial \psi}{\partial x} + \nabla^2 \theta. \tag{5.8}$$

We notice that the bottom friction manifests itself as a damping term proportional to $|\beta|^{1/2}$. Also, the damping due to Ekman friction originates from a term proportional to a velocity (see equation (5.1)). Therefore it is often referred to as a *scale-independent* damping since it affects all length scales in the same manner. Conversely, the damping due to viscous diffusion arises from a term proportional to $\nabla^2 \mathbf{U}$ and thus dampens small-scale structures more greatly than large-scale structures. Thus the addition of the effects of rigid boundaries, in the form of the bottom friction, increases the likelihood of the smaller-scale multiple jet solutions arising rather than the large-scale equatorial jets. In equations (5.7 - 5.8), we have also retained the non-linear terms given by the Jacobian terms from equations (4.26 - 4.27), which are the interactions of the small-scale perturbations that generate mean quantities such as the zonal flow and mean temperature gradient. By mean quantities we are referring to quantities that are averaged over the azimuthal, that is the x, coordinate. In fact, for convenience, we shall henceforth refer to the zonal flows and mean temperature gradients together as the ‘mean quantities’. Our boundary conditions remain unchanged from chapter 4 so that we retain

$$\psi = \frac{\partial^2 \psi}{\partial y^2} = \theta = 0, \tag{5.9}$$

on $y = 0$ and $y = 1$. We wish to solve equations (5.7 - 5.8) by numerically integrating forward in time from an initial state.

5.2 Numerical implementation

In this section we discuss the numerical method used to integrate the non-linear equations (5.7 - 5.8) forward in time. The methods that we describe here are discussed in more detail in, for example, Boyd (2001). We first rewrite the equations as

$$\frac{\partial \nabla^2 \psi}{\partial t} - \beta \frac{\partial \psi}{\partial x} + Ra\frac{\partial \theta}{\partial x} + C|\beta|^{1/2}\nabla^2\psi - \nabla^4\psi = -\frac{\partial(\psi, \nabla^2\psi)}{\partial(x,y)} \equiv F, \tag{5.10}$$

$$\frac{\partial \theta}{\partial t} + Pr^{-1}\frac{\partial \psi}{\partial x} - Pr^{-1}\nabla^2\theta = -\frac{\partial(\psi,\theta)}{\partial(x,y)} \equiv H, \tag{5.11}$$

where we have introduced F and H as the right-hand-sides of these equations. We wish to use a pseudo-spectral collocation method by expanding the fields as Fourier components in x and a sine expansion in y. Hence we first write

$$\psi(x,y,t) = \sum_{l=-(N_x-1)}^{N_x-1} \hat{\psi}_l(y,t)e^{-\mathrm{i}lx(2\pi/L_x)}, \tag{5.12}$$

$$\theta(x,y,t) = \sum_{l=-(N_x-1)}^{N_x-1} \hat{\theta}_l(y,t)e^{-\mathrm{i}lx(2\pi/L_x)}, \tag{5.13}$$

where L_x is the length of our domain in the x-direction so that $0 \leq x \leq L_x$. In fact, we choose $L_x = 2\pi$ throughout for simplicity. Also, N_x is the x-resolution. We substitute these expansions into equations (5.10 - 5.11) to give

$$(\partial_{yy} - l^2)\partial_t\hat{\psi}_l + \Big(\mathrm{i}l\beta + C|\beta|^{1/2}(\partial_{yy} - l^2) - (\partial_{yy} - l^2)^2\Big)\hat{\psi}_l - \mathrm{i}lRa\hat{\theta}_l = \hat{F}_l, \tag{5.14}$$

$$\partial_t\hat{\theta}_l - \mathrm{i}lPr^{-1}\hat{\psi}_l - Pr^{-1}(\partial_{yy} - l^2)\hat{\theta}_l = \hat{H}_l, \tag{5.15}$$

where we have dropped the summation signs for convenience. Here we have introduced $\hat{F}_l$ and $\hat{H}_l$, which are the Fourier coefficients of the functions F and H respectively. The boundary conditions of equation (5.9) now become

$$\hat{\psi}_l = \partial_{yy}\hat{\psi}_l = \hat{\theta}_l = 0, \tag{5.16}$$

on $y = 0$ and $y = 1$. We use a semi-implicit scheme by applying a Crank-Nicolson method to the left-hand-side of equations (5.14 - 5.15) and the second order Adams-Bashforth method to the right-hand-side to give

$$\begin{aligned}(\partial_{yy} - l^2)\frac{\hat{\psi}_l^{n+1} - \hat{\psi}_l^n}{\Delta t} + \frac{1}{2}\Big(\mathrm{i}l\beta + C|\beta|^{1/2}(\partial_{yy} - l^2) - (\partial_{yy} - l^2)^2\Big)(\hat{\psi}_l^{n+1} + \hat{\psi}_l^n)& \\ - \frac{\mathrm{i}lRa}{2}(\hat{\theta}_l^{n+1} + \hat{\theta}_l^n) = \frac{1}{2}(3\hat{F}_l^n - \hat{F}_l^{n-1}),&\end{aligned} \tag{5.17}$$

$$\frac{\hat{\theta}_l^{n+1} - \hat{\theta}_l^n}{\Delta t} - \frac{\mathrm{i}lPr^{-1}}{2}(\hat{\psi}_l^{n+1}+\hat{\psi}_l^n) - \frac{Pr^{-1}}{2}(\partial_{yy}-l^2)(\hat{\theta}_l^{n+1}+\hat{\theta}_l^n) = \frac{1}{2}(3\hat{H}_l^n - \hat{H}_l^{n-1}), \tag{5.18}$$

where we have used the notation $\hat{f}_l^n = \hat{f}_l(y, n\Delta t)$ for some function $\hat{f}$. The timestep is given by Δt. We must now choose the y-dependence of our functions where we wish to implement a collocation method. By choosing a sine, rather than Chebyshev, expansion there is the advantage of implicit boundary conditions. Therefore we write

$$\hat{\psi}_l(y,t) = \sum_{m=1}^{N_y-1} \hat{\psi}_{lm}(t)\sin(m\pi y), \tag{5.19}$$

$$\hat{\theta}_l(y,t) = \sum_{m=1}^{N_y-1} \hat{\theta}_{lm}(t)\sin(m\pi y), \tag{5.20}$$

where we see that the boundary conditions of equation (5.16) are automatically satisfied since $\sin(m\pi y) = 0$ for $y = 0$ and $y = 1$ $\forall m \in \mathbb{N}$. We have introduced N_y, which is the y-resolution. As the collocation points, y_j, we use equally spaced points in y-space so that

$$y_j = \frac{j}{N_y}, \quad j = 1, ..., N_y - 1. \tag{5.21}$$

We now substitute the expansions of equations (5.19 - 5.20) into equations (5.17 - 5.18) and evaluate at the collocation points to give

$$\begin{aligned}
\Big[-(l^2+m^2\pi^2) + \frac{\Delta t}{2}\Big(\mathrm{i}l\beta - C|\beta|^{1/2}(l^2+m^2\pi^2) - (l^2+m^2\pi^2)^2\Big)\Big]\hat{\psi}_{lm}^{n+1}\sin(m\pi y_j) \\
- \frac{\mathrm{i}lRa\Delta t}{2}\hat{\theta}_{lm}^{n+1}\sin(m\pi y_j) \quad = \\
\Big[-(l^2+m^2\pi^2) - \frac{\Delta t}{2}\Big(\mathrm{i}l\beta - C|\beta|^{1/2}(l^2+m^2\pi^2) - (l^2+m^2\pi^2)^2\Big)\Big]\hat{\psi}_{lm}^{n}\sin(m\pi y_j) \\
+ \frac{\mathrm{i}lRa\Delta t}{2}\hat{\theta}_{lm}^{n}\sin(m\pi y_j) + \frac{\Delta t}{2}\Big(3\hat{F}_{lm}^{n} - \hat{F}_{lm}^{n-1}\Big)\sin(m\pi y_j),
\end{aligned} \tag{5.22}$$

$$\begin{aligned}
\left(1 + \frac{\Delta t}{2Pr}(l^2+m^2\pi^2)\right)\hat{\theta}_{lm}^{n+1}\sin(m\pi y_j) - \frac{\mathrm{i}l\Delta t}{2Pr}\hat{\psi}_{lm}^{n+1}\sin(m\pi y_j) = \\
\left(1 - \frac{\Delta t}{2Pr}(l^2+m^2\pi^2)\right)\hat{\theta}_{lm}^{n}\sin(m\pi y_j) + \frac{\mathrm{i}l\Delta t}{2Pr}\hat{\psi}_{lm}^{n}\sin(m\pi y_j) \\
+ \frac{\Delta t}{2}\Big(3\hat{H}_{lm}^{n} + \hat{H}_{lm}^{n-1}\Big)\sin(m\pi y_j),
\end{aligned} \tag{5.23}$$

where we have again dropped the summation signs. This system of equations must now be solved for each $l = -(N_x - 1), ..., N_x - 1$. To do this we rewrite the above system of equations in matrix form with j and m as the row and column indices respectively. Equations (5.22 - 5.23) in matrix form are

$$\mathbf{A}\mathbf{X}_l^{n+1} = \mathbf{B}\mathbf{X}_l^{n} + \frac{\Delta t}{2}(3\mathbf{F}_l^{n} - \mathbf{F}_l^{n-1}), \tag{5.24}$$

where

$$\mathbf{X}_l^n = [\hat{\psi}_{l1}^n, ..., \hat{\psi}_{l(N_y-1)}^n, \hat{\theta}_{l1}^n, ..., \hat{\theta}_{l(N_y-1)}^n]^{\mathrm{T}}, \tag{5.25}$$

$$\mathbf{F}_l^n = [\hat{F}_{l1}^n, ..., \hat{F}_{l(N_y-1)}^n, \hat{H}_{l1}^n, ..., \hat{H}_{l(N_y-1)}^n]^{\mathrm{T}}. \tag{5.26}$$

For a given (j,m) the matrices $\mathbf{A}$ and $\mathbf{B}$ contain the coefficients of $\hat{\psi}_{lm}^{n+1}$, $\hat{\theta}_{lm}^{n+1}$, $\hat{\psi}_{lm}^{n}$ and $\hat{\theta}_{lm}^{n}$ from equations (5.22 - 5.23). The rows and columns of $\mathbf{A}$ and $\mathbf{B}$ correspond to the collocation points and the sine expansion respectively. Take matrix $\mathbf{A}$ as an example; the setup of matrix $\mathbf{B}$ is similar. For the Mth column, the first $N_y - 1$ rows contain the coefficients of $\hat{\psi}_{lM}^{n+1}$ and $\hat{\theta}_{lM}^{n+1}$ from equation (5.22) evaluated at the jth collocation point. Similarly, rows N_y to $2(N_y - 1)$ contain the coefficients of $\hat{\psi}_{lM}^{n+1}$ and $\hat{\theta}_{lM}^{n+1}$ from equation (5.23) evaluated at the jth collocation point. Specifically, for each row, the first $N_y - 1$ columns contain the coefficients of $\hat{\psi}_{lm}^{n+1}$ whereas columns N_y to $2(N_y - 1)$ contain the coefficients of $\hat{\theta}_{lm}^{n+1}$.

The form of equation (5.24) is similar to the matrix form of the equations solved by Chebyshev collocation in chapters 2 and 4. However, there are now extra terms on the right-hand-side which must be calculated at each timestep in order to calculate the fields at the next timestep. The vector $\mathbf{F}_l^n$ can be found, at each timestep, from the definitions of F and H in equations (5.10 - 5.11). Linear terms and their derivatives can be calculated directly in spectral space since

$$\frac{\partial \psi}{\partial x} = -\mathrm{i}l\hat{\psi}_{lm}e^{-\mathrm{i}lx}\sin(m\pi y), \tag{5.27}$$

$$\frac{\partial \psi}{\partial y} = m\pi\hat{\psi}_{lm}e^{-\mathrm{i}lx}\cos(m\pi y). \tag{5.28}$$

Combinations of these terms arising in the non-linear Jacobians of equation (5.10 - 5.11) must be evaluated in real space. Thus, the required fields are found in spectral space, transformed to real space using

$$\frac{\partial \psi}{\partial x} = -\sum_{l=-(N_x-1)}^{N_x-1}\sum_{m=1}^{N_y}\mathrm{i}l\hat{\psi}_{lm}e^{-\mathrm{i}lx}\sin(m\pi y), \tag{5.29}$$

$$\frac{\partial \psi}{\partial y} = \sum_{l=-(N_x-1)}^{N_x-1}\sum_{m=1}^{N_y}m\pi\hat{\psi}_{lm}e^{-\mathrm{i}lx}\cos(m\pi y), \tag{5.30}$$

and then multiplication for all non-linear terms is done in real space. Note that a Fourier transform in x as well as a Fourier sine and cosine transform must be used for the x and y-derivatives respectively. Once the non-linear terms have been calculated they are inverse-Fourier transformed back to spectral space for use in the vector $\mathbf{F}_l^n$. Finally $\mathbf{X}_l^{n+1}$ can be found by multiplying equation (5.24) through on the left by $\mathbf{A}^{-1}$. The vector $\mathbf{X}_l^{n+1}$ then contains $\hat{\psi}_{lm}$ and $\hat{\theta}_{lm}$ for $1 \leq m \leq N_y - 1$ at the new timestep for any value of l.

At any given timestep the real space fields, ψ and θ, can be calculated from $\hat{\psi}_{lm}$ and $\hat{\theta}_{lm}$ using a Fourier transform and a Fourier sine transform from the definitions of equations (5.12 - 5.13) via equations (5.19 - 5.20). These are the quantities that we shall plot in our results in the next section. We are also able to define the mean quantities as follows. The zonal flow is the x-average of the azimuthal component of the velocity. In the annulus model the azimuthal direction is the x-direction and hence the zonal flow, $\bar{\mathbf{U}}$, is defined as

$$\bar{\mathbf{U}} = \bar{U}\hat{\mathbf{x}} = \langle u_x \rangle_x \hat{\mathbf{x}} = -\frac{\partial \langle \psi \rangle_x}{\partial y}\hat{\mathbf{x}}, \tag{5.31}$$

where we have used equation (4.7) to substitute for u_x. The x-average is defined as

$$\langle A \rangle_x = \frac{1}{L_x}\int_0^{L_x} A\mathrm{d}x, \tag{5.32}$$

for a scalar quantity, A. Hence, assuming (for the moment) that $l \neq 0$

$$\bar{U} = -\frac{1}{L_x}\int_0^{L_x} \frac{\partial \psi}{\partial y}\mathrm{d}x \tag{5.33}$$

$$= -\frac{1}{L_x}\int_0^{L_x} \sum_{l=-(N_x-1)}^{N_x-1} \sum_{m=1}^{N_y-1} m\pi\hat{\psi}_{lm} e^{-\mathrm{i}lx(2\pi/L_x)} \cos(m\pi y)\mathrm{d}x \tag{5.34}$$

$$= \sum_{l=-(N_x-1)}^{N_x-1} \sum_{m=1}^{N_y-1} \frac{m}{2\mathrm{i}l}\hat{\psi}_{lm}\cos(m\pi y)\left[e^{-2\pi\mathrm{i}l} - 1\right] \tag{5.35}$$

$$= 0, \tag{5.36}$$

since $\exp(2\pi\mathrm{i}l) = 1 \ \forall l \in \mathbb{Z}$ and we have substituted for ψ using equations (5.12) and (5.19). Therefore there is no contribution to the zonal flow from modes with $l \neq 0$. We now specifically consider the case of $l = 0$ and find that

$$-\frac{1}{L_x}\int_0^{L_x} \sum_{m=1}^{N_y-1} m\pi\hat{\psi}_{0m}\cos(m\pi y)\mathrm{d}x = -\sum_{m=1}^{N_y-1} m\pi\hat{\psi}_{0m}\cos(m\pi y), \tag{5.37}$$

and hence

$$\bar{U} = -\sum_{m=1}^{N_y-1} m\pi\hat{\psi}_{0m}\cos(m\pi y). \tag{5.38}$$

We can follow a similar procedure to gain an expression for the mean temperature:

$$\bar{\theta} = \langle \theta \rangle_x \tag{5.39}$$

$$\Rightarrow \quad \bar{\theta} = \sum_{m=1}^{N_y-1} \hat{\theta}_{0m}\sin(m\pi y). \tag{5.40}$$

Also of interest are the total kinetic energy and the zonal part of the kinetic energy, defined by

$$E_T = \frac{1}{L_x}\int (\nabla\psi)^2 \mathrm{d}S, \quad \text{and} \tag{5.41}$$

$$E_Z = \frac{1}{L_x}\int (\langle\nabla\psi\rangle_x)^2 \mathrm{d}S, \tag{5.42}$$

respectively. These quantities can be evaluated via a similar procedure to the derivation of $\bar{U}$ above where we find that

$$E_T = \frac{1}{8}\sum_{l=-(N_x-1)}^{N_x-1}\sum_{m=1}^{N_y-1}(l^2+m^2\pi^2)\hat{\psi}_{lm}^2, \quad \text{and} \tag{5.43}$$

$$E_Z = \frac{1}{8}\sum_{m=1}^{N_y-1} m^2\pi^2\hat{\psi}_{0m}^2. \tag{5.44}$$

The numerical method described above is implemented in Fortran with the Fourier transforms performed by various NAG library routines. Specifically, the x-Fourier transform is performed using routine C06FQF and the sine and cosine transforms using routines C06HAF and C06HBF respectively. In order to perform the method an initial state from which to begin the timestepping must be chosen as well as values for the parameters: N_x and N_y.

5.3 Results of the non-linear theory

Here we present the results from simulations of the time evolution of equations (5.7 - 5.8) using the method discussed in section 5.2. We expect the results to closely match those of Jones *et al.* (2003); Rotvig & Jones (2006) where under certain parameter regimes multiple jets and the bursting phenomenon are observed. We perform numerous runs of the code for various parameter sets. In table 5.1 we have presented a notation for the runs that are performed and we shall use this notation to refer to the runs in this section and the next. We see from table 5.1 that the runs performed are for similar parameter ranges of the Prandtl number and beta parameter as were used in chapter 4; namely $0.5 \leq Pr \leq 5$ and $10^3 < \beta < 10^6$. In the previous work by Jones *et al.* (2003); Rotvig & Jones (2006) only Prandtl number unity was considered and hence we go further with our parameter range here. We consider Rayleigh numbers above critical so that the initial state does not simply decay away. Specifically, we perform runs with the Rayleigh number 2.5, 2.75 and 5 times that of the critical Rayleigh number for a given Pr and β as indicated in table 5.1. We use the rapid rotation approximation to the critical Rayleigh number as defined in chapter 4 for the classic Busse annulus case without any basic state zonal flow so that

$$Ra_c = \frac{3\beta^{4/3}Pr^{4/3}}{2^{2/3}(1+Pr)^{4/3}}, \tag{5.45}$$

recalling equation (4.47). The first six runs, I to VI, are run for the same parameter values as some of the runs performed by Jones *et al.* (2003); Rotvig & Jones (2006) in order to compare with previous work. However, we perform additional runs where we focus primarily on $\beta = 5 \times 10^5$ and $C = 0$ for various Prandtl and Rayleigh numbers. The mean quantities that arise out of these later runs are used in the next section to consider how they affect the growth rates of the linear theory.

In order to aid discussion in this section we take the average of the vorticity equation over the azimuthal coordinate since this helps to explain zonal flow generation. The x-average of equation (5.7) is

$$\frac{\partial}{\partial t}\langle\nabla^2\psi\rangle_x + \left\langle\frac{\partial(\psi,\nabla^2\psi)}{\partial(x,y)}\right\rangle_x - \beta\left\langle\frac{\partial\psi}{\partial x}\right\rangle_x = \tag{5.46}$$

$$- Ra\left\langle\frac{\partial\theta}{\partial x}\right\rangle_x - C|\beta|^{1/2}\langle\nabla^2\psi\rangle_x + \langle\nabla^4\psi\rangle_x \tag{5.47}$$

$$\Rightarrow \quad -\frac{\partial}{\partial y}\frac{\partial\bar{U}}{\partial t} + \left\langle\frac{\partial(\psi,\nabla^2\psi)}{\partial(x,y)}\right\rangle_x = -\frac{\partial}{\partial y}\left(-C|\beta|^{1/2}\bar{U} + \frac{\partial^2\bar{U}}{\partial y^2}\right), \tag{5.48}$$

where we have used the definition of $\bar{U}$ from equation (5.31). The non-linear Jacobian term can be written

$$\left\langle\frac{\partial(\psi,\nabla^2\psi)}{\partial(x,y)}\right\rangle_x = \langle\hat{\mathbf{z}}\cdot\nabla\times((\mathbf{u}\cdot\nabla)\mathbf{u})\rangle_x = -\frac{\partial}{\partial y}\langle\hat{\mathbf{x}}\cdot((\mathbf{u}\cdot\nabla)\mathbf{u})\rangle_x \tag{5.49}$$

$$\Rightarrow \quad \left\langle\frac{\partial(\psi,\nabla^2\psi)}{\partial(x,y)}\right\rangle_x = -\frac{\partial}{\partial y}\left\langle\frac{\partial}{\partial x_j}(u_j u_x)\right\rangle_x = -\frac{\partial^2}{\partial y^2}\langle u_x u_y\rangle_x, \tag{5.50}$$

where we have used the fact that the velocity field is solenoidal. Throughout the derivation of equations (5.46 - 5.50) we have used the fact that x-derivatives average to zero when taking the x-average due to the periodicity of the fields in x over the domain. If we take the y-integral of equation (5.48) with the non-linear term from equation (5.50) inserted we obtain

$$\frac{\partial\bar{U}}{\partial t} = -\frac{\partial}{\partial y}\langle u_x u_y\rangle_x - C|\beta|^{1/2}\bar{U} + \frac{\partial^2\bar{U}}{\partial y^2}, \tag{5.51}$$

which is the equation that governs zonal flow generation. We note that zonal flow can be created by the Reynolds force, confirming that $\bar{U}$ is a non-linear phenomenon as expected, and destroyed by the friction terms. The addition of the bottom friction term is expected therefore to dampen the zonal flow; however, as discussed earlier, it increases the likelihood of multiple jet solutions arising.

Run	Pr	β	C	Ra/Ra_c	τ	m_*
I	1	7.07×10^3	0.316	2.5	13.1202	2
II	1	7.07×10^5	0	2.5	1.6540	2
III	1	7.07×10^4	0	2.5	3.6307	1
IV	1	7.07×10^4	0.00316	2.5	1.2348	1
V	1	7.07×10^4	0.316	2.5	8.0784	3
VI	1	7.07×10^5	0.316	2.5	2.6814	5
VII	1	5×10^5	0	2.75	3.2907	2
VIII	1	5×10^5	0	5	0.9302	2
IX	1	5×10^5	0.05	2.75	1.4378	3
X	1	5×10^5	0.5	2.75	3.3784	5
XI	0.5	5×10^5	0	2.75	2.6873	2
XII	0.5	5×10^5	0	5	0.2528	1
XIII	0.5	5×10^5	0.5	2.75	2.6440	4
XIV	2	5×10^5	0	2.75	2.1137	2
XV	2	5×10^5	0	5	1.0321	2
XVI	2	5×10^5	0.05	2.75	2.4241	3
XVII	2	5×10^5	0.5	2.75	2.4677	7
XVIII	5	5×10^5	0	2.75	4.6855	2
XIX	5	5×10^5	0	5	0.5579	2

Table 5.1: Table displaying the parameter sets used for the various non-linear runs.

Each of the runs displayed in table 5.1 are run until a quasi-steady or quasi-periodic state has evolved from the initial condition. As with previous work, the initial condition is not found to influence the final state so the solutions are unique. Therefore a random initial state is used for each run. In figures 5.1 to 5.19 we plot snapshots of the state of the simulation for each run in table 5.1 once a final state has been achieved for each run. The condition that we wait for a final state to be achieved means that the snapshots in these figures are taken after a different number of timesteps and a different amount of diffusion time for each run. Recall that we are using the viscous timescale in these simulations and thus the timescale is inversely proportional to ν and hence also inversely proportional to $Pr = \nu/\kappa$. Therefore runs with larger values of the Prandtl number are more readily integrated over multiple turnover times than runs with small Prandtl numbers. The quantity τ, appearing in table 5.1, represents the amount of time elapsed prior to the snapshots, of figures 5.1 to 5.19, being taken. Hence each snapshot is taken at time $t = \tau$ with the values of τ presented in table 5.1. Also in table 5.1 we display m_*, which denotes the dominant radial wavenumber at time τ. The value of m_* determines whether multiple jets are present; a solution has $m_* + 1$ jets and we define $m_* \geq 3$ to denote a multiple jet solution. The reason for this choice of definition for multiple jets is two-fold. Firstly, the definition matches that of the previous literature (Jones *et al.*, 2003; Rotvig & Jones, 2006). Secondly, we recall from our discussion at the start of this chapter that solutions with strong prograde equatorial jets flanked by two retrograde jets are commonly produced in simulations but solutions with more jets are more difficult to obtain (Heimpel *et al.*, 2005). Here it will be of particular interest if the solution displays more than just the three commonly found jets. Therefore it makes sense to define a multiple jet as a solution which contains more than three jets. We have predominantly used the resolution $(N_x, N_y) = (256, 128)$ although runs VIII, XIV, XVI and XVII have $(N_x, N_y) = (384, 128)$ and runs XV, XVIII and XIX have $(N_x, N_y) = (512, 128)$.

The three plots displayed in each figure 5.1 to 5.19 from top to bottom represent the following. The top two plots display the ψ-contours and the θ-contours at time τ, respectively. In the case of the ψ-contours, positive and negative values represent clockwise and anti-clockwise motion respectively. In the third plot of each figure we plot four quantities: the zonal flow, $\bar{U}$, the mean temperature profile, $\bar{\theta}$, the *total* temperature profile, $T = T_0 + \bar{\theta}$, and the mean temperature gradient, $\bar{\theta}'$. The values of $\bar{U}$ have been normalised using either $\max(\bar{U})$ or $-\min(\bar{U})$, whichever is larger. Likewise, $\bar{\theta}'$ has been normalised using either $\max(\bar{\theta}')$ or $-\min(\bar{\theta}')$. Also, the exact value of T has been plotted, whereas $\bar{\theta}$ has been amplified by a factor of five in order to be more clearly displayed. The range over which the quantities vary are presented beneath the third plot.

The first six runs are for parameter regimes used by Jones *et al.* (2003); Rotvig & Jones

(2006) so that $Pr = 1$ and $Ra/Ra_c = 2.5$ throughout. We begin by making some general observations about the dynamics seen in many of the figures. From figures 5.1 to 5.6 it is clear that the non-linear effects have significantly altered the simple structure of the fields predicted by the linear theory of section 4.2. The form of ψ and θ given by equation (4.45) indicated thin disturbances that stretched across the whole annular layer (that is, from $y = 0$ to $y = 1$). However, although this structure can be seen in certain regions for some runs (for example figure 5.1), the overall flow pattern is rather different to that predicted in the linear theory.

In figure 5.1, for run I with $\beta = 7.07 \times 10^3$ and $C = 0.316$, a net eastward zonal flow is produced at $y = 1/2$. This is caused by the interaction of the predominantly clockwise motions for $y < 1/2$ with the predominantly anti-clockwise motions for $y > 1/2$. The resultant negative y-gradient in ψ produces an eastward zonal flow ($\bar{U} > 0$) as expected from equation (5.31). Further examples of the production of the zonal flow in a similar way can be seen in the other plots. However, the annulus model with sloped boundaries, neglects any preference that there may be for waves to propagate in one x-direction over the other. Therefore, for each solution we produce with a zonal flow in the positive x-direction, there is an equivalent solution with the zonal flow acting in the opposite direction. In order to overcome this degeneracy, curvature of the end wall boundaries must be included in the model. Busse & Or (1986) consider the effect of such curvature of the end walls. In some plots, for example the ψ-plots of figures 5.2 and 5.3, the zonal flow is strong enough to dominate the dynamics so much that convective cell patterns are no longer visible. In such cases, the correlation between regions of strong zonal flow and regions of strong $\partial\psi/\partial y$ is very clear.

There are also general observations that can be made from the θ-plots of figures 5.1 to 5.6. The $\sin(\pi y)$ dependence of the linear theory, where one would expect alternating yellow and blue vertical stripes, has again been suppressed by non-linear effects. In fact, the preference is almost exclusively for yellow ($\theta > 0$) and blue ($\theta < 0$) in the regions $y < 1/2$ and $y > 1/2$ respectively. This is a result of the mean temperature, $\bar{\theta}$, attempting to balance, or 'flatten out' the static temperature profile. We also notice that often the regions of most active heat transport occur when the gradient of $\bar{U}$ is approximately zero. This is because convection can be carried along with the zonal flow in areas where the flow strength is near-constant. However, the shearing effect of a gradient in the zonal

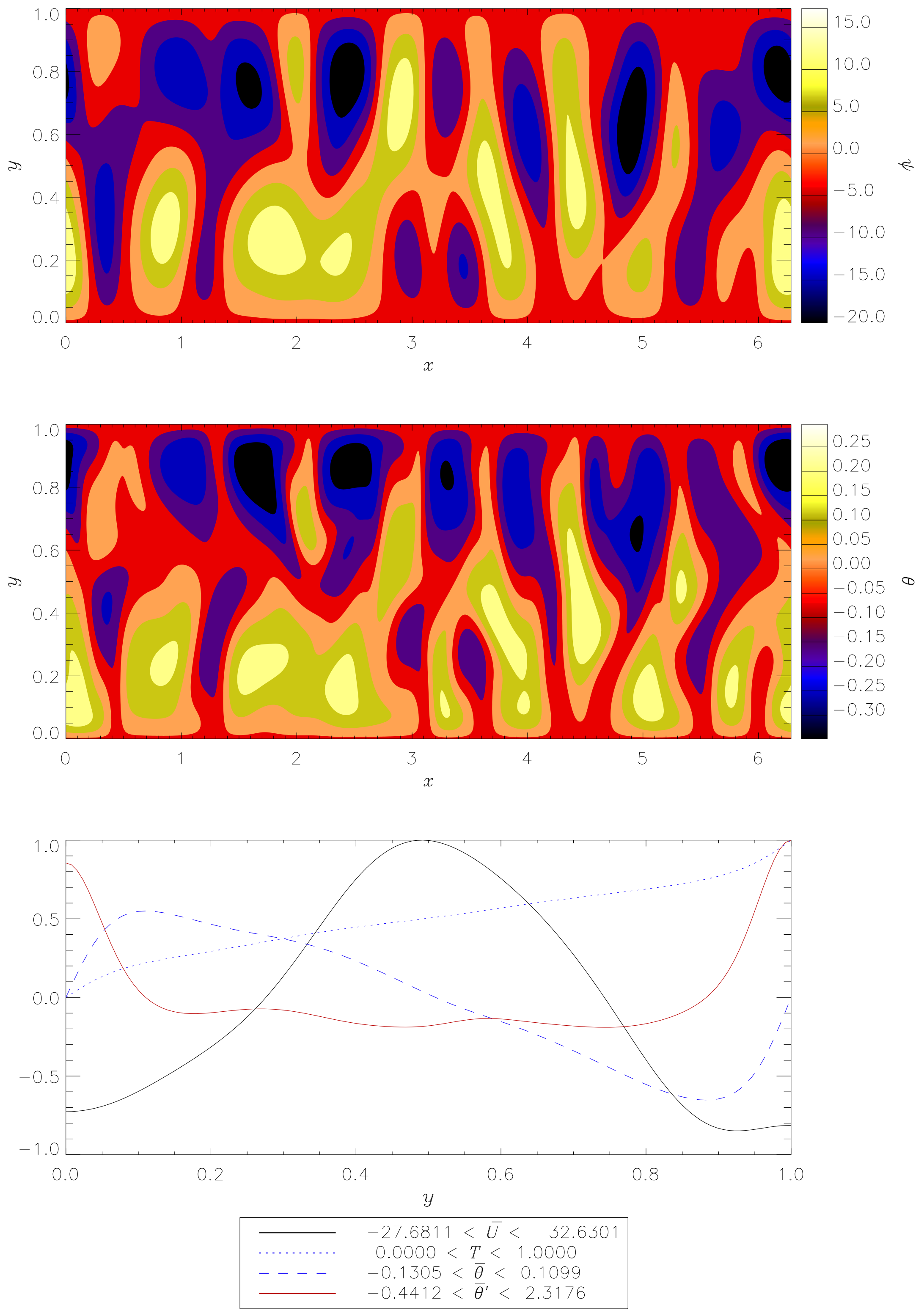

Figure 5.1: Contour plot for run I: $Pr = 1$, $\beta = 7.07 \times 10^3$, $C = 0.316$, $Ra/Ra_c = 2.5$.

flow significantly disrupts convection cells by tearing them apart. Many of the runs also display a striking correlation of the θ-contours with the slope of $\bar{U}$. The θ-contours show the local slope of the flow because temperature is advected with the flow. This slope then gives the sign of the Reynolds stress, which via equation (5.51) determines the form of the zonal flow. Therefore this explains why the slope of the θ-contours is correlated with the slope of the zonal flow.

We now discuss how the general features of the dynamics described above alter in various parameter regimes. For the first six runs, which are for parameter regimes used by Jones *et al.* (2003); Rotvig & Jones (2006), we see excellent agreement with the previous results. For each parameter set the state has evolved into a final state with the same properties as those found in the previous literature. In particular, the number of jets produced for the parameter sets of these first six runs matches exactly with those of table 1 from Rotvig & Jones (2006). As β is increased the disturbances become smaller in the x-direction. Thus there are fewer convection cells in figure 5.1 where $\beta = 7.07 \times 10^3$ compared with later runs (see, for example, figure 5.2, run II where $\beta = 7.07 \times 10^5$). This is due to the dependence of k on β given in equation (4.47). In fact, in figure 5.2 we see that the convection is localised rather than occurring throughout the domain, unlike most of the other figures. Run II has settled into a quasi-periodic state where bursts of convection occur. During a burst, the convection takes place everywhere in the domain and drives up the zonal flow. The snapshot in figure 5.2 displays the situation shortly after a burst has taken place and the convection is localised. We will display further evidence for bursting solutions in the next set of runs.

There is also an increase in the strength of the zonal flow as β is increased; compare the magnitude of $\bar{U}$ in figures 5.3 and 5.2, for runs III and II, where $C = 0$ or alternatively in figures, 5.5 and 5.6, for runs V and VI, where $C \neq 0$. Since the forcing is the same for all of these runs ($Ra = 2.5Ra_c$), there must be another explanation for the differing magnitudes of the zonal flow. Recall from equation (5.51) that the magnitude of the zonal flow is determined by the balance of the Reynolds forcing against the frictional terms. Therefore in order to maintain a larger zonal flow at increased values of β, the Reynolds stresses must be larger. There are two ways in which the Reynolds stresses could be larger: either the convection is stronger or the streamlines slope more. The former explains why a larger value of Ra results in a larger zonal flow; the Reynolds

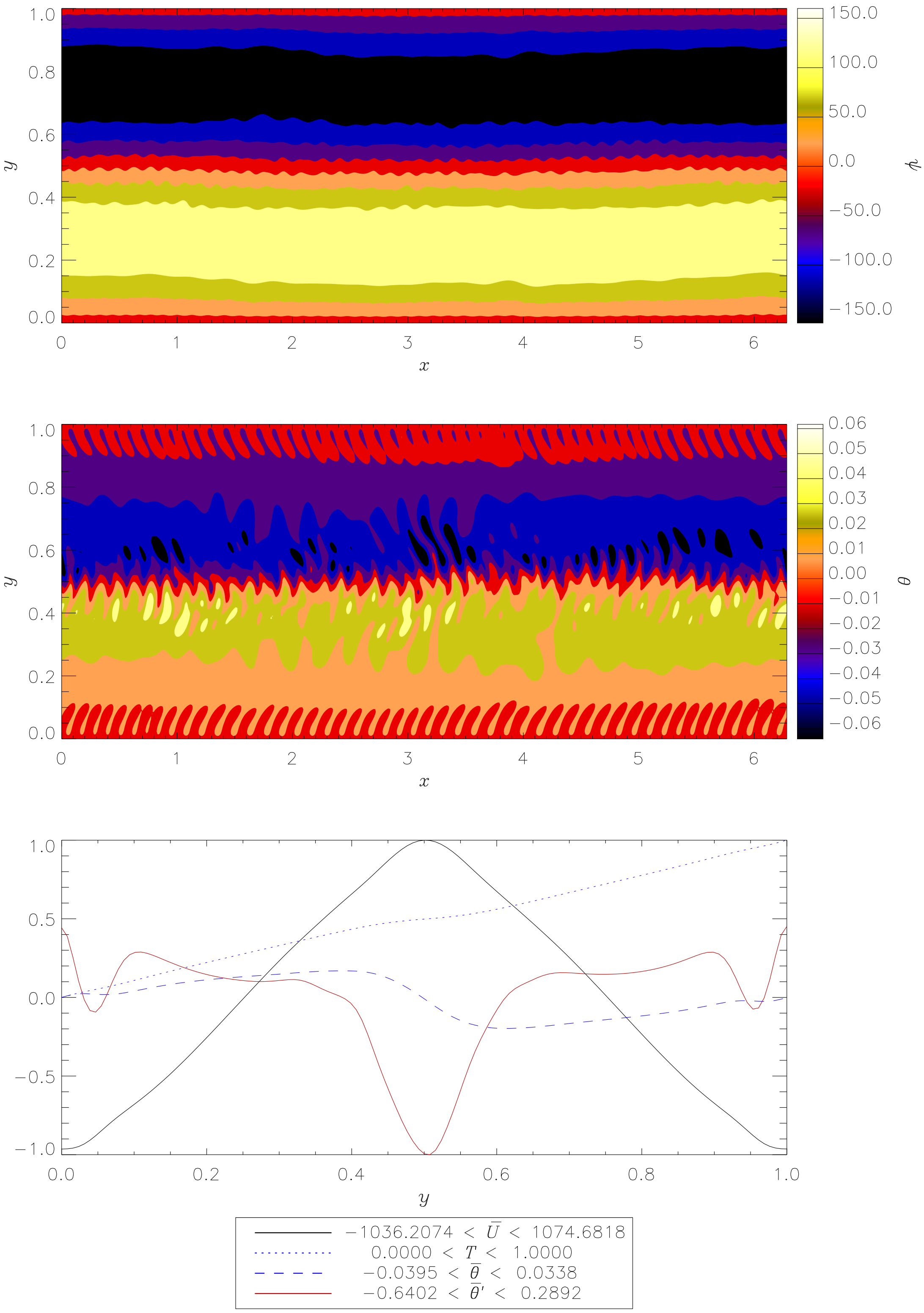

Figure 5.2: Contour plot for run II: $Pr = 1$, $\beta = 7.07 \times 10^5$, $C = 0$, $Ra/Ra_c = 2.5$.

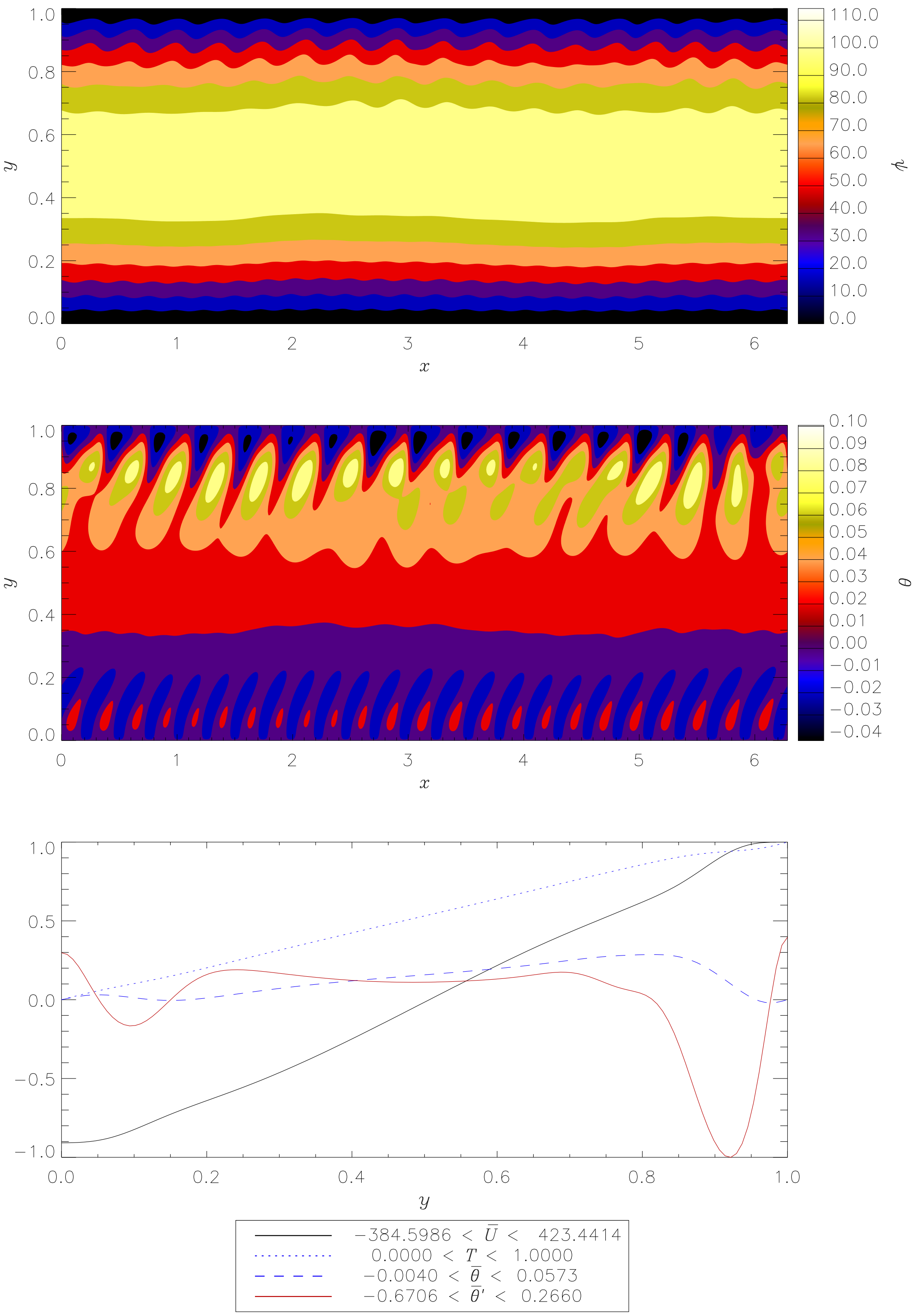

Figure 5.3: Contour plot for run III: $Pr = 1$, $\beta = 7.07 \times 10^4$, $C = 0$, $Ra/Ra_c = 2.5$.

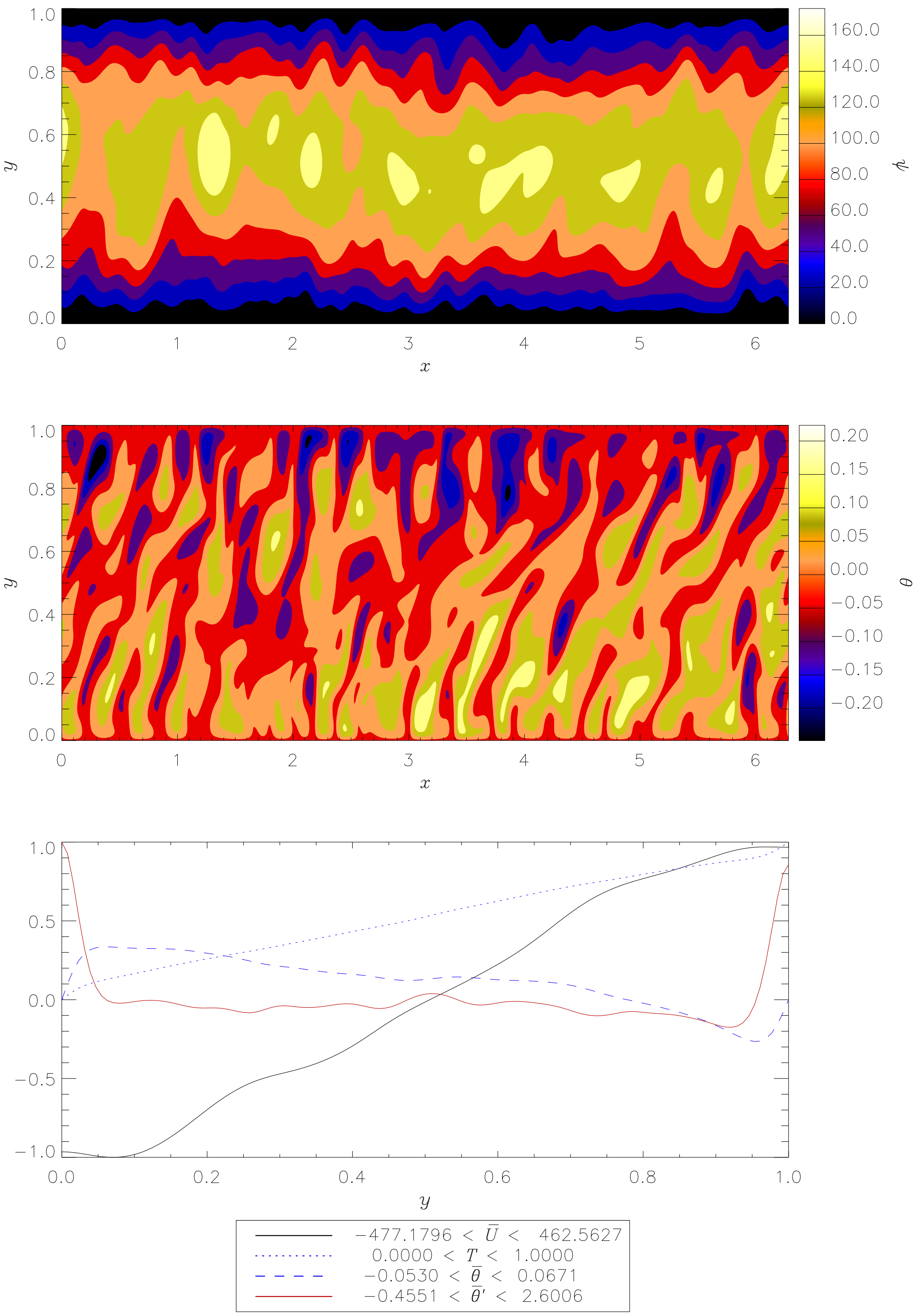

Figure 5.4: Contour plot for run IV: $Pr = 1$, $\beta = 7.07 \times 10^4$, $C = 0.00316$, $Ra/Ra_c = 2.5$.

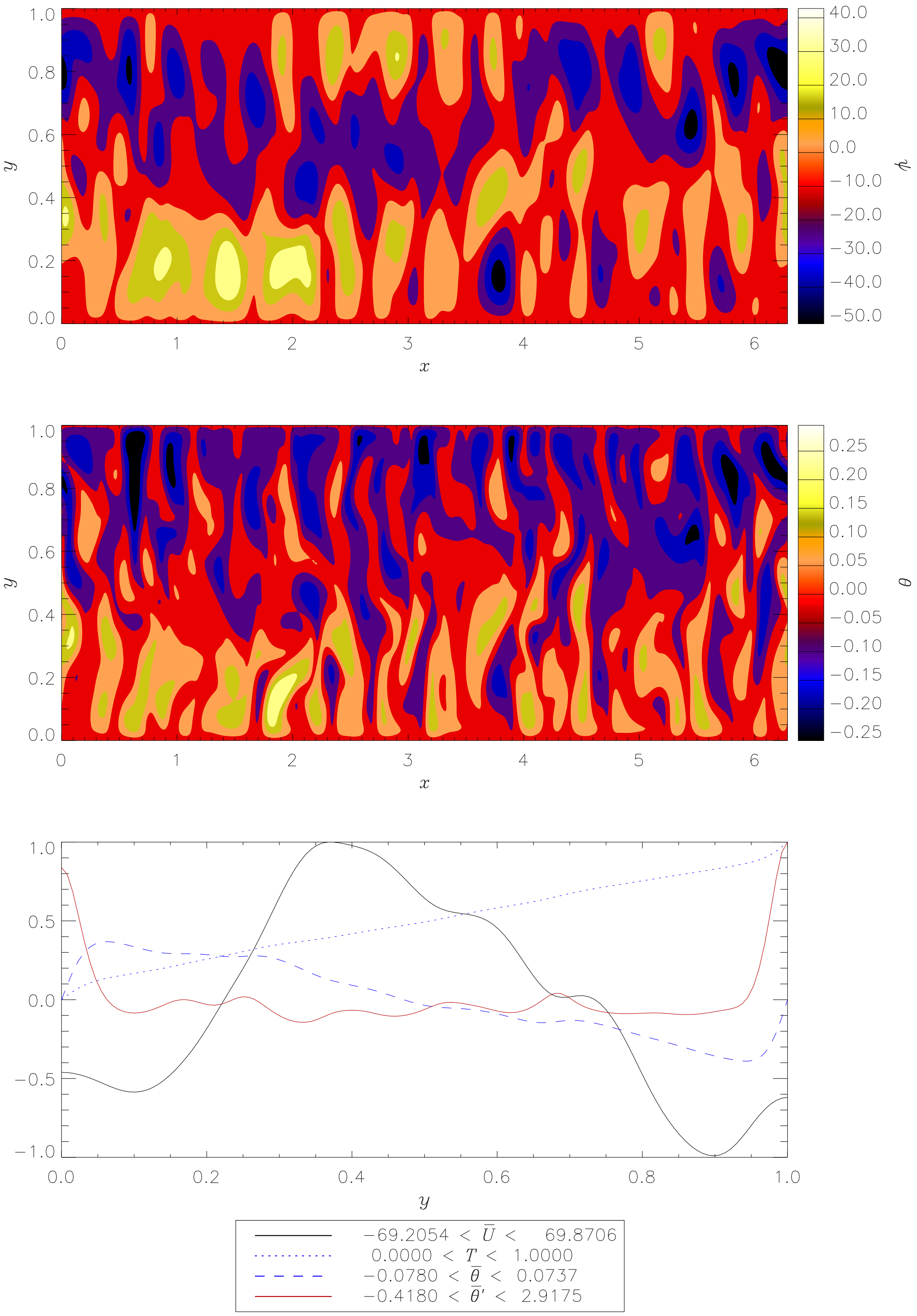

Figure 5.5: Contour plot for run V: $Pr = 1$, $\beta = 7.07 \times 10^4$, $C = 0.316$, $Ra/Ra_c = 2.5$.

stresses scale like ψ^2. However, in runs I and II the forcing is the same and the convective velocities are comparable. Therefore we expect that at larger β the streamlines slope more in order to give rise to the increased Reynolds forcing and larger zonal flow. This also explains why no zonal flow is produced in the absence of rotation since the ψ-contours do not slope when $\beta = 0$. The general increase in the magnitude of the zonal flow must saturate at some large value of β since the sloping of the streamlines cannot continue indefinitely.

For runs where $C = 0$ we also do not find any evidence of multiple jets since runs II and III are dominated by wavenumbers $m = 2$ and $m = 1$ respectively. For runs where the zonal flow is strong (for example runs II and III) the contour plots display large-scale structures in the x-direction so that the flow pattern is banded. In figure 5.2 it appears as though there is very little change of the flow pattern in the x-direction, which may result in negligible radial flow since $u_y = \partial\psi/\partial x$. However, the radial (convective) flow here may actually be comparable with previous cases (for example run I), since the ψ-contours are larger in the former case. The zonal flow is very dominant in run II so that any structure in the x-direction is swamped by the y-structure. However, it is certainly true that u_x and u_y are far more similar in size in run I compared with run II. In the y-direction there is more structure with strong y-dependence near the boundaries and at $y = 1/2$ resulting in the strong zonal flow there since $u_x = -\partial\psi/\partial y$.

The zonal flow is weakened by the introduction of the bottom friction as expected from equation (5.51). This is best shown by comparing figures 5.4 and 5.5, for runs IV and V, which have the same value of β but different values of C. The zonal flow has depleted in strength from $\approx \pm 400$, in run IV, to $\approx \pm 70$ in run V. Note also that there is far less order in the contour plots for ψ and θ in figure 5.5 since the zonal flow is weak. This is also the case in figure 5.1. The introduction of the Ekman layer also drastically improves the likelihood of multiple jet solutions. The only runs, of these first six, where multiple jets are presented are runs V and VI. These two runs both have $C = 0.316$, which is the largest value of C tested, for these initial runs. The possibility of multiple jets arising also increases as β is increased. Thus, relatively large values of C and β are preferred for multiple jets, as evidenced by figure 5.6 which has the most jets (six in total) of any of these first six runs. The number of jets found for each run can be compared directly with

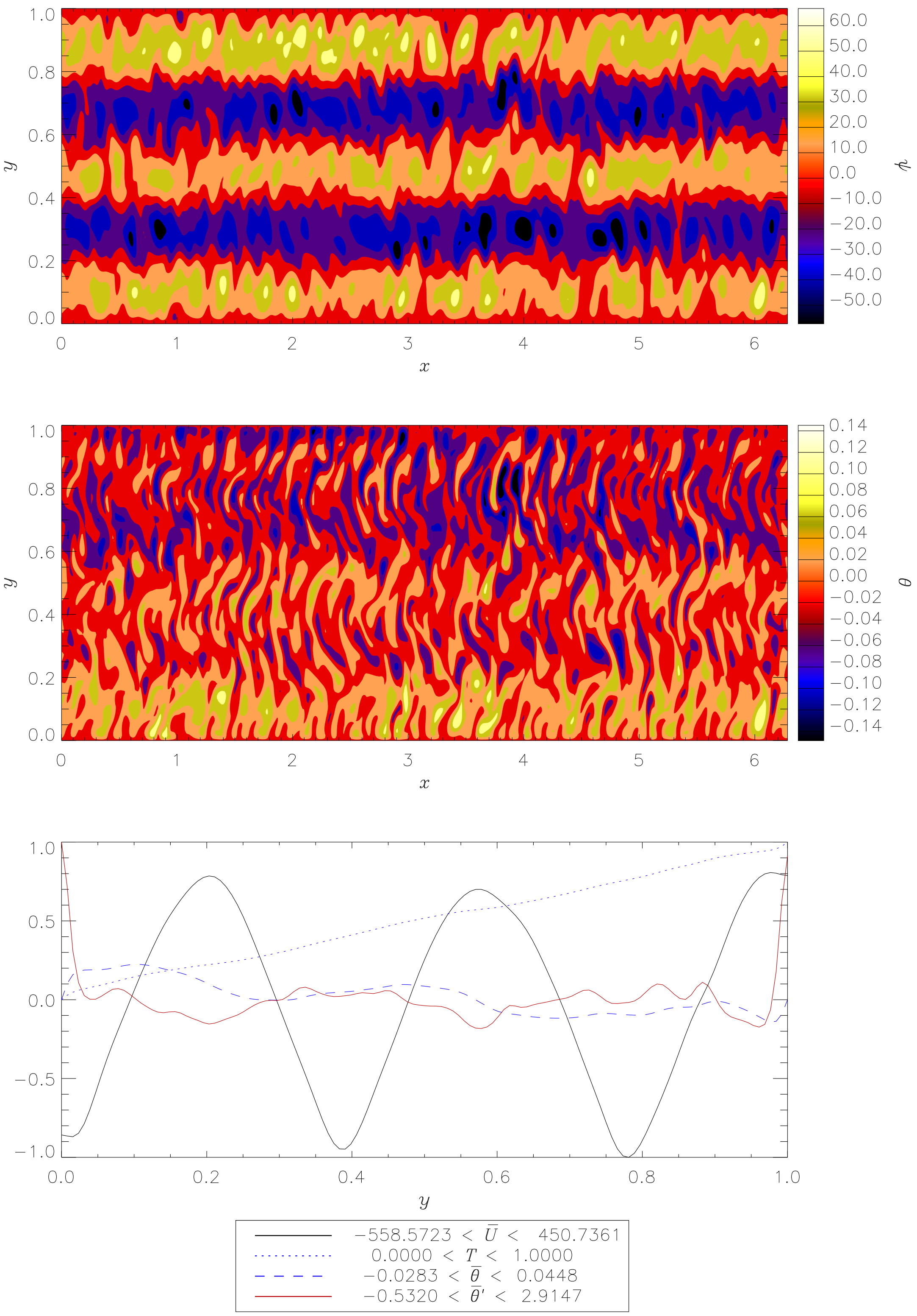

Figure 5.6: Contour plot for run VI: $Pr = 1$, $\beta = 7.07 \times 10^5$, $C = 0.316$, $Ra/Ra_c = 2.5$.

those of table 1 from Jones *et al.* (2003) and table 1 from Rotvig & Jones (2006), where we see excellent agreement.

The replication of previous results gives us confidence to explore further parameter regimes and the bursting phenomenon. This is what we perform in runs VII to XIX. The parameter regimes used for these runs can, again, be found in table 5.1, where we see that all have $\beta = 5 \times 10^5$. We have considered further values of the Prandtl number and Rayleigh number, whilst continuing to vary C.

From figures 5.7 to 5.19 we see the same general dependence on C emerging as was found for runs I to VI, for different Prandtl numbers. The introduction of C reduces the strength of the zonal flow. We first consider runs VII to X where $Pr = 1$. Figure 5.7 for run VII compares very well to that of figure 5.2 where the parameters are almost the same. We see in figure 5.8 for run VIII that increasing the Rayleigh number to five times critical increases the zonal flow strength (compare with run VII). This is to be expected, and was also found to be the case in previous work (Rotvig & Jones, 2006). A higher Rayleigh number increases the driving thereby also increasing the magnitude of the zonal flow that can be produced. Figure 5.8 also shows that the increase in the Rayleigh number has caused a rise in the peak value of the mean temperature gradient (again compare with run VII). If the Rayleigh number is held constant and instead C is increased progressively we see the same dependence on C as was discussed earlier. When increasing C from figures 5.7 to 5.9 to 5.10 we observe a weakening of the zonal flow but an increase in the number of jets. In run VIII we also notice some thermal boundary layer structure. From figure 5.8 we see that the gradient of T increases in magnitude sharply at $y = 0$ and $y = 1$ indicating enhanced heat transport.

We now move on to the case where the Prandtl number has been reduced to $Pr = 0.5$, shown in figures 5.11, 5.12 and 5.13 for runs XI, XII and XIII. We are able to compare these runs directly with the runs VII, VIII and X where the only parameter to have changed in each case is the Prandtl number. By lowering the Prandtl number we notice that the field contours and the pattern of the zonal flow remain quite similar between runs VII and XI though the zonal flow strength is slightly less in the $Pr = 0.5$ case. When $Ra = 5Ra_c$ we see much more of a difference between the $Pr = 0.5$ and $Pr = 1$ cases in figures 5.12 and 5.8. There are just two jets when $Pr = 0.5$ though the strength of the zonal

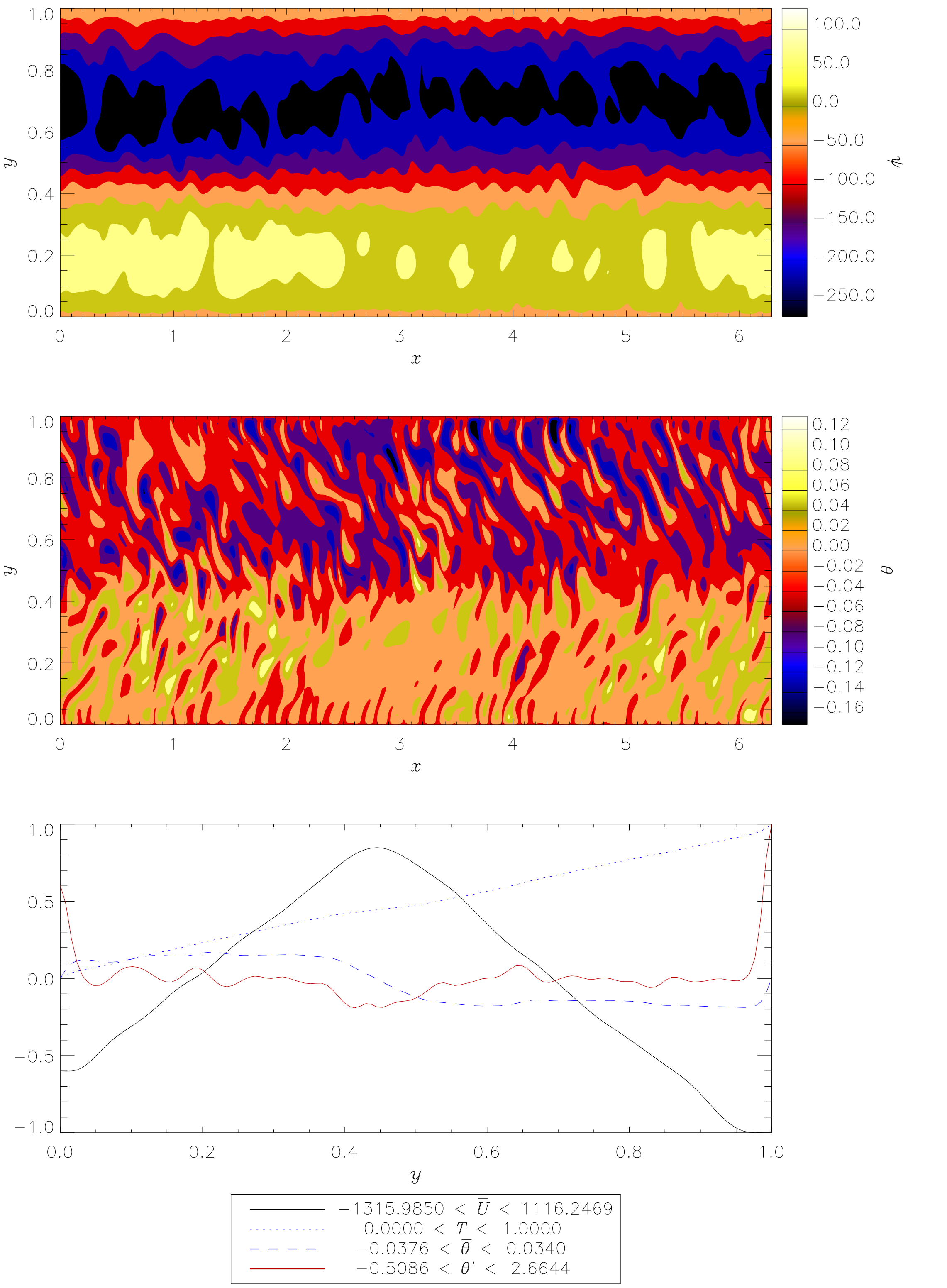

Figure 5.7: Contour plot for run VII: $Pr = 1$, $\beta = 5 \times 10^5$, $C = 0$, $Ra/Ra_c = 2.75$.

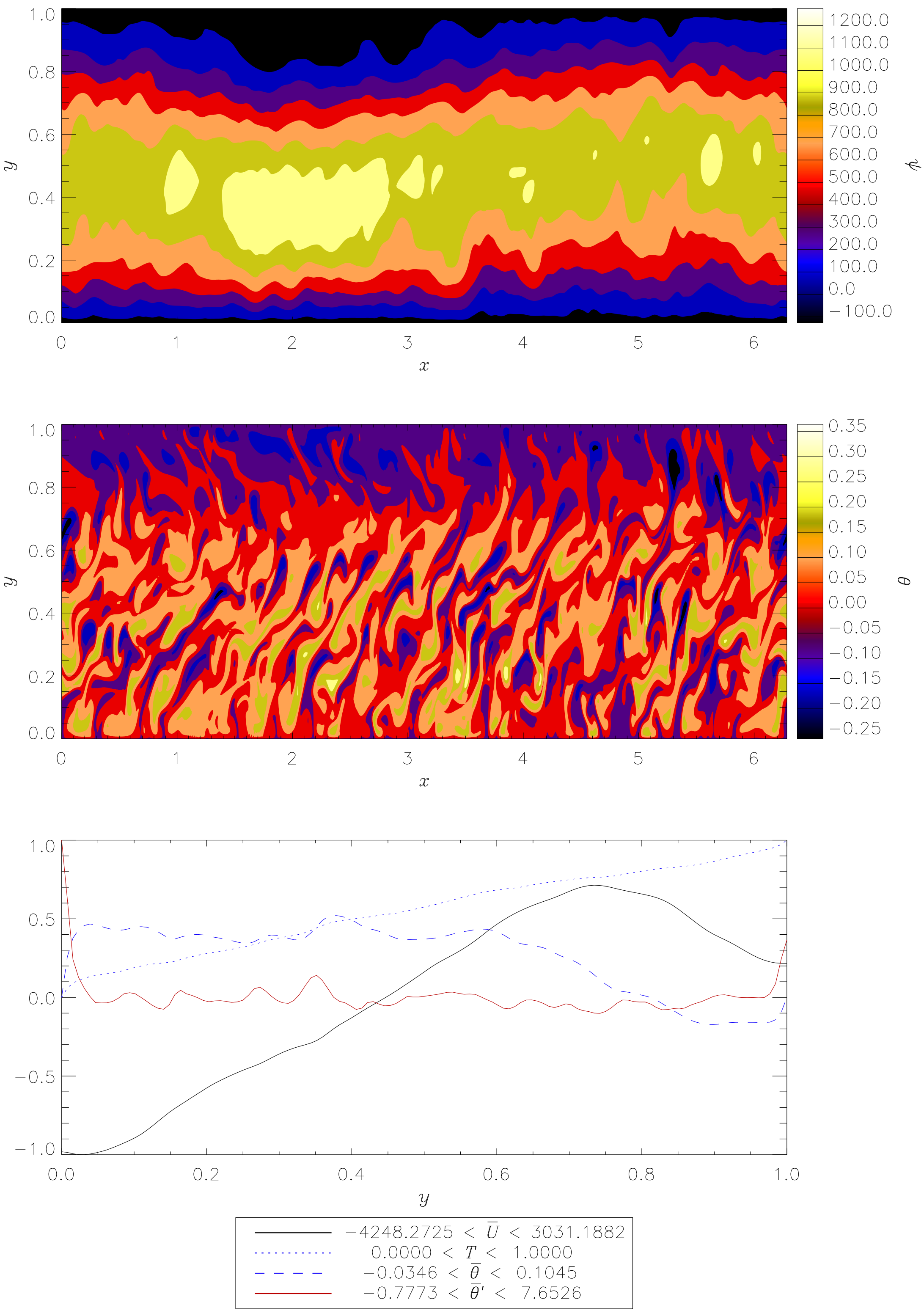

Figure 5.8: Contour plot for run VIII: $Pr = 1$, $\beta = 5 \times 10^5$, $C = 0$, $Ra/Ra_c = 5$.

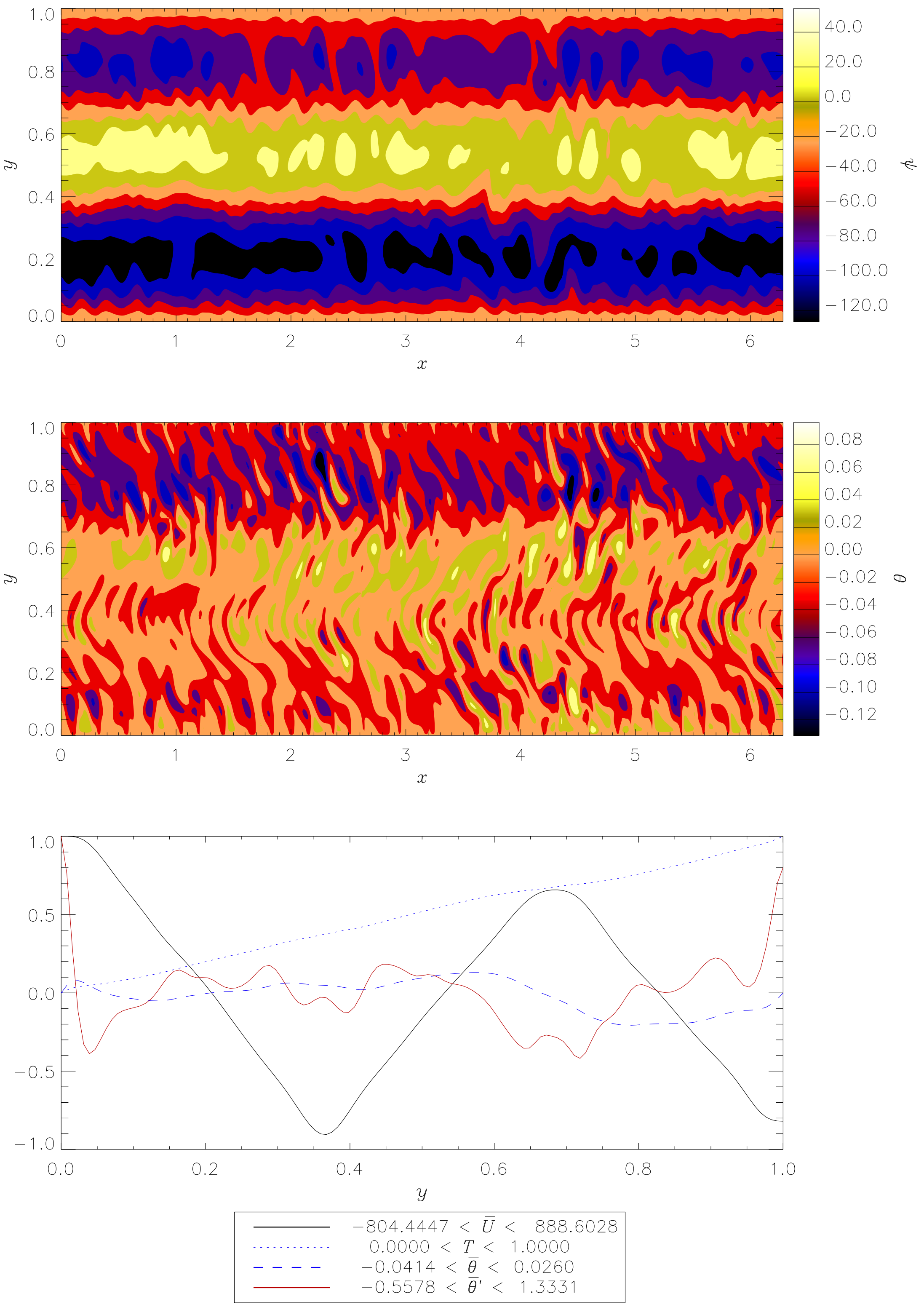

Figure 5.9: Contour plot for run IX: $Pr = 1$, $\beta = 5 \times 10^5$, $C = 0.05$, $Ra/Ra_c = 2.75$.

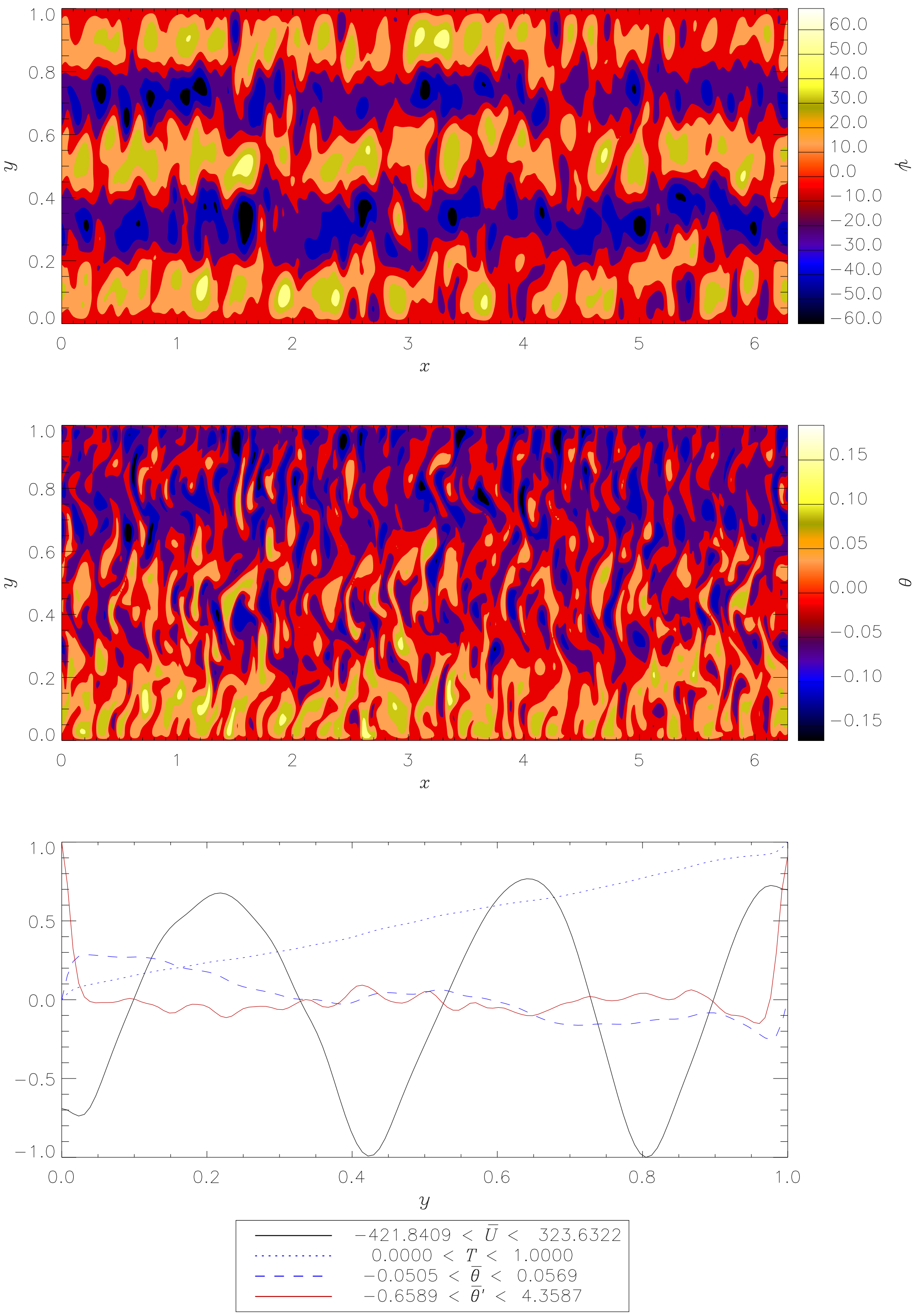

Figure 5.10: Contour plot for run X: $Pr = 1$, $\beta = 5 \times 10^5$, $C = 0.5$, $Ra/Ra_c = 2.75$.

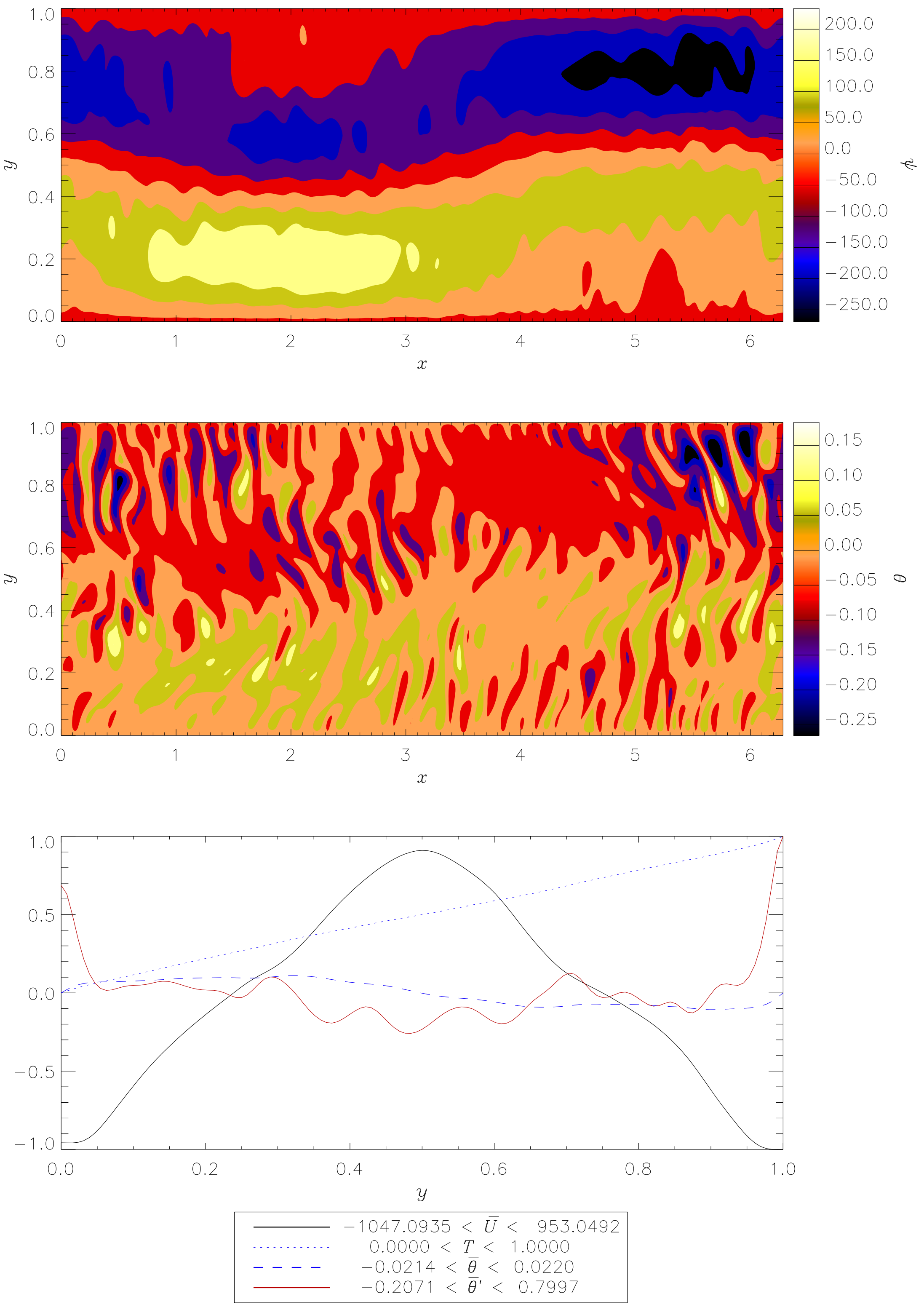

Figure 5.11: Contour plot for run XI: $Pr = 0.5$, $\beta = 5 \times 10^5$, $C = 0$, $Ra/Ra_c = 2.75$.

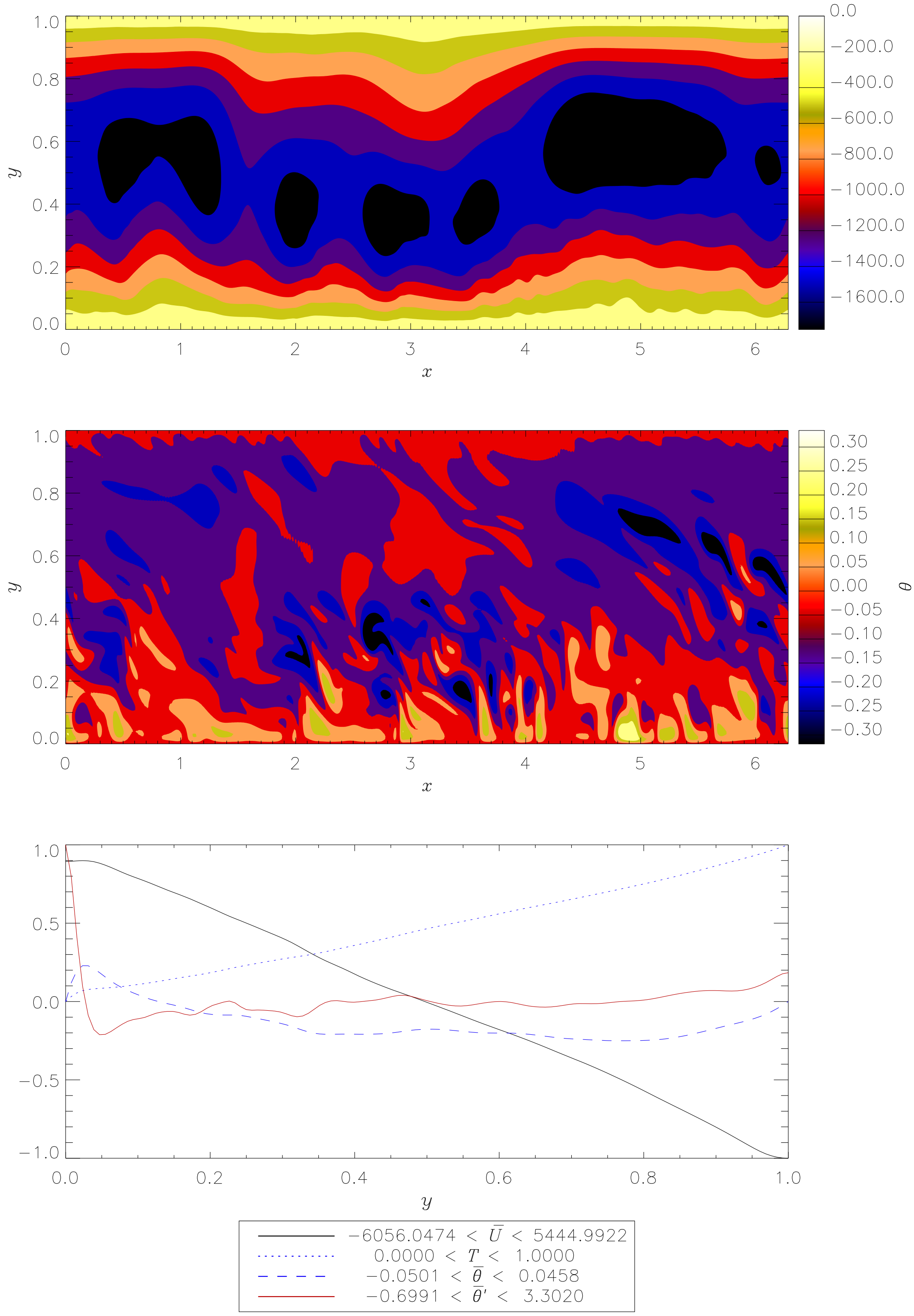

Figure 5.12: Contour plot for run XII: $Pr = 0.5$, $\beta = 5 \times 10^5$, $C = 0$, $Ra/Ra_c = 5$.

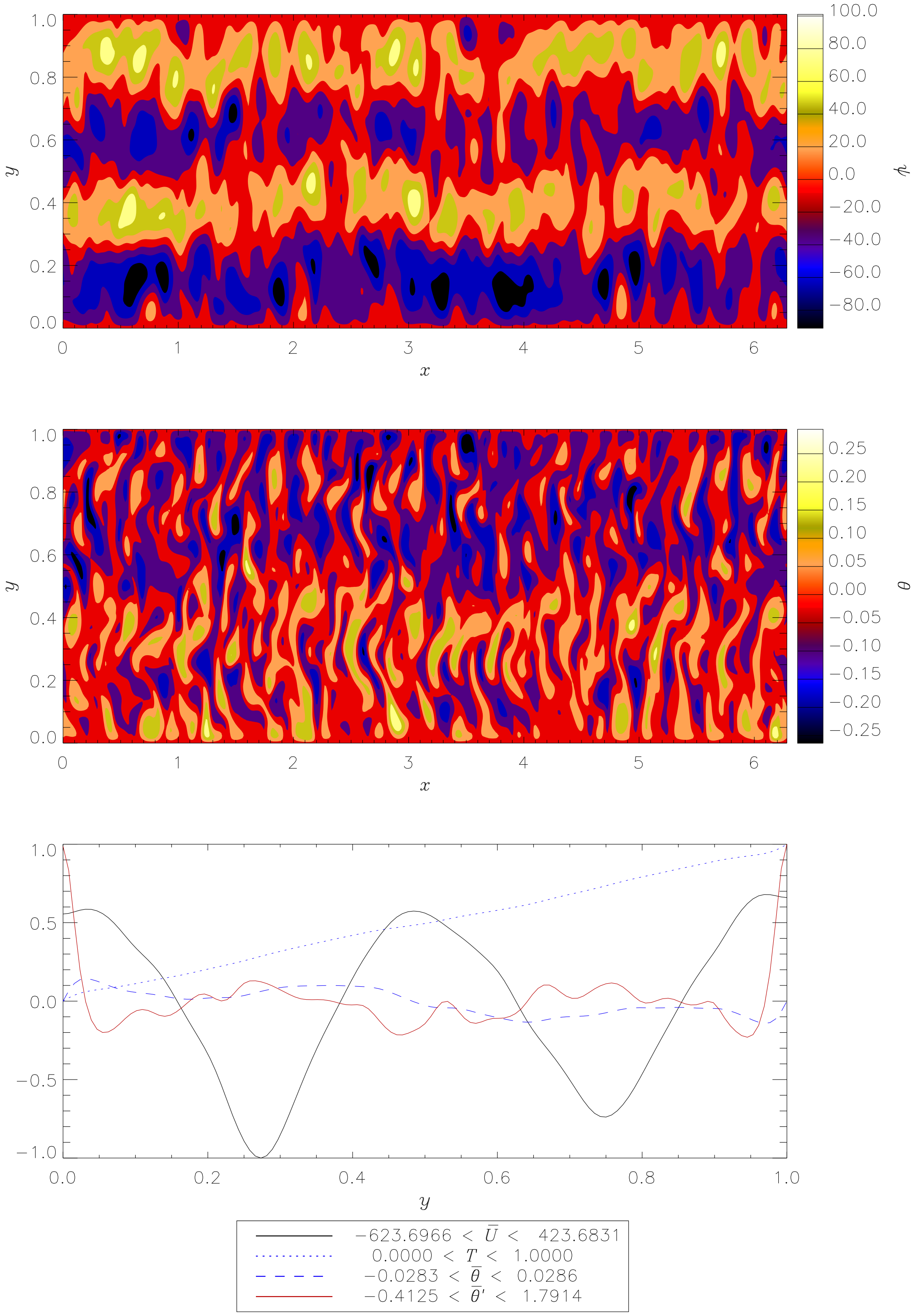

Figure 5.13: Contour plot for run XIII: $Pr = 0.5$, $\beta = 5 \times 10^5$, $C = 0.5$, $Ra/Ra_c = 2.75$.

flow is larger than in the $Pr = 1$ case. Figures 5.13 and 5.10 show that the reduction of the Prandtl number also has some effect on the case where $C = 0.5$. The zonal flow is slightly stronger with one fewer jets in the $Pr = 0.5$ case but otherwise the form of the convection is comparable in both figures. Also of note, when comparing runs XI, XII and XIII to VII, VIII and X is that the peak mean temperature gradient is larger in all three cases when $Pr = 1$.

We now discuss increasing the Prandtl number from $Pr = 1$ to $Pr = 2$. We can compare figures 5.14 to 5.17 for runs XIV to XVII with those of runs VII to X respectively, since the only parameter change is in the Prandtl number. By comparing these two sets of figures we see that there is, other than in a couple of cases, a general depletion of all quantities as the Prandtl number is increased. The convection patterns are similar in the cases where $C = 0$ as shown by comparing figures 5.7 and 5.8 with 5.14 and 5.15. However the zonal flow strength, as well as the contours, are reduced in the $Pr = 2$ case. There is remarkable similarity between the plots for the two Prandtl numbers currently in question when $C = 0.05$, see figures 5.9 and 5.16. The number of jets is the same in both cases and many of the quantities are of a similar size. However, there is again a smaller zonal flow strength when the Prandtl number is larger. The final run with $Pr = 2$, namely run XVII, appears to have a large number of jets, which is expected since the bottom friction is $C = 0.5$. There is, however, only a weak zonal flow resulting in the ψ-contours lacking a clear banded structure. This was not the case when $Pr = 1$ (see figure 5.10). Thus it seems that increasing the Prandtl number causes the system to lose its banded structure at a lower value of C. We should also note that the reduction in flow strength with increasing Prandtl number is to be expected. This is because the momentum diffusivity rate, ν, is larger so it is more difficult for large-scale flows to evolve before being diffused away.

The Prandtl number is increased further to $Pr = 5$, in figures 5.18 and 5.19 for runs XVIII and XIX respectively. In these plots the zonal flow is again, as expected, weaker than in the equivalent cases with smaller Prandtl numbers. However, there is an increase in the extrema values of the mean temperature gradient, which continues a general trend from the aforementioned figures. This can be explained by the increased Prandtl number resulting in a smaller thermal diffusivity, κ. Hence, in contrast to the zonal flow, a relatively large mean temperature gradient can develop more easily due to the increased

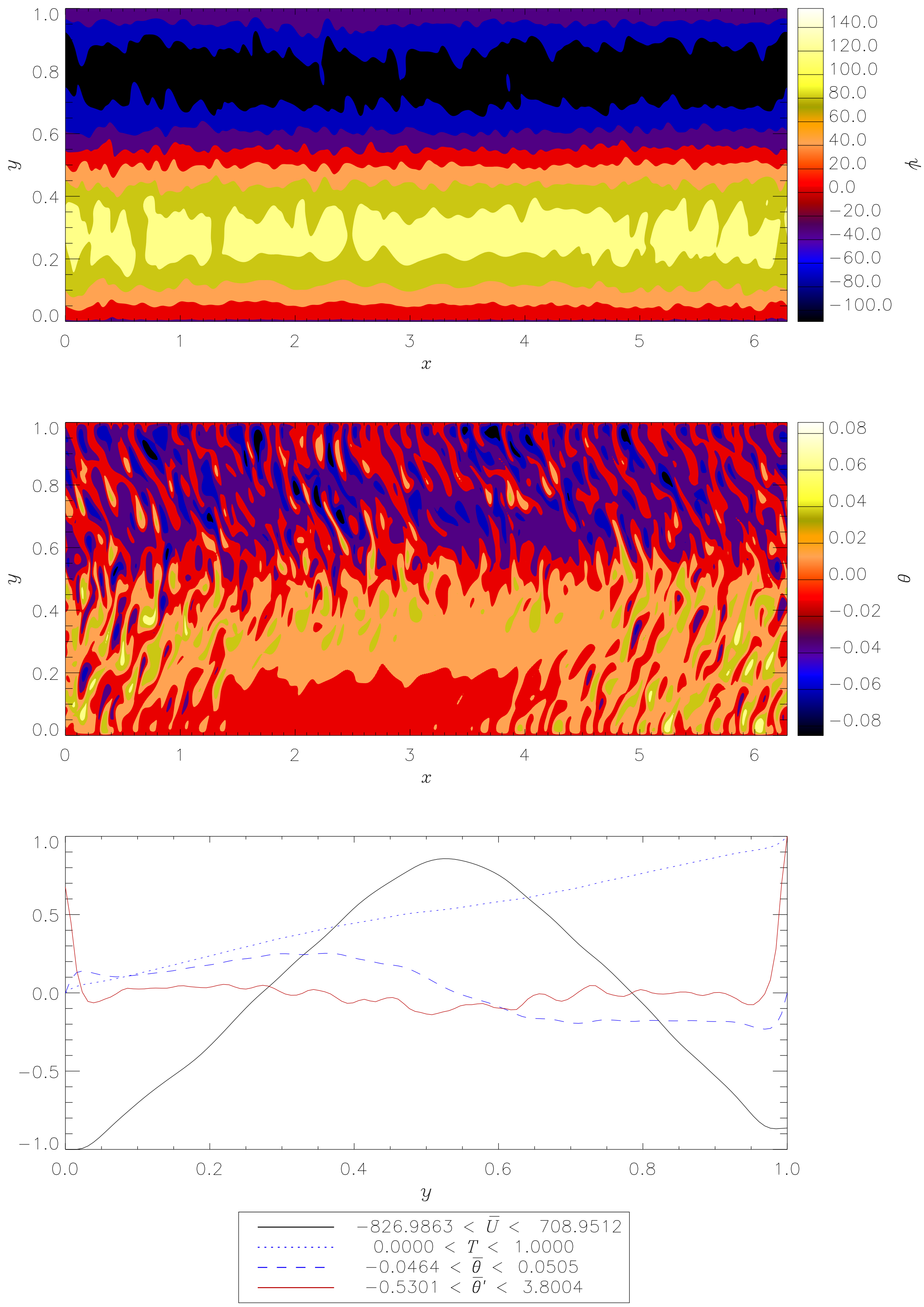

Figure 5.14: Contour plot for run XIV: $Pr = 2$, $\beta = 5 \times 10^5$, $C = 0$, $Ra/Ra_c = 2.75$.

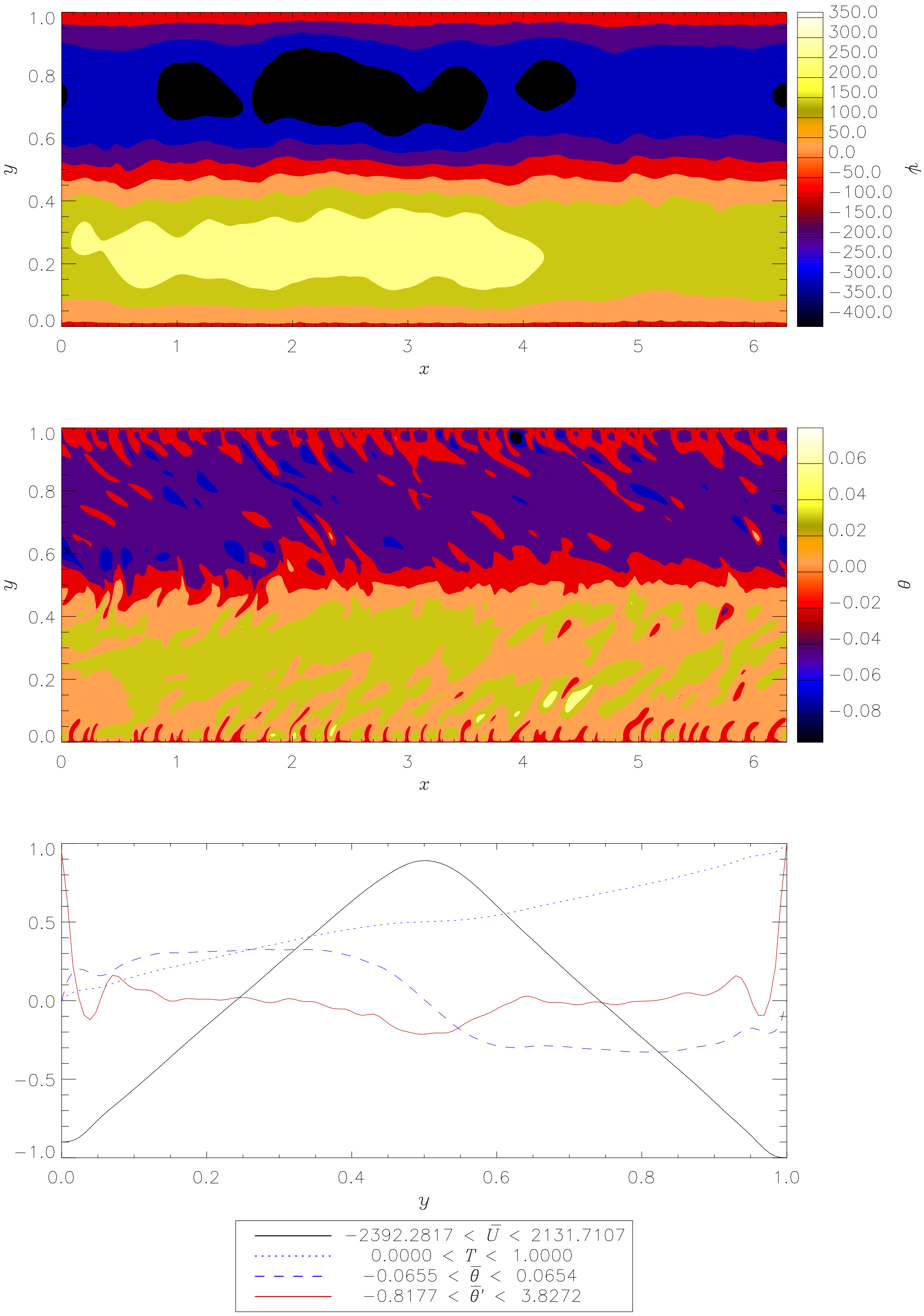

Figure 5.15: Contour plot for run XV: $Pr = 2$, $\beta = 5 \times 10^5$, $C = 0$, $Ra/Ra_c = 5$.

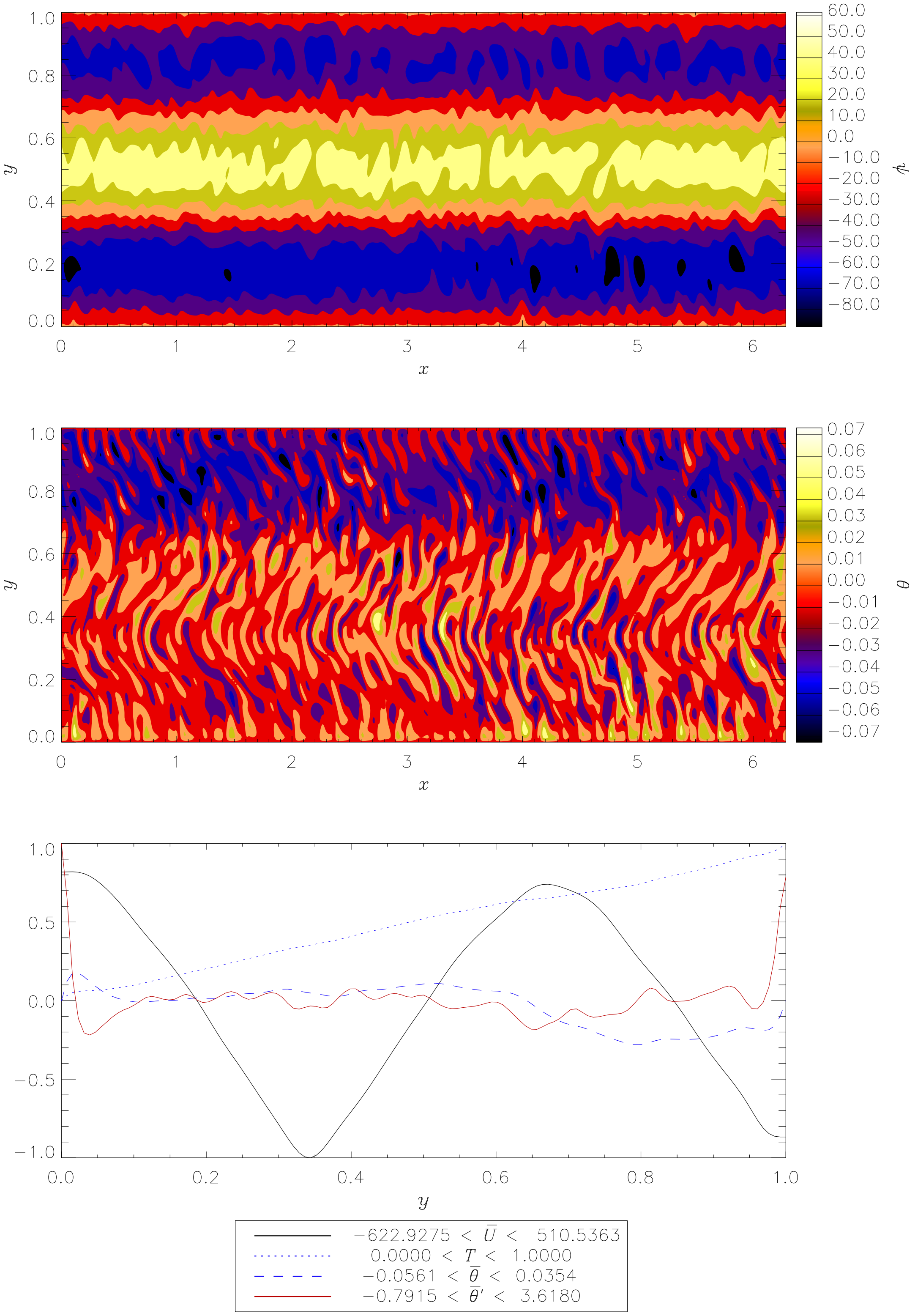

Figure 5.16: Contour plot for run XVI: $Pr = 2$, $\beta = 5 \times 10^5$, $C = 0.05$, $Ra/Ra_c = 2.75$.

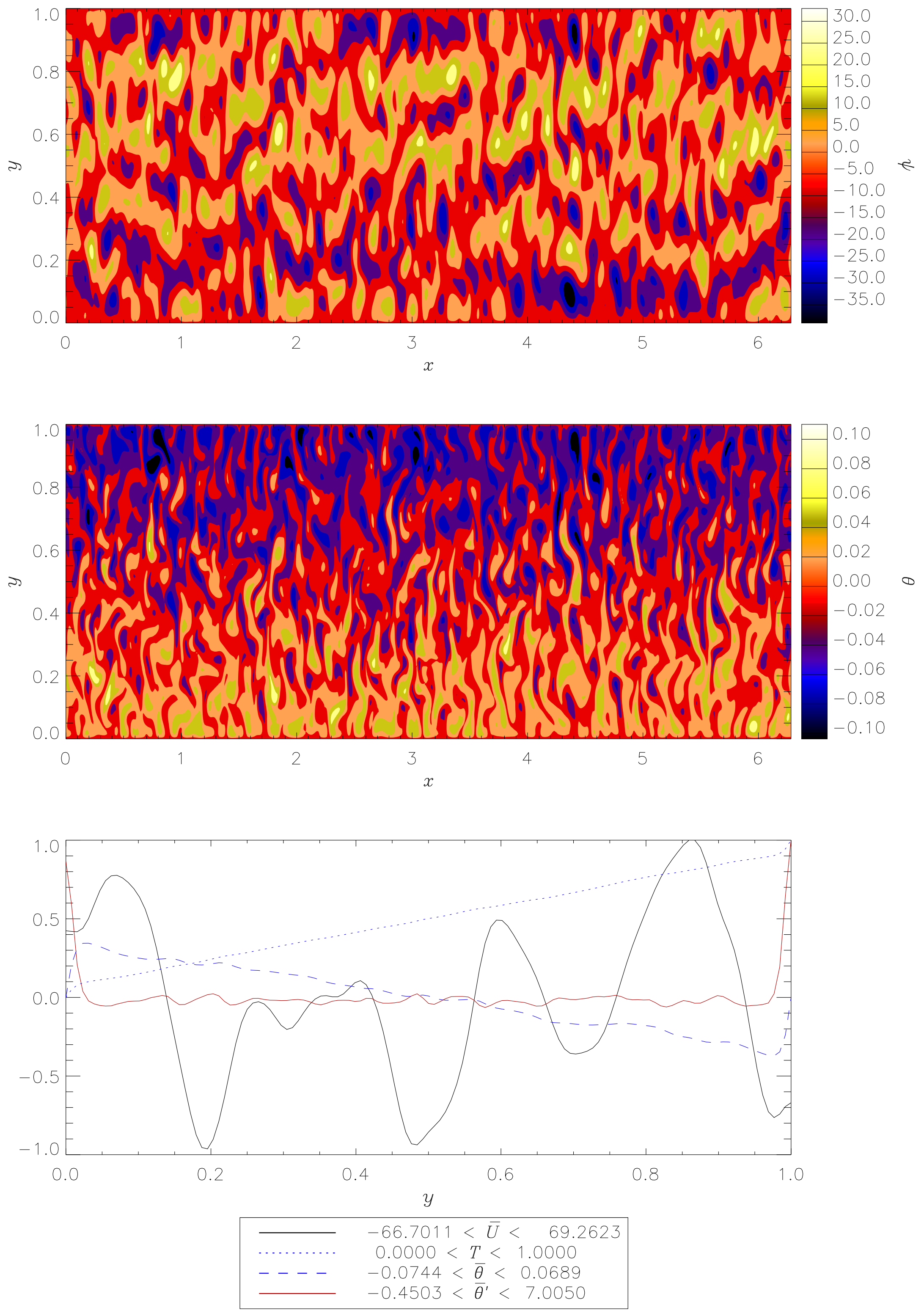

Figure 5.17: Contour plot for run XVII: $Pr = 2$, $\beta = 5 \times 10^5$, $C = 0.5$, $Ra/Ra_c = 2.75$.

time it takes to be diffused away. Also of note from figures 5.18 and 5.19 is the fact that the disturbances are becoming increasingly small-scale as the Prandtl number is increased. This is the cause of the increased resolution used for these, and other runs of the code, as we mentioned earlier. The increasingly small-scale nature in the x-direction of the fields is to be expected. The critical wavenumber (in the limit of rapid rotation) is given in equation (4.47) and we see that it is proportional to $(Pr/1 + Pr)^{1/3}$. Therefore the wavenumber, k, at onset becomes greater and the disturbances themselves become increasingly small-scale as Pr is increased.

For several of the runs VI to XIX we also plot, in figures 5.20 to 5.27, several more quantities as they evolve, for a period of time prior to each snapshot culminating at the timestep of the snapshot itself. The three plots displayed in each figure 5.20 to 5.27 from top to bottom represent the following. The top plot displays the various energies, at each timestep, which were defined by equations (5.43 - 5.44), namely the total kinetic energy, E_T, the zonal kinetic energy, E_Z, and the difference between the two, E_D. The remaining two plots contain the extremum values (that is, the maxima and minima) of the mean quantities, at each timestep. Figures 5.20 to 5.27 allow us to observe the bursting phenomenon that has been found in previous work (Rotvig & Jones, 2006).

Figure 5.20 shows that the zonal energy is relatively small for run XI. There are also no large fluctuations in the zonal flow though there are fluctuations in the energies. With such small fluctuations in the various quantities we can perhaps conclude that only very weak bursting is occurring in this run, if at all. The Rayleigh number is increased to five times critical in figure 5.21, for run XII, and the zonal energy now forms the majority of the kinetic energy in the system. There is also evidence of the bursting phenomenon with a gradual decline in of all the quantities in the three plots before a sharp increase at $t \approx 2.48$. The energy and mean quantity extrema plot for run XIII is omitted due to its similarity to other figures; the run does not show evidence of bursting.

Figure 5.22, which is for run VII, perhaps best showcases the bursts of convection with several bursts apparent. A clear quasi-periodic phenomenon is occurring with all quantities displaying an oscillatory nature. The zonal flow is oscillating over a range of approximately 500. At times when there is a sharp increase in the energy and the extrema of $\bar{U}$, the zonal flow is driven up by the convection. However, the strong shear of the

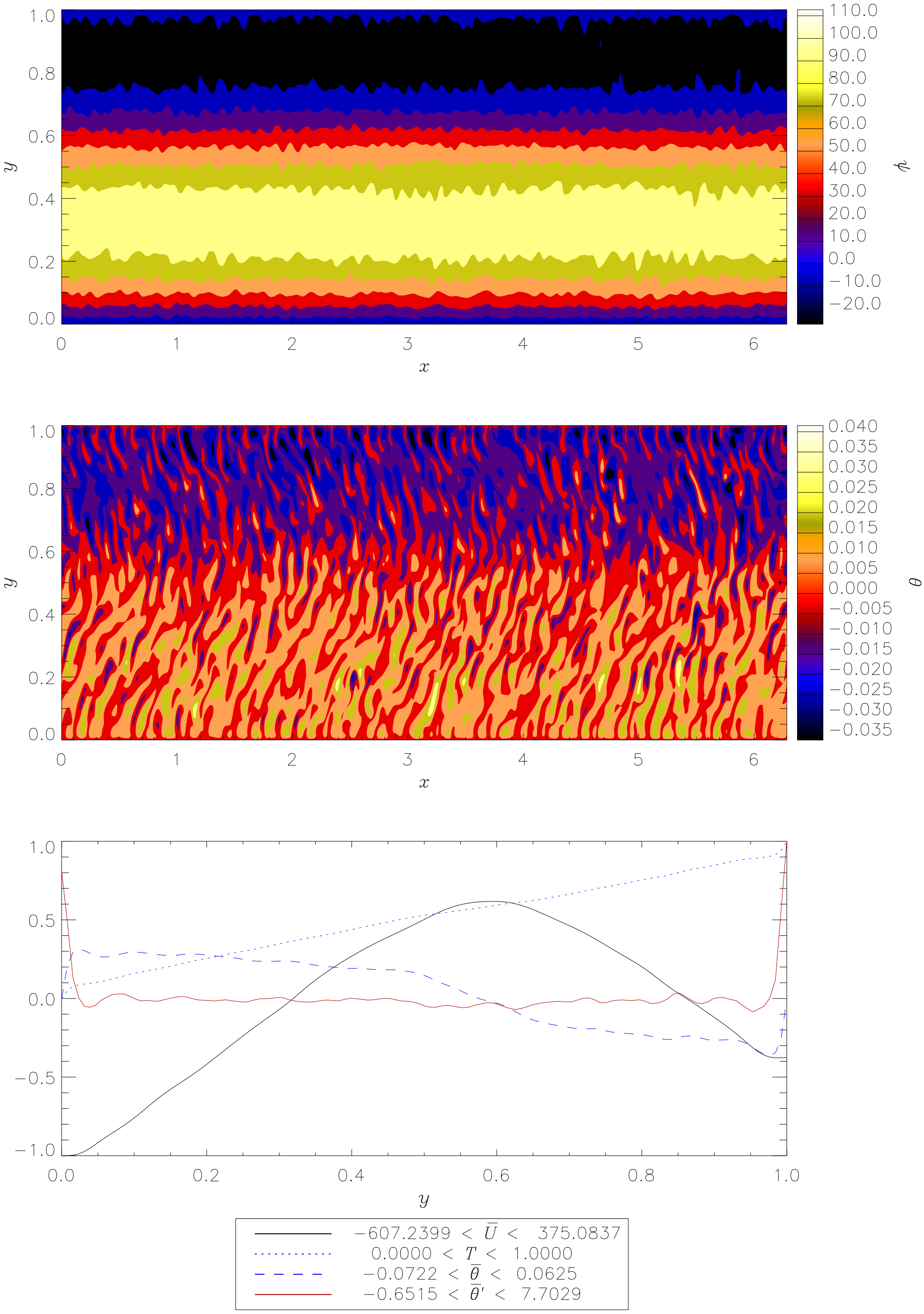

Figure 5.18: Contour plot for run XVIII: $Pr = 5$, $\beta = 5 \times 10^5$, $C = 0$, $Ra/Ra_c = 2.75$.

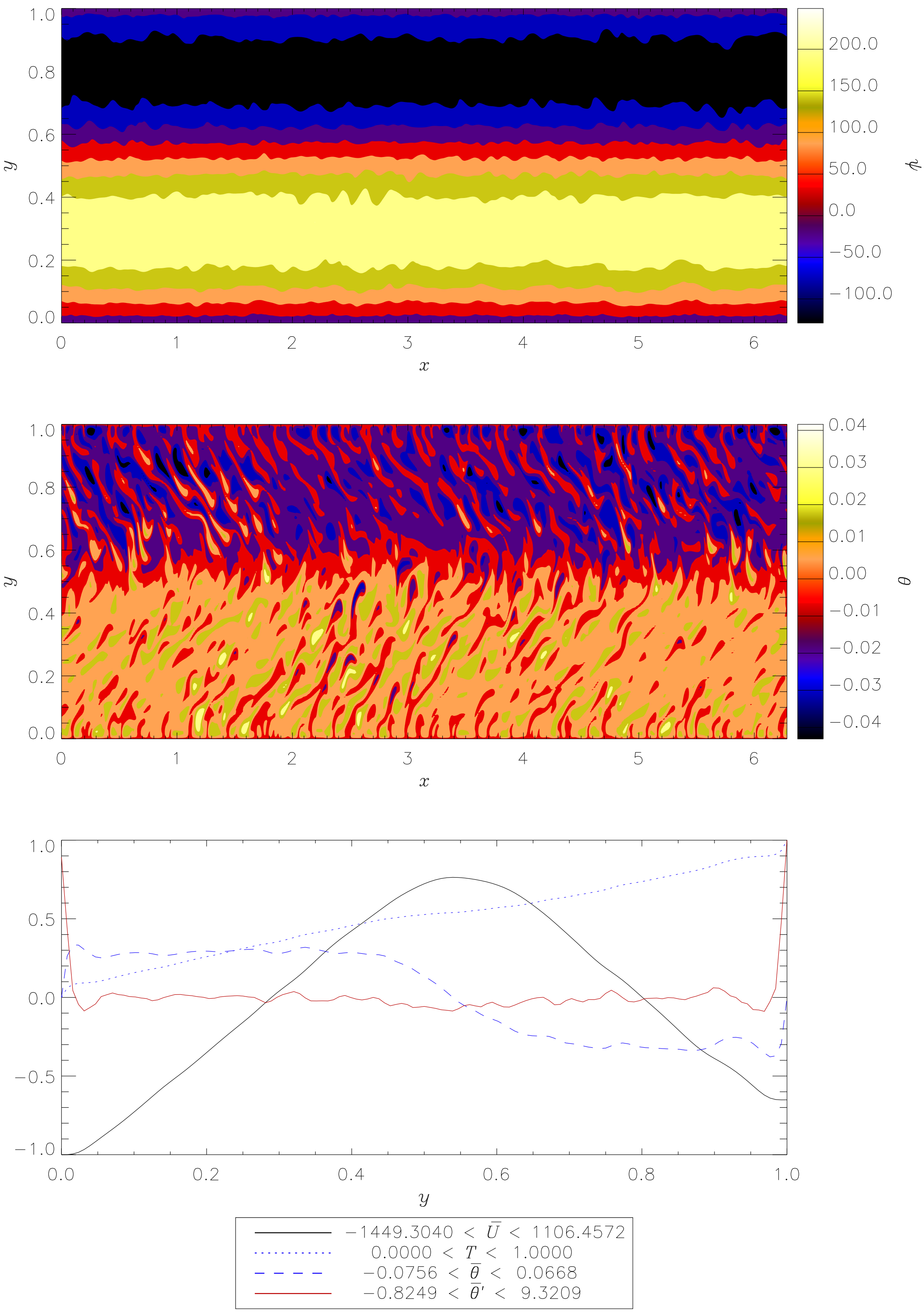

Figure 5.19: Contour plot for run XIX: $Pr = 5$, $\beta = 5 \times 10^5$, $C = 0$, $Ra/Ra_c = 5$.

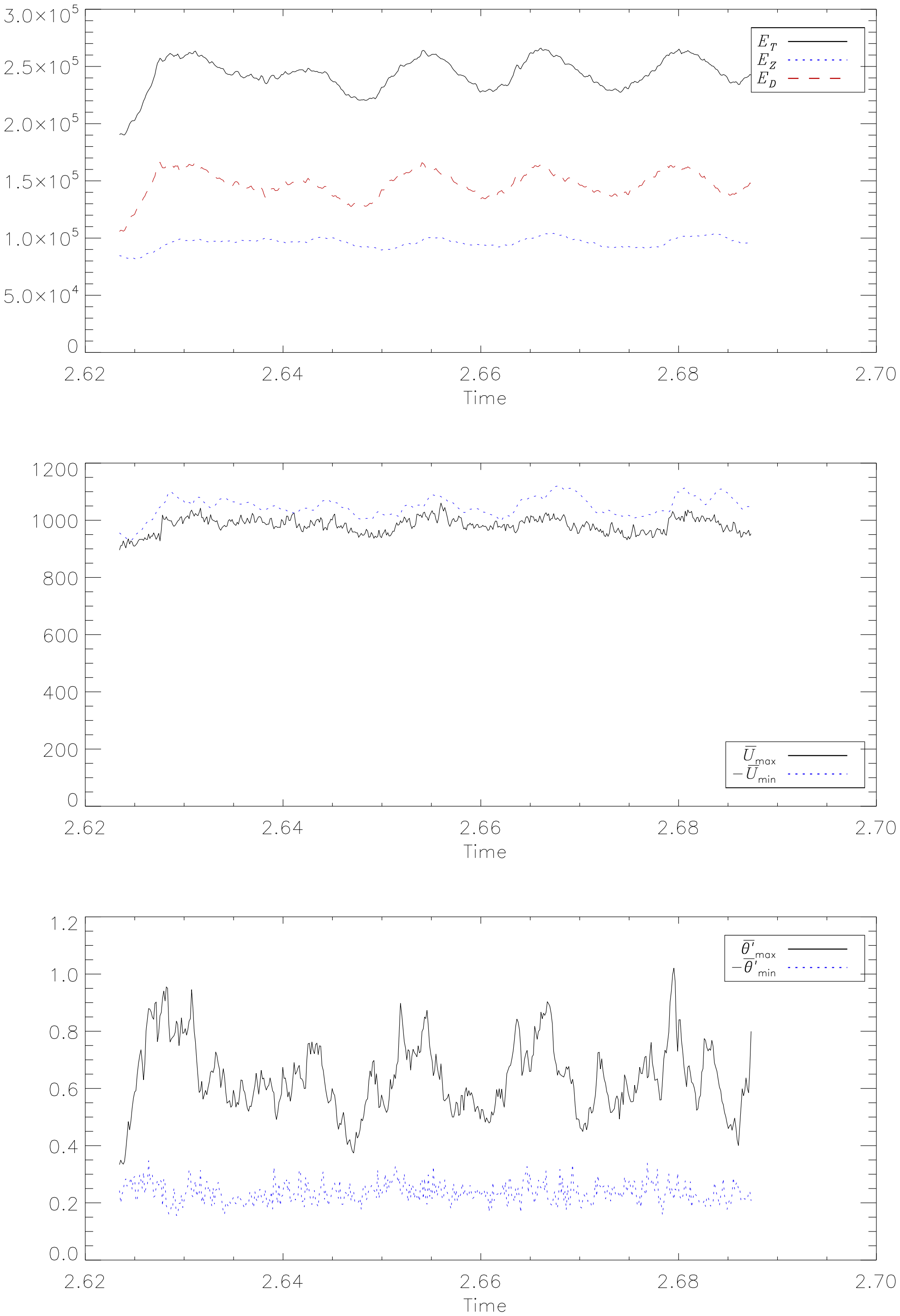

Figure 5.20: Energy and mean quantity extrema plots for run XI.

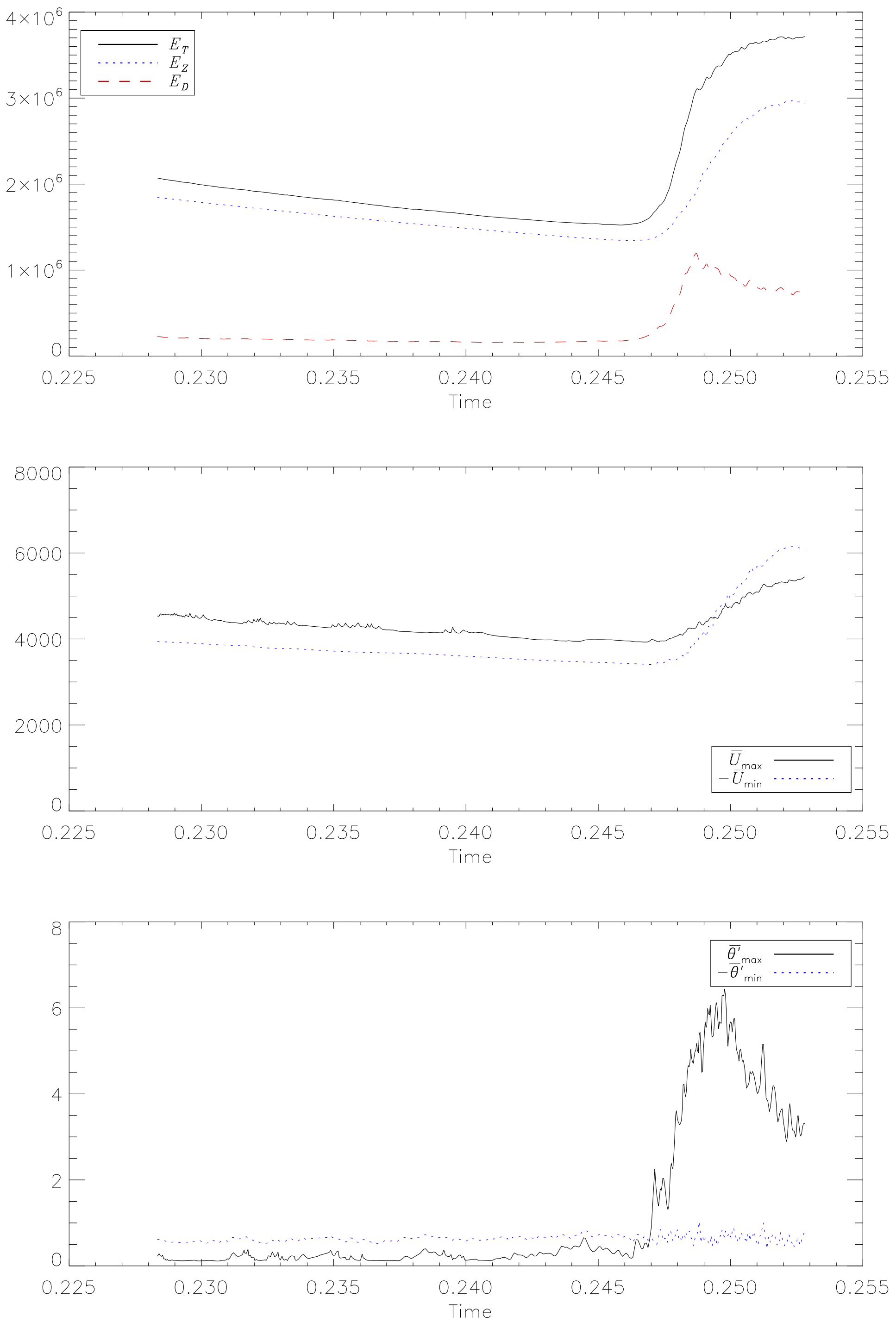

Figure 5.21: Energy and mean quantity extrema plots for run XII.

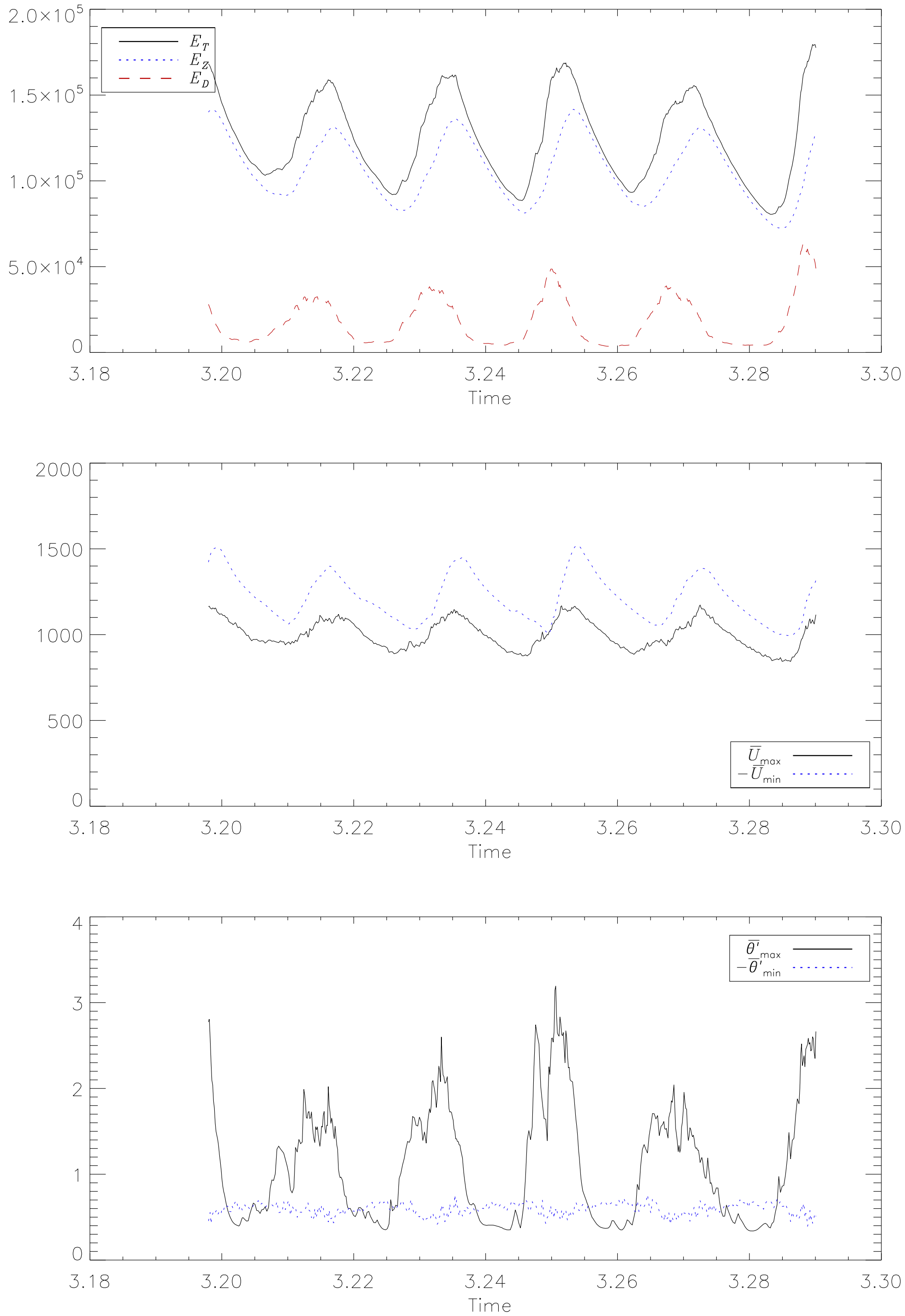

Figure 5.22: Energy and mean quantity extrema plots for run VII.

zonal flow then inhibits the convection, which depletes the source of energy for the zonal flow. Note that the maxima of the zonal energy occurs shortly after the maximum values of the extrema of $\bar{U}$. The zonal energy then decreases to a level that allows the convection to build up and a new burst can occur. Also of interest is the clear periodic nature of the mean temperature gradient in the third plot. This quantity was not studied in the previous work. However, the clear alignment of peaks of mean temperature gradient with the increase of the zonal energy suggests that it may too play an important role in the bursting phenomenon. Taken at the end of the time period displayed in figure 5.22 is the snapshot for this run, which was displayed earlier in figure 5.7. From figure 5.22 we see that the snapshot occurs when E_D is near a peak and figure 5.7 shows that convection is occurring almost everywhere. This is typical of many runs for times when the convective energy is large and therefore the convection occurs throughout the domain and is able to drive up the zonal flow. The figure for run VIII is omitted here due to its similarity to figure 5.21, though it too shows bursting.

We now move on to figures 5.23 and 5.24 which are also for $Pr = 1$ but bursting is less evident. In figure 5.23, for run IX with $C = 0.05$, bursting appears to be occurring but it is sporadic with certain time periods only producing small bursts. The range of the oscillations of the zonal flow is also smaller, now ≈ 300. For figure 5.24, where $C = 0.5$, the zonal flow is weak as shown by the energy plot. Also, bursting appears to have ceased with only very small oscillations in the extrema of the zonal flow occurring. Therefore, we can conclude that the bottom friction hinders the bursting phenomenon, which is in agreement with the previous work (Jones *et al.*, 2003; Rotvig & Jones, 2006). For the runs where bursting occurs for $Pr = 1$ (that is, runs VII, VIII and IX) the period of the bursting is found to be ≈ 0.02 of a diffusion time. This can be observed from figures 5.22 and 5.23.

We have again omitted a plot for run XIV (where $Pr = 2$) due to its similarity to figure 5.22. The only significant difference to be found is a reduction in the zonal energy and zonal flow extremum, which is to be expected for larger Prandtl numbers. However, in figures 5.25 and 5.26 we plot the energy and mean quantity extrema plots for runs XV and XVII where $Pr = 2$. Figure 5.25 once again shows clear evidence of bursting, this time at five times critical. The maximum values of E_T and $\bar{\theta}'_{\text{max}}$ continue to occur shortly before the peaks in $\bar{U}_{\text{max}}$ and $-\bar{U}_{\text{min}}$. The period of time between bursts has also

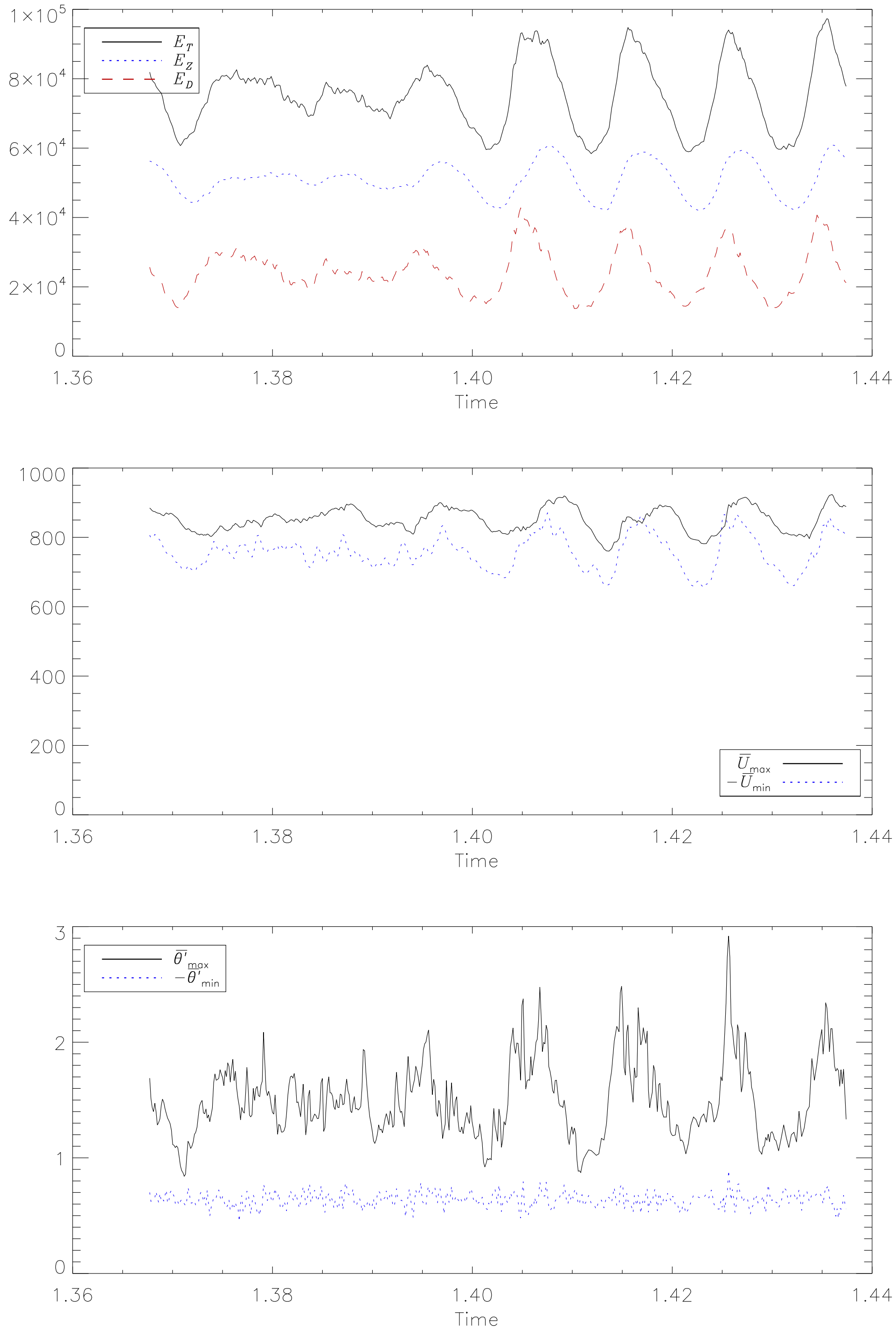

Figure 5.23: Energy and mean quantity extrema plots for run IX.

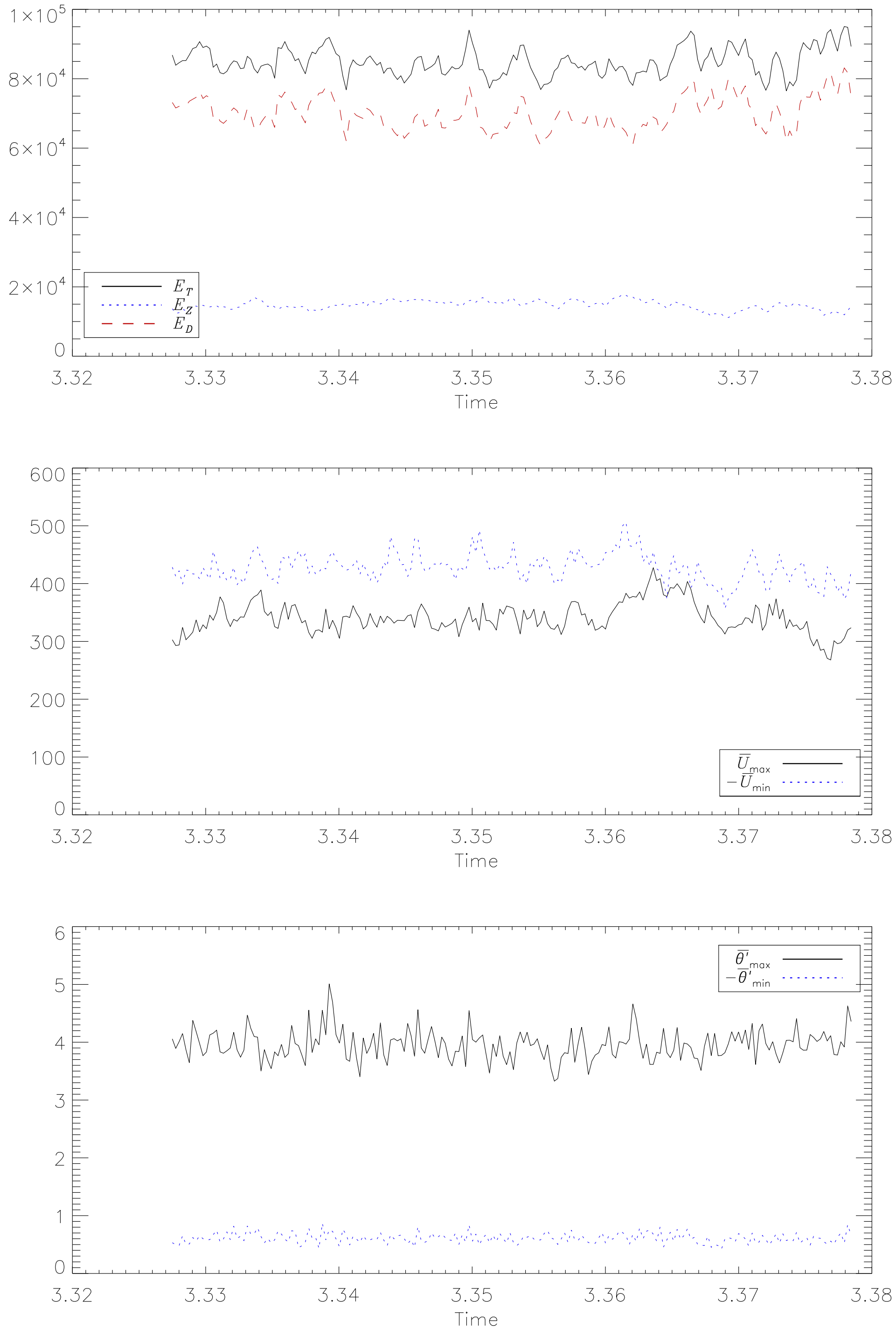

Figure 5.24: Energy and mean quantity extrema plots for run X.

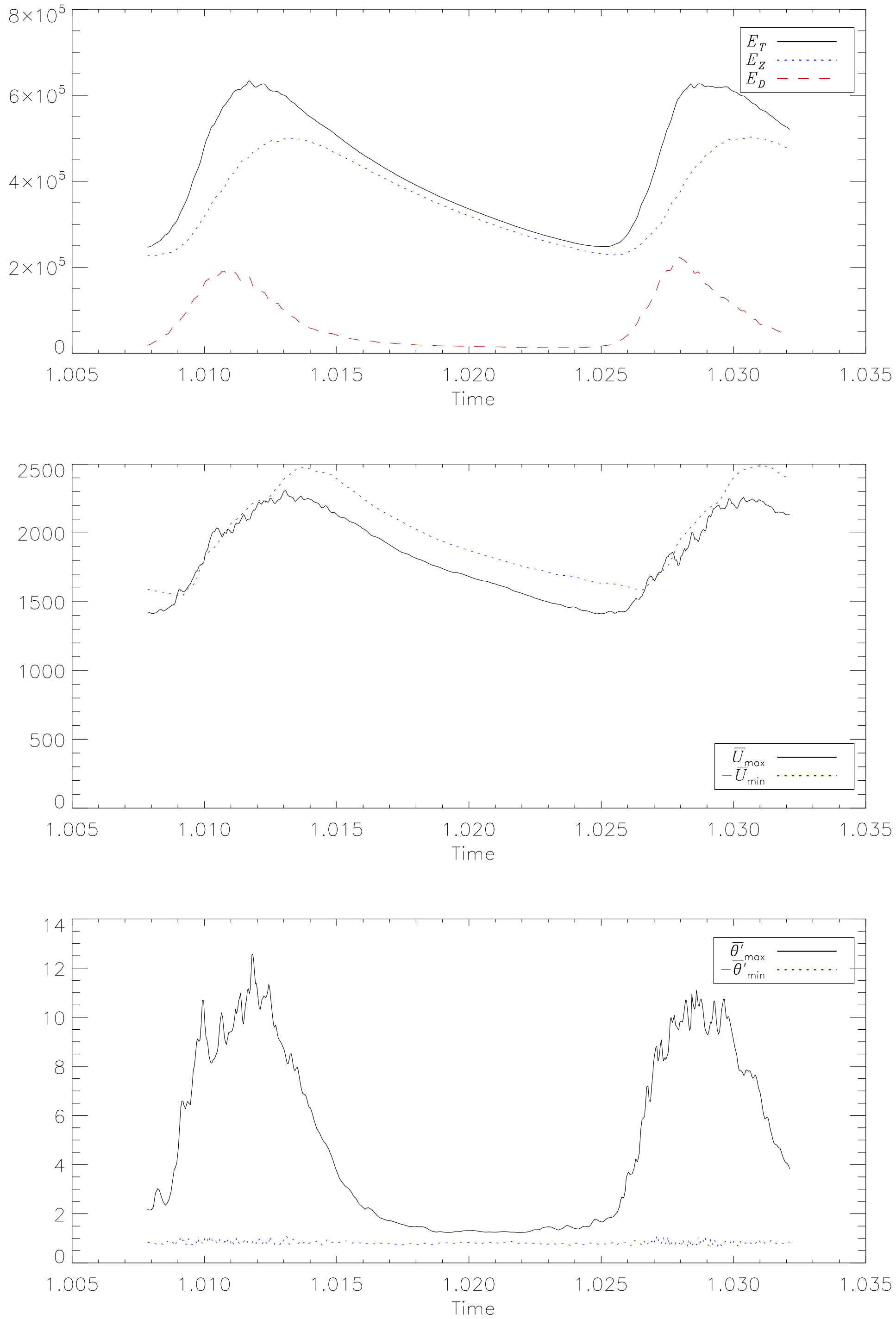

Figure 5.25: Energy and mean quantity extrema plots for run XV.

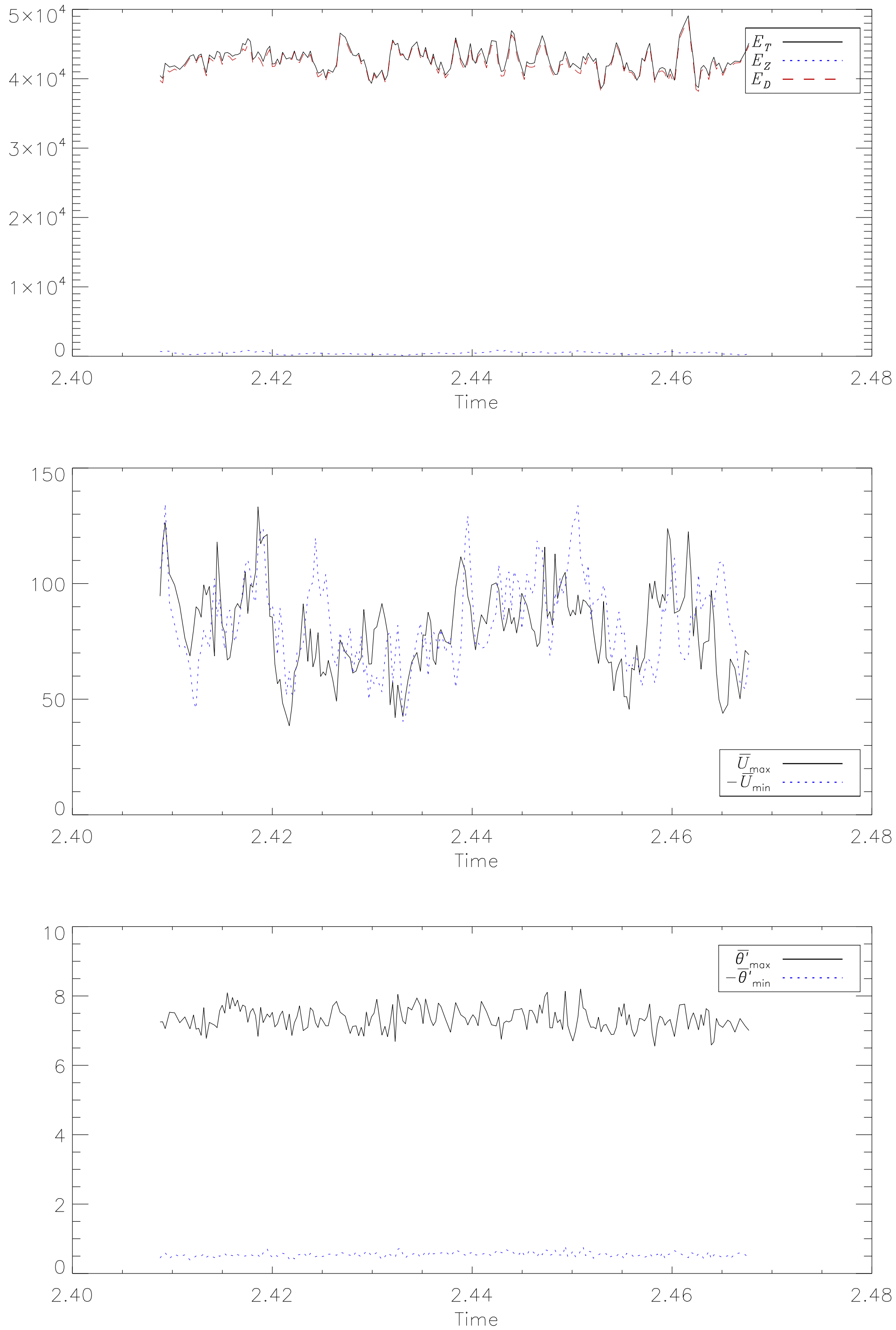

Figure 5.26: Energy and mean quantity extrema plots for run XVII.

remained constant at ≈ 0.02 despite the increase in the Prandtl and Rayleigh numbers compared with the earlier runs. This suggests that the period of the bursts is not strongly dependent on either Pr nor Ra. From figure 5.25 it is clear that the snapshot for this run (see figure 5.15) is taken during a time of strong zonal flow; that is post-convective burst. The convection in figure 5.15 is also localised due to the strong zonal flow. This is in contrast to figure 5.7 which is taken during a burst. This shows that during a bursting cycle there are both periods where convection occurs everywhere and where convection is localised. Also of note is that the range of the fluctuation in the maximum value of the mean temperature gradient is larger than in the cases of lower Prandtl number (compare with figure 5.21). We do not give a plot for run XVI; it is similar to figure 5.23. Figure 5.26 again shows that increasing the bottom friction causes the bursting to halt, as well as reducing the magnitude of the zonal flow itself. In particular, the energy plot of figure 5.26 shows that the zonal energy is extremely small indeed.

Our final plot of energies and extremum values of mean quantities in figure 5.27 is for run XVIII, where $Pr = 5$. We see that despite the zonal energy forming the majority of the kinetic energy the bursting has certainly ceased. The values of all quantities are nearly constant over a relatively long period of time. The same situation was found for run XIX, which has a larger Rayleigh number so bursting does not occur even for values of Ra that are several times critical.

We conclude this section by summarising the novel work performed. We have observed that the bursting phenomenon seems to only occur for a finite range of Prandtl numbers. Figures 5.20 and 5.21 showed that bursting can occur for $Pr = 0.5$ but is weak, at best, unless the Rayleigh number is large. There is plenty of evidence of bursting for $Pr = 1$ and $Pr = 2$ for both values of the Rayleigh number tested. However, as the Prandtl number is increased further the bursts of convection no longer arise, even for large Rayleigh numbers suggesting that the phenomenon ceases for some $Pr > 2$. In this section we also described how there were oscillations of the mean temperature gradient occurring along with the bursts of convection. This appears to have been overlooked in previous work. As we shall see in the next section the periodic nature of the mean temperature gradient plays a significant role in the production of the bursting phenomenon itself.

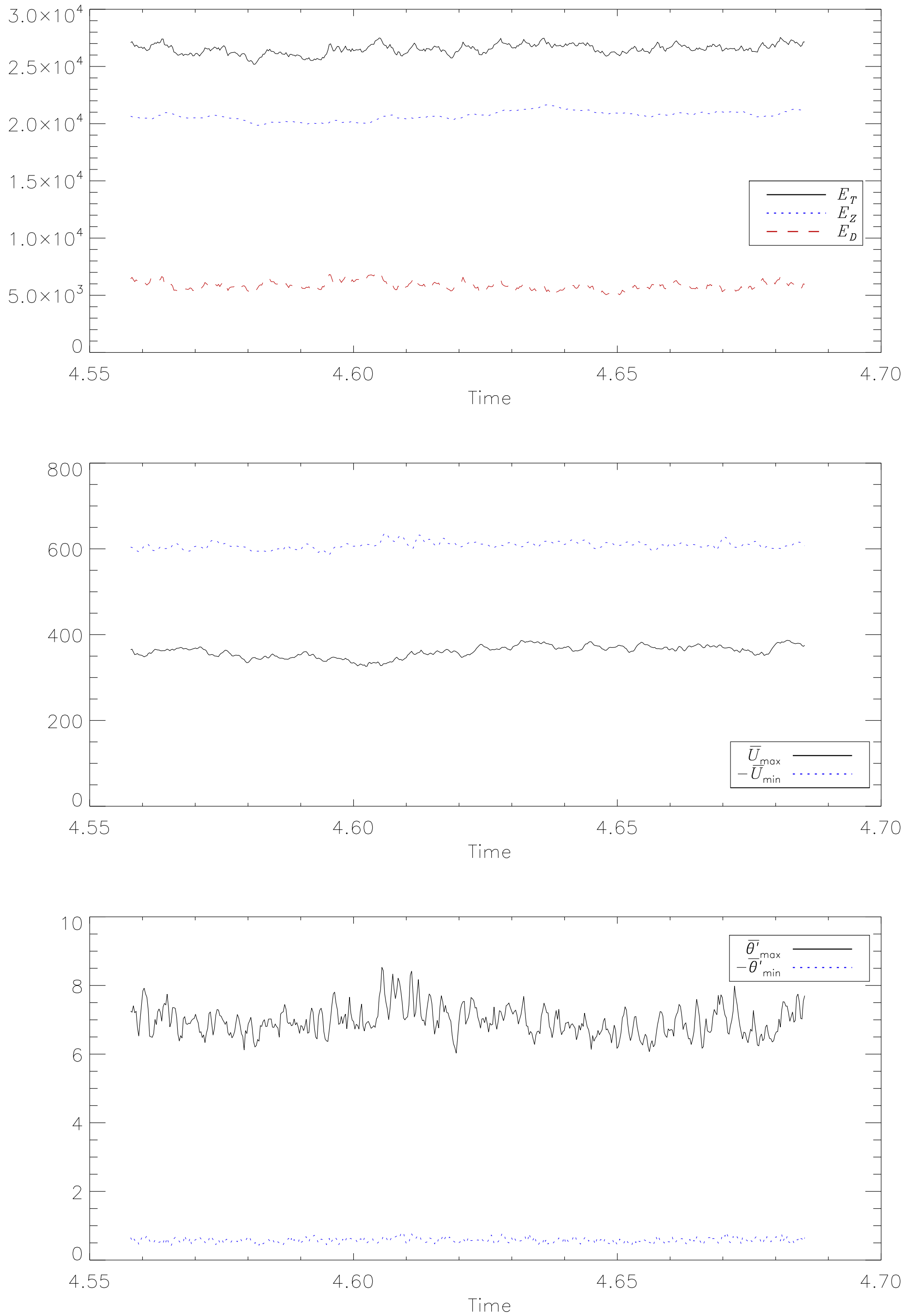

Figure 5.27: Energy and mean quantity extrema plots for run XVIII.

5.4 Linear results with mean quantities

In section 5.3 we were able to reproduce many of the results obtained by Jones *et al.* (2003); Rotvig & Jones (2006) including multiple jets and the appearance of the bursting phenomenon. In particular, we saw how large zonal flows and mean temperature gradients readily appeared under many parameter regimes. These zonal flows, which were formed by the time integration of the non-linear equations, will have a more realistic form than the zonal flows we posed in chapter 4. In fact, we mentioned in chapter 4 that there are infinitely many choices for the form of the zonal flow prescribed in the linear theory; that is $U_0(y)$. Hence it is sensible to perform the linear theory, as in chapter 4, with $U_0(y)$ set equal to the zonal flows evolved in the non-linear theory. This is what we consider in section 5.4.1. We also set $Re = 1$ throughout so that the magnitude of the zonal flow comes directly from its non-linear form.

In section 5.2 we also defined the mean temperature gradient and noticed that it too took a quasi-periodic form in time. It is possible to incorporate this mean temperature gradient into the linear theory in a similar way to the zonal flow. To do this we suppose that the basic state temperature used in the linear theory now takes the form

$$T_0 = \frac{\Delta T y}{D} + G_0(y), \tag{5.52}$$

where $\Delta Ty/D$ is the static temperature profile used previously (recall equation 4.4). Here $G_0(y)$ is a mean temperature profile, which gives rise to a mean temperature gradient in the basic state. This mean temperature gradient arises from non-linear interactions between the velocity and temperature perturbations and alters the basic state temperature gradient from that of the static gradient, $\Delta T/D$. Hence we can visualise this mean temperature gradient as the temperature profile analogy of $U_0(y)$ for the basic state velocity. Rather than having the basic state as being static (that is, $\mathbf{u_0} = \mathbf{0}$ and $T_0 = \Delta Ty/D$) we have now introduced the effects of non-linear terms into the basic state for both the velocity and temperature profiles.

We must now use the form of T_0 given in equation (5.52) to derive extra terms in our linear theory equations. This amounts to considering what terms arise from setting $T = G_0(y)$ in equations (4.5) and (1.15). Since G_0 has no x-dependence we see that no extra terms appear in equation (4.5) so that we retain

$$\frac{\partial \nabla^2 \psi}{\partial t} + ReU_0 \frac{\partial \nabla^2 \psi}{\partial x} - (\beta + ReU_0'')\frac{\partial \psi}{\partial x} = -Ra\frac{\partial \theta}{\partial x} + \nabla^4 \psi, \tag{5.53}$$

as the vorticity equation. Thus, recalling equation (4.26) we note that the vorticity equation remains unchanged under the addition of the mean temperature gradient. We must also consider new terms arising in the temperature equation, (1.15), with $T = G_0$. We ignore the zeroth order basic state terms so that only the second term (that is, the advection term) in equation (1.15) provides a new term, which is

$$(\mathbf{u} \cdot \nabla) G_0 \quad = \quad u_y \frac{\mathrm{d}G_0}{\mathrm{d}y} \quad = \quad \frac{\partial \psi}{\partial x}\frac{\mathrm{d}G_0}{\mathrm{d}y}, \tag{5.54}$$

using the definition of u_y from equation (4.7). Hence the heat equation, (4.27), is modified with this extra term so that it becomes

$$Pr\left(\frac{\partial \theta}{\partial t} + ReU_0\frac{\partial \theta}{\partial x} + \frac{\partial \psi}{\partial x}\frac{\mathrm{d}G_0}{\mathrm{d}y}\right) = -\frac{\partial \psi}{\partial x} + \nabla^2 \theta. \tag{5.55}$$

We use the runs discussed in section 5.3 to provide the mean quantities to be entered into the linear theory. Of course, as the system is evolved during these runs the zonal flow and mean temperature gradient change at each timestep. In order to fully analyse the effects of the mean quantities on the linear theory we perform the linear stability analysis *at each timestep*, rather than simply picking certain timesteps. This allows us to see how the growth rates of the linear system evolve as the dynamics of non-linear system evolve. Therefore we add the code that solves the linear theory from chapter 4 to the non-linear code (discussed in section 5.2) as a subroutine, which is called after every timestep. With the same parameter set as that being used in the non-linear run and with $U_0(y)$ and $G_0(y)$ set equal to $\bar{U}$ and $\bar{\theta}$ respectively, the subroutine outputs the growth rates.

In the plots that we shall discuss, the growth rate, wavenumber and frequency will be functions of time for the same time periods as those taken for the plots in figures 5.20 to 5.27. Therefore we shall be able to directly compare the outputs from the linear theory with those of the non-linear theory, over the same time intervals. We are primarily interested in the growth rate of the fastest growing mode and how it varies as the non-linear system is evolved. This is because we wish to ascertain if the magnitude of any growth varies with the mean quantities. Consequently, we primarily look at the linear outputs for runs of section 5.3 where the bursting phenomenon was witnessed. We split the remainder of this section into three subsections where we consider the linear theory with the addition of a) the non-linear zonal flow, b) mean temperature and c) both mean quantities.

5.4.1 Linear results with non-linear zonal flow

We first consider the linear stability results in the case where only the zonal flow, $\bar{U}$, is included in the linear theory. Hence in this subsection we set $U_0(y) = \bar{U}(y)$ and $G_0(y) = 0$ in the linear equations, (5.53) and (5.55). The procedure here is similar to that of chapter 4 where only a zonal flow was included in the basic state. However, unlike chapter 4 where marginal stability was considered so that $\sigma = 0$ and $Ra = Ra_c$, here we are looking for the fastest growing mode with the Rayleigh number equal to that of the non-linear runs. Figures 5.28 to 5.31 show how the growth rate, σ, frequency, ω, and wavenumber, k, vary as the non-linear system is evolved, for several runs from table 5.1.

We first consider figure 5.28, for run XII, which can be compared with the plots of figure 5.21. By doing so we see that there is certainly correlation between the growth rate and the zonal energy and extrema of the zonal flow. As the zonal flow strength gradually decreases the quantities plotted in figure 5.28 remain fairly constant. However, there is a sudden increase in σ and k at $t \approx 0.247$, which is where E_Z attains its minimum. This is to be expected as the growth of convection should occur when the zonal flow is weakest. Although the range of the growth rate is quite large, we notice that σ is never less than ≈ 1500. Therefore the zonal flow reduces the growth of the convection but does not completely cause it to cease. As E_Z increases after $t \approx 0.247$ the growth rate begins to decrease again due to the disruption of the convection by the additional strength of the zonal flow.

If we now move on to figure 5.29, for run VII, we again see some correlation with the plots of figure 5.22. Unlike in the case for run XII, the growth rate now remains relatively constant. The correlation with E_Z in figure 5.22 is also far less obvious, so it seems again that the zonal flow is not sufficiently affecting the growth of convection. There is excellent correlation however between the frequency, ω, and the zonal flow strength. The frequency is smallest in magnitude when the zonal flow is weakest. Peaks in k also coincide with locations of strong zonal flow although the range of the wavenumber is small.

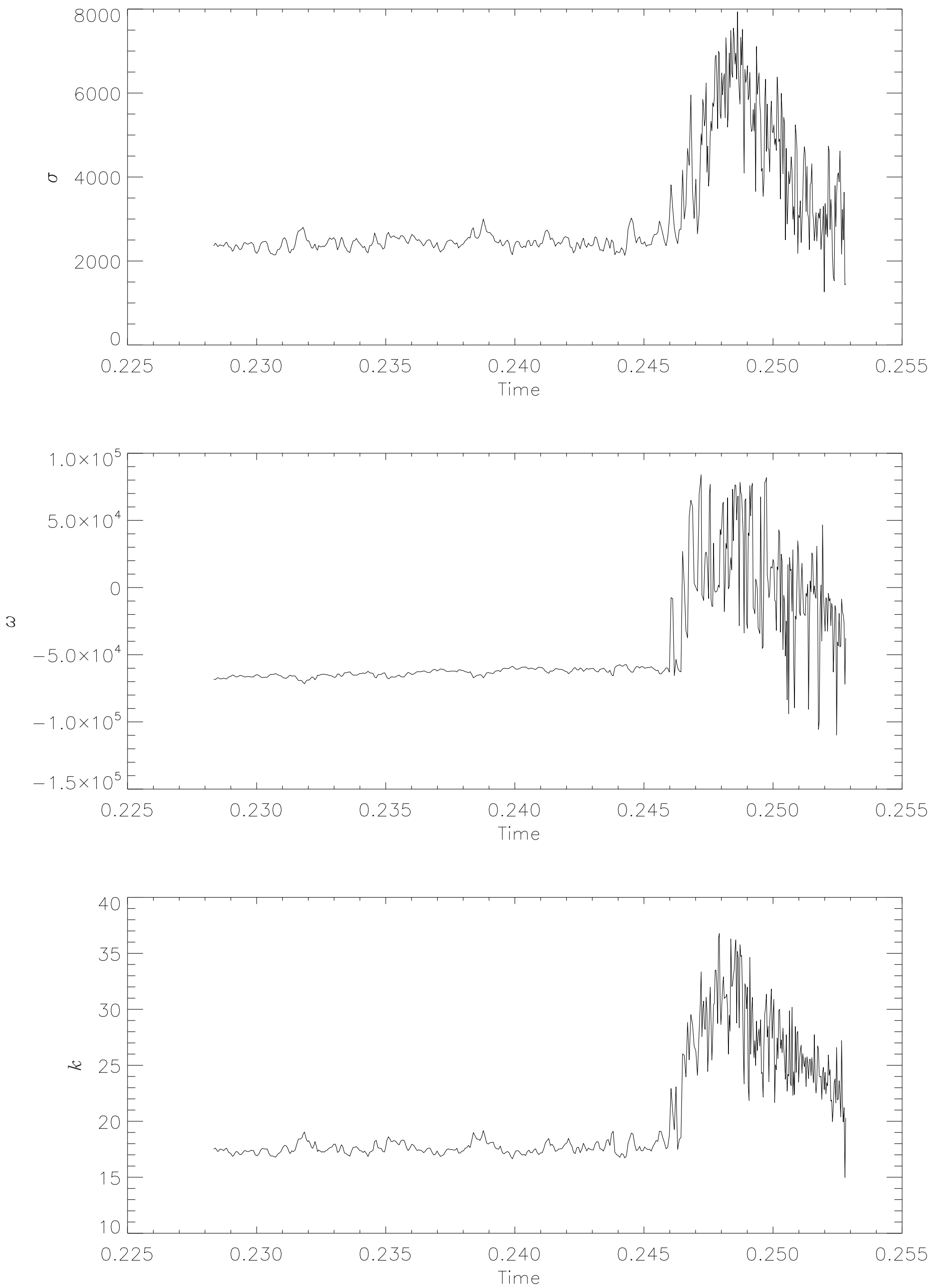

Figure 5.28: Growth rate, frequency and wavenumber plots for run XII with non-linear zonal flow.

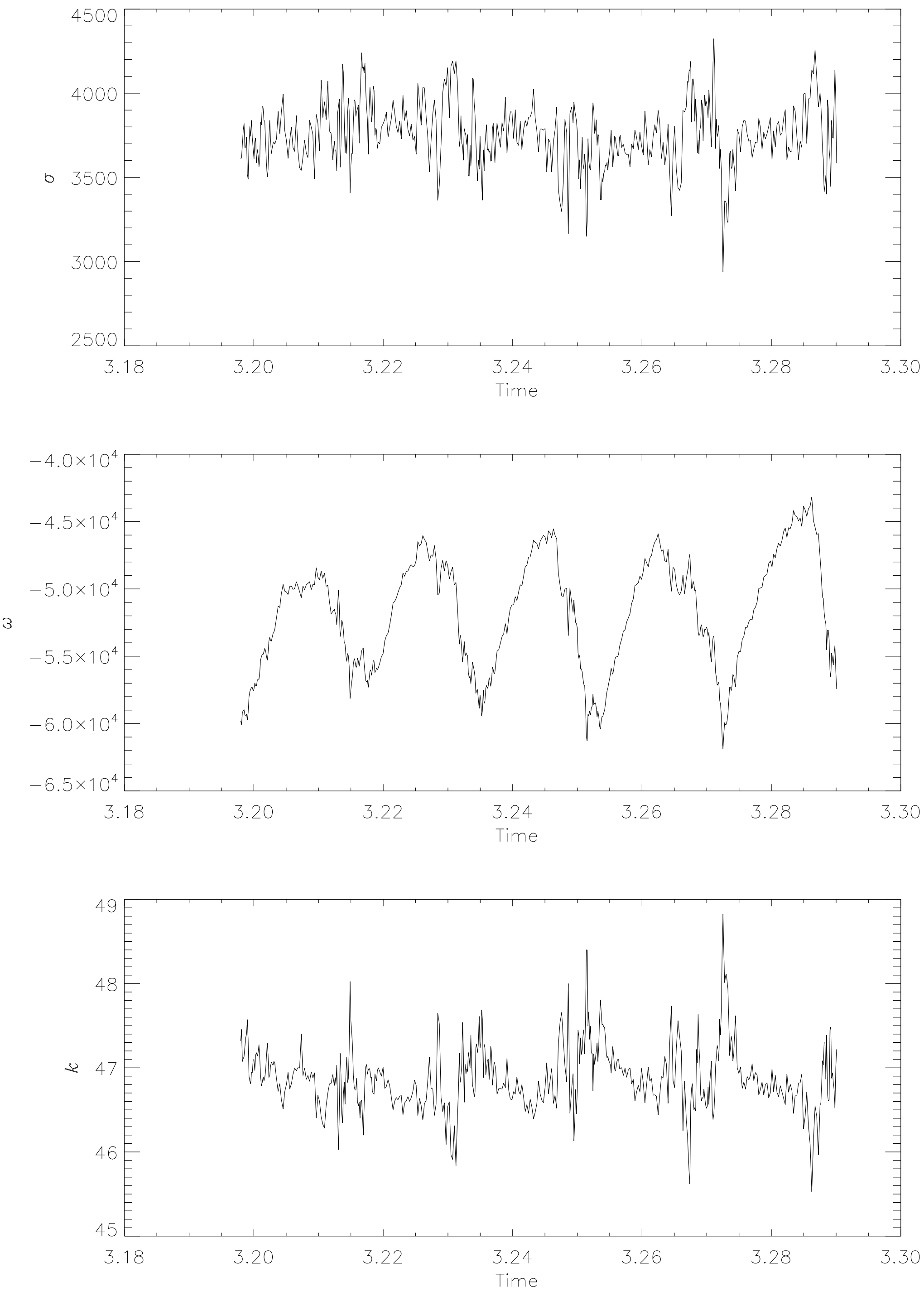

Figure 5.29: Growth rate, frequency and wavenumber plots for run VII with non-linear zonal flow.

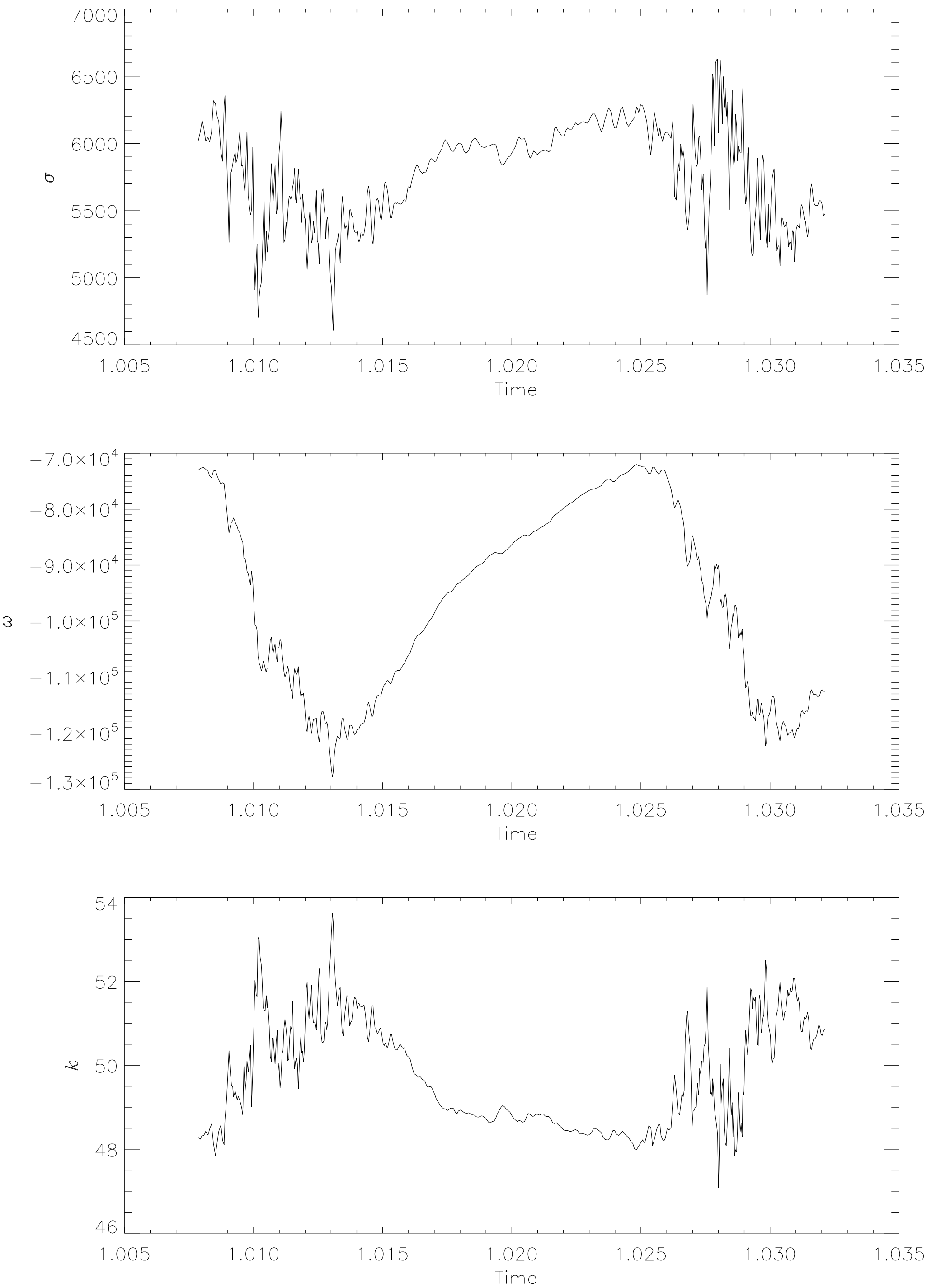

Figure 5.30: Growth rate, frequency and wavenumber plots for run XV with non-linear zonal flow.

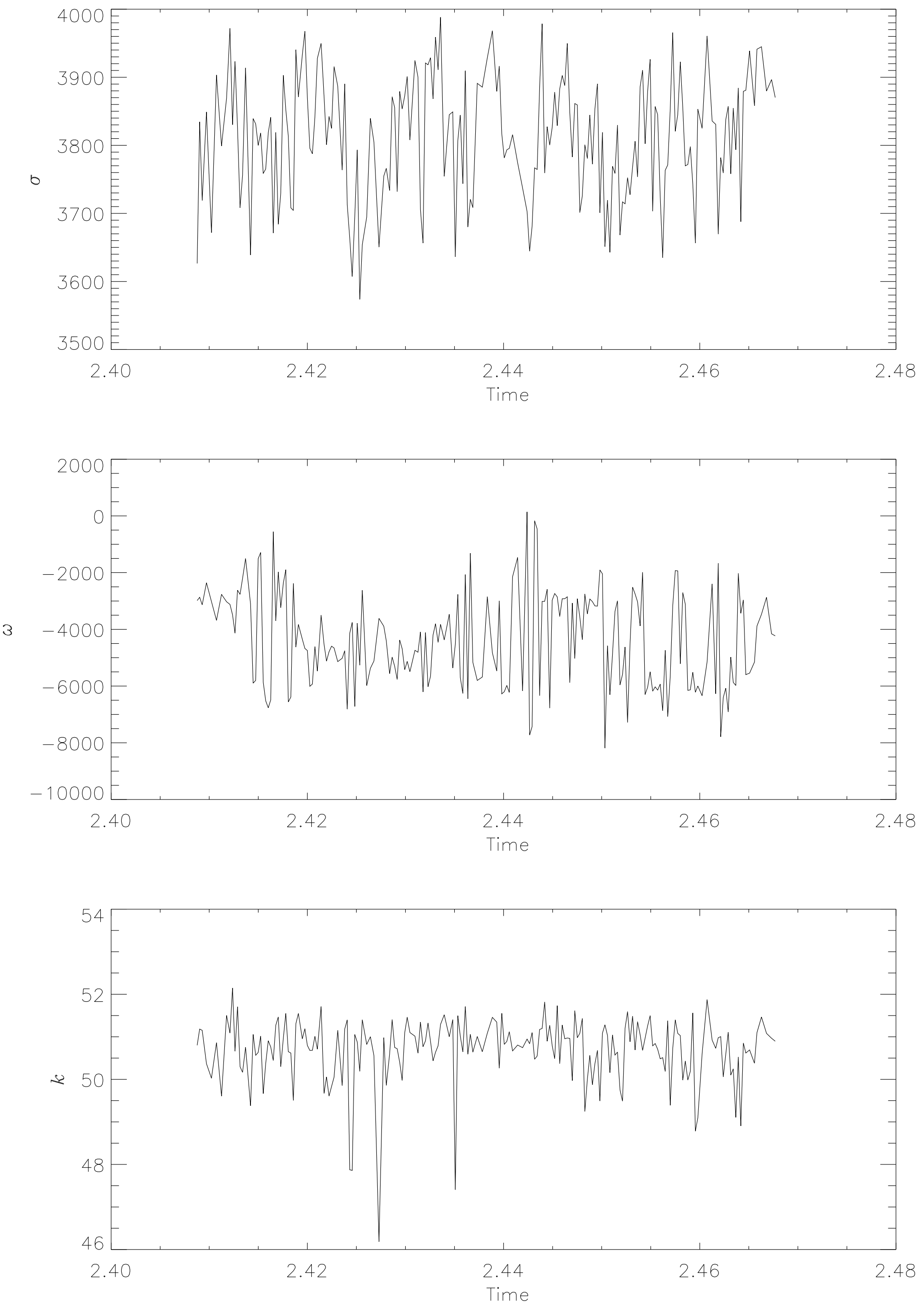

Figure 5.31: Growth rate, frequency and wavenumber plots for run XVII with non-linear zonal flow.

Run XV also displays bursting and again there is correlation between the quantities of figures 5.30 and 5.25. Once again the minimum growth rate is attained when the zonal energy is largest and the zonal flow is unable to reduce the growth rate to marginal or decaying modes. Peaks in $|\omega|$ and k are again found when E_Z acquires a maximum, at $t \approx 1.013$ and $t \approx 1.030$. Finally for this subsection we consider a run for which bursting was not observed; namely run XVII. When comparing figures 5.31 and 5.26 we immediately notice the lack of correlation between quantities that was present for the previous runs discussed. The range of σ, ω and k is far smaller due to the weakened zonal flow in this run and thus the departure from the $U_0 = 0$ case is minimal.

We can conclude from this subsection that the zonal flows of the non-linear theory certainly have a profound effect on the linear growth rates of convection. For runs where bursting is observed, the peaks in the growth rate coincide with times when the zonal flow is weakest. However, the zonal flow is unable to halt the growth of convection altogether as evidenced by the lack of negative growth rates in figures 5.28 to 5.31. Therefore another process, at least in part, must be responsible for the sufficient reduction in convective growth. In the next subsection we consider whether the non-linear mean temperature gradient can fulfill this role.

5.4.2 Linear results with non-linear mean temperature gradient

We now consider the linear stability results in the absence of any zonal flow but with the mean temperature gradient, $\bar{\theta}'$, included. Thus, in this subsection we set $U_0 = 0$ and $G_0 = \bar{\theta}$ in the linear equations, (5.53) and (5.55). Figures 5.32 to 5.35 contain plots displaying how σ, ω and k vary as the non-linear system is evolved when only the mean temperature gradient is included in the linear system. As with the previous subsection we can compare these plots with the energy and mean quantity extremum plots for the relevant runs from section 5.3.

We first consider figure 5.32, for run XII, which can be compared with figure 5.21. All three of the quantities in figure 5.32 remain near constant to begin with since the extrema of the mean temperature gradient are also approximately constant for $t < 0.247$. The sudden increase in $\bar{\theta}'_{\max}$ at $t \approx 0.247$ is accompanied by an abrupt reduction in the growth rate. This is to be expected since if the mean temperature gradient is able to partially (or indeed, fully) cancel out the static temperature gradient, the overall gradient will be less adverse. Thus the system will be less eager to convect, resulting in smaller growth rates. However, even when the mean temperature gradient is strong the growth rate is only reduced by approximately 10%. In fact, this is a smaller reduction of the growth rate than was present in the previous subsection. Associated with the region of strong mean temperature gradient there is also a reduction in $|\omega|$ and the wavelengths of the modes.

The plots in figure 5.33, for run VII, show clear correlation with 5.22. The growth rate oscillates, though again does not reduce significantly. Shortly after each peak in $\bar{\theta}'_{\text{max}}$ there is minimum of the growth rate, as expected. The correlation of the frequency and wavenumber is also clear with the same dependence as seen before. In figure 5.34, for run XV, we again see the same pattern of correlation by comparing with figure 5.25. Peaks of $\bar{\theta}'_{\text{max}}$ at $t \approx 1.012$ and $t \approx 1.029$ are associated with weak growth and short wavelengths whilst the intermediate period has increasing growth. There is a lack of order in the plots for run XVII, displayed in figure 5.35, where only small fluctuations in σ, ω and k are observed. This is to be expected due to the near constant values that the extrema of the mean temperature gradient take in figure 5.26.

In this subsection we have discussed the effect that the addition of the non-linear mean temperature gradient has on the linear stability in the absence of zonal flow. The observations are similar to the previous subsection. A strong mean temperature gradient can indeed reduce the growth rate of convection due to a reduction in the overall adverse temperature gradient present. However, the growth rate does not become marginal or negative even during times of strong mean temperature gradient. We would expect to find $\sigma \approx 0$ during the periods just prior to the convective bursts and hence it does not seem that a mean temperature gradient alone can produce bursting. The analogous result was found in the previous subsection for systems with zonal flow but no mean temperature gradient included. Therefore we propose that *both* mean quantities are required to produce bursts and we test this conjecture in the next subsection.

5.4.3 Linear results with both non-linear mean quantities

We have seen in the previous two subsections that including only one of the mean quantities in the linear theory does not yield the required range of the growth rate expected

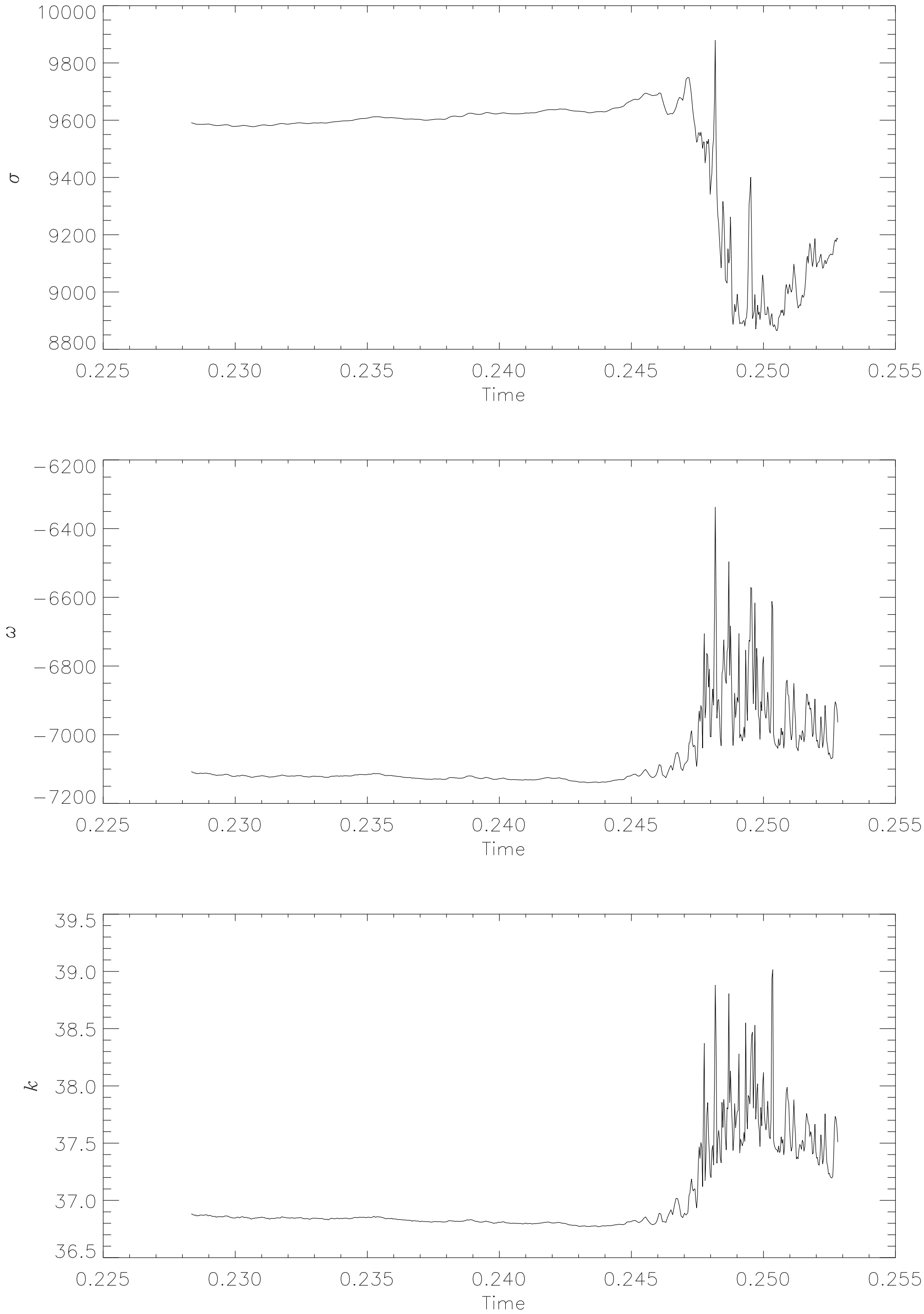

Figure 5.32: Growth rate, frequency and wavenumber plots for run XII with non-linear mean temperature gradient.

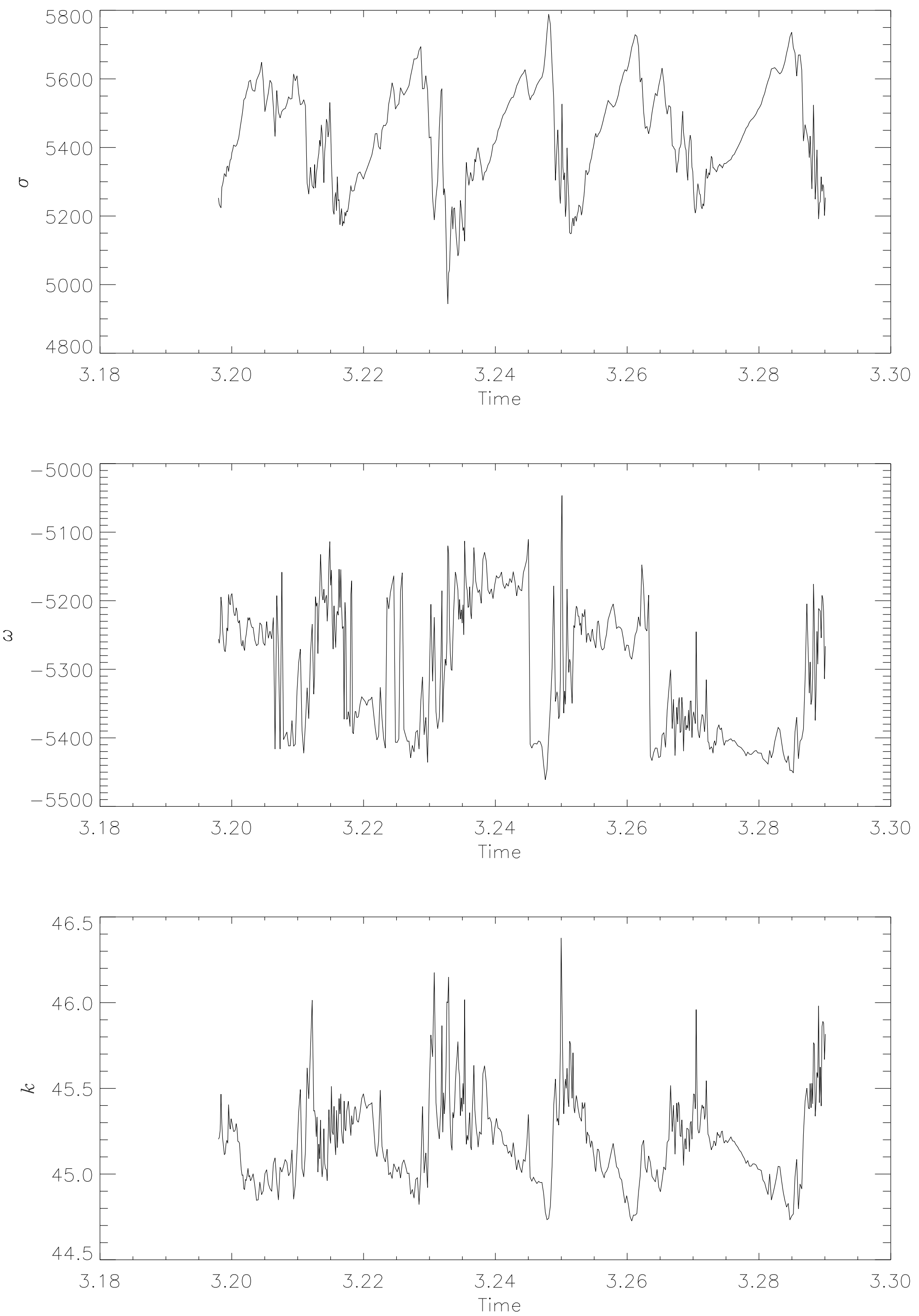

Figure 5.33: Growth rate, frequency and wavenumber plots for run VII with non-linear mean temperature gradient.

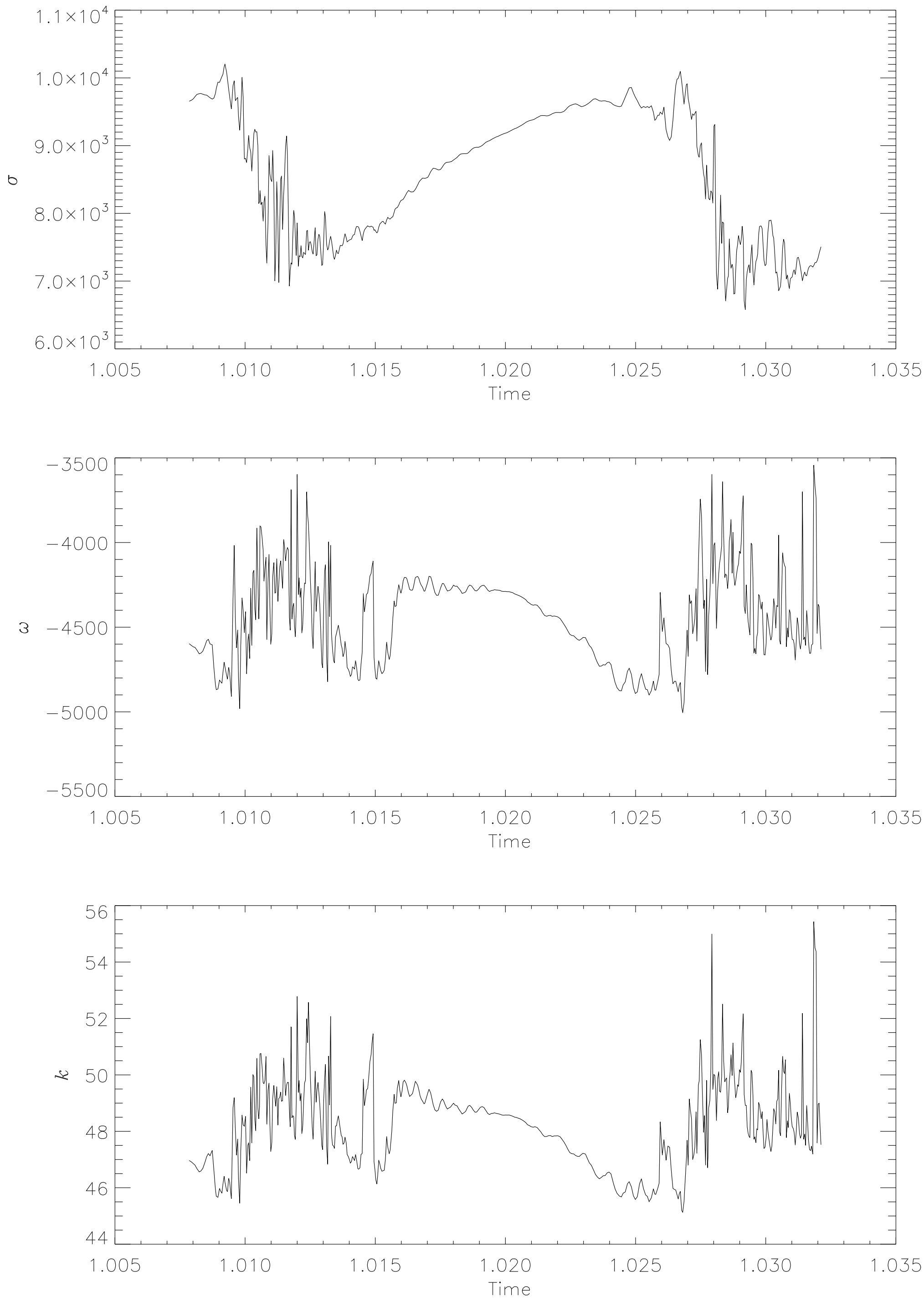

Figure 5.34: Growth rate, frequency and wavenumber plots for run XV with non-linear mean temperature gradient.

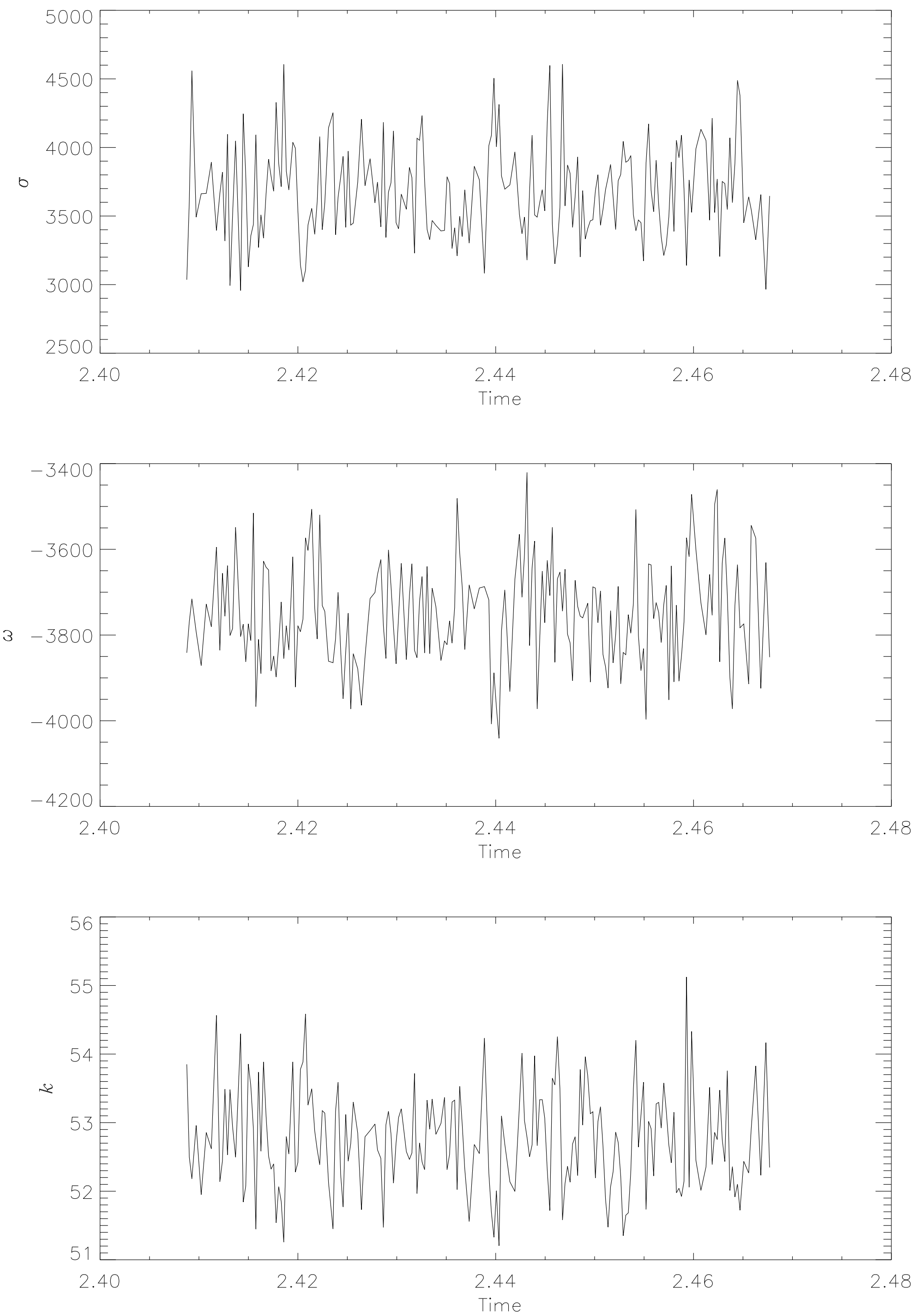

Figure 5.35: Growth rate, frequency and wavenumber plots for run XVII with non-linear mean temperature gradient.

for bursts of convection. We therefore expect that the bursting is controlled by both a zonal flow and a mean temperature gradient together and that both are necessary to produce the phenomenon. Hence we now finally consider the linear stability results with both mean quantities, $\bar{U}$ and $\bar{\theta}'$, included. Therefore in this subsection we set $U_0 = \bar{U}$ and $G_0 = \bar{\theta}$ in the linear equations, (5.53) and (5.55). As with the previous subsections, we compare the plots of figures 5.36 to 5.39 for σ, ω and k with the energy and mean quantity extremum plots for the relevant runs from section 5.3.

The comparison of figure 5.36, for run XII, with figure 5.21 shows that there is again correlation between the linear quantities and the non-linear energies. In fact, the plots of figure 5.36 are extremely similar to those of figure 5.28 where only the zonal flow was included. Strong growth of the same order of magnitude remains possible at times when the zonal flow and mean temperature gradient are weak. However, the key difference between these sets of plots is that, for the case where both mean quantities are included, the growth rate is approximately zero when the mean quantities are large. This was not the case previously and therefore including both mean quantities has given the desired result which is the ceasing of the convection.

The correlation of σ in figure 5.37, for run VII, with the quantities plotted in figure 5.22 is striking. As with figure 5.33 there is strong growth located where the zonal flow and mean temperature gradient are weak. However, unlike figures 5.29 and 5.33, the growth rate becomes negative when it attains its minimum values. Hence when the mean quantities are large the convective modes of the linear theory decay. The combination of the zonal flow and the mean temperature gradient in the linear theory causes the convection to cease. Also of note is that the wavenumber and the frequency of the modes both tend to zero at times of weak convective growth or, equivalently, times of strong zonal flow.

Figure 5.38, for run XV, also appears to show that both mean quantities are necessary for bursting. There is an initial period of strong growth at $t \approx 1.010$ where we see from figure 5.25 that the mean quantities are weak. Followed by the strong growth there is a period where $\sigma \approx 0$ coinciding with the time between which E_Z reduces from its maxima to its minima. After the zonal energy attains its minimum value, the zonal flow is weak enough to allow a second period of strong growth located at $t \approx 1.026$. Also of interest is that k and ω again tend to zero during periods of weak growth. The marginal modes, found

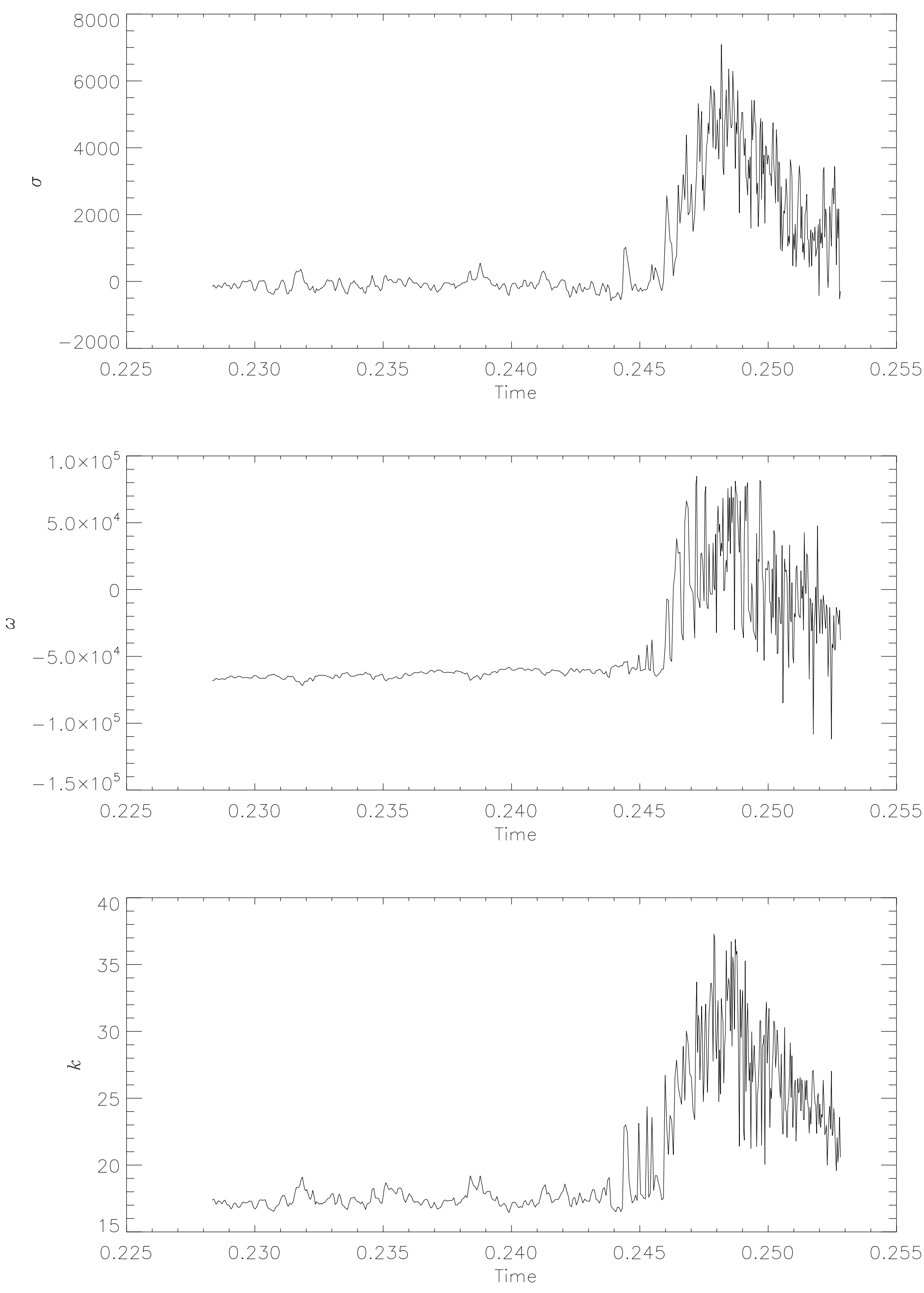

Figure 5.36: Growth rate, frequency and wavenumber plots for run XII with both non-linear zonal flow and mean temperature gradient.

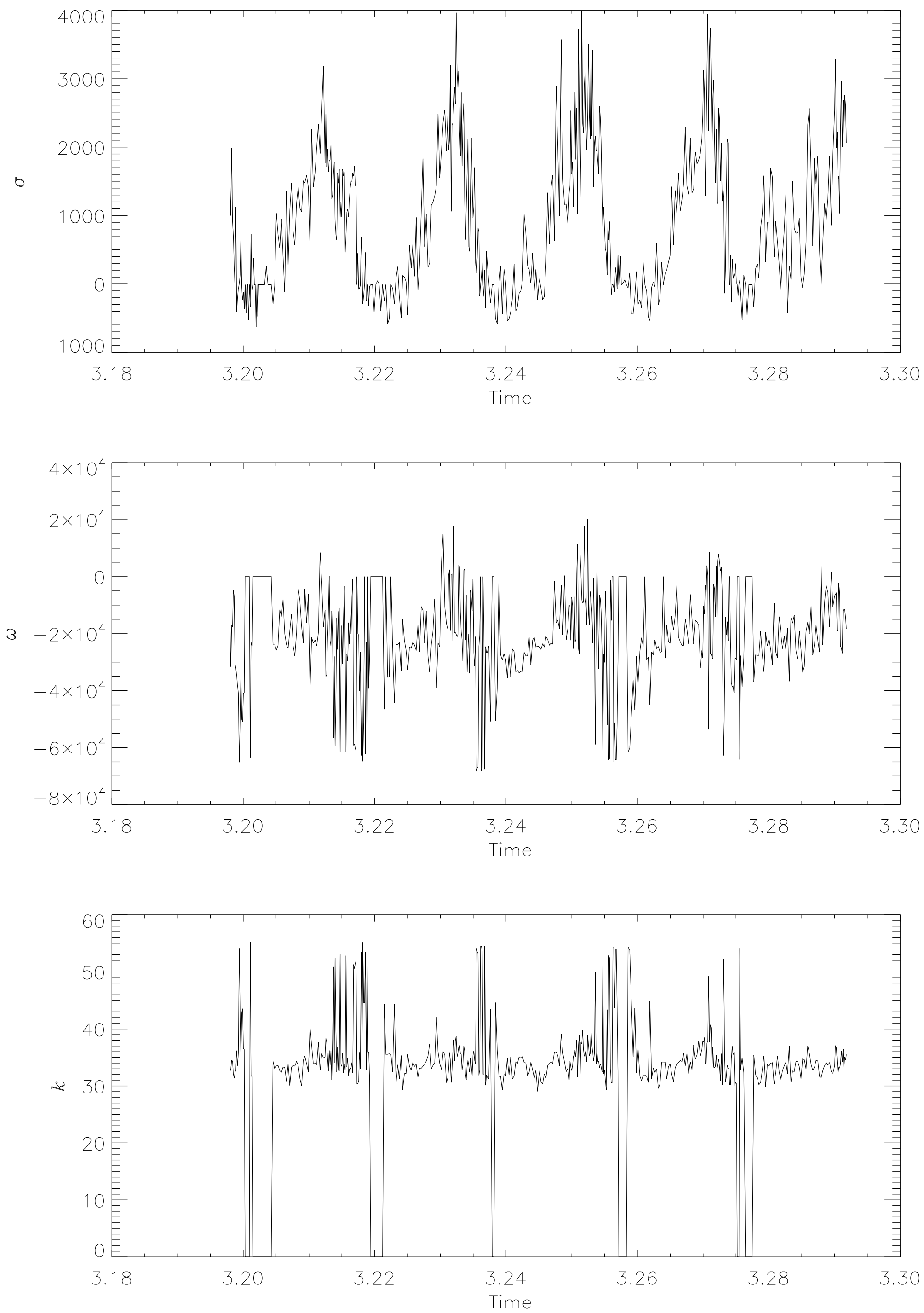

Figure 5.37: Growth rate, frequency and wavenumber plots for run VII with both non-linear zonal flow and mean temperature gradient.

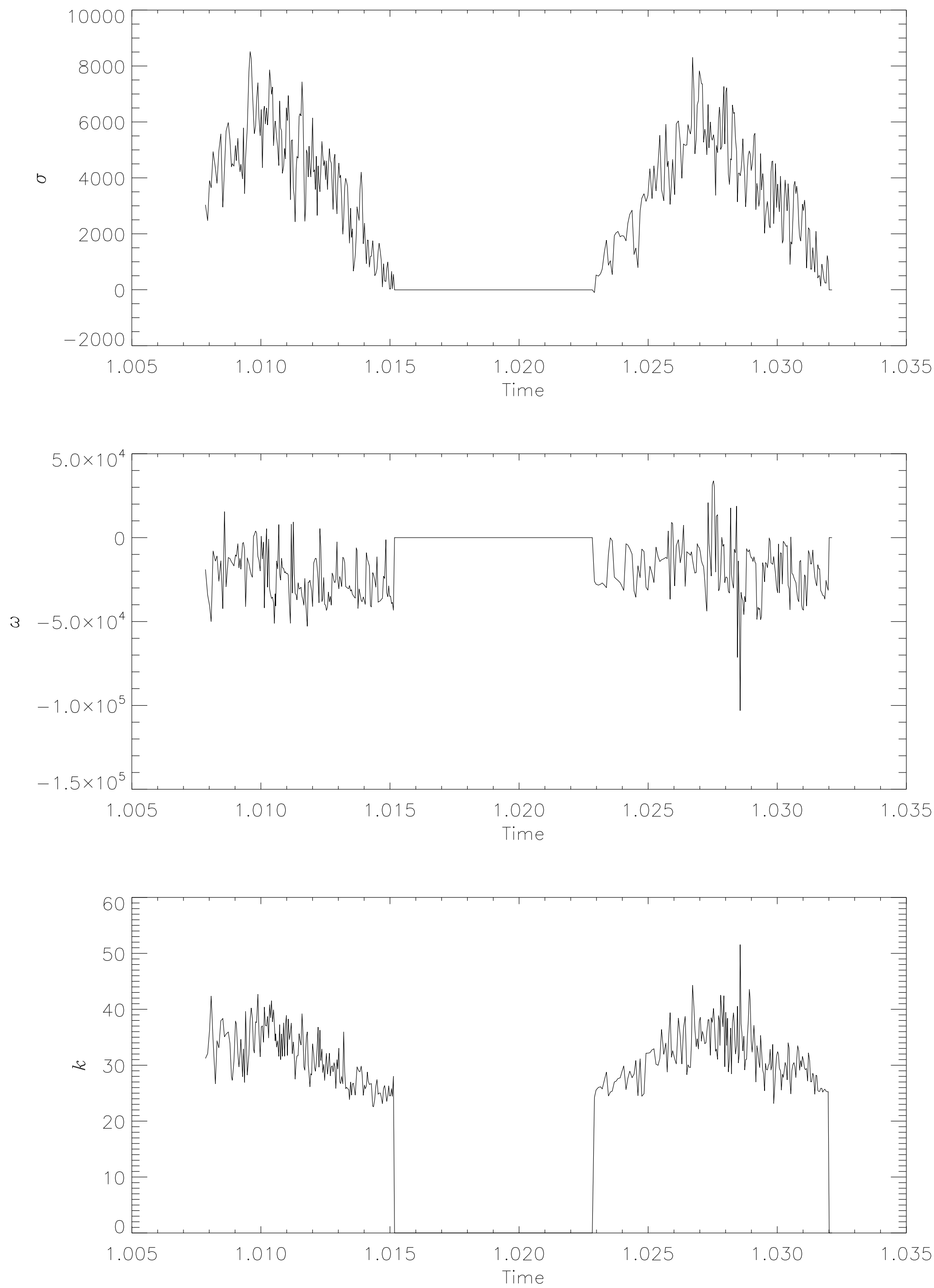

Figure 5.38: Growth rate, frequency and wavenumber plots for run XV with both non-linear zonal flow and mean temperature gradient.

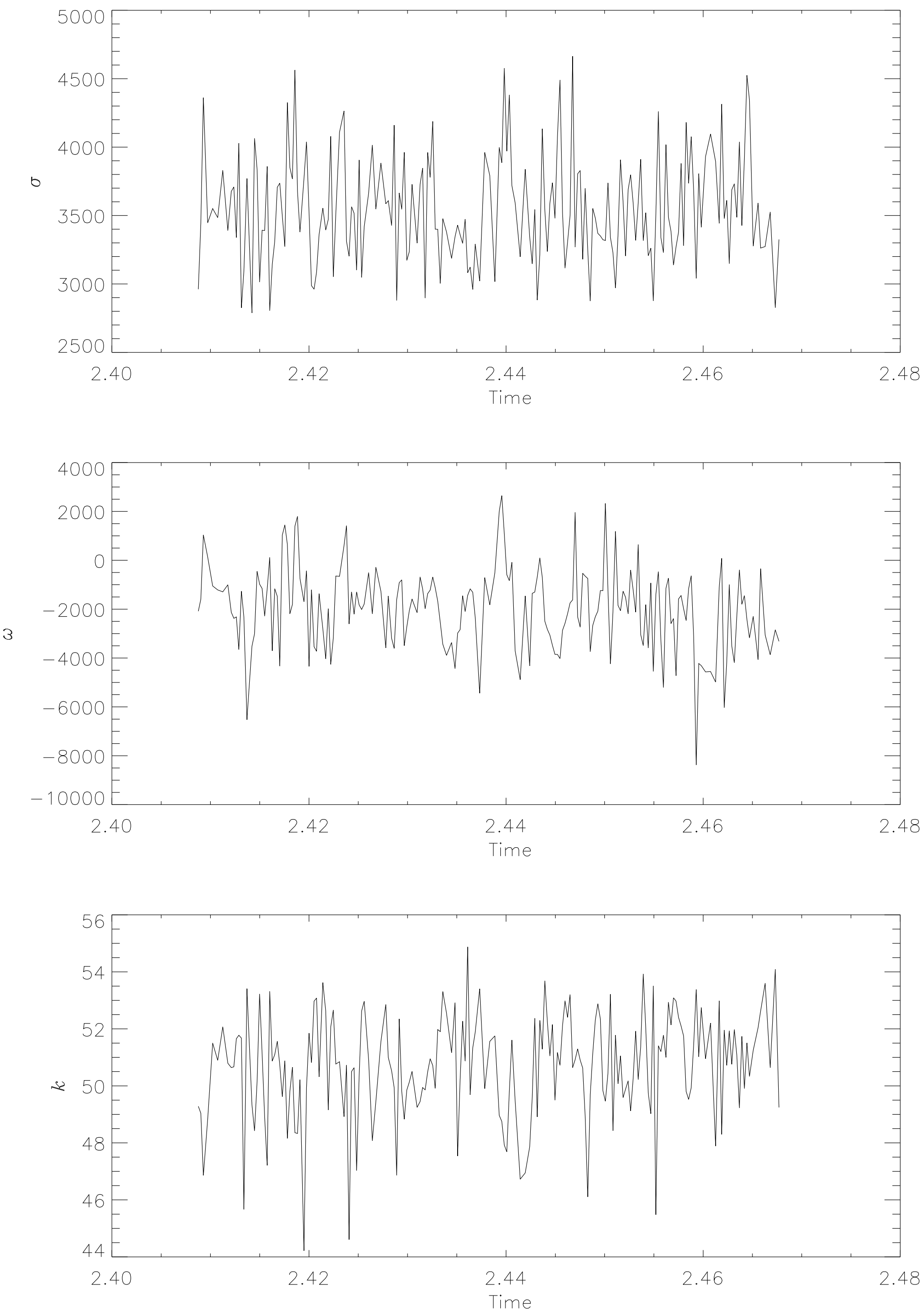

Figure 5.39: Growth rate, frequency and wavenumber plots for run XVII with both non-linear zonal flow and mean temperature gradient.

when the mean quantities are strong, are therefore steady in this case. The plots displayed in figure 5.39 are similar to those found for run XVII in the previous subsections. Once again all three quantities take (non-zero) near-constant values as expected, due to the weak mean quantities for run XVII.

We can conclude from this subsection that it appears that the necessary condition for bursts of convection is the existence of both a zonal flow and a mean temperature gradient. We have observed marginal growth rates in all three runs that admit bursting. The Rayleigh number in all runs is several times critical. Thus, when the mean quantities are strong and of the correct form, they are able to reduce the system to near-onset behaviour. This was not the case in sections 5.4.1 and 5.4.2 where there could be a large range in the growth rate as the non-linear system evolved, but not marginal values of σ.

Physically, the zonal flow certainly disrupts the convection as expected and as observed in section 5.4.1. Similarly, the introduction of a strong mean temperature gradient can result in the reduction of the overall temperature gradient, $T' = \Delta T/D + \bar{\theta}'$. The adverse temperature gradient must exceed some value in order for convection to be beneficial. Also, the steeper the adverse temperature gradient the stronger the resulting convection will be. Hence a partial cancellation of the static temperature gradient, $\Delta T/D$, will also weaken the convection. We believe that the shearing of the zonal flow, coupled with the partial balancing of the adverse temperature gradient, is the requirement to halt convection. This is in contrast to previous work on the subject where it was believed that the zonal flow could sufficiently disrupt the convection to cause bursts. Both the zonal flow strength and the mean temperature gradient must also exceed some critical value in order for the convection to cease. In the case of the zonal flow the shearing must be great enough and in the case of the mean temperature gradient the static temperature gradient must be sufficiently balanced. When this occurs, the driving force of both of the mean quantities is removed. Consequently, there is a depletion in the strength of the zonal flow and the temperature gradient reverts to approximately that of the static case so that convection is once again beneficial and a burst occurs. This argument also explains why bursting is only observed at Prandtl number of order unity. In order for a large enough zonal flow *and* mean temperature gradient to coexist the diffusivity rates must be of a similar order of magnitude resulting in $Pr = \nu/\kappa \sim O(1)$.

The above reasoning on the origin of the convective bursts poses the question of whether we can model the phenomenon in a simplified way without the need for 2D non-linear simulations. This will enable us to better understand the dynamics of the bursting. Moreover, we shall also be able to validate our conjecture on the necessary conditions for bursting to occur. The development of such a model is our objective in the next chapter.

Chapter 6

A simplified model of the bursting phenomenon

In this chapter we develop a simple model in an attempt to describe the bursting phenomenon seen in chapter 5. We do this in order to better understand the role that the various parameters and variables have in controlling the existence and evolution of the bursting. We are therefore interested specifically in the dynamics of the bursting phenomenon in this chapter. Since we are going to consider under what conditions bursting can exist and not what form it takes we choose to neglect the spatial dependence of our variables. Hence we assume our variables have only a temporal dependence. This allows us to model the system by a set of coupled ODEs with the only independent variable being time. We then consider the linear theory for this problem and also solve the non-linear equations by integrating forward in time for different parameter sets and different initial conditions.

In section 6.1 we discuss how we mathematically construct this bursting model by discussing the equations we use and justifying their form. In section 6.2 we find the equilibrium solutions and then consider the linear stability of the steady state. We study further linear theories in section 6.3, in order to show that the presence of both a zonal flow and a mean temperature gradient are required for bursting. Then in section 6.4 we integrate the non-linear equations forward in time. Finally, in section 6.5 we discuss asymptotics that can be performed on the equations at low diffusivity rates.

6.1 Mathematical setup

In this section we setup our problem mathematically by presenting the equations and justifying their form. We wish to introduce a set of evolution equations, each of which describes the evolution of a physical property of the system. In chapter 5 we saw that the bursting phenomenon occurs periodically over time. At some times during the cycle, convection and the mean temperature gradient are strong and at other times the zonal flow is strong. There are several physical quantities which we believe to play an important role in the existence of bursting. There must be temperature fluctuations to drive convection from which the convective velocities drive up zonal flow. From chapter 5 we are also aware that both zonal flow and a mean temperature gradient are required to enable bursting.

Therefore we assume that there are four crucially relevant physical quantities involved in the production of bursting: the zonal flow, Z, the convective velocity, V, the temperature fluctuations, T, and a mean temperature gradient, G. We now propose a set of evolution equations for these quantities and discuss why they take the form we have chosen. Our fourth order system of coupled ODEs are

$$\frac{\mathrm{d}Z}{\mathrm{d}t} = V^2 - c_Z Z, \tag{6.1}$$

$$\frac{\mathrm{d}V}{\mathrm{d}t} = RaT - FVZ - PrV, \tag{6.2}$$

$$\frac{\mathrm{d}T}{\mathrm{d}t} = VG - T, \tag{6.3}$$

$$\frac{\mathrm{d}G}{\mathrm{d}t} = -VT + c_G(1 - G), \tag{6.4}$$

where $c_Z > 0$ and $c_G > 0$ measure the diffusion rates of the zonal flow and the mean temperature gradient respectively. These diffusion rates are expected to be small since small-scale structures, such as the convective fluctuations, are more heavily damped by dissipative terms than large-scale structures, such as the zonal flow. We also have the parameters $Ra > 0$ and $Pr > 0$, which we refer to as the Rayleigh number and Prandtl number respectively. Finally, $F > 0$ is a coupling parameter. In order to define physical quantities we demand that $Z, V, T, G \in \mathbb{R}$. We note that the set of equations (6.1 - 6.4) does not explicitly contain a rotation term, nor a parameter measuring the rotation despite the fact that we have considered rotating systems thus far. However, zonal flows are a phenomenon of rotating systems as evidenced by previous work (see, for example, Zhang, 1992). Therefore by including an evolution equation for the zonal flow (6.1), we have implicitly included the rotation in this set of equations.

Recall from equations (5.12 - 5.13) and (5.19 - 5.20) that ψ and θ were expanded in terms of Fourier modes. Equations (6.1 - 6.4) can be derived by considering a suitable truncation of these normal forms in a similar way to that performed by Lorenz (1963). Our resulting system of evolution equations have a different symmetry to that of the original equations involving ψ and θ; that is equations (5.7 - 5.8).

We now discuss the terms in each evolution equation in order to further justify their form. We begin with the evolution equation for the zonal flow, equation (6.1). In this equation the zonal flow, Z, is driven up by Reynolds stresses arising from the convective velocity and damped by viscosity as well as possibly bottom friction. The Reynolds stresses in general take the form $\partial_k(u_j u_k)$ so that when neglecting spatial dependence, they will be proportional to V^2. We include diffusion in the equations so that each evolution equation has a damping term, the size of which is controlled by a parameter. Here the dissipation of the zonal flow is controlled by the diffusion parameter c_Z.

The second equation, (6.2), is the evolution equation for the convective velocity. The convection is driven up by temperature fluctuations where Ra represents the Rayleigh number. This term is equivalent to the buoyancy term seen in the full equations. The convection will be damped by the zonal flow, representing the disruption of convection by shear. This effect is represented by the $-FVZ$ term, which is the interaction between the zonal flow and the convective velocity. When the zonal flow is large the convection will be strongly suppressed by this term as expected. However, if the convection at a given time is small, then this term may be overcome by the buoyancy term leading to the convection being driven up once more. Here F is a coupling parameter, which represents how strongly the interaction between the zonal flow and the convection damps the convective velocity. As with the zonal flow evolution equation, we also have a damping term due to the viscosity, which is represented by PrV. If t is non-dimensionalised on the thermal timescale, which is what we have considered when writing equations (6.1 - 6.4), then Pr is essentially the Prandtl number.

Thirdly we consider the evolution equation for the temperature fluctuations, (6.3). The temperature fluctuations are created by advection by the convective velocity down the temperature gradient, which takes the form $u_j\partial_j\theta$ in the full equations. Hence ignoring spatial variations, with G representing the mean temperature gradient, this term would take the form VG. Advection with $G = 1$ corresponds to the basic state of temperature gradient of $\Delta T/D$ and when $G = 0$, the basic state temperature gradient is completely canceled out. Therefore when the system is strongly convecting we would expect G to be just above zero. There is also a damping term for the temperature fluctuations, represented by $-T$, which has a diffusion coefficient set to unity since we have chosen to use the thermal timescale.

Finally we have the evolution equation, (6.4), which is for the mean temperature gradient. The mean temperature gradient is controlled by the convective heat flux, which is proportional to both V and T. This term is balanced by the thermal diffusion, which is trying to restore the basic state temperature gradient so that $G = 1$. We should note that the sign of G has been chosen in order for the mean temperature gradient in this chapter to match that of chapter 5.

We note that equations (6.1 - 6.4) admit an equilibrium solution (where $\mathrm{d}/\mathrm{d}t = 0$) with $Z = V = T = 0$ and $G = 1$. This steady state represents the basic state considered in the non-linear work of chapter 5 where the fluid is at rest and the temperature gradient is simply the basic state temperature gradient. We shall refer to this solution as the ‘null solution’ throughout this chapter. We expect the Rayleigh number, Ra, to be large in order to observe bursting. However, by large here we actually mean compared with whatever value the critical Rayleigh number takes for the onset of convection in the null solution. The parameters c_Z and c_G should be small, because the diffusion of the zonal flow and the large-scale mean temperature gradient are small compared to the larger diffusion rate of the small-scale convection. We shall consider a range of Prandtl numbers as with earlier work: $0.1 \leq Pr \leq 10$. The magnitude of the coupling parameter F is not obvious, but we predict that it will not be too large since if it were then the convection would be strongly suppressed even for very small zonal flows. For ease of reference we henceforth let the parameter set Γ be defined as $\Gamma \equiv \{c_Z, c_G, Pr, F\}$.

6.2 Steady state and linear theory

In this section we find the steady states and consider the linear theory of the equations presented in section 6.1. Hence we obtain an eigenvalue problem and are interested in the possible form of the eigenvalues. In order for the equations (6.1 - 6.4) to be of interest as a model for the bursting phenomenon there must exist eigenvalues with an imaginary part and in particular, complex eigenvalues with a positive real part, indicating an oscillating instability.

In order to consider the linear stability of the problem posed by equations (6.1 - 6.4) we must first find the equilibrium points of the problem. We do this by setting the time derivatives equal to zero and equations (6.1 - 6.4) then become

$$V_0^2 = c_Z Z_0, \tag{6.5}$$

$$RaT_0 = FV_0 Z_0 + PrV_0, \tag{6.6}$$

$$V_0 G_0 = T_0, \tag{6.7}$$

$$V_0 T_0 = c_G(1 - G_0), \tag{6.8}$$

where the subscript zeros simply denote that we are solving for basic state variables here. We let E_0 be the set of steady state variables so that $E_0 = \{Z_0, V_0, T_0, G_0\}$.

We are able to write the system of basic state equations as one quadratic equation, which can be solved given values of the input parameters: c_Z, c_G, F, Pr and Ra; that is, Γ and Ra. We note that all four equations involve V_0 and thus we aim to derive an equation involving only this variable. We first note from equations (6.5) and (6.8) that

$$Z_0 = \frac{V_0^2}{c_Z}, \tag{6.9}$$

$$G_0 = \frac{c_G}{c_G + V_0^2}, \tag{6.10}$$

where we have substituted for T_0 using equation (6.7), which also gives

$$T_0 = \frac{c_G V_0}{c_G + V_0^2}. \tag{6.11}$$

We eliminate Z_0 and T_0 from equation (6.6) using equations (6.9) and (6.11) respectively whereby we obtain

$$Ra\frac{c_G V_0}{c_G + V_0^2} = \frac{FV_0^3}{c_Z} + PrV_0, \tag{6.12}$$

and rearranging we acquire

$$\frac{F}{c_Z}V_0^5 + \left(Pr + \frac{c_G F}{c_Z}\right)V_0^3 + c_G(Pr - Ra)V_0 = 0. \tag{6.13}$$

At no point in the derivation of this equation have we assumed that any of the steady state variables are non-zero. Indeed $V_0 = 0$ is a solution of equation (6.13), which results in

$$Z_0 = V_0 = T_0 = 0, \quad G_0 = 1, \tag{6.14}$$

as a possible steady state. This is the null solution for the steady state, which we briefly mentioned in the previous section. Recall that it represents the case where the basic state is at rest with no temperature fluctuations and a basic state temperature gradient equal to that of the static temperature gradient from the full annulus model. In other words the null solution as a steady state in this bursting model represents the basic state considered in the non-linear solution of the annulus equation in chapter 5.

If we now assume that V_0 is non-zero then we can divide equation (6.13) through by V_0 to leave a quadratic equation in V_0^2, namely

$$V_0^4 + \left(\frac{c_Z Pr}{F} + c_G\right)V_0^2 + \frac{c_Z c_G}{F}(Pr - Ra) = 0, \tag{6.15}$$

which can be solved for V_0 given values for the remaining parameters. Alternatively if V_0 and the parameter set Γ are prescribed then the Rayleigh number can be determined with

$$Ra = \frac{FV_0^4}{c_Z c_G} + V_0^2\left(\frac{F}{c_Z} + \frac{Pr}{c_G}\right) + Pr. \tag{6.16}$$

If required the other basic state variables can also be found from equations (6.9 - 6.11). Equation (6.15) can be solved using the quadratic formula, which gives the solution

$$V_0^2 = \frac{-(c_Z Pr + c_G F) \pm \sqrt{(c_Z Pr + c_G F)^2 - 4Fc_z c_G(Pr - Ra)}}{2F} \tag{6.17}$$

$$\Rightarrow \quad V_0^2 = \frac{-(c_Z Pr + c_G F) \pm \sqrt{(c_Z Pr - c_G F)^2 + 4Fc_z c_G Ra}}{2F}. \tag{6.18}$$

Two complex roots are always possible as solutions to equation (6.15) since the coefficient of the V_0^2 term is positive. These roots do not relate to any physical solution and thus we ignore them. The remaining two roots may be real (in which case they are equal and opposite) if $Ra > Pr$, which can be seen from equation (6.18). Without loss of generality we may choose the positive root since the system of equations (6.1 - 6.4) remains unchanged under the transformation $(Z, V, T, G) \to (Z, -V, -T, G)$.

We now wish to perform a linear stability analysis on the problem for the equilibrium solutions. We add small perturbations to the basic state variables so that $Z = Z_0 + z$, $V = V_0 + v$, $T = T_0 + \theta$ and $G = G_0 + g$. Then we substitute these expressions into equations (6.1 - 6.4) and linearise (retaining only terms that are linear in the small perturbations). We also assume that the variables have temporal dependence $\exp(st)$ so that $\mathrm{d}/\mathrm{d}t = s$ where $s = \sigma + \mathrm{i}\omega$ is the complex growth rate. Then equations (6.1 - 6.4) become

$$sz = 2V_0 v - c_Z z, \tag{6.19}$$

$$sv = Ra\theta - FV_0 z - FZ_0 v - Prv, \tag{6.20}$$

$$s\theta = V_0 g + G_0 v - \theta, \tag{6.21}$$

$$sg = -V_0\theta - T_0 v - c_G g. \tag{6.22}$$

We can write these four equations as a single matrix eigenvalue equation $\mathbf{J}\mathbf{w} = s\mathbf{w}$ where $\mathbf{w} = [z, v, \theta, g]^{\mathrm{T}}$ and

$$\mathbf{J} = \begin{pmatrix} -c_Z & 2V_0 & 0 & 0 \\ -FV_0 & -FZ_0 - Pr & Ra & 0 \\ 0 & G_0 & -1 & V_0 \\ 0 & -T_0 & -V_0 & -c_G \end{pmatrix}. \tag{6.23}$$

This simple eigenvalue problem can now be solved for the eigenvalue, s, by considering the characteristic equation $\det(\mathbf{J} - s\mathbf{I}) = 0$ where $\mathbf{I}$ is the identity matrix to find

$$\begin{aligned}(s + c_Z)\Big((s + FZ_0 + Pr)\Big((s+1)(s+c_G) + V_0^2\Big) + Ra(T_0V_0 - G_0(s + c_G))\Big) \\ + 2FV_0^2\Big((s+1)(s+c_G) + V_0^2\Big) = 0,\end{aligned} \tag{6.24}$$

which is a quartic in the growth rate, s. If we first consider the null solution for the basic state, given by equation (6.14), we find that this reduces to

$$(s + c_Z)(s + c_G)\Big((s + Pr)(s+1) - Ra\Big) = 0. \tag{6.25}$$

Since the diffusion coefficients are greater than zero by definition we see that two of the four roots for s are real and negative and therefore always stable. The remaining two roots arise from the solution of the quadratic equation

$$s^2 + (1 + Pr)s + Pr - Ra = 0, \tag{6.26}$$

which has the solutions

$$s = \frac{1}{2}\left(-(1+Pr) \pm \sqrt{(1+Pr)^2 - 4(Pr-Ra)}\right) \tag{6.27}$$

$$\Rightarrow \quad s = \frac{1}{2}\left(-(1+Pr) \pm \sqrt{(1-Pr)^2 + 4Ra}\right). \tag{6.28}$$

The solutions are real since the discriminant $(1-Pr)^2 + 4Ra$ is always greater than zero and it is clear that taking the negative square root always results in $s < 0$ and therefore another stable solution. The remaining solution is found by taking the positive root in equation (6.28), which results in a positive value of s if

$$-(1+Pr) + \sqrt{(1-Pr)^2 + 4Ra} \ > \ 0 \tag{6.29}$$

$$\Rightarrow \quad (1-Pr)^2 + 4Ra \ > \ (1+Pr)^2 \tag{6.30}$$

$$\Rightarrow \quad Ra \ > \ Pr. \tag{6.31}$$

Hence the null solution admits one unstable mode if the Rayleigh number is greater than the Prandtl number, which as we saw earlier is also a requirement for V_0 to be defined. Recall that the null solution corresponds to a basic state with no motion so this criteria is to be expected as the usual form of the thermal instability where the system becomes unstable if the Rayleigh number exceeds some critical value, Ra_c. However, the above analysis also tells us that oscillating modes are not found and hence bursting is not possible for a steady state given by the null solution basic state. Therefore we do not discuss the null solution further and instead consider the other possible equilibrium point where all four basic state variables are non-zero.

We simplify equation (6.24) by collecting coefficients of powers of s to give

$$\begin{aligned} s^4 + s^3 &\left[\frac{FV_0^2}{c_Z} + 1 + Pr + c_Z + c_G\right] \\ &+ s^2\left[V_0^2\left(1 + \frac{c_G F}{c_Z} + 3F\right) + (c_Z + c_G)(1+Pr) + c_Z c_G\right] \\ &+ s\left[V_0^4 \frac{2F}{c_Z} + V_0^2(2Pr + c_Z + 3c_G F + 2F) + c_Z c_G(1+Pr)\right] \\ &+ 4FV_0^4 + 2V_0^2(c_Z Pr + c_G F) = 0, \end{aligned} \tag{6.32}$$

or,

$$s^4 + P_3 s^3 + P_2 s^2 + P_1 s + P_0 = 0. \tag{6.33}$$

Note that we have also substituted for Z_0, T_0 and G_0 from equations (6.9 - 6.11) here. We note that this quartic for s only contains V_0 and does not contain the Rayleigh number explicitly. We wish to consider the four possible roots of equation (6.32) for various parameter sets as we slowly increase the Rayleigh number. For a given Γ and Ra we can find solutions of equation (6.15) where we set V_0 equal to the positive real root without loss of generality as discussed earlier. We then use Maple to find the roots of the quartic with this value of V_0. This procedure can be repeated for various Rayleigh numbers and Γs. In order to be of interest to the bursting phenomenon s must have an imaginary part and in particular we wish to find *growing*, oscillatory solutions where $\Re[s] \equiv \sigma > 0$ and $\Im[s] \equiv \omega \neq 0$.

In figure 6.1 we plot the roots of equation (6.32) as a function of Ra for various parameter sets. In these plots the solid and dotted lines represent the real and imaginary (when existent) parts of the possible roots of the quartic. For all parameter sets tested we found two purely real roots and two complex roots. The two complex roots, of course, appear as a conjugate pair and therefore we only plot the real and imaginary parts for one of these roots in figure 6.1. We multiply certain growth rates and frequencies by an integer factor in order to more clearly display the results along side plotted quantities with larger values.

The two real roots are found to be negative for all Rayleigh numbers and for all parameter sets and thus they are always stable. More interesting are the complex roots, which for most parameter sets have a positive real part for a large enough Rayleigh number. Therefore unstable, oscillatory solutions are possible above a critical value of Ra (see figures 6.1(a) to 6.1(e)). Figure 6.1(f) does not permit growing solutions even as Ra becomes very large. In fact, this was a characteristic of all solutions with $F > 0.5$ suggesting that if the coupling parameter is too large bursting may not be possible. For the plots with parameter regimes that permit growing solutions we see that the preference (that is the largest growth rate) is for the parameter set in figure 6.1(b). Since the fastest growing mode is found for a finite value of the coupling parameter ($F = 0.05$), it may be that there is a finite optimum value of F.

The fact that growing oscillatory solutions are found means that the system of equations (6.1 - 6.4) may be a useful simple model for investigating the nature of the bursting phenomenon. In order to ascertain whether we have developed a model that displays the dynamics of bursting we must investigate how the critical Rayleigh number varies for different parameter sets and also consider non-linear solutions. We discuss the non-linear problem in section 6.4 but first we consider the dependence of the critical Rayleigh number on the remaining parameters.

We have seen that oscillating solutions for s are permitted by equation (6.33) for large enough values of Ra. We can improve our efficiency for searching for the critical Rayleigh number (where $\Re[s] = 0$) by making an additional requirement. We wish for the system of equations (6.1 - 6.4) to admit oscillating solutions since the bursting phenomenon is a periodic phenomenon. Hence we wish for s to be complex so we require a conjugate pair of eigenvalues, which lose stability above some critical value of the Rayleigh number. Therefore a Hopf bifurcation must occur when $Ra = Ra_c$ where the growth rate vanishes (that is $\sigma = 0$) and $s = \pm\mathrm{i}\omega$ for some frequency, $\omega \in \mathbb{R}$. A limit cycle will occur, the stability of which depends on whether the bifurcation is subcritical or supercritical. This cannot be determined by the linear theory and will be investigated in section 6.4.

At the position of the bifurcation, two of the possible four growth rates must be marginal with $s^2 = -\omega^2$ so we assume that the quartic in s, given by equation (6.32), can be written as

$$(s^2 + \omega^2)(s^2 + as + b) = 0. \tag{6.34}$$

This allows for the most general form for the characteristic eigenvalue equation that also admits a Hopf bifurcation when $s = \pm\mathrm{i}\omega$ and we expand to find

$$s^4 + as^3 + (\omega^2 + b)s^2 + \omega^2 as + \omega^2 b = 0. \tag{6.35}$$

By comparing the coefficients of the two forms of the quartic in s given by equations (6.33) and (6.35) we are able to derive a condition on the P_is for the existence of a Hopf bifurcation. Clearly we acquire

$$P_3 = a, \tag{6.36}$$

$$P_2 = \omega^2 + b, \tag{6.37}$$

$$P_1 = \omega^2 a \quad \Rightarrow \quad \omega^2 = \frac{P_1}{a} \quad \Rightarrow \quad \omega^2 = \frac{P_1}{P_3}, \tag{6.38}$$

$$P_0 = \omega^2 b \quad \Rightarrow \quad b = \frac{P_0}{\omega^2} \quad \Rightarrow \quad b = \frac{P_0 P_3}{P_1}, \tag{6.39}$$

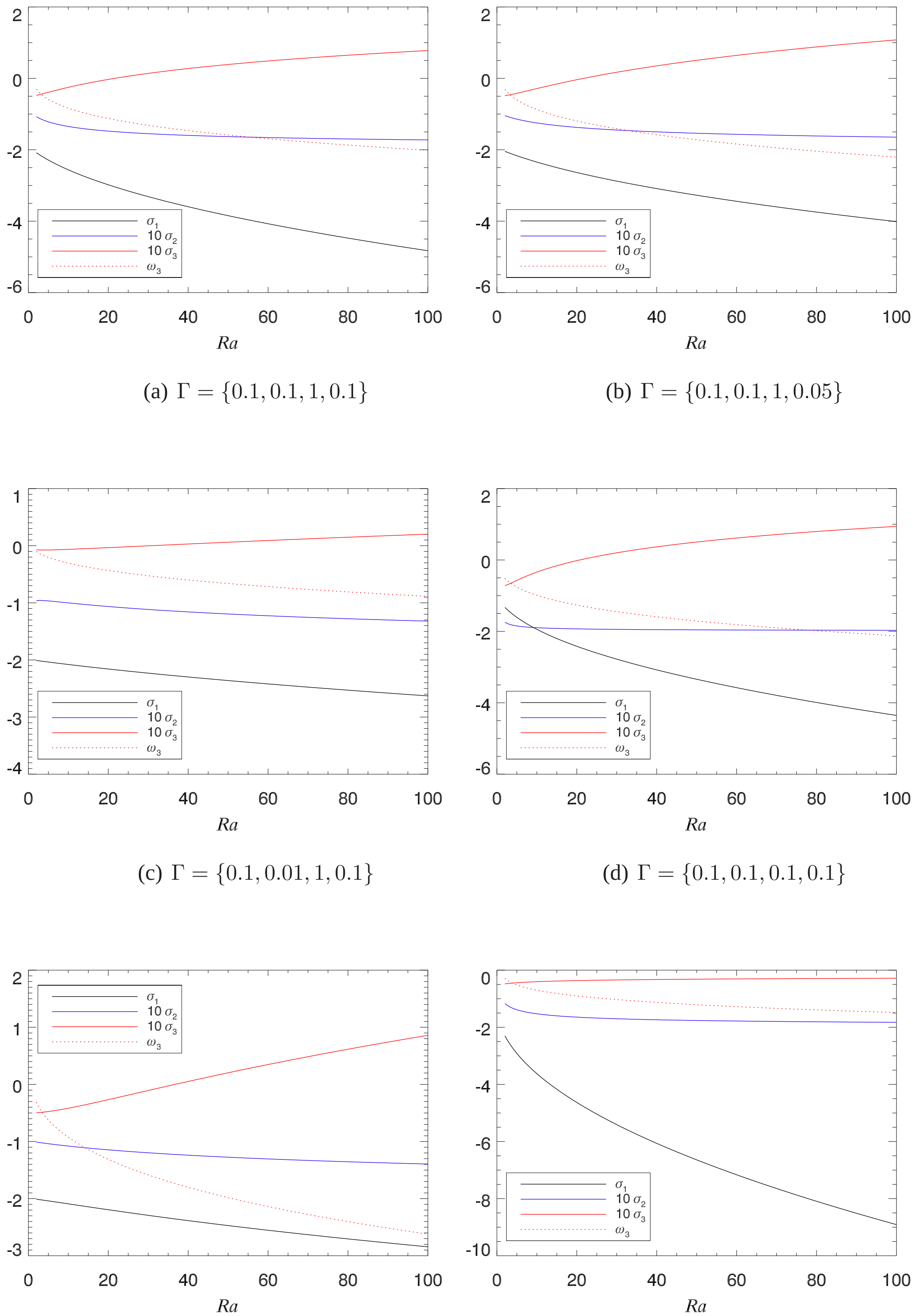

(a) $\Gamma = \{0.1, 0.1, 1, 0.1\}$

(b) $\Gamma = \{0.1, 0.1, 1, 0.05\}$

(c) $\Gamma = \{0.1, 0.01, 1, 0.1\}$

(d) $\Gamma = \{0.1, 0.1, 0.1, 0.1\}$

(e) $\Gamma = \{0.1, 0.1, 1, 0.01\}$

(f) $\Gamma = \{0.1, 0.1, 1, 0.6\}$

Figure 6.1: Plots of possible eigenvalues, s, against the Rayleigh number for various parameter sets, Γ.

and from equation (6.37) we get

$$P_2 = \frac{P_1}{P_3} + \frac{P_0 P_3}{P_1} \tag{6.40}$$

$$\Rightarrow \quad P_1^2 + P_0 P_3^2 - P_1 P_2 P_3 = 0. \tag{6.41}$$

The P_is are functions of the parameters belonging to Γ and V_0 only. In fact the condition given by equation (6.41) is a polynomial in V_0 of degree eight. Hence for a given set Γ the condition given by equation (6.41) finds eight possible roots for V_0. Only two of these values are real and without loss of generality we set V_0 equal to the positive real root. The value of V_0 (along with the parameter set Γ) can then be substituted into equation (6.16) to acquire the critical Rayleigh number, Ra_c. We can also use equations (6.9 - 6.11) to find the values of the remaining basic state variables at the location of the bifurcation.

Thus, we now have a procedure that finds the critical Rayleigh number and the (non-zero) equilibrium solution, E_0, at the Hopf bifurcation. Equivalently our procedure finds the location of a Hopf bifurcation in Ra-E_0-space given a parameter set, Γ. To summarise the procedure:

- Choose a parameter set, Γ.
- Solve equation (6.41) using, for example, Maple and set V_0 to the positive real root.
- Substitute Γ and V_0 into equation (6.16) and solve to find Ra, which we denote Ra_c.

The plots of figure 6.2 show how the critical Rayleigh number varies with F for several values of the Prandtl number. Each plot displays results for a different choice of $\{c_Z, c_G\}$ and the Rayleigh number is represented on a logarithmic axis. The plots inform us that the critical Rayleigh number can significantly depend on the input parameters. If we were to minimise the critical Rayleigh number over any one of the parameters from the set Γ, we notice the preference is, in general, for smaller values of c_Z, c_G and F. However the dependence on the Prandtl number is more complicated.

We see that the form of the plots do not change greatly as the diffusion rates are reduced together (so that $c_Z = c_G$) although the critical Rayleigh number is smaller for smaller $\{c_Z, c_G\}$ for most Prandtl numbers. The cases where $Pr = 5$ and $Pr = 10$ seem to be almost immune to the reduction of the diffusion rates with their lines almost identical in figures 6.2(b), 6.2(c) and 6.2(d). However when the diffusion rates are not equal the critical Rayleigh number increases significantly. This can be seen by comparing figures 6.2(b) and 6.2(e), which are for cases where the diffusion rates have and do not have equality respectively, though the magnitude of the rates are similar. This is seen again in figure 6.2(f) where there is two orders of magnitude between the diffusion rates. Therefore the preference for instability is for equality between asymptotically small diffusion rates.

We now discuss the dependence of Ra_c on F. We first note that for smaller values of the Prandtl number, the critical Rayleigh number tends to infinity as $F \to 0$. There is also a singularity at $F = 1/2$ for all Pr when $c_Z = c_G$ (see figures 6.2(a) to 6.2(d)). Discussion of how this singularity arises mathematically is presented in section 6.5. Figures 6.2(e) and 6.2(f) show that in the case where $c_Z \neq c_G$ the critical Rayleigh number is minimised by a Prandtl number of order unity for all values of F. However, this case is inherently more stable than the case of equal diffusion rates (as discussed above) and we do not discuss it further. More interesting is the case with $c_Z = c_G$ where smaller values of Ra_c can always be found. In this case, for the larger values of F, a smaller value of the Prandtl number is preferable for instability to onset. However, as F is reduced, Prandtl numbers of order unity become preferred. There is a minimising value of F, which we call F_c and this value depends on the Prandtl number (and the diffusion rates). For larger Prandtl numbers the preference is for $F_c = 0$ with non-zero values of F_c possible for smaller Prandtl numbers. For parameter sets with $F > 1/2$ we are unable to find real roots of equation (6.41) and thus the condition for the existence of a Hopf bifurcation is not satisfied. Therefore a critical Rayleigh number does not exist for the onset of growing oscillatory solutions and bursting is not possible when $F > 1/2$.

The above discussion indicates that the linear results of our current model agree well with the non-linear simulations of chapter 5 where bursts of convection were observed. The simplified model is able to produce oscillatory solutions above a critical value of the Rayleigh number. Oscillatory solutions in this simple linear model may correspond to the quasi-periodic bursting found in chapter 5. Also in chapter 5 we found that Prandtl numbers of approximately unity were preferred to observe bursts. The dependence of the onset of bursts on the Prandtl number in the current model shows is in agreement with $Pr = 1$ and $Pr = 0.5$ the most preferred, so long as F is not too large. This suggests that in the non-linear simulations of chapter 5 we are in the low, but finite, F regime. Larger

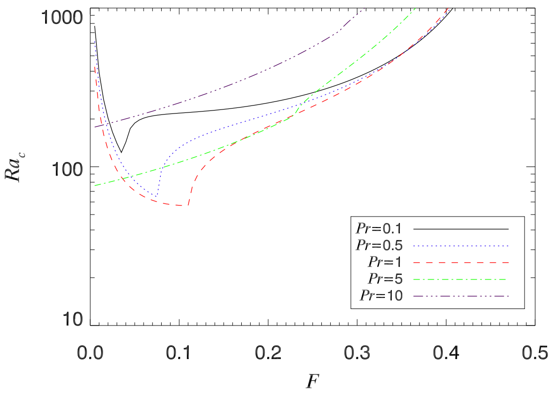

(a) $c_Z = 1$, $c_G = 1$

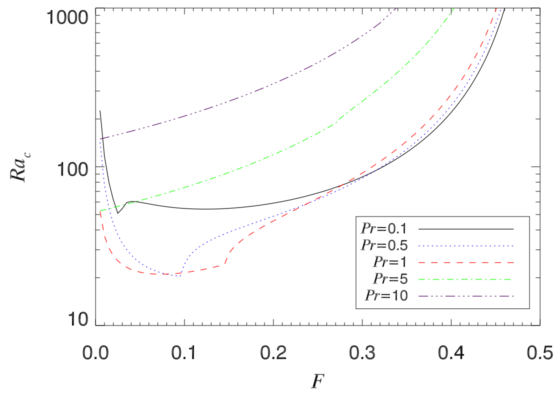

(b) $c_Z = 0.1$, $c_G = 0.1$

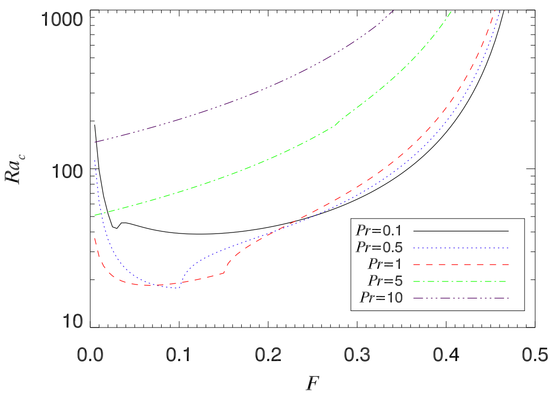

(c) $c_Z = 0.01$, $c_G = 0.01$

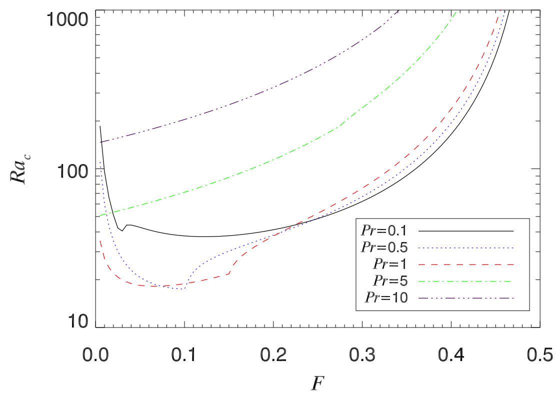

(d) $c_Z = 0.001$, $c_G = 0.001$

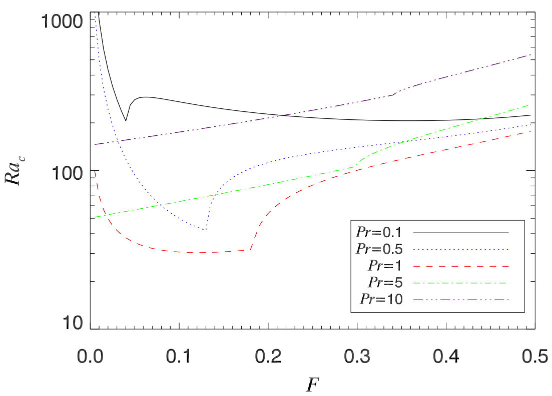

(e) $c_Z = 0.1$, $c_G = 0.01$

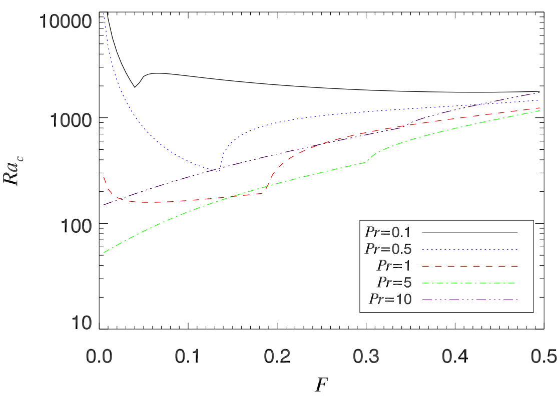

(f) $c_Z = 0.1$, $c_G = 0.001$

Figure 6.2: Plots showing how the critical Rayleigh number varies with F for various Prandtl numbers and diffusion rates.

values of the Prandtl number are certainly not preferred, even at larger F, since the critical Rayleigh number for the onset of bursts is greatly increased in that regime. In chapter 5 we found no evidence of bursting at $Pr = 5$. Hence our current model also replicates this behaviour.

6.3 Necessary conditions for bursting

We observed in chapter 5 that the bursting phenomenon was driven by a combination of zonal flow and a mean temperature gradient. Therefore we would expect both of these physical quantities to necessarily exist in order for our simple model for bursting discussed in this chapter to allow periodic solutions. In this section we discuss the linear theory for the two cases where the model is lacking one of these necessary attributes. We refer to the case discussed in section 6.2 where both zonal flow and a mean temperature gradient are present in the model as the 'full model'. The derivation of the linear theory for the full model was discussed in detail earlier. For this reason we do not present such an in depth derivation here since the two cases here are simplified versions of section 6.2.

6.3.1 Linear theory in the absence of zonal flow

We first investigate the linear theory of the simple model for bursting developed in this chapter in the absence of zonal flow. We expect that bursting will not be observed and therefore oscillatory solutions for the eigenvalue s will not be found. In the absence of zonal flow we drop the evolution equation for Z, given by equation (6.1), and set $Z = 0$ in the remaining bursting model equations, (6.2 - 6.4), which become

$$\frac{\mathrm{d}V}{\mathrm{d}t} = RaT - PrV, \tag{6.42}$$

$$\frac{\mathrm{d}T}{\mathrm{d}t} = VG - T, \tag{6.43}$$

$$\frac{\mathrm{d}G}{\mathrm{d}t} = -VT + c_G(1 - G). \tag{6.44}$$

These equations are equivalent to the Lorenz equations and hence are related to them via a transformation. The Lorenz equations were originally derived from a model of fluid convection and were were first introduced by Lorenz (1963). They are of significant mathematical interest due to their extremely complicated solutions, found when numerically integrated. A review of the literature on the Lorenz equations is presented by Sparrow (1982), where many of the various solutions are discussed. Sparrow presents the Lorenz equations (see page 1 of Sparrow, 1982) in the form

$$\frac{\mathrm{d}x}{\mathrm{d}t} = \hat{\sigma}(y - x), \tag{6.45}$$

$$\frac{\mathrm{d}y}{\mathrm{d}t} = rx - y - xz, \tag{6.46}$$

$$\frac{\mathrm{d}z}{\mathrm{d}t} = xy - bz, \tag{6.47}$$

where $\hat{\sigma}$, r and b are parameters. Note that here $\hat{\sigma}$ is *not* a growth rate; we merely use it as a symbol in order to ease comparison with Sparrow (1982). The relevant transformation from Sparrow's equations (6.45 - 6.47) to our equations (6.42 - 6.44) is then given by:

$$\hat{\sigma} = Pr, \qquad r = \frac{Ra}{Pr}, \qquad b = \frac{c_G Ra}{Pr}, \tag{6.48}$$

$$x = V, \qquad y = \frac{RaT}{Pr}, \qquad z = \frac{Ra}{Pr}(1 - G). \tag{6.49}$$

Sparrow (1982) analyses these equations in great depth and informs us that growing, oscillating solutions are possible for certain parameter regimes (see page 11 of Sparrow, 1982). However, the solutions of the Lorenz equations do not have the correct form to replicate bursting, despite their origins in the field of convection. In particular, the Lorenz equations give rise to chaotic solutions for the parameter regimes of interest to us. Hence equations (6.42 - 6.44) describe a mathematically similar but not necessarily physically similar situation to our full equations. Despite this however, we do solve these equations here to see the relationship to section 6.2.

We solve equations (6.42 - 6.44) for the basic state (denoted again with subscript zeros) where the time derivatives are set to zero and obtain

$$V_0^3 + c_G\left(1 - \frac{Ra}{Pr}\right)V_0 = 0, \tag{6.50}$$

with

$$T_0 = \frac{Pr}{Ra}V_0, \tag{6.51}$$

$$G_0 = 1 - \frac{Pr}{c_G Ra}V_0^2. \tag{6.52}$$

Hence the null solution, given by $V_0 = 0 = T_0$ and $G_0 = 1$, remains a solution since it is a root of the now cubic equation for V_0, (6.50). Recall that the equivalent equation for V_0 in the full linear theory was a quintic, equation (6.13). The remaining two roots of equation (6.50) are given by

$$V_0 = \pm\sqrt{c_G\left(\frac{Ra}{Pr} - 1\right)}, \tag{6.53}$$

and thus in order for V_0 to be a physical quantity we require $Ra > Pr$, as found in the full model. From equation (6.53) we can also find an expression for the Rayleigh number, which is given by

$$Ra = Pr\left(1 + \frac{V_0^2}{c_G}\right). \tag{6.54}$$

We now perturb the basic state so that $V = V_0 + v$, $T = T_0 + \theta$ and $G = G_0 + g$. We also assume the disturbances for the perturbations are of the form $\exp(st)$. This, as discussed in more depth earlier for the linear theory of the full equations, results in an eigenvalue problem of the form $\mathbf{J_1 w_1} = s\mathbf{w_1}$ where $\mathbf{w_1} = (v, \theta, g)^{\mathrm{T}}$ and

$$\mathbf{J_1} = \begin{pmatrix} -Pr & Ra & 0 \\ G_0 & -1 & V_0 \\ -T_0 & -V_0 & -c_G \end{pmatrix}. \tag{6.55}$$

Now by considering the characteristic eigenvalue equation $\det(\mathbf{J_1} - s\mathbf{I}) = 0$ we obtain

$$(Pr + s)\Big((1 + s)(c_G + s) + V_0^2\Big) - Ra\Big(G_0(c_G + s) - V_0T_0\Big) = 0, \tag{6.56}$$

which for the null solution results in two negative real roots (stable solutions) and one positive real root (unstable solution) for $Ra > Pr$. Thus the null solution retains the same characteristics as in the linear theory of the full equations albeit with one fewer stable roots.

In order to consider the case where $V_0 \neq 0$ we expand equation (6.56) and collect the terms as powers of s to give

$$s^3 + s^2[1 + c_G + Pr] + s\Big[V_0^2 + c_G(1 + Pr)\Big] + 2PrV_0^2 = 0, \tag{6.57}$$

or,

$$s^3 + P_2s^2 + P_1s + P_0 = 0, \tag{6.58}$$

where we have substituted for T_0, G_0 and Ra from equations (6.51), (6.52) and (6.54) respectively. In order for there to be a Hopf bifurcation equation (6.58) must have a pair of purely imaginary complex conjugate roots with $s = \pm i\omega$ for $\omega \in \mathbb{R}$. Hence

$$
\begin{aligned}
& (s^2+\omega^2)(as+b) = 0 && (6.59)\\
\Rightarrow \quad & as^3 + bs^2 + \omega^2 s + b\omega^2 = 0 && (6.60)\\
\Rightarrow \quad & a = 1, \quad b = P_2, \quad a\omega^2 P_1, \quad b\omega^2 = P_0 && (6.61)\\
\Rightarrow \quad & P_1 P_2 - P_0 = 0, && (6.62)
\end{aligned}
$$

where we have compared coefficients with equation (6.58). The condition (6.62) results in

$$
\begin{aligned}
& (1 + c_G + Pr)\Big(V_0^2 + c_G(1+Pr)\Big) - 2PrV_0^2 = 0 && (6.63)\\
\Rightarrow \quad & V_0^2 = \frac{c_G(1+Pr)(1+c_G+Pr)}{Pr-(1+c_G)}, && (6.64)
\end{aligned}
$$

where we immediately see that V_0 is real iff $Pr > 1 + c_G$ since the numerator of equation (6.64) is always positive. This condition can certainly be satisfied for small diffusion rates and thus the equations in the absence of zonal flow admit a Hopf bifurcation. However, as we mentioned previously, the solutions are not quasi-periodic for parameter regimes of interest (Sparrow, 1982).

6.3.2 Linear theory in the absence of a mean temperature gradient

In the absence of a mean temperature gradient we drop the evolution equation for G, given by equation (6.4), and set $G = 1$ in the remaining bursting model equations, (6.1 - 6.3), which become

$$
\begin{aligned}
\frac{dZ}{dt} &= V^2 + c_Z Z, && (6.65)\\
\frac{dV}{dt} &= RaT - FVZ - PrV, && (6.66)\\
\frac{dT}{dt} &= V - T. && (6.67)
\end{aligned}
$$

We now proceed to find the basic state for this situation by setting the time derivatives to zero and eliminating Z_0 and T_0 to acquire one equation in V_0. Once again subscript zeros indicate basic state quantities and we find

$$
V_0^3 + \frac{c_Z}{F}(Pr - Ra)V_0 = 0, \qquad (6.68)
$$

with

$$Z_0 = \frac{V_0^2}{c_Z}, \tag{6.69}$$

$$T_0 = V_0. \tag{6.70}$$

Again the null solution, where $Z_0 = V_0 = T_0 = 0$, satisfies these equations and the remaining two roots of equation (6.68) are given by

$$V_0 = \pm\sqrt{\frac{c_Z}{F}(Ra - Pr)}, \tag{6.71}$$

where we demand that $Ra > Pr$ in order for V_0 to be a physical quantity. We can rearrange equation (6.71) to find an expression for the Rayleigh number given by

$$Ra = \frac{FV_0^2}{c_Z} + Pr. \tag{6.72}$$

We now perturb the basic state so that $Z = Z_0 + z$, $V = V_0 + v$ and $T = T_0 + \theta$ and again assume the disturbances for the perturbations are of the form $\exp(st)$. As we have already seen twice before, this results in an eigenvalue problem of the form $\mathbf{J_2 w_2} = s\mathbf{w_2}$ where $\mathbf{w_2} = (v, \theta, g)^{\mathrm{T}}$ and

$$\mathbf{J_2} = \begin{pmatrix} -c_Z & 2V_0 & 0 \\ -FV_0 & -FZ_0 - Pr & Ra \\ 0 & 1 & -1 \end{pmatrix}. \tag{6.73}$$

The characteristic equation, $\det(\mathbf{J_2} - s\mathbf{I}) = 0$ then gives

$$(c_Z - s)\Big((FZ_0 + Pr + s)(1 + s) - Ra\Big) + 2F(1 + s)V_0^2 = 0, \tag{6.74}$$

which for the null solution admits two negative real roots (stable solutions) and one positive real root (unstable solution) for $Ra > Pr$. Hence the null solution retains the same characteristics as those of the full model, again with one fewer stable roots.

We move on to consider the case when $V_0 \neq 0$ by expanding equation (6.74) and collecting the terms as powers of s. By doing this we acquire

$$s^3 + s^2\left[1 + c_Z + \frac{FV_0^2}{c_Z}\right] + s\Big[c_Z(1 + Pr) + 3FV_0^2\Big] + \Big[c_Z(Pr - 1) + 3FV_0^2\Big] = 0, \tag{6.75}$$

or,

$$s^3 + P_2 s^2 + P_1 s + P_0 = 0, \tag{6.76}$$

where we have substituted for Z_0, T_0 and Ra from equations (6.69), (6.70) and (6.72) respectively. Equation (6.76) is a cubic in s, which admits a Hopf bifurcation if it satisfies the condition we derived in the previous subsection, namely equation (6.62). Hence we now use the definitions of the P_is from equations (6.75 - 6.76) in the condition given by equation (6.62) to get

$$\left[c_Z(1+Pr)+3FV_0^2\right]\left[1+c_Z+\frac{FV_0^2}{c_Z}\right]-\left[c_Z(Pr-1)+3FV_0^2\right]=0 \quad (6.77)$$

$$\Rightarrow \quad \frac{3F^2}{c_Z}V_0^4+V_0^2\left[3Fc_Z+F(1+Pr)\right]+\left[2c_Z+c_Z^2(1+Pr)\right]=0. \quad (6.78)$$

This is a quadratic equation in V_0^2, which we can solve using the quadratic formula to give

$$V_0^2=\frac{-(3Fc_Z+F(1+Pr))\pm\sqrt{(3Fc_Z+F(1+Pr))^2-12F^2(2+c_Z(1+Pr))}}{6F^2/c_Z}, \quad (6.79)$$

where we immediately note that taking the negative square root results in the right hand side of this expression having a negative real part. This is not allowed since V_0 would then be complex, which is not permitted. The other possibility arises by taking the positive square root in equation (6.79), which may give rise to a positive quantity for V_0^2 if

$$-(3Fc_Z+F(1+Pr))+\sqrt{(3Fc_Z+F(1+Pr))^2-12F^2(2+c_Z(1+Pr))}\ >\ 0 \quad (6.80)$$

$$\Rightarrow \quad (3Fc_Z+F(1+Pr))^2-12F^2(2+c_Z(1+Pr))\ >\ (3Fc_Z+F(1+Pr))^2 \quad (6.81)$$

$$\Rightarrow \quad -12F^2(2+c_Z(1+Pr))\ >\ 0. \quad (6.82)$$

However, we have reached a contradiction here since the bracketed term is always greater than zero. Hence taking the positive square root in equation (6.79) also results in a complex value for V_0. Therefore, since V_0 must be real, equation (6.78), which is the condition for a Hopf bifurcation, cannot be satisfied. Hence we have proved that there is not a Hopf bifurcation, which means that growing oscillating solutions are not permitted in the absence of a mean temperature gradient. Therefore, we conclude that the existence of a mean temperature is a necessary condition for bursting.

In this section we have shown that the existence of a zonal flow and a mean temperature gradient are both necessary conditions for growing oscillatory solutions to the linear theory. Hence, both Z and G play vital roles for the system of equations (6.1 - 6.4) to permit bursting solutions. This is in agreement with results from chapter 5 where we also found that both attributes were necessary to observe bursting.

6.4 Non-linear results

After gaining insight into the problem by performing the linear stability analysis in the previous sections we now wish to solve the non-linear equations. Fortunately the full non-linear governing equations, (6.1 - 6.4), are simple enough to be integrated using a standard procedure in, for example, Maple. We enter equations (6.1 - 6.4) into Maple and use Maple's built-in 'dsolve' procedure in order to integrate forward in time. We do this for various parameter sets and results are presented in figures 6.3 to 6.5. For each parameter set we plot the evolution for a time range where the solution has become periodic or quasi-periodic, that is where the solution is longer growing nor decaying from its initial state. Each figure contains three plots, which are each for an identical parameter set Γ and initial condition but for different Rayleigh numbers, namely $Ra = 0.9Ra_c$, $Ra = Ra_c$ and $Ra = 2Ra_c$. Here Ra_c is the critical Rayleigh number (for a given parameter set Γ) found in section 6.2.

In order for the solution to show dynamical behaviour we must not evolve from a branch of the bifurcation diagram since this is an equilibrium point and the evolution of the solution would simply be the steady state. In other words, for each parameter set Γ, we must not use the steady state, E_0, as the initial condition. Hence we must choose an alternate initial state. We found that the solution was only weakly dependent on the initial conditions and thus we use the same initial state for the plots displayed in figures 6.3 to 6.5, namely $I_S \equiv \{2Z_0, 2V_0, 2T_0, 2G_0\}$.

Many of the parameter sets tested evolve into the same periodic or quasi-periodic solution, which can be seen in the similarity of the plots in figures 6.3 to 6.5, particularly for plots with the same value of Ra. We note from the top plots of figures 6.3 to 6.5, which have subcritical values of the Rayleigh number, that is $Ra < Ra_c$, the solution does not evolve into a steady state. Hence the Hopf bifurcation that we identified in section 6.2 must be *subcritical*. Since this is the case, we can search along the subcritical branch for the point in Ra-space where the unstable limit cycle can no longer be found. We denote the value

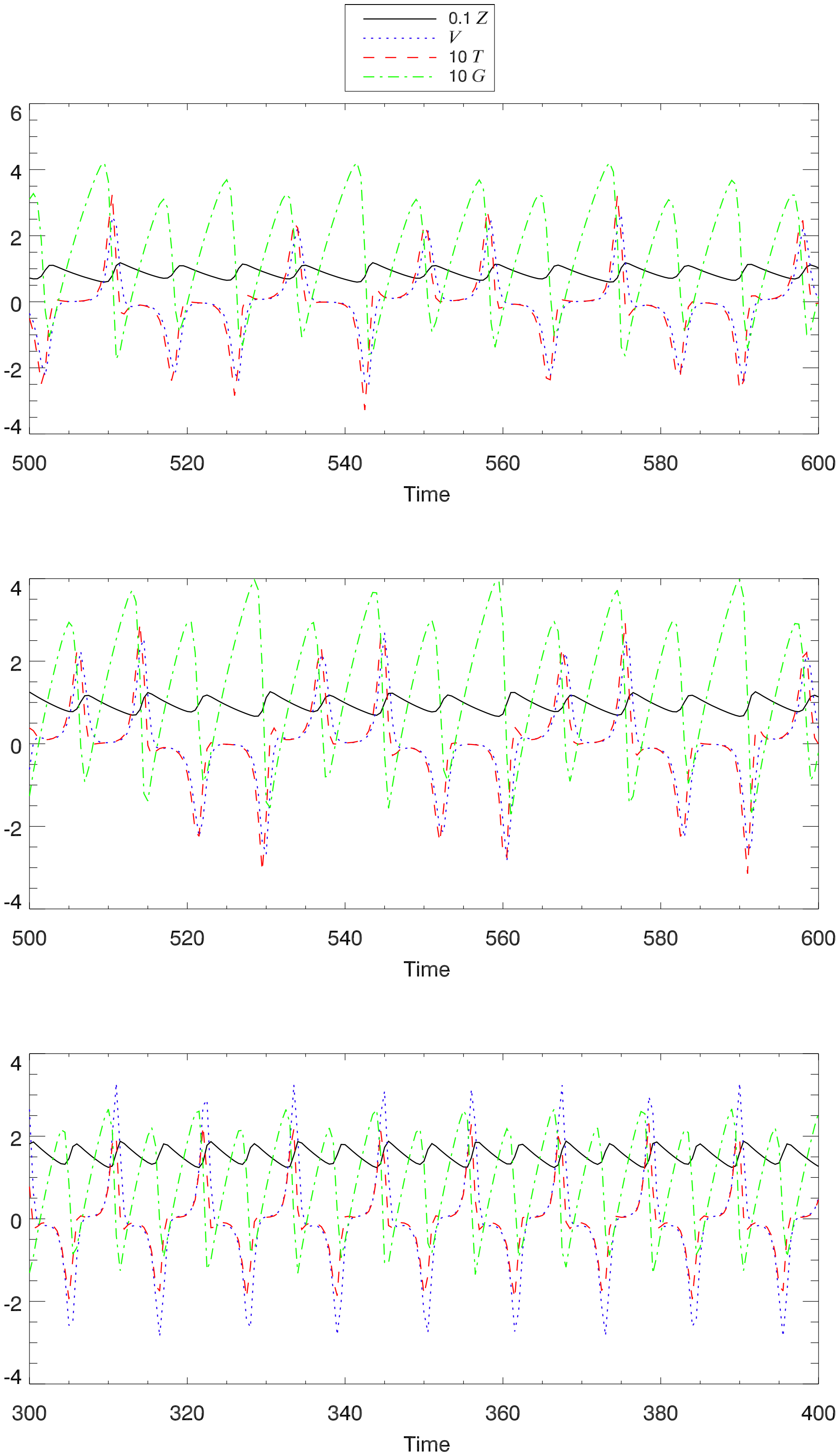

Figure 6.3: Plots showing the time evolution of the functions for $\Gamma = \{0.1, 0.1, 1, 0.1\}$. From the top the plots are for $Ra = 0.9Ra_c$, $Ra = Ra_c$ and $Ra = 2Ra_c$ respectively.

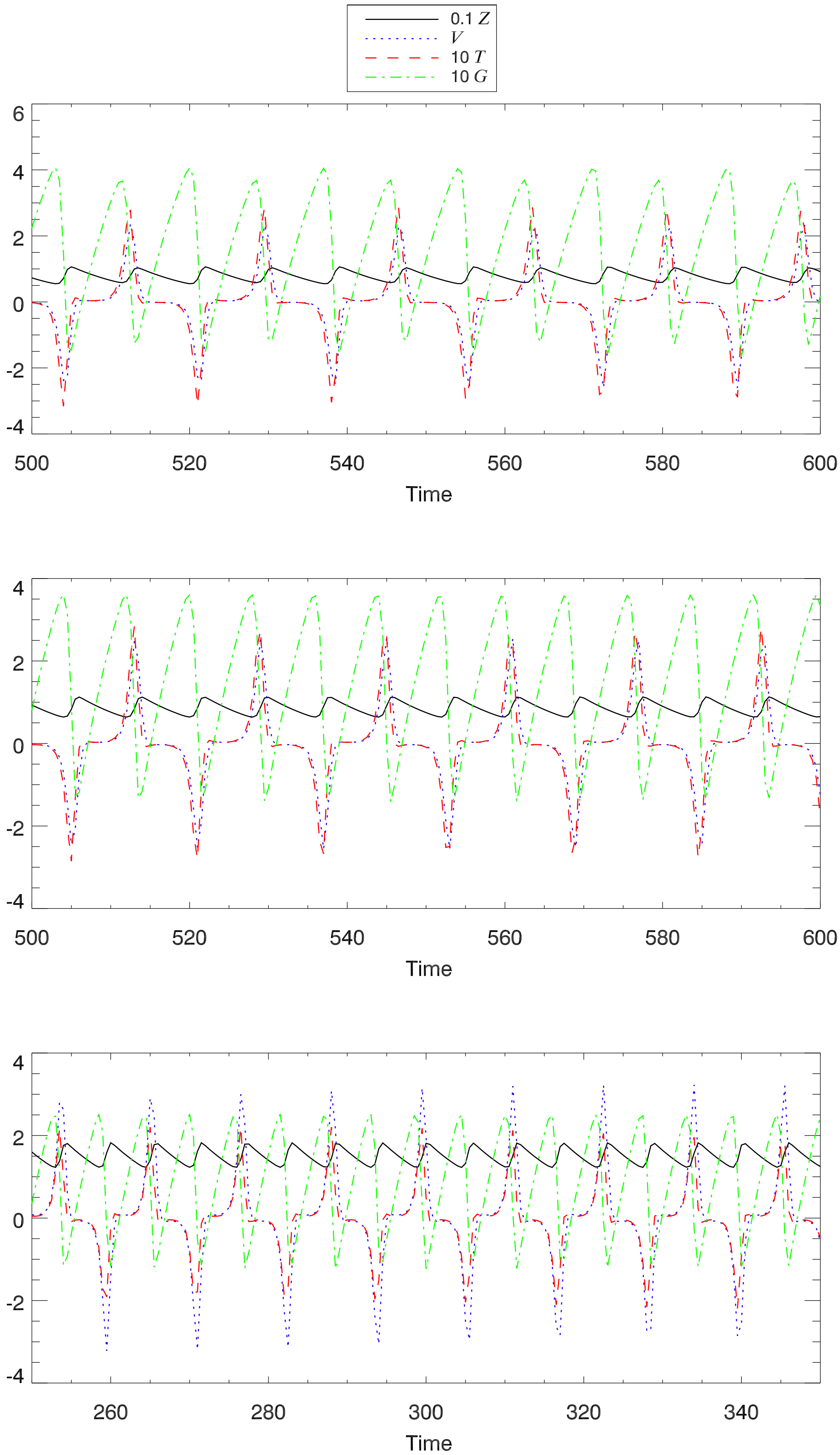

Figure 6.4: Plots showing the time evolution of the functions for $\Gamma = \{0.1, 0.1, 2, 0.1\}$. From the top the plots are for $Ra = 0.9Ra_c$, $Ra = Ra_c$ and $Ra = 2Ra_c$ respectively.

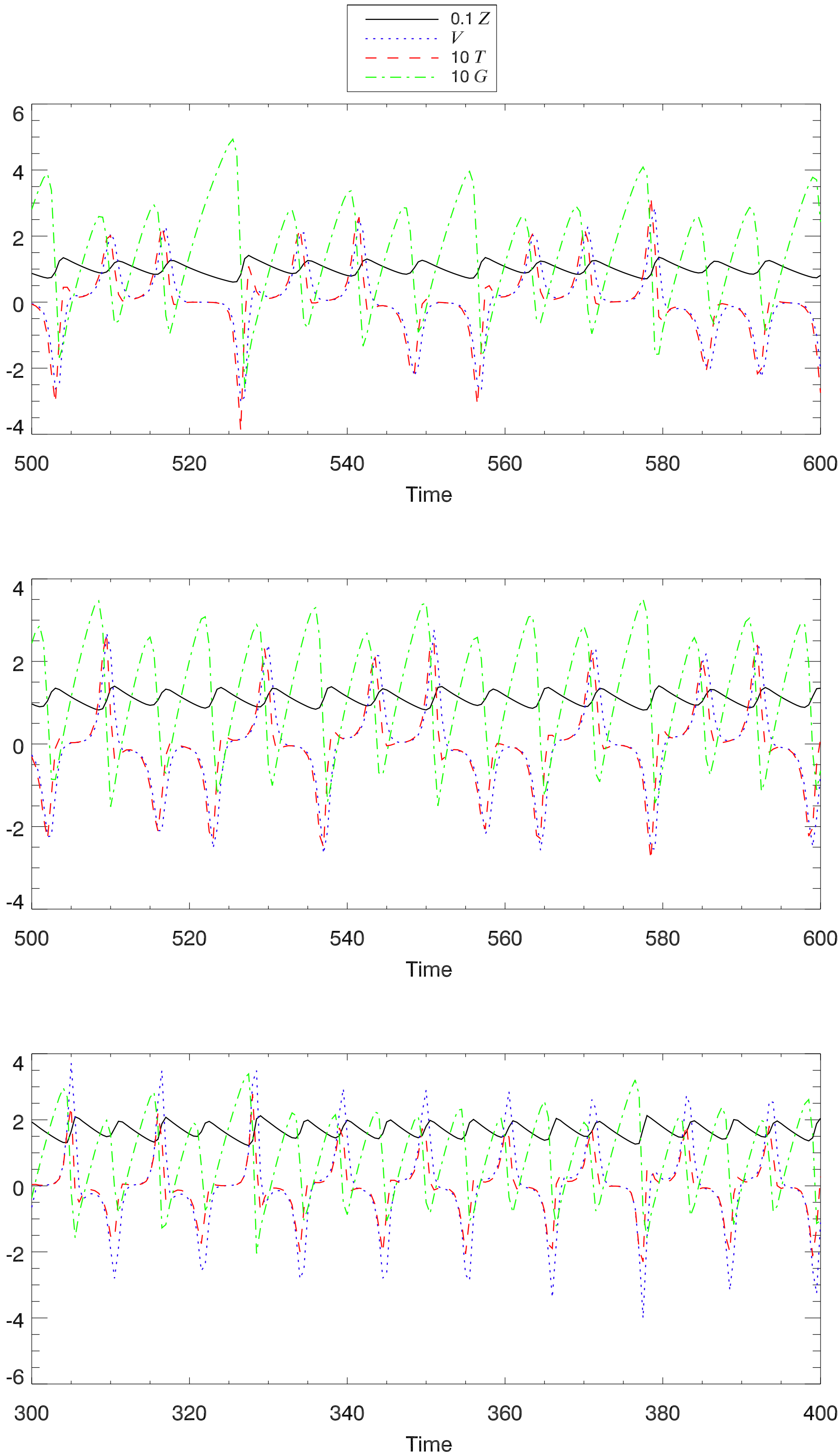

Figure 6.5: Plots showing the time evolution of the functions for $\Gamma = \{0.1, 0.1, 0.5, 0.1\}$. From the top the plots are for $Ra = 0.9Ra_c$, $Ra = Ra_c$ and $Ra = 2Ra_c$ respectively.

of the Rayleigh number for which this occurs as $\widetilde{Ra}$. We can then measure the depth of subcriticality (denoted by $Ra_c - \widetilde{Ra}$) for various parameter sets, the results of which are given in table 6.1. For parameter regimes where the critical Rayleigh number becomes large (for example large F and $c_Z \neq c_G$), the value of $\widetilde{Ra}$ remains relatively constant. This results in a large depth of subcriticality for these regimes due to the increased value of Ra_c.

Γ	Ra_c	$\widetilde{Ra}$	$Ra_c - \widetilde{Ra}$
$\{0.1, 0.1, 1, 0.1\}$	21.6236	12.5118	9.1118
$\{0.1, 0.01, 1, 0.1\}$	30.7341	10.1375	20.5966
$\{0.01, 0.01, 1, 0.1\}$	19.9536	8.4316	11.5220
$\{0.1, 0.1, 0.5, 0.1\}$	20.4274	12.7743	7.6531
$\{0.1, 0.1, 2, 0.1\}$	28.9975	15.9223	13.0752
$\{0.1, 0.1, 1, 0.2\}$	30.4251	13.7154	16.7097
$\{0.1, 0.1, 1, 0.3\}$	58.3434	18.7833	39.5601

Table 6.1: Numerically calculated values for the critical Rayleigh number and the depth of subcriticality for various parameter sets, Γ.

The linear theory of section 6.2 informed us that periodic solutions were possible and therefore it is not surprising to obtain periodic or quasi-periodic solutions in the non-linear theory. However, the linear theory was unable to predict the phase difference between the physical quantities Z, V, T and G. We see that in all plots in figures 6.3 to 6.5 that there is a common phase difference between the variables we plot. We see that V and T are completely in phase throughout so that the temperature fluctuations and the convective velocities are intrinsically linked, as expected. More significant is the phase relationship between V (or T) and the 'mean quantities' Z and G. The convective velocity is greatest in magnitude when the zonal flow acquires its minimum value. Conversely, during periods of strong zonal flow we find that V and T are relatively small. These phase relationships are in excellent agreement with results from chapter 5 and once again inform us that equations (6.1 - 6.4) provide a good model for the bursting phenomenon.

The similarity of the plots of figures 6.3 to 6.5 is clear, with few obvious differences despite the changing parameter regimes throughout the plots. This was also found to be the case for further parameter regimes tested and perhaps is the drawback of a simple model where the spatial dependence of the quantities has been removed. However, it is certainly clear from each of the three sets of plots that the period of the bursts becomes shorter for larger Rayleigh numbers. Equivalently, the frequency of the bursts increases as the Rayleigh number is increased. This is in agreement with the linear theory (see figures 6.1(a) to 6.1(f)) where ω increases with Ra.

6.5 Asymptotic theory for low diffusivity rates

In this section we consider the asymptotic limit of very low diffusion. We do this to simplify the model by effectively removing two parameters from the problem so that the parameter space to be covered is smaller. This limit is of interest since we saw in section 6.2 that reducing the diffusion rates lowered the critical Rayleigh number. The small diffusion limit is also a reasonable limit to take since we expect the physical diffusion rates to be small and the values that we worked with in sections 6.2 and 6.4 were small.

We assume equality between the small diffusion rates since this was the most preferable option for instability. Guided by the numerics we set

$$c_Z = \epsilon, \tag{6.83}$$

$$c_G = \epsilon, \tag{6.84}$$

$$V_0 = \epsilon^{1/2}\hat{V}_0, \tag{6.85}$$

for a small parameter ϵ and at this stage we do not assume the order of s. We also assume that the parameters F, Pr and Ra are $O(1)$. We are not interested in the null solution discussed in section 6.2 since it does not allow for bursting solutions. We substitute the expressions of equations (6.83 - 6.85) into the quartic for s given by equation (6.32) to get

$$\begin{aligned} s^4 + s^3 &\left[(1 + Pr + F\hat{V}_0^2) + 2\epsilon\right] \\ &+ s^2 \left[\epsilon\left(\hat{V}_0^2(1+4F) + 2(1+Pr)\right) + \epsilon^2\right] \\ &\quad + s\left[\epsilon\left(2F\hat{V}_0^4 + 2\hat{V}_0^2(Pr+F)\right) + \epsilon^2\left(\hat{V}_0^2(1+3F) + (1+Pr)\right)\right] \\ &\qquad + \epsilon^2\left(4F\hat{V}_0^4 + 2\hat{V}_0^2(Pr+F)\right) = 0. \end{aligned} \tag{6.86}$$

Since ϵ is a small parameter, in order for this equation to balance the order of s must be chosen accordingly. There are three different balances possible depending on the order of s. In each case the leading order balance is between two terms and the remaining terms are neglected since they are of a higher order. Firstly, by choosing $s = s_1 \sim O(1)$ a leading order balance of $O(1)$ is possible between the quartic and cubic terms in equation (6.86), which yields

$$s_1^4 + s_1^3 \left(1 + Pr + F\hat{V}_0^2\right) = 0 \tag{6.87}$$

$$\Rightarrow \quad s_1 = -\left(1 + Pr + F\hat{V}_0^2\right). \tag{6.88}$$

Secondly, by choosing $s = s_2 \sim O(\epsilon)$ a leading order balance of $O(\epsilon^2)$ is possible between the linear and constant terms, which gives

$$s_2\Big(2F\hat{V}_0^4 + 2\hat{V}_0^2(Pr + F)\Big) + \Big(4F\hat{V}_0^4 + 2\hat{V}_0^2(Pr + F)\Big) = 0 \tag{6.89}$$

$$\Rightarrow \quad s_2 = -\frac{\Big(4F\hat{V}_0^4 + 2\hat{V}_0^2(Pr + F)\Big)}{\Big(2F\hat{V}_0^4 + 2\hat{V}_0^2(Pr + F)\Big)}. \tag{6.90}$$

We observe from equations (6.88) and (6.90) that $s_1, s_2 \in \mathbb{R}$ so that the frequencies $\omega_1 = 0 = \omega_2$ and the growth rates $\sigma_1, \sigma_2 < 0$ for these first two possible cases since the terms within the brackets are all positive. Therefore both of these balances result in stability.

Thirdly, there is a leading order balance of $O(\epsilon^{3/2})$ between the cubic and linear terms if we choose $s = s_3 \sim O(\epsilon^{1/2})$ in equation (6.86). If this is the case we acquire

$$s_3^3 \left(1 + Pr + F\hat{V}_0^2\right) + s_3 \left(2F\hat{V}_0^4 + 2\hat{V}_0^2(Pr + F)\right) = 0 \tag{6.91}$$

$$\Rightarrow \quad s_3 = \pm \mathrm{i}\omega_3, \tag{6.92}$$

where

$$\omega_3 = \frac{\Big(2F\hat{V}_0^4 + 2\hat{V}_0^2(Pr + F)\Big)}{\Big(1 + Pr + F\hat{V}_0^2\Big)}. \tag{6.93}$$

Since s_3 is imaginary in this third case we have oscillatory modes. However, at leading order we have not acquired information as to whether this mode is growing or decaying. In order to determine this the next order of equation (6.86) must be considered with $s = \mathrm{i}\epsilon^{1/2}\omega_3 + \epsilon\sigma_3$. The sign of the growth rate, σ_3 will determine whether the mode is stable or unstable. Hence we consider equation (6.86) at $O(\epsilon^2)$, which is the next order and we find that

$$\omega_3^4 - 3\omega_3\sigma_3(1 + Pr + F\hat{V}_0^2) - \omega_3\left(\hat{V}_0^2(1 + 4F) + 2(1 + Pr)\right) \\ + \sigma_3\left(2F\hat{V}_0^4 + 2\hat{V}_0^2(Pr + F)\right) + 4F\hat{V}_0^4 + 2\hat{V}_0^2(Pr + F) = 0. \quad (6.94)$$

Given $\hat{V}_0$ and the reduced parameter set $\hat{\Gamma} = \{Pr, F\}$ and using the definition of ω_3 from equation (6.93) this equation can be solved for σ_3. The value of σ_3 will be real since all the terms in equation (6.93) are real and it only appears as a linear term. For a given $\hat{\Gamma}$, the sign of σ_3 will depend on $\hat{V}_0$, with $\sigma_3 < 0$ and $\sigma_3 > 0$ indicating a stable and unstable solution respectively.

We have found the four possible roots of the characteristic eigenvalue equation in the asymptotic diffusionless limit. Each root corresponds to one of the complex growth rates found numerically and displayed in the plots of figure 6.1 from section 6.2. The first two roots are purely real and are given by equations (6.88) and (6.90), which are also always stable. They correspond to the two growth rates σ_1 and σ_2 displayed in figure 6.1, found in the numerics to be exclusively stable also. The two remaining roots are complex conjugate pairs and are therefore oscillatory in nature. The growth rate of these two roots is given by σ_3 and the frequency is given by $\pm\omega_3$. They correspond to the growth rate, frequency pair (σ_3, ω_3) plotted in figure 6.1 and its conjugate. Of particular interest here is the scaling of the oscillatory modes where we have found that

$$s_3 = \mathrm{i}\epsilon^{1/2}\omega_3 + \epsilon\sigma_3. \quad (6.95)$$

This is significant since we have found a possible scaling for the frequency, and thus also the duration, of the bursts of convection. By recalling that $\epsilon = c_Z = c_G$ we see that the duration of the bursts scales inversely with the diffusion rates of the mean quantities: the zonal flow and the mean temperature gradient. Therefore smaller diffusion rates give rise to longer bursts.

In section 6.2 we developed a procedure for finding the critical Rayleigh number more efficiently by assuming there existed a Hopf bifurcation in the system. This gave rise to the condition given by equation (6.41). We may continue to consider this method for finding Ra_c here in the asymptotic limit. We substitute the expressions from equations

(6.83 - 6.84) into equation (6.41) whilst noting that the definitions of the P_is are found from equations (6.32 - 6.33). The leading order in equation (6.41) is then $O(\epsilon)$, which gives

$$\begin{aligned}&\left[2F\hat{V}_0^4 + 2\hat{V}_0^2(Pr+F)\right]^2 + \left[4F\hat{V}_0^4 + 2\hat{V}_0^2(Pr+F)\right]\left[1+Pr+F\hat{V}_0^2\right]^2 \\ &- \left[2F\hat{V}_0^4 + 2\hat{V}_0^2(Pr+F)\right]\left[\hat{V}_0^2\,(1+4F)+2(1+Pr)\right]\left[1+Pr+F\hat{V}_0^2\right] = 0. \qquad (6.96)\end{aligned}$$

All terms in equation (6.16), which relates V_0 to Ra are of the same order, that is $O(1)$, so that we retain all terms at leading order to give

$$Ra = F\hat{V}_0^4 + \hat{V}_0^2(F+Pr) + Pr. \qquad (6.97)$$

Given $\hat{\Gamma}$, equation (6.96) can be solved for $\hat{V}_0$ and provided non-zero real roots are found we choose the positive real root without loss of generality. This value of $\hat{V}_0$ is then used to find Ra from equation (6.97). However, if there are no non-zero real roots of equation (6.96) this method cannot be used, which indicates that there is not a Hopf bifurcation present. Therefore given values for Pr and F this procedure gives the critical Rayleigh number (where the stable branch becomes unstable via a Hopf bifurcation) in the diffusionless limit, provided equation (6.96) has non-zero real roots.

In figure 6.6 we plot the critical Rayleigh number found by this method against F for various values of the Prandtl number. We expect this plot to closely match plots of figure 6.2 in the numerics of section 6.2 where the diffusion is not asymptotically small. Indeed, as the diffusion rates are reduced through figures 6.2(a) to 6.2(d) there appears to be significant convergence to the asymptotic plot of figure 6.6. Differences however, are present. Although the asymptotics capture the essence of the numerics for large Prandtl numbers and also in the limits $F \to 0$ and $F \to 1/2$, there is discrepancy for moderate values of F at small Prandtl numbers. This discrepancy becomes more apparent as the Prandtl number is reduced and is clearly visible by comparing the $P = 0.1$ lines of figures 6.2(d) and 6.6.

Figure 6.6 also indicates that the critical Rayleigh number tends to infinity as $F \to 1/2 \quad \forall Pr$ and also as $F \to 0$ for certain Prandtl numbers. For $F > 1/2$ no non-zero real solutions of equation (6.96) are found so that this region of the parameter space does not admit a Hopf bifurcation. This again agrees with the numerics of section 6.2. In the asymptotic limit we can more easily investigate the behaviour at $F = 0$ and $F = 1/2$. To

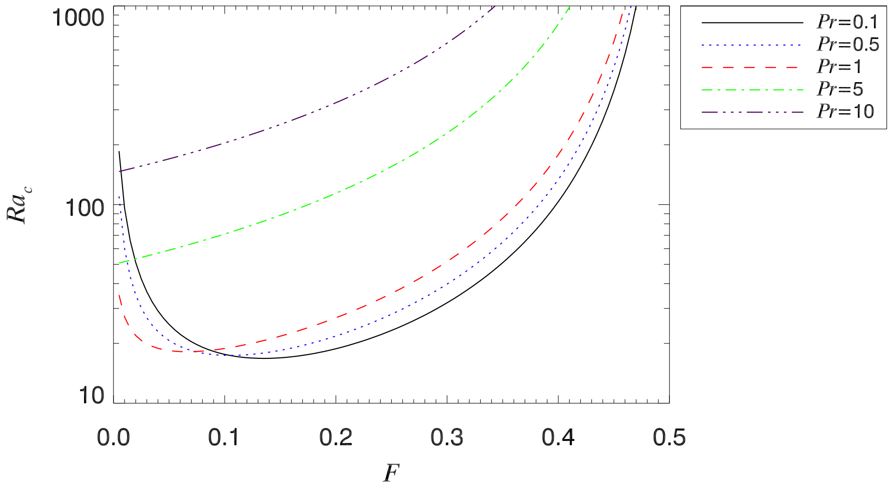

Figure 6.6: Plot showing how the critical Rayleigh number varies with the coupling parameter, F, for various values of the Prandtl number.

do this we expand equation (6.96) and collect the terms as coefficients of powers of $\hat{V}_0$ to give

$$\Big[2F^2(1-2F)\Big]\hat{V}_0^6 + \Big[2F\Big(3B(1-F) - A(1+2F)\Big)\Big]\hat{V}_0^4 + \Big[2B\Big(2B - A(1+4F)\Big)\Big]\hat{V}_0^2 - 2A^2B = 0, \quad (6.98)$$

where $A = 1 + Pr$ and $B = Pr + F$. In forming equation (6.98) we have also divided through by $\hat{V}_0^2$ and in doing so assumed that we are not interested in the null roots. Equation (6.98) is a sextic but also a cubic in $\hat{V}_0^2$. We are interested in whether this equation admits real roots. However it is difficult to make further analytic progress without choosing specific values for F. This is because although the discriminant of a cubic equation can determine how many roots are real, it cannot determine the sign of the real roots. Since we are presented with a cubic in $\hat{V}_0^2$, rather than $\hat{V}_0$, real roots of the sextic will only be found if real roots of the cubic are positive.

We must consider equation (6.98) for specific values of F. Immediately clear is that the degree of the polynomial reduces when $F = 0$ or $F = 1/2$ since higher order terms vanish for these values of F. This allows us to make further analytical progress. We first consider the case when $F = 0$ whereby equation (6.98) reduces from a sextic to a quadratic to give

$$2Pr\Big(2Pr - (1+Pr)\Big)\hat{V}_0^2 - 2Pr(1+Pr) = 0 \quad (6.99)$$

$$\Rightarrow \quad \hat{V}_0 = \pm\frac{1+Pr}{\sqrt{Pr-1}}. \quad (6.100)$$

This expression shows that there are only finite real values for $\hat{V}_0$ when $Pr > 1$ in the case when $F = 0$. Hence $\hat{V}_0$ is undefined when $F = 0$ for Prandtl numbers less than unity. This explains why the nature of the limit $F \to 0$ for $Pr > 1$ is qualitatively different to that for $Pr \leq 1$, which is observed in figure 6.6.

We can also consider the case $F = 1/2$ where we see that the polynomial in equation (6.98) reduces from a sextic to a quartic to give

$$\begin{aligned} \hat{V}_0^4 \left[3\left(\frac{1}{2} + Pr\right) - \frac{3}{2}\left(\frac{1}{2} + Pr\right) - 2(1+Pr) \right] \\ + \hat{V}_0^2 \left[2\left(\frac{1}{2} + Pr\right)\left(2\left(\frac{1}{2} + Pr\right) - 3(1+Pr)\right) \right] \\ - 2(1+Pr)^2\left(\frac{1}{2} + Pr\right) = 0 \end{aligned} \tag{6.101}$$

$$\Rightarrow \quad \frac{1}{2}\left(\frac{5}{2} + Pr\right)\hat{V}_0^4 + (1+2Pr)(2+Pr)\hat{V}_0^2 + (1+Pr)(1+2Pr) = 0. \tag{6.102}$$

Since this quartic is a quadratic in $\hat{V}_0^2$, the quadratic formula can be used to find the roots and thus

$$\hat{V}_0^2 = \frac{-2(1+2Pr)(2+Pr) \pm 2\sqrt{(1+2Pr)^2(2+Pr)^2 - (5+2Pr)\,(1+Pr)(1+2Pr)}}{5+2Pr}. \tag{6.103}$$

By taking the negative square root in this expression we find that $\hat{V}_0^2 < 0$, since $Pr > 0$. Thus, $\hat{V}_0$ always has an imaginary part in this case and it does not constitute a permissible solution. However, there is the possibility of $\hat{V}_0$ being purely real by taking the positive square root. This occurs if the quantity inside the square root is positive and the square root itself is larger than $(1+2Pr)(2+Pr)$. We now consider whether these two conditions can be satisfied together. Firstly the argument of the square root in equation (6.103) is

$$(1+2Pr)^2(2+Pr)^2 - 2\left(\frac{5}{2} + Pr\right)(1+Pr)(1+2Pr) \tag{6.104}$$

$$= (1+2Pr)\left(Pr - \frac{1}{2}\right)(2Pr^2 - 7Pr + 2) \tag{6.105}$$

$$= (1+2Pr)\left(Pr - \frac{1}{2}\right)\left(Pr - \frac{1}{4}(7+\sqrt{33})\right)\left(Pr - \frac{1}{4}(7-\sqrt{33})\right), \tag{6.106}$$

where we have used the quadratic formula in order to factorise the quadratic in Pr. This quantity is positive for $Pr > (7+\sqrt{33})/4$ and for $(7-\sqrt{33})/4 < Pr < 1/2$ and in figure

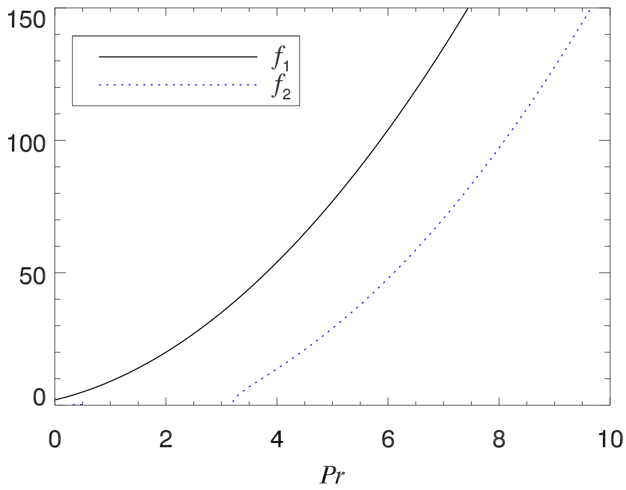

Figure 6.7: Plot depicting the dependence of the functions f_1 and f_2 on Pr.

6.7 we plot the two functions

$$f_1(Pr) = (1+2Pr)(2+Pr), \tag{6.107}$$

$$f_2(Pr) = \sqrt{(1+2Pr)\left(Pr-\frac{1}{2}\right)\left(Pr-\frac{1}{4}(7+\sqrt{33})\right)\left(Pr-\frac{1}{4}(7-\sqrt{33})\right)}, \tag{6.108}$$

against the Prandtl number. Figure 6.7 shows that $f_1 > f_2$ for all values of Pr and hence the expression for $\hat{V}_0^2$ given by equation (6.103) can never be greater than zero. Therefore for $F = 1/2$ there can be no real values for $\hat{V}_0$ and, as with the $F = 0$ case, the critical Rayleigh number tends to infinity as $\hat{V}_0$ becomes undefined.

We have shown in this section how the limits as $F \to 0$ and $F \to 1/2$ arise in the asymptotic limit of low diffusivity. When $Pr \leq 1$ the lack of a Hopf bifurcation, necessary for a bursting solution, for $F = 0$ and $F > 1/2$ results in the critical Rayleigh number for the onset of oscillatory modes tending to infinity as F approaches these limits. Hence there is a non-zero minimising value of the coupling parameter, which gives periodic solutions at the smallest possible Rayleigh number. With $Pr > 1$ the same limit exists as $F \to 1/2$, however there is a Hopf bifurcation for $F = 0$. Therefore, for larger Prandtl numbers, this results in oscillatory solutions occurring at the lowest value of Ra when $F = 0$. These results are in agreement with the numerics of section 6.2.

Chapter 7

Conclusions

In this chapter we summarise the research work of this thesis. The primary theme throughout this work has been an investigation of how zonal flows interact with thermal convection. In particular, we have looked at how zonal flows affect the onset of convection in chapters 2, 3 and 4. We have also considered the supercritical dynamics of convection and the production of zonal flows in chapter 5. Chapters 2 and 3 contained work performed in plane layer geometry with the zonal flow produced by a thermal wind whereas chapters 4 and 5 used the annulus geometry with the Reynolds stresses generating zonal flows.

In chapters 2 and 3 the way in which convective instability and baroclinic instability interact in rapidly rotating systems was elucidated. We found that the thermal wind destabilises convective modes, lowering the critical Rayleigh number at which they onset. We also find that the critical azimuthal wavelength at onset lengthens. At a sufficiently large Reynolds number, which in view of the very small viscosity occurring in many geophysical systems can correspond to a rather small thermal wind, instability becomes predominantly baroclinic, and the preferred azimuthal wavenumber tends to zero. In our ideal plane layer geometry, there is no restriction on possible wavelengths, but in more realistic spherical geometries, the boundaries will provide a limit. We found that convective modes and baroclinic modes are smoothly connected, going through a transition region which can be studied asymptotically where the critical Rayleigh number smoothly goes between positive and negative values. At the low azimuthal wavenumbers preferred by baroclinic modes, an asymptotic analysis is possible which gives good agreement with the numerics in the stress-free case, and illuminates which terms are important for instability. We also found that generally waves with non-zero latitudinal wavenumber k_y are not preferred in this problem, onset occurring in all cases examined at the lowest Ra when $k_y = 0$. At moderate Prandtl numbers, the onset of convection occurs with steady modes, but we found that at large Reynolds number oscillatory modes are preferred. This result links our finite diffusion work with the quasi-geostrophic shallow layer approximation used in atmospheric science, and in particular with the Eady problem.

The existence of baroclinic instability in the physical conditions obtaining in planetary interiors raises an interesting question of whether dynamo action could be driven by a heterogeneous core-mantle heat flux even if the core is stably stratified. This has also been investigated recently by Sreenivasan (2009) where lateral variations were found to support a dynamo even when convection is weak. It is widely believed that the heat flux passing from the Earth's core to its mantle can vary by order one amounts with latitude and longitude, as a result of cool slabs descending through the mantle and reaching the CMB from above. It is also generally believed that the key criterion for the existence of a dynamo is that convection should be occurring, and that the core is at least on average unstably stratified. However, this analysis has raised the possibility that instabilities leading to fluid motion driven by lateral temperature gradients can occur even when the fluid is strongly stably stratified. Of course, it is not yet known whether the resulting non-linear motions would be suitable for driving a dynamo. In the plane layer geometry used in chapters 2 and 3, the preferred motion appears to be two-dimensional and therefore will not drive a dynamo. However, in spherical geometry, and when secondary instabilities may occur, dynamo action may become possible, in which case the view that convection driven by an unstable temperature gradient is essential for dynamo action might have to be revised.

In chapter 4 we discovered that zonal flows in the annulus model can both stabilise and destabilise convection depending on the form of the flow in question. A linear flow pattern analogous to that used in the plane layer model was found to stabilise the system. However, the introduction of a sinusoidal flow pattern with multiple jets was found to destabilise convection. Both flow patterns resulted in a lengthening of the critical wavelength as the flow strength was increased in similarity with the plane layer model. However, for a large enough Reynolds number a transition to shear-dominated modes was found in the case of a sinusoidal flow pattern resulting in a possible shortening of the wavelength. Rotation stabilises the system as expected. However, interestingly a larger number of jets is destabilising since then the system can transfer to shear-dominated modes at a lower value of Re. This may be evidence of the desire for *multiple* jets to arise in the atmospheres of gas giants; by forming multiple jets a system becomes more susceptible to convection than would otherwise be possible.

We were able to explain several aspects of the results of chapter 4 by considering the potential vorticity, cementing its importance in understanding the multiple jet structure of the Jovian atmosphere as discussed in previous literature (Marcus & Lee, 1998). The potential vorticity gradient takes the role of the basic state rotation in our equations. If there are locations in the domain where the fluid vorticity gradient can partially balance the planetary vorticity gradient then the overall critical Rayleigh number of the whole system can be lowered. Instability then arises at these locations; for our sinusoidal flow pattern the location is the prograde jets. The limitations of this linear model include the fact that the basic state zonal flow has to be chosen and there are thus infinitely many possible forms for $U_0(y)$. We could envisage a flow pattern that more closely matches that seen in figure 1.3 for Jupiter such as that suggested by Marcus & Lee (1998).

The results of the non-linear annulus model in chapter 5 first produced good agreement with previous simulations (Jones *et al.*, 2003) with zonal flows readily occurring. The nature of the solutions can be rather different to that predicted by the linear theory. Multiple jets and a periodic nature of convection appearing in bursts can be found separately under certain parameter regimes. However, bursting multiple jet solutions do not appear to be possible or occur only for small windows of parameter regimes. As found in previous work by Rotvig & Jones (2006), rigid top and bottom boundaries are preferable for multiple jets whereas bursts of convection certainly prefer stress-free boundaries. Zonal flows are also found to be weaker with rigid boundaries implemented. We also found fluctuations in the mean temperature gradient on a similar timescale to the bursts of convection which have not been addressed in the previous literature.

As an extension to the previous work, we performed runs with $Pr \neq 1$. In general, increasing the Prandtl number depletes the strength of the zonal flow. The bursts of convection appear to be a phenomenon restricted to a finite range of Prandtl numbers.

At low Pr we found that bursts were possible but were weak unless the driving was large. For $Pr = 5$, bursting appears to cease even at large Rayleigh numbers suggesting that the convection is steady at large Prandtl numbers or requires a very large driving force to be oscillatory. For the linear growth rates of convection to cease, as required for existence of bursting, we found that both a strong zonal flow *and* a strong mean temperature gradient were required in the basic state of the linear theory. Thus, we are able to conclude that a necessary condition for periodic bursts of convection is the existence of both mean quantities. This is in contrast to previous work on the subject which assumed that the bursts were controlled by the zonal flow alone. Both mean quantities must drop below some critical value for a new burst of convection to occur.

In chapter 6 we developed a dynamical model for the bursting phenomenon that lacked the spatial dependence of the full equations. By allowing the zonal flow and the mean temperature gradient to evolve along with the small-scale velocity and temperature fluctuations we were able to reproduce many of the features of convective bursts seen in chapter 5. In particular, the linear theory of the simplified model showed that oscillatory solutions were only possible if both the zonal flow and mean temperature gradient evolution equations were included in the model.

It is not currently known if the jets of Jupiter (or any other gas giant for that matter) possess a periodic nature. The parameter regimes we have tested suggest it may be unlikely that the multiple jet structure of the Jovian atmosphere can coexist with bursts of convection. However, if the high latitude jets are driven by a different process to that of the strong equatorial jets (Heimpel *et al.*, 2005), it may be that some but not all jets display an oscillation in the zonal flow strength. Further observations of the wind speeds of the jets of the gas giants over time is required. The Juno mission is expected to launch this year and will be placed in a polar orbit of Jupiter in order make further observations of the planet including of the jet speeds (Matousek, 2007).

The work presented in this thesis has addressed various aspects of the interaction between convection and zonal flows. However, there are certainly further questions that could be asked. Perhaps the most obvious addition to the problems considered would be the introduction of a magnetic field since the physical systems of interest are known to possess dynamos. The rotation axis in the plane layer model could also be tilted so as to include the effects of the latitudinal dependence of the Coriolis force, whilst remaining in a simplified geometry. The introduction of curved, rather than sloped, end walls in the annulus model would be beneficial since this would more closely mimic spherical geometry and also set a preference for eastward equatorial jets. Better yet, our models could be extended to spherical geometry although this would create a significantly more complicated problem.

Appendix

A Differential Identities

For any vector fields $\mathbf{a}$ and $\mathbf{b}$:

$$\nabla \times (\mathbf{a} \times \mathbf{b}) = \mathbf{a}(\nabla \cdot \mathbf{b}) + (\mathbf{b} \cdot \nabla)\mathbf{a} - \mathbf{b}(\nabla \cdot \mathbf{a}) - (\mathbf{a} \cdot \nabla)\mathbf{b}, \tag{A.1}$$

$$\nabla \times (\nabla \times \mathbf{b}) = \nabla(\nabla \cdot \mathbf{b}) - \nabla^2 \mathbf{b}, \tag{A.2}$$

$$\mathbf{a} \cdot \frac{\partial \mathbf{a}}{\partial x} = \frac{1}{2}\frac{\partial}{\partial x}(\mathbf{a} \cdot \mathbf{a}) = \frac{1}{2}\frac{\partial}{\partial x}|\mathbf{a}|^2. \tag{A.3}$$

For vector fields $\mathbf{c}$ and $\mathbf{d}$ where $\mathbf{c} = \nabla \times \mathbf{d}$ we have

$$(\mathbf{c} \cdot \nabla)\mathbf{c} = \frac{1}{2}\nabla|\mathbf{c}|^2 - \mathbf{c} \times \mathbf{d}. \tag{A.4}$$

For any scalar field f:

$$\nabla \times (\nabla f) = 0, \tag{A.5}$$

$$\hat{\mathbf{z}} \cdot [\nabla \times (\nabla \times f\hat{\mathbf{z}})] = \frac{\partial^2 f}{\partial z^2} - \nabla^2 f = -\nabla_H^2 f, \tag{A.6}$$

where the horizontal Laplacian is defined as: $\nabla_H^2 = \partial^2/\partial x^2 + \partial^2/\partial y^2$.

B Useful identities

Beginning with the continuity equation, equation (1.9), and the definition of the vorticity: $\boldsymbol{\zeta} = \nabla \times \mathbf{u}$ we have that

$$\frac{\partial u_x}{\partial x} + \frac{\partial u_y}{\partial y} + \frac{\partial u_z}{\partial z} = 0, \tag{B.1}$$

$$\zeta = \frac{\partial u_y}{\partial x} - \frac{\partial u_x}{\partial y}, \tag{B.2}$$

where ζ is the z-component of the vorticity. Then if we take the x-derivative of (B.1) and the y-derivative of (B.2) we have

$$\frac{\partial^2 u_x}{\partial x^2} + \frac{\partial^2 u_y}{\partial x \partial y} + \frac{\partial^2 u_z}{\partial x \partial z} = 0, \tag{B.3}$$

$$\frac{\partial \zeta}{\partial y} = \frac{\partial^2 u_y}{\partial x \partial y} - \frac{\partial^2 u_x}{\partial y^2}. \tag{B.4}$$

and we can eliminate u_y from these equations to give

$$\nabla_H^2 u_x = -\left(\frac{\partial \zeta}{\partial y} + \frac{\partial^2 u_z}{\partial x \partial z} \right). \tag{B.5}$$

Similarly taking the y-derivative of (B.1) and the x-derivative of (B.2) and eliminating u_x gives

$$\nabla_H^2 u_y = \frac{\partial \zeta}{\partial x} - \frac{\partial^2 u_z}{\partial y \partial z}. \tag{B.6}$$

C Eigenfunction Identities

Let

$$v(x,z) = \frac{1}{2}\Big(\hat{v}(z)\exp(\mathrm{i}k_x x) + \hat{v}^*(z)\exp(-\mathrm{i}k_x x)\Big), \tag{C.1}$$

$$w(x,z) = \frac{1}{2}\Big(\hat{w}(z)\exp(\mathrm{i}k_x x) + \hat{w}^*(z)\exp(-\mathrm{i}k_x x)\Big), \tag{C.2}$$

where $\hat{v} = \hat{v}_{\mathrm{r}} + \hat{v}_{\mathrm{i}}$ and $\hat{w} = \hat{w}_{\mathrm{r}} + \hat{w}_{\mathrm{i}}$. Then

$$vw = \frac{1}{4}\Big(\hat{v}\hat{w}\exp(2\mathrm{i}k_x x) + \hat{v}\hat{w}^* + \hat{v}^*\hat{w} + \hat{v}^*\hat{w}^*\exp(-2\mathrm{i}k_x x)\Big), \tag{C.3}$$

$$\frac{\partial v}{\partial x} = \frac{\mathrm{i}k_x}{2}\Big(\hat{v}\exp(\mathrm{i}k_x x) - \hat{v}^*\exp(-\mathrm{i}k_x x)\Big), \tag{C.4}$$

$$\left(\frac{\partial v}{\partial x}\right)^2 = -\frac{k_x^2}{4}\Big(\hat{v}^2\exp(2\mathrm{i}k_x x) - 2\hat{v}\hat{v}^* + \hat{v}^*\exp(-2\mathrm{i}k_x x)\Big), \tag{C.5}$$

$$\frac{\partial^2 v}{\partial x^2} = -\frac{k_x^2}{2}\Big(\hat{v}\exp(\mathrm{i}k_x x) + \hat{v}^*\exp(-\mathrm{i}k_x x)\Big) = -k_x^2 v, \tag{C.6}$$

$$v\frac{\partial w}{\partial x} = \frac{\mathrm{i}k_x}{4}\Big(\hat{v}\hat{w}\exp(2\mathrm{i}k_x x) - \hat{v}\hat{w}^* + \hat{v}^*\hat{w} - \hat{v}^*\hat{w}^*\exp(-2\mathrm{i}k_x x)\Big). \tag{C.7}$$

Now let

$$\int \mathrm{d}V = \int_{-1/2}^{1/2}\int_{-\pi/k_x}^{\pi/k_x}\mathrm{d}x\mathrm{d}z. \tag{C.8}$$

Then for $n \in \mathbb{Z}$ and for any function $f(z)$

$$\begin{aligned}\int f(z)\exp(n\mathrm{i}k_x x)\mathrm{d}V &= \int_{-1/2}^{1/2} f(z)\mathrm{d}z \int_{-\pi/k_x}^{\pi/k_x}\exp(n\mathrm{i}k_x x)\mathrm{d}x \\ &= \int_{-1/2}^{1/2} f(z)\mathrm{d}z\left[\frac{\exp(n\mathrm{i}k_x x)}{n\mathrm{i}k_x}\right]_{-\pi/k_x}^{\pi/k_x} \\ &= 0,\end{aligned}$$

where we have used $\exp(n\mathrm{i}\pi) = \exp(-n\mathrm{i}\pi)$. Hence, using equations (C.3 - C.7)

$$\int v^2\mathrm{d}V = \frac{1}{2}\int \hat{v}\hat{v}^*\mathrm{d}V = \frac{1}{2}\int\Big(\hat{v}_{\mathrm{r}}^2 + \hat{v}_{\mathrm{i}}^2\Big)\mathrm{d}V, \tag{C.9}$$

$$\int vw\mathrm{d}V = \frac{1}{4}\int(\hat{v}\hat{w}^* + \hat{v}^*\hat{w})\mathrm{d}V, \tag{C.10}$$

$$\int\left(\frac{\partial v}{\partial x}\right)^2\mathrm{d}V = \frac{k_x^2}{2}\int\hat{v}\hat{v}^*\mathrm{d}V = \frac{k_x^2}{2}\int\Big(\hat{v}_{\mathrm{r}}^2 + \hat{v}_{\mathrm{i}}^2\Big)\mathrm{d}V, \tag{C.11}$$

$$\int v\frac{\partial w}{\partial x}\mathrm{d}V = \frac{\mathrm{i}k_x}{4}\int\Big(\hat{v}^*\hat{w} - \hat{v}\hat{w}^*\Big)\mathrm{d}V \tag{C.12}$$

$$= \frac{\mathrm{i}k_x}{4}\int\Big((\hat{v}_{\mathrm{r}} - \mathrm{i}\hat{v}_{\mathrm{i}})(\hat{w}_{\mathrm{r}} + \mathrm{i}\hat{w}_{\mathrm{i}}) - (\hat{v}_{\mathrm{r}} + \mathrm{i}\hat{v}_{\mathrm{i}})(\hat{w}_{\mathrm{r}} - \mathrm{i}\hat{w}_{\mathrm{i}})\Big)\mathrm{d}V \tag{C.13}$$

$$= \frac{k_x}{2}\int\Big(\hat{v}_{\mathrm{i}}\hat{w}_{\mathrm{r}} - \hat{v}_{\mathrm{r}}\hat{w}_{\mathrm{i}}\Big)\mathrm{d}V. \tag{C.14}$$

Bibliography

ABDULRAHMAN, A., JONES, C.A., PROCTOR, M.R.E., & JULIEN, K. 2000. Large wavenumber convection in the rotating annulus. *Geophys. Astrophys. Fluid Dynam.*, **93**, 227–252.

ANUFRIEV, A.P., JONES, C.A., & SOWARD, A.M. 2005. The Boussinesq and anelastic liquid approximations for convection in the Earth's core. *Phys. Earth Planet. Inter.*, **152**, 163–190.

AUBERT, J., BRITO, D., NATAF, H.C., CARDIN, P., & MASSON, J.P. 2001. A systematic experimental study of spherical shell convection in water and liquid gallium. *Phys. Earth Planet. Int.*, **128**, 51–74.

AURNOU, J., & OLSON, P. 2001. Strong zonal winds from thermal convection in a rotating spherical shell. *Geophys. Res. Lett.*, **28**, 2557–2559.

AURNOU, J., ANDREADIS, S., ZHU, L., & OLSON, P. 2003. Experiments on convection in the Earth's core tangent cylinder. *Earth Planet. Sci. Lett.*, **212**, 119–134.

BATCHELOR, G.K. 1967. *An introduction to fluid dynamics*. Cambridge University Press.

BÉNARD, H. 1900. Les tourbillons cellulaires dans une nappe liquide. *Revue Gén. Sci. Pur. Appl.*, **11**, 1261–1271.

BERCOVICI, D. 2007. Mantle dynamics past, present and future: an introduction and overview. *In:* BERCOVICI, D. (ed), *Treatise on geophysics, vol. 7: mantle dynamics*. Elsevier.

BOUSSINESQ, J. 1903. Théorie analytic de la chaleur. *Paris: Gauthier-Villars*, **2**, 172.

BOYD, J.B. 2001. *Chebyshev and Fourier spectral methods*. Dover.

BRAGINSKY, S.I. 1993. MAC-oscillations of the hidden ocean of the core. *J. Geomagn. Geoelectr.*, **45**, 1517–1538.

BRAGINSKY, S.I., & ROBERTS, P.H. 1995. Equations governing convection in the Earth's core and the geodynamo. *Geophys. Astrophys. Fluid Dynam.*, **79**, 1–97.

BRUMMELL, N.H., & HART, J.E. 1993. High Rayleigh number β-convection. *Geophys. Astrophys. Fluid Dynam.*, **68**, 85–114.

BULLARD, E.C., FREEDMAN, C., GELLMAN, H., & NIXON, J. 1950. The westward drift of the Earth's magnetic field. *Phil. Trans. R. Soc. A*, **243**, 67–92.

BUSSE, F.H. 1970. Thermal instabilities in rapidly rotating systems. *J. Fluid Mech.*, **44**, 441–460.

BUSSE, F.H. 1976. A simple model of convection in the Jovian atmosphere. *Icarus.*, **29**, 255–260.

BUSSE, F.H. 1986. Asymptotic theory of convection in a rotating, cylindrical annulus. *J. Fluid Mech.*, **173**, 545–556.

BUSSE, F.H. 2002. Convection flows in rapidly rotating spheres. *Phys. Fluids.*, **14**, 1301–1314.

BUSSE, F.H., & CARRIGAN, C.R. 1976. Laboratory simulation of thermal convection in rotating planets and stars. *Science.*, **191**, 81–83.

BUSSE, F.H., & OR, A. 1986. Convection in a rotating cylindrical annulus: thermal Rossby waves. *J. Fluid Mech.*, **166**, 173–187.

CANUTO, C.G., HUSSAINI, M.Y., QUARTERONI, A., & ZANG, T.A. 2006. *Spectral Methods: Fundamentals in Single Domains*. Springer.

CHANDRASEKHAR, S. 1961. *Hydrodynamic and Hydromagnetic Stability*. Oxford, Clarendon Press.

CHARNEY, J.G. 1947. The dynamics of long waves in a baroclinic westerly current. *J. Meteorology*, **4**, 135–162.

CHRISTENSEN, U.R. 2001. Zonal flow driven by deep convection in the major planets. *Geophys. Res. Lett.*, **28**, 2553–2556.

CHRISTENSEN, U.R. 2002. Zonal flow driven by strongly supercritical convection in rotating spherical shells. *J. Fluid Mech.*, **470**, 115–133.

CHRISTENSEN, U.R., AUBERT, J., CARDIN, P., DORMY, E., GIBBONS, S., GLATZMAIER, G.A., GROTE, E., HONKURA, Y., JONES, C., KONO, M., MATSUSHIMA, M., SAKURABA, A., TAKAHASHI, F., TILGNER, A., WICHT, J., & ZHANG, K. 2001. A numerical dynamo benchmark. *Phys. Earth Planet. Int.*, **128**, 25–34.

DEARDORFF, J.W. 1965. Gravitational instability between horizontal plates with shear. *Phys. Fluids*, **8**, 1027–1030.

DORMY, E., SOWARD, A.M., JONES, C.A., JAULT, D., & CARDIN, P. 2004. The onset of thermal convection in rotating spherical shells. *J. Fluid Mech.*, **501**, 43–70.

DRAZIN, P.G., & REID, W.H. 1981. *Hydrodynamic stability*. Cambridge University Press.

EADY, E.T. 1949. Long waves and cyclone waves. *Tellus*, **1**, 33–52.

FEARN, D.R. 1998. Hydromagnetic flow in planetary cores. *Rep. Prog. Phys.*, **61**, 175–235.

FEARN, D.R. 2007. The geodynamo. *Pages 201–256 of:* DORMY, E., & SOWARD, A.M. (eds), *Mathematical aspects of natural dynamos*. CRC Press.

FJØRTOFT, R. 1950. Application of integral theorems in deriving criteria of stability for laminar flows and the baroclinic circular vortex. *Geophys. Publ. Oslo*, **17**, 1–52.

GILLET, N., & JONES, C.A. 2006. The quasi-geostrophic model for rapidly rotating spherical convection outside the tangent cylinder. *J. Fluid Mech.*, **554**, 343–369.

GILMAN, P.A. 1977. Nonlinear dynamics of Boussinesq convection in a deep rotating spherical shell I. *Geophys. Astrophys. Fluid Dynam.*, **8**, 93–135.

GILMAN, P.A. 1978a. Nonlinear dynamics of Boussinesq convection in a deep rotating spherical shell II: Effects of temperature boundary conditions. *Geophys. Astrophys. Fluid Dynam.*, **11**, 157–179.

GILMAN, P.A. 1978b. Nonlinear dynamics of Boussinesq convection in a deep rotating spherical shell III: Effects of velocity boundary conditions. *Geophys. Astrophys. Fluid Dynam.*, **11**, 181–203.

GLATZMAIER, G.A., & ROBERTS, P.H. 1995. A three-dimensional convective dynamo simulation with rotating and finitely conducting inner core and mantle. *Phys. Earth Planet Int.*, **91**, 63–75.

GREENSPAN, H.P. 1968. *The theory of rotating fluids*. Cambridge University Press.

GROTE, E., & BUSSE, F.H. 2001. Correlation of Earth's magnetic field with lower mantle thermal and seismic structure. *J. Fluid Mech.*, **162**, 256–260.

GUBBINS, D., WILLIS, A.P., & SREENIVASAN, B. 2007. Correlation of Earth's magnetic field with lower mantle thermal and seismic structure. *J. Fluid Mech.*, **162**, 256–260.

HATHAWAY, D.H., GILMAN, P.A., & TOOMRE, J. 1979. Convective instability when the temperature gradient and rotation vector are oblique to gravity. I. Fluids without diffusion. *Geophys. Astrophys. Fluid Dynam.*, **13**, 289–316.

HATHAWAY, D.H., TOOMRE, J., & GILMAN, P.A. 1980. Convective instability when the temperature gradient and rotation vector are oblique to gravity. II. Real fluids with effects of diffusion. *Geophys. Astrophys. Fluid Dynam.*, **15**, 7–37.

HEIMPEL, M., AURNOU, J., & WICHT, J. 2005. Simulation of equatorial and high-latitude jets on Jupiter in a deep convection model. *Nature*, **438**, 193–196.

HOLLERBACH, R. 1996. On the theory of the geodynamo. *Phys. Earth Planet. Int.*, **98**, 163–185.

HOLLERBACH, R., & JONES, C.A. 1993. Influence of the Earth's inner core on geomagnetic fluctuations and reversals. *Nature*, **365**, 541–543.

HUTCHESON, K.A., & FEARN, D.R. 1995. The nonlinear evolution of magnetic instabilities in a rapidly rotating annulus. *J. Fluid Mech.*, **291**, 343–368.

JACOBS, J.A. 1984. *Reversals of the Earths magnetic field*. Cambridge University Press.

JONES, C.A. 2000. Convection driven geodynamo models. *Phil. Trans. Roy. Soc. A*, **358**, 873–897.

JONES, C.A. 2007. Thermal and compositional convection in the outer core. *In:* OLSON, P. (ed), *Treatise on geophysics, vol. 8: core dynamics*. Elsevier.

JONES, C.A., SOWARD, A.M., & MUSSA, A.I. 2000. The onset of convection in a rapidly rotating sphere. *J. Fluid Mech.*, **405**, 157–179.

JONES, C.A., ROTVIG, J., & ABDULRAHMAN, A. 2003. Multiple jets and zonal flow on Jupiter. *Geophys. Res. Lett.*, **30**, 1731.

LARMOR, J. 1919. How could a rotating body such as the Sun become a magnet? *Rep. Brit. Assoc. Adv. Sci.*, **87**, 159–160.

LIMAYE, S.S. 1986. Jupiter: new estimates of the mean zonal flow at the cloud level. *Icarus*, **65**, 335–352.

LORENZ, E.N. 1963. Deterministic non-periodic flows. *J. Atmos. Sci.*, **20**, 130–141.

MALKUS, W.V.R. 1994. Energy sources for planetary dynamos. *Pages 161–179 of:* PROCTOR, M.R.E., & GILBERT, A.D. (eds), *Lectures on solar and planetary dynamos*. Cambridge University Press.

MANNEVILLE, J.-B., & OLSON, P. 1996. Banded convection in rotating fluid spheres and the circulation of the Jovian atmosphere. *Icarus*, **122**, 242–250.

MARCUS, P.S., & LEE, C. 1998. A model for eastward and westward jets in laboratory experiments and planetary atmospheres. *Phys. Fluids*, **10**, 1474–1489.

MATOUSEK, S. 2007. The Juno New Frontiers mission. *Acta Astronaut.*, **61**, 932–939.

MERRILL, R.T., MCELHINEY, M.W., & MCFADDEN, P.L. 1996. *The magnetic field of the Earth - paleomagnetism, the core, and the deep mantle*. Vol. 63. Academic Press.

MOFFATT, H.K. 1978. *Magnetic field generation in electrically conducting fluids*. Cambridge University Press.

OLSON, P. 2003. Thermal interaction of the core and mantle. *In:* JONES, C.A., SOWARD, A.M., & ZHANG, K. (eds), *The fluid mechanics of astrophysicists and geophysicists, vol. 11: Earth's core and lower mantle*. Taylor and Francis.

OLSON, P., & AURNOU, J. 1999. A polar vortex in the Earth's core. *J. Geophys. Res.*, **402**, 170–173.

OR, A., & BUSSE, F.H. 1987. Convection in a rotating cylindrical annulus. Part 2. Transitions to asymmetric and vacillating flow. *J. Fluid Mech.*, **174**, 313–326.

PEDLOSKY, J. 1987. *Geophysical Fluid Dynamics*. Springer.

PORCO, C.C., WEST, R.A., & MCEWAN, A. *et al*. 2003. Cassini imaging of Jupiter's atmosphere, satellites and rings. *Science*, **299**, 1541–1547.

PROUDMAN, J. 1916. On the motion of solids in a liquid possessing vorticity. *Proc. Roy. Soc. A*, **92**, 408–424.

RASHID, F.Q., JONES, C.A., & TOBIAS, S.M. 2008. Hydrodynamic instabilities in the solar tachocline. *Astron. Astrophys.*, **488**, 819–827.

RAYLEIGH, LORD. 1880. On the stability, or instability, of certain fluid motions. *Proc. London Math. Soc.*, **11**, 57–70.

RAYLEIGH, LORD. 1916. On convective currents in a horizontal layer of fluid when the higher temperature is on the under side. *Philos. Mag.*, **32**, 529–546.

READ, P.L., GIERASCH, P.J., CONRATH, B.J., SIMON-MILLER, A.A., FOUCHET, T., & YAMAZAKI, Y.H. 2006. Mapping potential-vorticity dynamics on Jupiter I: Zonal-mean circulation from Cassini and Voyager 1 data. *Q. J. Roy. Meterol. Soc.*, **132**, 1577–1603.

READ, P.L., CONRATH, B.J., FLETCHER, L.N., GIERASCH, P.J., SIMON-MILLER, A.A., & ZUCHOWSKI, L.C. 2009. Mapping potential vorticity dynamics on Saturn: Zonal mean circulation from Cassini and Voyager data. *Planet. Space Sci.*, **57**, 1682–1698.

RHINES, P.B. 1975. Waves and turbulence on a beta-plane. *J. Fluid Mech.*, **69**, 417–443.

ROBERTS, P.H. 1968. On the thermal instability of a rotating fluid sphere containing heat sources. *Phil. Trans. Roy. Soc. A*, **263**, 93–117.

ROTVIG, J. 2007. Multiple zonal jets and drifting: Thermal convection in a rapidly rotating spherical shell compared to a quasigeostrophic model. *Phys. Rev. E*, **76**, 046306 (9 pages).

ROTVIG, J., & JONES, C.A. 2006. Multiple jets and bursting in the rapidly rotating convecting two-dimensional annulus model with nearly plane-parallel boundaries. *J. Fluid Mech.*, **567**, 117–140.

RUMFORD, COUNT. 1870. Of the propagation of heat in fluids. *Page 239 of: Complete Works, 1.* American Academy of Arts and Sciences, Boston.

SAKURABA, A., & KONO, M. 1998. Effect of the inner core on the numerical solution of the magnetohydrodynamic dynamo. *Phys. Earth Planet. Int.*, **111**, 105–121.

SAKURABA, A., & ROBERTS, P.H. 2009. Generation of a strong magnetic field using uniform heat flux at the surface of the core. *Nature Geosci.*, **2**, 802–805.

SCHMIDT, R.J., & MILVERTON, S.W. 1935. On the instability of a fluid when heated from below. *Proc. Roy. Soc. A*, **152**, 586–594.

SCHNAUBELT, M., & BUSSE, F.H. 1992. Convection in a rotating cylindrical annulus. Part 3. Vacillating and spatially modulated flows. *J. Fluid Mech.*, **245**, 155–173.

SPARROW, C. 1982. *The Lorenz equations: bifurcations, chaos, and strange attractors*. Springer-Verlag.

SQUIRE, H.B. 1933. On the stability of three-dimensional disturbances of viscous flow between parallel walls. *Proc. Roy. Soc. A*, **142**, 621–628.

SREENIVASAN, B. 2009. On dynamo action produced by boundary thermal coupling. *Phys. Earth Planet. Inter.*, **177**, 130–138.

SREENIVASAN, B., & JONES, C.A. 2005. Structure and dynamics of the polar vortex in the Earth's core. *Geophys. Res. Lett.*, **32**, L20301.

SREENIVASAN, B., & JONES, C.A. 2006. Azimuthal winds, convection and dynamo action in the polar region of the planetary cores. *Geophys. Astrophys. Fluid Dynam.*, **100**, 319–339.

STARCHENKO, S., & JONES, C.A. 2002. Typical velocities and magnetic field strengths in planetary interiors. *Icarus*, **157**, 426–435.

TAYLOR, G.I. 1922. The motion of a sphere in a rotating liquid. *Proc. Roy. Soc. A*, **102**, 180–189.

TEED, R.J., JONES, C.A., & HOLLERBACH, R. 2010. Rapidly rotating plane layer convection with zonal flow. *Geophys. Astrophys. Fluid Dynam.*, **104**, 457–480.

THOMSON, COUNT. 1882. On a changing tesselated structure in certain liquids. *Proc. Phil. Soc. Glasgow*, **13**, 464–468.

TILGNER, A., & BUSSE, F.H. 1997. Finite-amplitude convection in rotating spherical fluid shells. *J. Fluid. Mech.*, **332**, 359–376.

VALLIS, G.K. 2006. *Atmospheric and oceanic fluid dynamics*. Cambridge University Press.

VASAVADA, A.R., & SHOWMAN, A.P. 2005. Jovian atmospheric dynamics: an update after Galileo and Cassini. *Rep. Prog. Phys.*, **68**, 1935–1996.

WIGNER, E., & HUNTINGTON, H.B. 1935. On the possibility of a metallic modification of hydrogen. *J. Chem. Phys.*, **3**, 764–770.

YANO, J.-I. 1998. Deep convection in the interiors of the major planets: a review. *Aust. J. Phys.*, **51**, 875–889.

ZHANG, K. 1992. Spiralling columnar convection in rapidly rotating spherical shells. *J. Fluid Mech.*, **236**, 535–556.

ZHANG, K., & GUBBINS, D. 1996. Convection in a rotating spherical fluid shell with an inhomogeneous temperature boundary condition at finite Prandtl number. *Phys. Fluids*, **8**, 1141–1158.

ZHANG, K., & JONES, C.A. 1993. The effect of Ekman boundary layers on rotating convection. *Geophys. Astrophys. Fluid Dynam.*, **71**, 145–162.